

Toward the Clinical Application of the Prompt Gamma-Ray Timing Method for Range Verification in Proton Therapy

Dissertation

zur Erlangung des akademischen Grades
Doctor rerum naturalium (Dr. rer. nat.)

vorgelegt

der Fakultät Mathematik und Naturwissenschaften
der Technischen Universität Dresden

von

Dipl. Phys. Johannes Petzoldt
geboren am 05.04.1988 in Dresden

Institut für Kern- und Teilchenphysik
der Technischen Universität Dresden

2016

Eingereicht am 11.11.2016

Verteidigt am 08.05.2017

1. Gutachter: Prof. Dr. Kai Zuber

2. Gutachter: Prof. Dr. Wolfgang Enhardt

Kurzfassung

Die Prompt Gamma-Ray Timing (PGT) Methode ist ein vergleichsweise simpler Ansatz für die Reichweitenkontrolle in der Protonentherapie. Auf der Grundlage von früheren Experimenten wurden in dieser Arbeit verschiedene Schritte unternommen um die PGT Methode näher an die klinische Anwendung zu bringen. Im ersten Schritt wurden verschiedene Szintillationsmaterialien auf ihre Anwendbarkeit im Rahmen der PGT Methode untersucht. Hierbei wurde vor allem die Zeitauflösung bei hohen Photonenenergien im MeV-Bereich untersucht. Zusammenfassend hat sich gezeigt, dass der schnelle und lichtstarke Szintillator CeBr_3 in Kombination mit einem Sekundärelektronenvervielfältiger der Detektor der Wahl ist. In einer zweiten experimentellen Studie, welche an der Universitäts Protonen Therapie Dresden (UPTD) durchgeführt wurde, wurde die Protonenbündelstruktur des klinischen Strahles bezüglich ihrer zeitlichen Breite und der relativen Ankunftszeit charakterisiert. Die Ergebnisse werden für Simulationsstudien und Phasendrift-Korrekturen benötigt. Die gewonnenen Daten ermöglichten außerdem die erste 2D Bildgebung eines heterogenen Phantoms mittels prompter Gammastrahlung. Mit Hilfe der aus den ersten beiden Studien gewonnenen Resultaten wurde im letzten Schritt ein PGT-Prototyp entwickelt. Das Detektionssystem basiert auf einem CeBr_3 Detektor und einem neu entwickelten digitalen Spektrometer. Es wurde am Bremsstrahlungstrahl des ELBE Beschleunigers getestet, wo gezeigt werden konnte, dass das Gerät innerhalb der festgelegten Spezifikationen, wie Zeit- und Energieauslösung sowie Datendurchsatz, arbeitet. Schlussendlich wurde das PGT System zum ersten Mal unter klinischen Bedingungen im Behandlungsraum der UPTD eingesetzt. Hierbei konnten PGT Daten durch Abstrahlen von drei-dimensionalen Behandlungsplänen auf PMMA Phantome gewonnen werden. Dabei gelang es zum ersten Mal Reichweitevariationen von 5 mm mit einem unkollimierten Messsystem und bei klinisch relevanten Dosen nachzuweisen. Die gewonnenen Erkenntnisse helfen, die PGT Methode näher an die klinische Anwendung zu bringen.

Abstract

The prompt gamma-ray timing (PGT) method offers a relatively simple approach for range verification in proton therapy. Starting from the findings of previous experiments, several steps toward a clinical application of PGT have been performed in this work. First of all, several scintillation materials have been investigated in the context of PGT. The time resolution was determined at high photon energies in the MeV-region. In conclusion, the fast and bright scintillator CeBr_3 is the material of choice in combination with a timing photomultiplier tube as light detector. A second study was conducted at Universitäts Protonen Therapie Dresden (UPTD) to characterize the proton bunch structure of a clinical beam concerning its time width and relative arrival time. The data is mandatory as input for simulation studies and to correct for phase drifts. The obtained data could furthermore be used for the first 2D imaging of a heterogeneous phantom based on prompt gamma-rays. In a last step, a PGT prototype system was designed using the findings from the first two studies. The prototype system is based on a newly developed digital spectrometer and a CeBr_3 detector. The device is characterized at the ELBE bremsstrahlung beam. It was verified that the prototype operates within the specifications concerning time and resolution as well as throughput rate. Finally, for the first time the PGT system was used under clinical conditions in the treatment room of UPTD. Here, PGT data was obtained from the delivery of a three-dimensional treatment plan onto PMMA phantoms. The spot-by-spot analysis helped to investigate the performance of the prototype device under clinical conditions. As a result, range variations of 5 mm could be detected for the first time with an uncollimated system at clinically relevant doses. To summarize, the obtained results help to bring PGT closer to a clinical application.

Contents

List of Figures	ix
List of Tables	xiii
List of Acronyms and Abbreviations	xv
1. Introduction	1
1.1. Radiotherapy using Protons	1
1.1.1. Proton Interactions in Matter	2
1.1.2. Proton Range	3
1.1.3. Usage in Clinical Practice	4
1.1.4. Beam Production	5
1.2. Range Uncertainties	6
1.2.1. Sources of Range Variations	6
1.2.2. Implications for Clinical Practice	7
1.3. Reducing the Range Uncertainties	7
1.3.1. New CT Technologies	7
1.3.2. In-vivo Monitoring of the Proton Range	8
1.4. Outline of this Work	12
2. Theoretical Prerequisites	15
2.1. Terminology of Nuclear Reactions	15
2.1.1. Inelastic Nuclear Reactions occurring in Proton Therapy	15
2.1.2. Production of Positron Emitters	16
2.1.3. Production of Prompt Gamma Rays	16
2.1.4. Background Events	20
2.2. Principles for the Detection of High Energetic Photons	22
2.2.1. Interactions of Photons with Material	22
2.2.2. Attenuation Coefficients	24
2.3. Scintillation Detectors	25
2.3.1. Properties of Scintillation Materials	26
2.3.2. Light Readout	27
2.3.3. Properties of Scintillation Detectors	29

2.4.	Prompt Gamma-Ray Timing Method	31
2.4.1.	Principle	31
2.4.2.	Discovery	35
2.4.3.	PGT at a Clinical Accelerator	37
2.4.4.	Requirements for a Clinical PGT System	39
3.	Time Resolution of Scintillation Detectors	41
3.1.	Investigated Scintillation Materials	41
3.2.	Digital Silicon Photomultiplier	42
3.2.1.	Sensor Layout	43
3.2.2.	Data Acquisition	43
3.2.3.	Dark Count Map	45
3.2.4.	Photon Detection Efficiency	46
3.2.5.	Bias Voltage	46
3.2.6.	Data Handling and Timestamp Generation	47
3.2.7.	Practical Considerations	47
3.3.	Experimental Study on the Time Resolution at High Photon Energies	48
3.3.1.	Expected Timing Performance	48
3.3.2.	The Need for Monolithic Crystals	50
3.3.3.	Experimental Setup	50
3.3.4.	ELBE Accelerator: Excellent Timing Capabilities	51
3.3.5.	TOF Setup - RF as Clock Signal	52
3.3.6.	DPC Settings	53
3.3.7.	Data Analysis Procedure	53
3.3.8.	Results	57
3.4.	Discussion	61
3.5.	Applicability of the DPC in Clinical Practice	63
4.	Implications for PGT at a Clinical Facility	65
4.1.	Motivation	65
4.2.	Experimental Setup	66
4.2.1.	The IBA Proteus 235 System at UPTD	66
4.2.2.	Proton Bunch Monitor	68
4.2.3.	PGT Detector	69
4.2.4.	Readout Electronics	69
4.2.5.	Signal Processing	69
4.2.6.	Experimental Setup	70
4.3.	Methods	73
4.3.1.	Data Analysis	73

4.4.	Results	76
4.4.1.	Particle Identification	76
4.4.2.	Event Filtering	76
4.4.3.	Correction of RF-Bunch Phase Drifts and 2D PGT Imaging	77
4.4.4.	Systematic Measurements of Beam Parameters	82
4.5.	Discussion	90
5.	Prototype PGT Detector System under Therapeutic Conditions	93
5.1.	Introduction	93
5.2.	Solution - CeBr ₃ and the Digital Spectrometer U100	94
5.2.1.	CeBr ₃ Detector Setup	94
5.2.2.	U100 - Design	94
5.2.3.	Experimental Characterization based on Classical Analogue Electronics	96
5.2.4.	Experimental Characterization based on the U100 Spectrometer	97
5.3.	PGT under Clinical Conditions	100
5.3.1.	Materials and Methods	101
5.3.2.	First Results	104
5.3.3.	Spot-by-Spot Data Analysis	108
5.3.4.	Discussion	113
6.	Summary	119
A.	Appendix	121
A.1.	Time Resolution Measurements based on the DPC	121
A.2.	PGT under Clinical Conditions	125
	Bibliography	127

List of Figures

1.1.1.	Dose deposition of 15 MV bremsstrahlung photons, a 150 MeV proton beam, and a corresponding SOBP with 4 cm modulation.	2
1.1.2.	Stopping power of protons in water as a function of particle energy.	3
1.1.3.	Mean proton range in water as a function of particle energy.	4
1.2.1.	Dose deposition of protons and photons with and without range variation due to an air cavity.	6
2.1.1.	Prompt γ -ray spectrum produced by a proton beam impinging on a PMMA phantom.	17
2.1.2.	Differential cross section data of prompt γ -ray production when irradiating ^{12}C and ^{16}O with protons.	20
2.1.3.	Prompt γ -ray emission and proton dose deposition over the target depth.	21
2.4.1.	Detection principle of the PGT method.	32
2.4.2.	Proton transit time and kinetic energy as a function of the target depth.	33
2.4.3.	Simulated PGT spectrum for 150 MeV protons impinging on PMMA.	33
2.4.4.	Energy versus relative time distribution and PGT spectrum measured at KVI-CART.	36
2.4.5.	Experimental and simulated PGT spectra and PGT mean values for the stacked target experiment.	37
2.4.6.	PGT spectra measured at WPE for different beam energies.	38
3.2.1.	Schematic drawing and a photography of the DPC-3200 tile.	44
3.2.2.	Event acquisition sequence of the DPC.	44
3.2.3.	Photon detection efficiency of the DPC-3200.	46
3.3.1.	Experimental setup of the DPCs used at the bremsstrahlung facility of ELBE.	51
3.3.2.	Layout of the bremsstrahlung facility of ELBE.	52
3.3.3.	Photon count versus number of validated dies measured with CeBr_3 under different DPC settings at the ELBE bremsstrahlung beam.	54
3.3.4.	Photon counts measured with GAGG for different photon sources.	55
3.3.5.	Linear energy calibration functions and the relative LY of all crystals when used with the DPC.	56
3.3.6.	Energy versus relative time measured with LYSO without and with skew correction.	57

3.3.7.	Energy versus relative time measured with CeBr ₃ for different VLs.	58
3.3.8.	Energy versus relative time measured with CeBr ₃	59
3.3.9.	Time resolution versus energy measured with CeBr ₃	60
3.3.10.	Energy versus relative time measured with LYSO.	60
3.3.11.	Energy versus relative time measured with GAGG.	61
3.3.12.	Time resolution versus energy of all investigated materials.	62
4.2.1.	Schematic drawing of the proton therapy system of the UPTD facility.	67
4.2.2.	Schematic drawing of the proton bunch monitor.	68
4.2.3.	Block diagram of the experimental setup used to measure the proton bunches and PGT data.	71
4.2.4.	Schematic drawings of the experimental setups as well as photographs of the inhomogeneous target and the PBM setup.	72
4.3.1.	Energy deposition in plastic and both scintillators of PBM0.	75
4.4.1.	Exemplary 2D distribution of the short gate integral versus the long gate integral.	77
4.4.2.	Coincident time versus time of both PBMs without and with energy filters.	78
4.4.3.	Experimental data obtained with the PBM setup in campaign 1.	79
4.4.4.	PGT spectra measured in campaign 1 without and with phase drift correction.	81
4.4.5.	Schematic drawing of the inhomogeneous target, exemplary PGT difference spec- trum, and the 2D distribution of all PGT difference spectra.	83
4.4.6.	Comparison between the shapes of the relative time distributions measured with C2 and PBM0 for different beam energies.	84
4.4.7.	Relative time distributions measured with PBM0 for different beam energies and momentum limiting slit openings.	85
4.4.8.	Bunch time spread as a function of the beam energy for different momentum limiting slit openings.	86
4.4.9.	Bunch time spread at 225 MeV beam energy as a function of momentum limiting slit opening.	87
4.4.10.	Calculated bunch time spread as a function of the beamline length.	88
4.4.11.	Proton transmission rate as a function of the beam energy and for different momentum limiting slit openings.	89
4.4.12.	Absolute and relative energy spread as a function of the beam energy for different momentum limiting slit openings.	90
5.2.1.	Photography of the CeBr ₃ scintillation detector and the U100 digital spectrom- eter.	95
5.2.2.	Schematic drawing of the U100 digital spectrometer.	95
5.2.3.	Time resolution as a function of energy measured with CeBr ₃ and PMT readout.	97
5.2.4.	Energy versus relative time distribution measured at ELBE and the energy spec- trum measured using a ⁶⁰ Co source.	98

5.2.5.	Measured signal charge of the small CeBr ₃ detector as a function of detector load.	99
5.2.6.	Energy resolution as a function of trigger threshold and detector load.	100
5.2.7.	Time resolution as a function of energy for different trigger settings and detector loads.	101
5.3.1.	Schematic drawing and photography of the experimental setup for PGT measurements under clinical conditions as well as a drawing of the dose cube plan.	103
5.3.2.	Count rate versus measurement time of the PBS irradiation.	105
5.3.3.	Signal charge versus measurement time in PBS mode measured with p0006.	106
5.3.4.	Energy spectra measured in PBS mode with p0006.	107
5.3.5.	Energy versus relative time distribution and PGT spectra measured in PBS mode.	108
5.3.6.	Number of detected photons per spot of the distal layer and per incident number of protons and the average number of detected photons as a function of the lower energy threshold.	110
5.3.7.	PGT mean values of each spot of the distal layer measured with both detectors.	112
5.3.8.	PGT shift due to an air cavity for each spot of the distal layer measured with both detectors.	113
5.3.9.	Relative photon yield of the distal layer of a target with a bone insert in reference to a full PMMA measurement.	114
5.3.10.	Sensitivity of the PGT method under different scenarios.	117
A.1.1.	Energy versus relative time measured with GSO and BGO.	121
A.1.2.	Energy versus relative time measured with CaF ₂ (Eu) and CsI(Tl) for different TL and VS settings.	121

List of Tables

2.1.1.	Selection of prompt γ -rays for proton interactions with ^{12}C and ^{16}O	18
2.3.1.	Selection of inorganic scintillation materials with their most important properties.	28
3.2.1.	Different trigger level and validation scheme settings of the DPC.	45
3.3.1.	Integral photon detection efficiency, effective light yield and theoretical timing performance.	49
4.2.1.	Summary of the detector types used in both campaigns.	70
4.2.2.	Summary of the experimental setups used in both campaigns.	74
A.1.1.	Part one of the different settings used for the DPC at ELBE.	122
A.1.2.	Part two of the different settings used for the DPC at ELBE.	123
A.1.3.	Part three of the different settings used for the DPC at ELBE.	124
A.2.1.	Layer structure of the dose cube plan.	125
A.2.2.	List of delivered PBS plans and the corresponding target settings.	126

List of Acronyms and Abbreviations

ADC Analog to Digital Converter

BGO Bismuth-Germanate ($\text{Bi}_4\text{Ge}_3\text{O}_{12}$)

BTS Bunch Time Spread

C230 Cyclone 230

CC Coarse Counter

CT Computed Tomography

CFD Constant Fraction Discriminator

DCM Dark Count Map

DCR Dark Count Rate

DPC Digital Photon Counter

DS Double Scattering

dSiPM digital Silicon Photomultiplier

ELBE Electron Linear accelerator of high Brilliance and low Emittance

ESS Energy Selection System

FC Fine Counter

FPGA Field Programmable Gate Array

GAGG Gadolinium-Aluminum-Gallium-Garnet ($\text{Gd}_3\text{Al}_2\text{Ga}_3\text{O}_{12}$)

GSO Gadolinium-Oxy-Orthosilicate (Gd_2SiO_5)

HZDR Helmholtz-Zentrum Dresden-Rossendorf, Germany

IBA Ion Beam Applications SA, Louvain-La-Neuve, Belgium

KVI-CART KVI-Center for Advanced Radiation Technology, Groningen, the Netherlands

LY Light Yield

LYSO Lutetium-Yttrium-Oxy-Orthosilicate ($\text{Lu}_{2(1-x)}\text{Y}_{2x}\text{SiO}_5$)

MLSO Momentum Limiting Slit Opening

NIM Nuclear Instrumentation Module

PBM Proton Bunch Monitor

PBS Pencil Beam Scanning

PDE Photon Detection Efficiency

PDPC Philips Digital Photon Counting, Aachen, Germany

PET Positron Emission Tomography

PG Prompt Gamma ray

PGI Prompt Gamma-ray Imaging

PGS Prompt Gamma-ray Spectroscopy

PGT Prompt Gamma-ray Timing

PMMA Polymethyl Methacrylate ($\text{C}_5\text{O}_2\text{H}_8$)

PMT Photomultiplier Tube

PT-PET Particle Therapy Positron Emission Tomography

QDC Charge to Digital Converter

QE Quantum Efficiency

RF Radio Frequency

SiPM Silicon Photomultiplier

SOBP Spread-Out Bragg Peak

SPAD Single Photon Avalanche Diode

TDC Time to Digital Converter

TL Trigger Level

TOF Time-Of-Flight

UPTD Universitäts Protonen Therapie Dresden, Germany

VL Validation Length

VME Versa Module Eurocard

VS Validation Scheme

WET Water Equivalent Thickness

WPE Westdeutsches Protonentherapiezentrum Essen, Germany

1. Introduction

This chapter presents the clinical principles of proton therapy and the advantages to conventional radiotherapy. Furthermore, the main motivation of our work is described in more detail: The potential occurrence of range variations during the treatment. Their origin and the impact on clinical practice are shown. In a next step, several approaches for determining the proton range to improve the treatment quality are discussed. The focus is mainly set on monitoring methods. The status of selected state-of-the-art devices is shown with special emphasize on prompt γ -ray based concepts. Finally, the outline of this thesis is presented.

1.1. Radiotherapy using Protons

High energetic radiation as curative treatment is often applied in combination with chemotherapy or surgery and is one of the main cornerstones for the treatment of cancer. The principal concept is based on breaking the DNA strands of the tumour cells by ionizing the target atoms. Depending on the incident dose and on the ionization density of the impinging radiation, the DNA is less likely to repair itself possibly resulting in the death of the tumour cell. However, the applicable dose is often limited by radiation induced complications of the surrounding normal tissue. In summary, radiotherapy aims at controlling the tumour while minimizing side effects to the patient.

Nowadays, X-rays, produced by linear electron accelerators, are the most commonly used external radiation in radiotherapy. However, using protons and heavier ions instead of photons is gaining more and more importance due to the different physical and radio-biological properties of the heavy particles.

The situation is depicted in figure 1.1.1, showing the dose deposition of 15 MV bremsstrahlung photons and a proton beam of around 150 MeV. After a short build up region, the dose deposition of the photon beam reaches a maximum closely to the target entrance. Afterwards, the dose decreases exponentially as photons are statistically removed from the beam due to scattering and absorption processes with the target atoms. Thus, tissue in front and behind the tumour volume is exposed to severe radiation doses. Even by applying several fields, i.e. by irradiating from different directions, the energy deposition to normal tissue can only be spread over a higher volume without lowering its total amount.

In contrast, a proton continuously transfers energy via ionization as it traverses matter. The ionization density reaches a maximum, the so-called Bragg peak, which is close to the end of the particle range. For covering an extended tumour volume, the Bragg peak position can be varied by changing the beam energy. By applying several beams of different energy and with

an additional intensity modulation, the tumour volume can be conformally irradiated with a so-called Spread-Out Bragg Peak (SOBP) (see also figure 1.1.1). Besides the lower overall dose to normal tissue, the distal dose fall off behind the particle range can be used to spare organs at risk (OAR). Hence, the usage of protons offers, at least theoretically, a better outcome for the patient in terms of tumour control and reduced side effects compared to conventional radiotherapy based on photons.

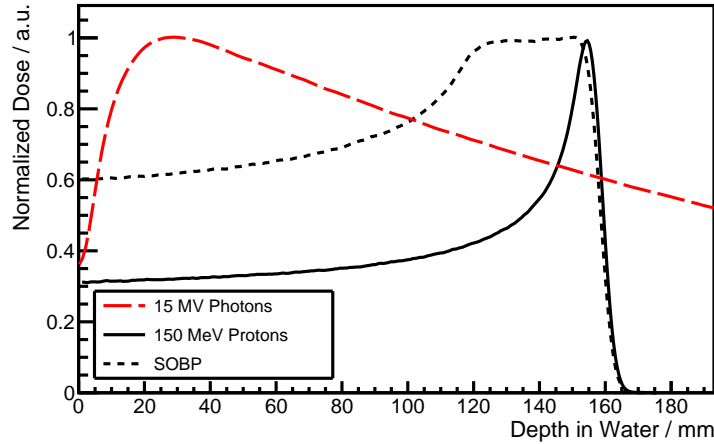


Figure 1.1.1.: Dose deposition of 15 MV bremsstrahlung photons, a 150 MeV proton beam, and a corresponding SOBP with 4 cm modulation. Courtesy of C. Hoinkis and P. Wohlfahrt.

1.1.1. Proton Interactions in Matter

The dose deposition of protons is not determined by the statistical thinning of the beam like for photons. Instead, protons mainly transfer their energy via electromagnetic interactions to electrons which then ionize the target atoms. The energy transfer is described by the stopping power $S(E)$ of the material or the mean loss of energy E per unit path length x of the particle:

$$S(E) = -\frac{dE}{dx}. \quad (1.1.1)$$

The mean energy loss of an individual charged particle travelling with velocity v and charge z in a medium with electron density n and a mean excitation potential I can be described by the relativistic Bethe formula [1]

$$\frac{dE}{dx} = \frac{4\pi n z^2}{m_e c^2 \beta^2} \cdot \left(\frac{e^2}{4\pi \epsilon_0} \right)^2 \cdot \left[\ln \left(\frac{2m_e c^2 \beta^2}{I \cdot (1 - \beta^2)} \right) - \beta^2 \right], \quad (1.1.2)$$

where m_e is the electron rest mass, c the speed of light, $\beta = v/c$, e the elementary charge, and ϵ_0 the vacuum permittivity. In the energy region used in particle therapy, the mean energy loss is

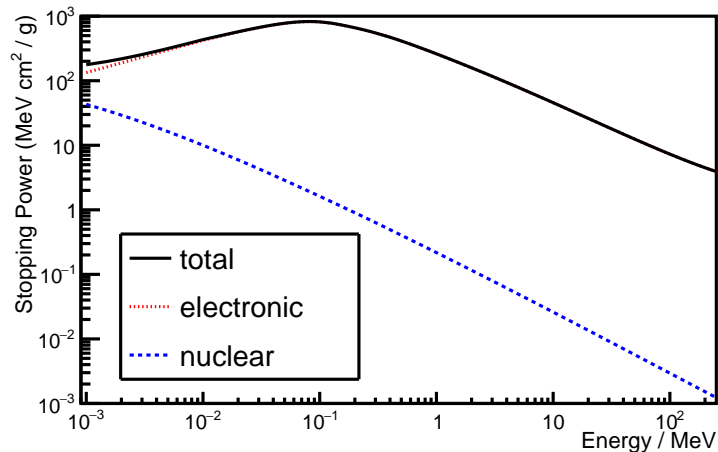


Figure 1.1.2.: Electronic (red), nuclear (blue), and total stopping power (black) of protons in water as a function of particle energy. Reproduced with data taken from [5].

proportional to $\frac{1}{v^2}$. Hence, the lower the particle's energy, the higher is the energy transfer to the material. Additional corrections from Bloch [2] and Barkas [3] are required in addition to (1.1.2) for describing the energy transfer from protons with energies between 0.5-230 MeV to material [4].

In reality, the interactions are subject to small statistical fluctuations, resulting in a broadening of the Bragg peak (see figure 1.1.1).

In addition to electronic interactions, protons undergo also elastic nuclear scattering with the target nuclei which also contributes to the dose deposition. The electronic, nuclear (comprising elastic scattering reactions), and total stopping power of protons in water are depicted in figure 1.1.2 using data from the proton stopping power and range tables (PSTAR) [5]. Especially the rapidly increasing energy transfer for lower particle energies is visible, which was already discussed as increased ionization density and dose deposition (see figure 1.1.1). We also see that the nuclear stopping power has only minor contributions to the total energy transfer.

For energies above the Coulomb barrier, also inelastic interactions between protons and the target nuclei can occur. The channels range from single nucleon exchange like (p,p') or (p,n)-reactions to the release of more than one nucleon. In the process, secondary particles (protons, neutrons, and other nuclear fragments) as well as de-excitation photons are released which also contribute to the overall dose deposition. However, their overall share is relatively small [4].

1.1.2. Proton Range

A mean proton range R can be defined by integrating the reciprocal of (1.1.1) from the incident energy E_0 to 0

$$R = - \int_{E_0}^0 \frac{1}{S(E)} dE. \quad (1.1.3)$$

The result as function of the particle energy is shown in figure 1.1.3. Obviously, the proton range can be chosen as required in the treatment by varying the kinetic energy. Furthermore, we see that protons with energies between 200-250 MeV are sufficient to penetrate enough tissue for irradiating also deep seated tumours as they exhibit ranges between 26-38 cm Water Equivalent Thickness (WET).

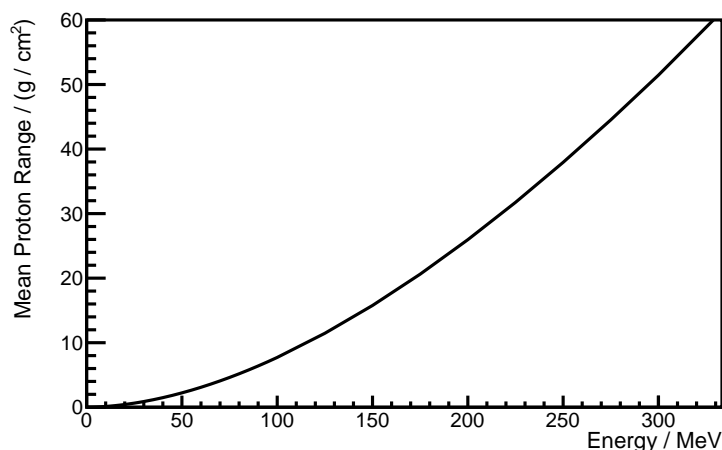


Figure 1.1.3.: Mean proton range in water as a function of particle energy. Reproduced with data taken from [5] using the Continuously Slowing Down Approximation (CSDA).

1.1.3. Usage in Clinical Practice

The radiological usage of proton beams was first proposed by Wilson in 1946 [6]. Since then, from the first treatment in 1954 [7] at Lawrence Berkeley Laboratory, Berkeley (USA), using a research synchrocyclotron, the conditions for the treatment shifted to commercially available particle therapy systems. In 2014, worldwide about 15,000 patients were treated with proton and ion beams in 48 facilities [8], with both numbers increasing every year.

The treatment is planned with the help of a Computed Tomography (CT) scan of the patient. After determining the tumour location, the Clinical Target Volume (CTV) is defined. According to the prescription by the physician, the treatment is divided into several fractions, each with a usual dose of about 2 Gy. Each fraction can be further divided into several radiation fields of lower incident dose.

Commonly, proton beams are delivered in two different modalities to the patient: via Double Scattering (DS) and Pencil Beam Scanning (PBS). In DS, the proton field is passively formed to the shape of the tumour volume. Thin metallic foils are used to increase the beam cross-section by scattering the pencil beam. The beam is then guided through the aperture where the field size is confined to the tumour shape. A range compensator is furthermore used for the distal field formation. For creating the SOBP, a combination of several Bragg peaks with varying intensity

is required. Here, the variation of the proton range is achieved by deploying a modulator wheel, which is a spinning wheel with steps of different WET. To vary the intensity of each mono-energetic Bragg peak, each step has a different angle on the wheel and the beam current is also modulated. As a result, a conformal dose distribution is created. However, scattering foils, modulator wheel, and the aperture produce γ -rays and neutrons, which create an additional background dose for the patient. Nevertheless, DS mode is used in most treatment facilities due to its robustness and the experience gathered over several decades.

On the other hand, PBS is a relatively new technique for patient treatment with a first system being tested in 1980 in Chiba (Japan) [9]. With PBS, the tumour volume is actively scanned by the pencil beam. The treatment volume is segmented into iso-energy layers perpendicular to the beam-direction, which are further divided into spots. By using two dipole magnets, the trajectory of the beam can be varied to precisely irradiate each spot position. Commonly, the treatment is started by delivering the distal layer, i.e. the layer with the highest range. After finishing a layer, the beam energy is reduced and the next layer is delivered. The dose for each spot can vary over several orders of magnitudes since the pencil beam size is usually bigger than the distance between neighbouring spots. Strong spots have usually up to 10^8 incident protons or more. In summary, the precise application of the pencil beam to the three-dimensional tumour volume is achievable when using PBS. Furthermore, because of the absence of the aperture etc., the additional background dose from neutrons and γ -rays is reduced.

1.1.4. Beam Production

Isochronous cyclotrons are often used at proton therapy facilities for the beam generation [10]. An ion source in the centre of the cyclotron provides a constant supply of hydrogen ions. The protons are accelerated by an electric field which alternates at a high frequency. This so-called Radio Frequency (RF) is fixed (naming the cyclotrons *isochronous*) and is usually in the range of 50-110 MHz. A magnetic field with magnitude B vertical to the electrical field is used to keep the protons on a circular orbit with radius r . The radius can be described as follows [11]:

$$r = \frac{m_p v}{qB}, \quad (1.1.4)$$

where m_p is the mass of the protons, v their velocity and q the electrical charge. With each acceleration step, the radius increases as the proton gains more kinetic energy. Hence, the proton follows a spiral path. For relativistic velocities ($v/c > 0.1$), the proton mass becomes also a function of the radius. As a result, the magnetic field strength $B(r)$ is increased to keep the resonance condition, i.e. a constant angular velocity at all radii [11]. If the so-called extraction radius is reached, the protons are extracted from the accelerator. Due to the constant acceleration process, a quasi continuous beam is produced with a time separation between successive extractions of $1/\text{RF}$, i.e. 9-20 ns.

Beam currents for patient treatment are usually around 2 nA [12, 13]. Therefore, under clinical

conditions, protons are not extracted as individual particles but as bunches. Those proton bunches comprise about 100-200 particles, where the exact number per bunch depends on the RF and the actual beam current. As a result, the beam exhibits a further microbunch structure in addition to the continuous macrobunch character, which will be important for further considerations.

1.2. Range Uncertainties

Protons are more prone to variations of the target composition compared to photons due to the different dose deposition characteristics.

Figure 1.2.1 depicts the situation for a dose distribution covering a tumour volume with a small range variation due to an air cavity compared to the planned case. In case of protons, the dose deposition drastically changes resulting in an overdosage to normal tissue and the OAR as well as an underdosage to the tumour volume. On the other hand, the dose deposition remains nearly similar when using photons. Hence, for proton therapy a varying range compared to the planned case has to be minimized or at least identified to guarantee a treatment according to the prescription. The origins of such range uncertainties are intensively discussed in [14] and will be briefly presented in the following.

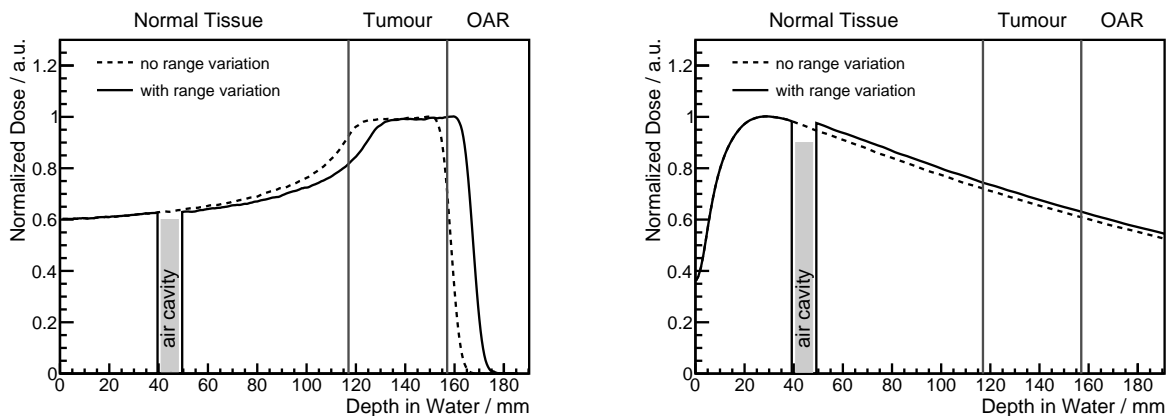


Figure 1.2.1.: Dose deposition of protons (left) and photons (right) with (solid lines) and without (dashed lines) range variation due to an air cavity (1 cm thickness). With a range variation, an overdosage to normal tissue and the organ at risk (OAR) as well as an underdosage to the tumour volume are visible for protons. In contrast, the dose deposition only slightly changes in case of photons. Courtesy of C. Hoinkis and P. Wohlfahrt.

1.2.1. Sources of Range Variations

The main source of range uncertainties is already introduced in the treatment planning phase. Here, the CT data is converted from Hounsfield Units (HUs), which are equivalent to the X-ray absorption in the material, to proton stopping power. The conversion is based on calibrated data

from CT measurements of phantoms with known density and elemental composition. However, those measurements incorporate uncertainties from statistical noise, as well as from the resolution of the CT scanner. Furthermore, different materials can result in the same X-ray attenuation while exhibiting different proton stopping power. The CT uncertainties are a function of the proton range and reach values of about 0.8% [14, 15, 16, 17, 18]. Furthermore, the mean excitation energy I is an experimentally determined parameter and hence afflicted by measurement uncertainties, contributing to the range uncertainty with about 1.5% [14].

Further range variations can arise from the patient setup and the beam reproducibility, together contributing with about 1 mm uncertainty [14]. Additionally, other sources like anatomical changes compared to the planning CT (e.g. tumour shrinkage, weight loss etc.) as well as organ motion have to be considered due to their potentially higher range variation.

In summary, range uncertainties from different sources occur in clinical practice. They can reach up to 1 mm plus an additional range dependent relative uncertainty of about 2.7 to 4.6% [14].

1.2.2. Implications for Clinical Practice

The occurrence of range uncertainties is considered by applying safety margins around the CTV. Hence, the increased treatment volume, the so-called Planning Target Volume (PVT), ensures the complete coverage of the tumour. This, however, increases the dose to normal tissue as the additional volume is irradiated like the tumour tissue which potentially reduces the benefits of protons compared to photons.

The safety margins vary from each facility, however, a fixed value plus an additional range dependent margin is usually applied [14]. In case of Universitäts Protonen Therapie Dresden, Germany (UPTD), 3.5% of the range plus an additional 2 mm are used¹.

For common clinical cases with proton ranges of 15 cm, the safety margin is about 7 mm. Consequently, improving the accuracy of the treatment below those 7 mm would mean a reduction of the margins and an increase of the therapeutic effect of the, compared to photons, more expensive ions.

1.3. Reducing the Range Uncertainties

1.3.1. New CT Technologies

The highest contribution to range uncertainties arises from the conversion of HUs to proton stopping power [14]. Hence, an improvement or even an avoidance of the conversion process would be highly advantageous. Two different approaches aiming at the reduction of conversion uncertainties are briefly shown in the following.

The first method tries to circumvent the conversion problem by Dual Energy CT (DECT)

¹Private communication with C. Golnik.

measurements utilizing two different electron acceleration voltages. As a result, the measured attenuation coefficients can be combined to extract information about the electron density and the effective atomic number Z_{eff} of the material [19] as both parameters are required for the stopping power (see equation 1.1.2). In a recent study [20], the relative electron density to water and Z_{eff} of 20 materials with known composition were calculated based on DECT data. They found agreement between the predicted stopping power ratio and the measured water-equivalent path lengths of the materials within 0.6% for most of the materials which is far below the stated 2% from Paganetti et al. [14].

An alternative approach is the direct usage of protons for diagnostic purposes instead of X-rays. Consequently, a unit conversion from the planning to the treatment phase is avoided. This so-called proton CT (pCT) promises a high potential for reducing range uncertainties [21]. However, the proton beam has to penetrate the body and its residual energy has to be measured e.g. in a calorimeter for obtaining the stopping power. With current treatment facilities, pCT is only applicable for the planning of tumour treatments in the head region. On the other hand, an all-round pCT would mean further developments and investments into new treatment facilities with higher available beam energies. Nevertheless, research is on-going at several institutes showing promising results of the imaging of complex phantoms [21].

1.3.2. In-vivo Monitoring of the Proton Range

In contrast to the previously described methods trying to reduce the uncertainties of treatment planning, concepts based on in-vivo monitoring aim at directly measuring the proton range and, with exceptions, even the dose deposition. In order to achieve this goal, different signatures of proton interactions with tissue are exploited. Most approaches like Particle Therapy Positron Emission Tomography (PT-PET) and Prompt Gamma-ray Imaging (PGI) utilize by-products from nuclear reactions between projectile and target nuclei. A list of selected concepts will be discussed in this section.

Particle Therapy Positron Emission Tomography

In PT-PET, the activity map of coincident 511 keV annihilation photons is measured to determine the distribution of β^+ decaying nuclei which were produced in nuclear reactions during the irradiation. The measured map of β^+ -activity is compared to a simulated one which is based on the planned dose distribution [22].

PT-PET systems are distinguished according to their utilization within the treatment procedure between in-beam (measurement during treatment, sometimes in beam pauses), in-room (scanner inside the treatment room), and offline Positron Emission Tomography (PET) (scanner in another room). Each implementation has different advantages and disadvantages. The overall time for a patient inside the treatment room decreases from in-room to offline PET (the additional time for in-beam measurements is negligible), which is a plus for offline PET concerning the patient throughput. However, the time between irradiation and diagnosis increases the other way round

(from 0 for in-beam to several minutes for offline PET). This means a lower remaining β^+ -activity in case of offline PET resulting in higher noise. Furthermore, biological washout effects due to blood flow etc. increase with higher waiting times and result in a blurring of the PET image [23]. The solution for most of those problems would be an in-beam PET scanner. However, those devices have to cope with very high detector loads and false coincidences coming from other photon sources and neutrons. Additionally, conventional full ring detectors are not applicable in every irradiation scenario as the beam path might be blocked by the scanner. This has implications on the reconstruction algorithms. The applicability of PT-PET as range verification system is therefore a trade-off between image quality (washout and β^+ -activity), clinical workflow (time per patient inside the treatment room), and technical feasibility (detector systems).

Up to now, PT-PET is the only clinically established method for range monitoring. The GSI Helmholtzzentrum für Schwerionenforschung in Darmstadt (Germany) was the first facility which included a treatment verification based on PET into their workflow [24]. The in-beam PT-PET system was used from 2004 until 2008 for more than 400 patients [25]. The ^{12}C -beam produced by the Schwerionensynchrotron (SIS18) had a suitable macro pulse structure for measurements in beam pauses, where the detector load is manageable. Nevertheless, the in-beam method from GSI has not yet been adapted to other types of accelerators like the more commonly used proton cyclotrons operated in a variety of facilities. Furthermore, protons are less favourable for PT-PET as the production yield of β^+ isotopes is lower and less concentrated close to the end of the particle range as it is for heavier ions. However, research is ongoing and experiments have been conducted at several research centres aiming at an in-beam PT-PET adapted to cyclotrons [26, 27].

Further treatment facilities applying PT-PET are located in Heidelberg (Germany) [28], Chiba (Japan) [29] and Boston (United States) [30, 31].

Prompt Gamma-Ray Imaging

Compared to the PET signal, Prompt Gamma rays (PGs) are a more direct probe for detecting the proton range. They emerge as de-excitation photons from nuclear reactions between protons and target nuclei within a timescale of pico- to nanoseconds at the interaction vertex. Furthermore, PGs mainly exhibit high energies between 1-15 MeV [32]. In addition, their emission profile is correlated with the dose deposition and the mass density [33, 34]. All those attributes make them the ideal probe for online range verification: they are not affected by biological washout, spatial uncertainties (like in PET, where the annihilation point is different from the interaction point due to the motion of the positron) and they undergo only slight attenuation inside the patient. However, the high photon energies are also a major drawback due to the lower interaction probability with a detection system. Furthermore, high background rates, mainly coming from neutrons as well as scattered protons and photons, have to be dealt with when measuring during the treatment.

The usage of PGs as treatment verification has been proposed in 2003 [35]. Since then, several concepts in the field of Prompt Gamma-ray Imaging (PGI) have emerged trying to determine

the spatial emission profile of the photons as it is a measure for the proton range and dose deposition. In order to obtain this goal, actively and passively collimated systems are being developed by research groups worldwide. The first category is dominated by Compton Cameras (CCs) which are commonly used in astrophysics for the detection of high energetic γ -ray bursts. In case of a two-stage CC, they exploit the Compton effect occurring in a scatter detector and a complete photoabsorption of the scattered photon in an absorber. By measuring the energy deposition in both detectors (Compton electron and scattered photon), as well as the position of both events, one can calculate the scattering angle according to the Compton equation. From this information, a cone opening can be retrieved resembling the possible positions of the emission point of the photon. With the detection of several events and by overlaying all obtained cones in a virtual plane, it is possible to reconstruct the origin of the photon emission, i.e. the spatial PG distribution. This reconstruction process can furthermore be optimized using maximum-likelihood estimation methods.

A two-stage CC based on a Cadmium Zinc Telluride (CZT) scatterer and a Bismuth-Germanate ($\text{Bi}_4\text{Ge}_3\text{O}_{12}$) (BGO) scintillation detector as absorber was developed in the research group at OncoRay [36, 37]. The position of a ^{22}Na γ -ray source could be successfully reconstructed as well as the emission point of a 4.44 MeV photon source [37]. However, it was also found that the probability of a true Compton event (scattering plus photoabsorption) is very low in the energy region of PGs [37]. Hence, with the limited dose deposition in a real treatment scenario, an insufficient number of events is detected to ensure a proper reconstruction [37]. This major drawback could be encountered by increasing the number of detectors, which then, on the other hand, heavily increases the cost and the complexity of the system. Several types of CCs are currently under investigation [38, 39, 40, 41, 42, 43, 44], however, none has yet shown its applicability under clinical conditions.

In contrast to CCs, a simpler approach is sought by passively collimated systems. They are usually based on a spatially-resolved detector plane and a collimator, whose designs vary from pinhole [45], knife-edge slits [46], and coded apertures [47]. The collimator usually consist of tungsten to absorb most of the background radiation and to be as opaque as possible for PGs. The idea of a such a system is to map the spatial PG emission on the detector plane by using the collimator design as an optical system. Up to now, the single knife-edge slit camera of Ion Beam Applications SA, Louvain-La-Neuve, Belgium (IBA) [46] was the first and only device used for range verification based on PGs in patient treatment [48]. In comparison to actively collimated systems, the efficiency of the slit camera is sufficient to detect range shifts of 2 mm under clinical conditions [49]. However, the size of the detector plane as well as the collimator make the system not only expensive but also very heavy and voluminous which is problematic in the limited space of the treatment room.

The Need for a simpler Method

A suitable detector system meeting the requirements in the field of PGI is usually very complex, expensive and has a large footprint. Different approaches are therefore aiming at the detection of other information encoded in the PG signals. Especially, Prompt Gamma-ray Spectroscopy (PGS) [50] and Prompt Gamma-ray Timing (PGT) [51] have shown the feasibility to detect the proton range by deploying a rather simple setup. While PGS will be briefly described in the following, the PGT method is the main rationale of this work and will be, after a short introduction in this section, discussed in more detail in section 2.4.

Prompt Gamma-Ray Spectroscopy In principle, PGS relates measurements of discrete PG lines to nuclear reactions cross sections to extract information about the proton range and the target composition [50]. PGS aims therefore at determining the yield of several PG lines at a certain target depth. Using the ratio of the intensities of those distinctive lines and combining this information with existing cross section data, it is possible to retrieve the primary proton energy at this discrete target depth, and then the residual range.

Hence, the proton range can be determined by deploying several detector devices, where each is aligned to a different target depth. In order to resolve the γ -lines, very high energy resolution as well as sufficient background discrimination is required. Furthermore, as the detector should only measure events from a certain depth in the target, a collimated system is required. Additional Time-Of-Flight (TOF) information [52], i.e. measuring the arrival time of the photons relative to the incident proton beam, is used to reduce uncorrelated background.

The PGS method was first proposed in 2014 [50] and is currently being developed at Massachusetts General Hospital, Boston (USA). The detector setup is based on a 3" \times 3" LaBr₃ scintillator coupled to a Photomultiplier Tube (PMT) with custom digital readout. A tungsten collimator with a slit opening of 9.5 mm realizes the alignment to the desired target depth. An anti-Compton shielding consisting of four BGO crystals reduces background from uncorrelated sources as well as from photons leaving the detector after an initial interaction so that only full energy depositions are counted. The detector system uses the accelerator RF to realize a TOF setup. By selecting PGs in the TOF information, neutron induced reactions and other background sources are reduced.

Although the realization uses heavy collimators as well as expensive detectors and electronics, the method itself is very simple and shows very promising results. Verburg et al. report the possibility to detect range shifts of about 2 mm at clinical relevant doses [50]. First measurements in patient treatment are planned with a prototype system comprising 8 detector units [53].

Prompt Gamma-Ray Timing Like PGS, the PGT method is also based on a single scintillation detector operated in a TOF setup [52]. However, PGT waives any kind of collimation making the technique less complex and easier to integrate. The basic idea is to measure the proton transit time through matter as it is a function of the particle range [51]: the further the proton travels,

the more time is required to reach its end point, and the longer PGs are emitted. The time-wise PG emission can be measured by detecting the arrival time of the photon relative to the incident proton, usually by using the RF of the accelerator as reference signal.

The correlation between proton transit time and PG emission was first shown in 2013 in an experimental study where homogeneous targets of different thickness were irradiated with proton beams [51]. The PG emission was measured against the RF of the accelerator with a scintillation detector of decent time resolution. The capability to detect target variations could be verified by analysing the first and second momenta of the PGT spectra, i.e. mean and variance. With raising target thickness, the mean value shifted to higher relative times and the variance of the PGT peak increased. Hence, Golnik et al. [51] could show that the proton range can be retrieved from the PGT information.

In a further experiment, the method was tested in a clinical environment [12]. Dedicated scintillation detectors for timing measurements were deployed. Measurements with homogeneous targets were performed for different beam energies. Furthermore, by including inhomogeneities like bone inserts or air cavities, the feasibility to detect range shifts of 5 mm at clinical relevant doses was shown. However, instabilities of the RF signal of the accelerator were observed which could potentially destroy the detection of range variations. Furthermore, the beam characteristics varies for different energy and beamline settings and has therefore consequences on the detectability of range shifts. Both implications need further investigation to bring the PGT method closer to a clinical application.

1.4. Outline of this Work

The potential of proton therapy in contrast to conventional radiotherapy is diminished by range uncertainties as they induce the application of safety margins around the tumour volume. An online range verification system is therefore key to guarantee the advantages of proton beams, namely the conformal dose deposition and the sparing of normal tissue. Several signatures induced by proton interactions are investigated for a potential range verification system. Especially, PGs offer the possibility to verify the particle range *in-vivo* during the treatment. However, detection concepts in the field of PGI, aiming for the spatial information, require high investments due to the complexity of such systems. In contrast, the PGT method is as an alternative and more simple approach.

In this thesis, the PGT method is further developed from the experimental phase toward a prototype system for the application in clinical practice. Consequently, in chapter 2 the basic principles, like the production of PGs and the detection of high energetic photons using scintillation detectors, are discussed. Additionally, the route is drawn from the discovery of PGT, the first experiments in a clinical facility to the requirements for a prototype system. The implementation of each requirement is further discussed in an individual chapter.

First, different scintillation materials for an application in the PGT prototype system are in-

investigated in chapter 3. The time resolution is hereby the main rationale without losing sight to more practical considerations, like detection efficiency and availability of the material. The investigation concludes with a detector system to consist of a CeBr_3 scintillation crystal and a PMT as light detector.

In the next step, the obstacles for PGT at a clinical therapy system are investigated in chapter 4. The investigation is motivated by the results from [12], where RF instabilities and energy dependent beam characteristics have been observed. In more detail, phase drifts between the RF signal and the arrival time of the proton bunches can potentially destroy the detection of range variations and have to be identified and corrected for. Additionally, the PGT spectra are smeared out by the intrinsic time width of the bunches, which we will later refer to Bunch Time Spread (BTS). This parameter is of great importance as it determines the sensitivity of the PGT method, i.e. which range shift is detectable for a certain treatment scenario. Consequently, the BTS is investigated in a dedicated study at the UPTD for different beam energies and settings of the therapy system.

Finally, the clinical prototype system is presented and tested in chapter 5. The PGT detection unit is characterized at the ELBE accelerator concerning detector load and throughput rate as well as energy and time resolution. The results are presented to evaluate the performance of the newly developed digital spectrometer U100, which serves as compact readout electronics. The prototype is further used for the first application of PGT under clinical conditions. 3D PBS plans are delivered to simple phantoms and the PG emission is measured by two detector units. The PGT data is analysed spot-by-spot to evaluate the number of detected PGs per spot which determines the achievable sensitivity of the prototype system. Additionally, range shifts due to an air cavity and a bone insert could be detected based on the analysis of PGT and photon yield data, respectively.

2. Theoretical Prerequisites

For a better understanding of Prompt Gamma rays (PGs) as range verification probe, the underlying nuclear reactions as well as the most dominant PG lines are discussed in this chapter. The energy dependent cross sections for the production of the de-excitation photons will also be presented. Furthermore, the basic interactions between photons and matter as well as the principle of γ -ray measurements based on scintillation detectors are discussed.

In a next step, the possibility to determine the proton range by using the timing information of PGs is shown. The discovery of the PGT approach is discussed as well as the proof-of-principle experiment performed at a medical accelerator. Additionally, the requirements for a clinical range verification system are outlined.

2.1. Terminology of Nuclear Reactions

In the irradiation of a material with a high energetic particle beam, the projectiles can trigger different reactions with the target nuclei. The possible reaction channels are divided into elastic and inelastic types, where the first one describes the change in direction of the projectile without changing its energy in the centre-of-mass frame. In inelastic nuclear reactions however, energy is transferred between the reaction partners. Occasionally, the projectile is captured by the target nucleus and single nucleons, smaller nuclei or other fragments are knocked-out.

In general, the reaction rate of an event dR to occur in a thin target slice with thickness dx is a function of the density of atoms in the target n and the energy dependent cross-section $\sigma(E)$:

$$dR = \sigma(E) \cdot n \cdot dx. \quad (2.1.1)$$

The cross-section parameter includes hereby all relevant physical processes and is usually subject of experimental studies. For a fixed target density (i.e. $n = \text{const.}$), $\sigma(E)$ determines therefore the probability of an event. Hence, for a concrete question the cross-section data can be used to select the most important reaction channels.

2.1.1. Inelastic Nuclear Reactions occurring in Proton Therapy

In case of proton therapy, therapeutic beams with energies between 70 and 200 MeV are impinging on soft tissue. The human body is, except from bone structures, mainly composed of carbon, oxygen, and hydrogen atoms. Hence, when neglecting isotopes with small natural abundances,

the target composition is made of ^1H , ^{12}C , and ^{16}O . The inelastic reaction channels vary from (p, p') -scattering to following types of knockout-reactions (which are not possible for ^1H):

- The exchange of a single nucleon: (p, n) , (p, p') .
- The knockout of light nuclei: (p, d) , (p, t) , $(p, ^3\text{He})$, (p, α) .
- A combination of both, e.g. $(p, 2p)$, $(p, p'n)$, $(p, p'2n)$, $(p, \alpha n)$, etc.

As a consequence, neutrons, secondary protons and heavier nuclei fragments are released possibly with energies up to that of the primary proton. They may interact also within the target material producing further cascades of secondary radiation until they are stopped. High energetic neutrons, however, have relatively small interaction probabilities and can leave the target, which will play an important role when discussing the background problematic in PG measurements.

2.1.2. Production of Positron Emitters

In the different knockout-reactions on ^{12}C and ^{16}O , several isotopes of oxygen, nitrogen, carbon, and boron are produced. Some of them are stable (e.g. ^{15}N , ^{14}N , ^{13}C , ^{10}B , etc.), while others further decay via β^- - or β^+ -emission or electron capture. In case of β^+ -decay, a positron is emitted, which, after slowing down, annihilates with an electron. Following, two 511 keV photons are emitted in opposite direction [54] which is exploited in PT-PET. Hereby, especially ^{11}C and ^{15}O are interesting nuclei due to their high production yield and their moderate half-lives of 20.4 min and 122.2 s, respectively. In case of in-beam PT-PET, also the detection of shorter-lived isotopes like ^{12}N with a half-life $T_{1/2} = 11$ ms is considered due to the high immediate activity [55].

2.1.3. Production of Prompt Gamma Rays

After a nuclear collision, the remaining nucleus is usually left in an excited state, i.e. nucleons are on a higher energy level compared to the ground state. With typical lifetimes τ between 10^{-19} to 10^{-9} s, the nuclei transition from their excited to the ground state. In this process, one or more γ -rays are emitted. The emission is anisotropic and depends on the individual decay [56]. Because of their origin and the time scale of the emission after the nuclear reaction, the photons are called Prompt Gamma rays (PGs). They have discrete energies (except for the continuum states at higher excitation levels), usually in the MeV-range, and vary for each residual nucleus. As previously discussed, mostly carbon, oxygen, and hydrogen atoms are irradiated by the proton beam. ^1H has no excitation levels and is therefore no source of PGs. However, the presence of hydrogen is important for later background considerations (see section 2.1.4). Thus, PGs are mainly produced in proton interactions with ^{12}C and ^{16}O . Given the number of neutrons and protons from the projectile and the target, all nuclei with atomic number $Z \leq 9$ and neutron number $N \leq 8$ can be produced. However, not all of them have short-lived excitation levels in the interesting energy region, or the corresponding reaction cross sections are small (for details,

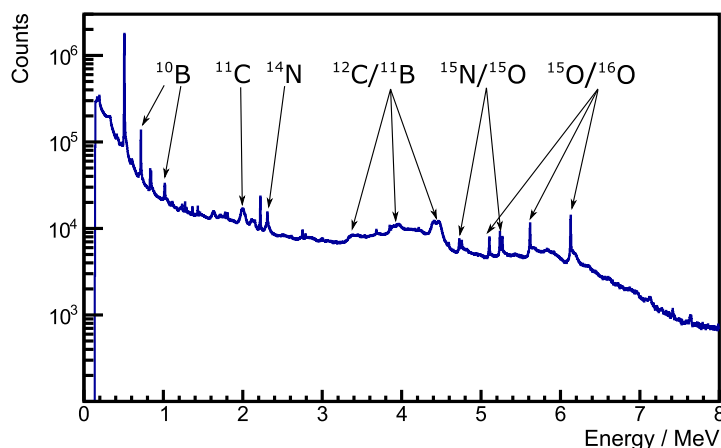


Figure 2.1.1.: Prompt γ -ray spectrum produced by a 150 MeV proton beam impinging on a PMMA phantom measured with a HPGe detector at KVI-CART, Groningen (the Netherlands).

see below). Accordingly, using selected data from [50, 57] and nuclear databases [58], a list of the most important PG lines for proton interactions on ^{12}C and ^{16}O and the corresponding nuclear reactions is shown in table 2.1.1. We see a wide range of γ -lines between 0.718-7.3 MeV with an exception of a ^{12}C de-excitation photon with 15.10 MeV. Most nuclei de-excite to the ground state. Others, however, branch into different channels with intermediate steps resulting in a γ -ray cascade (e.g. $^{10}\text{B}^{*1.740} \rightarrow ^{10}\text{B}^{*0.718} \rightarrow ^{10}\text{B}^{\text{gs}}$).

An experimental PG energy spectrum is shown in figure 2.1.1. The measurement was performed with a 150 MeV proton beam impinging on a Polymethyl Methacrylate ($\text{C}_5\text{O}_2\text{H}_8$) (PMMA) phantom which was used as its material composition is similar to soft tissue. The photons were measured with a high purity germanium (HPGe) detector with an energy resolution far below 1% to individually resolve the γ -ray lines.

Several energy lines from table 2.1.1 can be identified as sharp peaks in the energy spectrum, like 0.718 MeV from $^{10}\text{B}^*$, 2.313 MeV from $^{14}\text{N}^*$ and further peaks between about 4.7 and 6.2 MeV. Here, several peaks are actually from the same PG but with different energy deposition in the detector, which is a result of pair production processes and annihilation photons leaving the detector volume. Thus, for a certain high energetic line (e.g. 6.129 MeV), there is the so-called Single Escape (SE) peak (one 511 keV photon escapes) at 5.618 MeV and the Double Escape (DE) peak at 5.107 MeV. Further details can be found in section 2.2.1.

Furthermore, broader structures at about 2 and 4.44 MeV are visible. Those peaks correspond e.g. to the de-excitation of $^{11}\text{C}^{*2.000}$ and $^{12}\text{C}^{*4.439}$ to the ground state, respectively. Their wider shape is a result of a Doppler broadening due to the motion of the residual nucleus [50, 59]. In case of 4.44 MeV, the SE and DE peak are also visible.

Besides PGs, several lines from other sources can be identified, like 511 keV from annihilation

Table 2.1.1.: Selection of prompt γ -rays produced in nuclear reactions between protons and ^{12}C or ^{16}O , respectively. Data taken from [50, 57, 58].

Energy (MeV)	Transition	Nuclear Reaction	Mean life (s)
0.718	$^{10}\text{B}^{*0.718} \rightarrow \text{g.s.}$	$^{12}\text{C}(p, x)^{10}\text{B}^*$	1.0×10^{-9}
		$^{12}\text{C}(p, x)^{10}\text{C}(\epsilon)^{10}\text{B}^*$	27.8
		$^{16}\text{O}(p, x)^{10}\text{B}^*$	1.0×10^{-9}
1.022	$^{10}\text{B}^{*1.740} \rightarrow ^{10}\text{B}^{*0.718}$	$^{12}\text{C}(p, x)^{10}\text{B}^*$	7.5×10^{-15}
		$^{16}\text{O}(p, x)^{10}\text{B}^*$	7.5×10^{-15}
1.436	$^{10}\text{B}^{*2.154} \rightarrow ^{10}\text{B}^{*0.718}$	$^{12}\text{C}(p, x)^{10}\text{B}^*$	1.5×10^{-12}
1.635	$^{14}\text{N}^{*3.948} \rightarrow ^{14}\text{N}^{*2.313}$	$^{16}\text{O}(p, x)^{14}\text{N}^*$	6.9×10^{-15}
1.885	$^{15}\text{N}^{*7.155} \rightarrow ^{15}\text{N}^{*5.270}$	$^{16}\text{O}(p, 2p)^{15}\text{N}^*$	1.2×10^{-15}
2.000	$^{11}\text{C}^{*2.000} \rightarrow \text{g.s.}$	$^{12}\text{C}(p, x)^{11}\text{C}^*$	1.0×10^{-14}
2.035	$^{15}\text{O}^{*7.276} \rightarrow ^{15}\text{O}^{*5.241}$	$^{16}\text{O}(p, x)^{15}\text{O}^*$	4.9×10^{-13}
2.124	$^{11}\text{B}^{*2.125} \rightarrow \text{g.s.}$	$^{12}\text{C}(p, 2p)^{11}\text{B}^*$	5.5×10^{-15}
2.154	$^{10}\text{B}^{*2.154} \rightarrow \text{g.s.}$	$^{12}\text{C}(p, x)^{10}\text{B}^*$	1.5×10^{-12}
2.313	$^{14}\text{N}^{*2.313} \rightarrow \text{g.s.}$	$^{16}\text{O}(p, x)^{14}\text{N}^*$	9.8×10^{-14}
2.742	$^{16}\text{O}^{*8.872} \rightarrow ^{16}\text{O}^{*6.130}$	$^{16}\text{O}(p, p')^{16}\text{O}^*$	1.8×10^{-13}
2.794	$^{14}\text{N}^{*5.106} \rightarrow ^{14}\text{N}^{*2.313}$	$^{16}\text{O}(p, x)^{14}\text{N}^*$	4.4×10^{-12}
2.804	$^{11}\text{C}^{*4.804} \rightarrow ^{11}\text{C}^{*2.000}$	$^{12}\text{C}(p, d)^{11}\text{C}^*$	$< 7.6 \times 10^{-15}$
2.868	$^{10}\text{B}^{*3.587} \rightarrow ^{10}\text{B}^{*0.718}$	$^{12}\text{C}(p, x)^{10}\text{B}^*$	1.0×10^{-13}
3.684	$^{13}\text{C}^{*3.685} \rightarrow \text{g.s.}$	$^{16}\text{O}(p, x)^{13}\text{C}^*$	1.6×10^{-15}
3.853	$^{13}\text{C}^{*3.854} \rightarrow \text{g.s.}$	$^{16}\text{O}(p, x)^{13}\text{C}^*$	1.2×10^{-11}
4.438	$^{12}\text{C}^{*4.439} \rightarrow \text{g.s.}$	$^{12}\text{C}(p, p')^{12}\text{C}^*$	6.1×10^{-14}
		$^{16}\text{O}(p, x)^{12}\text{C}^*$	6.1×10^{-14}
4.444	$^{11}\text{B}^{*4.445} \rightarrow \text{g.s.}$	$^{12}\text{C}(p, 2p)^{11}\text{B}^*$	5.6×10^{-19}
4.804	$^{11}\text{C}^{*4.804} \rightarrow \text{g.s.}$	$^{12}\text{C}(p, d)^{11}\text{C}^*$	$< 7.6 \times 10^{-15}$
5.105	$^{14}\text{N}^{*5.106} \rightarrow \text{g.s.}$	$^{16}\text{O}(p, x)^{14}\text{N}^*$	6.3×10^{-12}
5.180	$^{15}\text{O}^{*5.181} \rightarrow \text{g.s.}$	$^{16}\text{O}(p, x)^{15}\text{O}^*$	$< 4.9 \times 10^{-14}$
5.240	$^{15}\text{O}^{*5.241} \rightarrow \text{g.s.}$	$^{16}\text{O}(p, x)^{15}\text{O}^*$	3.3×10^{-12}
5.269	$^{15}\text{N}^{*5.270} \rightarrow \text{g.s.}$	$^{16}\text{O}(p, 2p)^{15}\text{N}^*$	2.6×10^{-12}
5.298	$^{15}\text{N}^{*5.299} \rightarrow \text{g.s.}$	$^{16}\text{O}(p, 2p)^{15}\text{N}^*$	1.2×10^{-14}
6.129	$^{16}\text{O}^{*6.130} \rightarrow \text{g.s.}$	$^{16}\text{O}(p, p')^{16}\text{O}^*$	2.7×10^{-11}
6.175	$^{15}\text{O}^{*6.176} \rightarrow \text{g.s.}$	$^{16}\text{O}(p, x)^{15}\text{O}^*$	$< 2.3 \times 10^{-14}$
6.322	$^{15}\text{N}^{*6.324} \rightarrow \text{g.s.}$	$^{16}\text{O}(p, 2p)^{15}\text{N}^*$	1.0×10^{-15}
6.337	$^{11}\text{C}^{*6.339} \rightarrow \text{g.s.}$	$^{12}\text{C}(p, x)^{11}\text{C}^*$	$< 1.1 \times 10^{-13}$
6.476	$^{11}\text{C}^{*6.478} \rightarrow \text{g.s.}$	$^{12}\text{C}(p, x)^{11}\text{C}^*$	$< 8.7 \times 10^{-15}$
6.741	$^{11}\text{B}^{*6.743} \rightarrow \text{g.s.}$	$^{12}\text{C}(p, 2p)^{11}\text{B}^*$	4.3×10^{-20}
6.790	$^{11}\text{B}^{*6.792} \rightarrow \text{g.s.}$	$^{12}\text{C}(p, 2p)^{11}\text{B}^*$	5.6×10^{-19}
6.916	$^{16}\text{O}^{*6.917} \rightarrow \text{g.s.}$	$^{16}\text{O}(p, p')^{16}\text{O}^*$	6.8×10^{-15}
7.115	$^{16}\text{O}^{*7.117} \rightarrow \text{g.s.}$	$^{16}\text{O}(p, p')^{16}\text{O}^*$	1.2×10^{-14}
7.299	$^{15}\text{N}^{*7.301} \rightarrow \text{g.s.}$	$^{16}\text{O}(p, 2p)^{15}\text{N}^*$	1.4×10^{-16}
15.10	$^{12}\text{C}^{*15.11} \rightarrow \text{g.s.}$	$^{12}\text{C}(p, p')^{12}\text{C}^*$	1.5×10^{-17}

photons or 2.225 MeV from thermal neutron capture in hydrogen [60].

Altogether, we see that the intensities of the PG lines vary over several orders of magnitude which is partly an effect of the energy dependent interaction probability between photons and detector material (further details are discussed in section 2.2.1).

Cross Section Data

In addition to the detection probability, the intensity of each measured line depends on the number of produced PGs and therefore on the production cross section of the corresponding states (see (2.1.1)).

The first direct¹ cross section measurements have been performed by [61, 62]. However, only few data points were taken with NaI(Tl) scintillation detectors exhibiting only a decent energy resolution. Consequently, further experimental studies [63, 64, 65, 66] used HPGe detectors to resolve the individual γ -ray lines. The obtained results have been combined in [57] with indirect proton recoil measurements to cover a wider range of incident proton energies.

In a more recent study by Verburg et al. [50], cross section data was determined with respect to the requirements for a PG measurement in proton therapy (e.g. proton energy range, detector position, etc.). By irradiating homogeneous H₂O and (CH₂)_n targets with a 165 MeV proton beam, PG signals were measured using a collimated 3" × 3" LaBr₃ detector system (see section 1.3.2 for more details). The detector provides sufficient energy resolution and detection efficiency to resolve most of the lines. The detection unit was located perpendicular to the beam axis and consecutively monitored the photon emission at 90 different targets depths (i.e. at 90 proton energies). The differential cross section data has been obtained as part of the development of the PGS method and was optimized at lower proton energies with previously published data [61, 62, 65, 66, 67]. The results are shown in figure 2.1.2. Note that several PG lines have been combined in the presented data as they can not be resolved individually with the deployed detector. Furthermore, not all lines from table 2.1.1 have been included in the work of Verburg et al. [50]. This is a result of the reduction to the, for PGS and other proton range verification methods, relevant energies. Very high energies (e.g. the 15.10 MeV line) are hardly detectable, while PGs with energies below about 2 MeV are shadowed by the high uncorrelated background (see section 2.1.4 for details).

In case of ¹²C as target nuclei, 4.44 MeV γ -rays, produced in the ¹²C(*p*, *p'*)¹²C*-reaction, have the highest cross section in the interesting proton energy region. Furthermore, the reaction has the lowest energy threshold (i.e. *Q*-value) compared to other channels and the yield peaks at about 17 MeV proton energy, which is close to the proton stopping point. In contrast, the irradiation of ¹⁶O produces more high energetic PG lines. The 6.1 MeV peak, a combination of 6.129 MeV (from ¹⁶O*) and 6.175 MeV (from ¹⁵O*), has the highest production cross section over most of the energy region, the lowest *Q*-value, and an increased production close to the stopping

¹Direct means in this case to measure the γ -ray yield for a known detection efficiency and to calculate the production cross section.

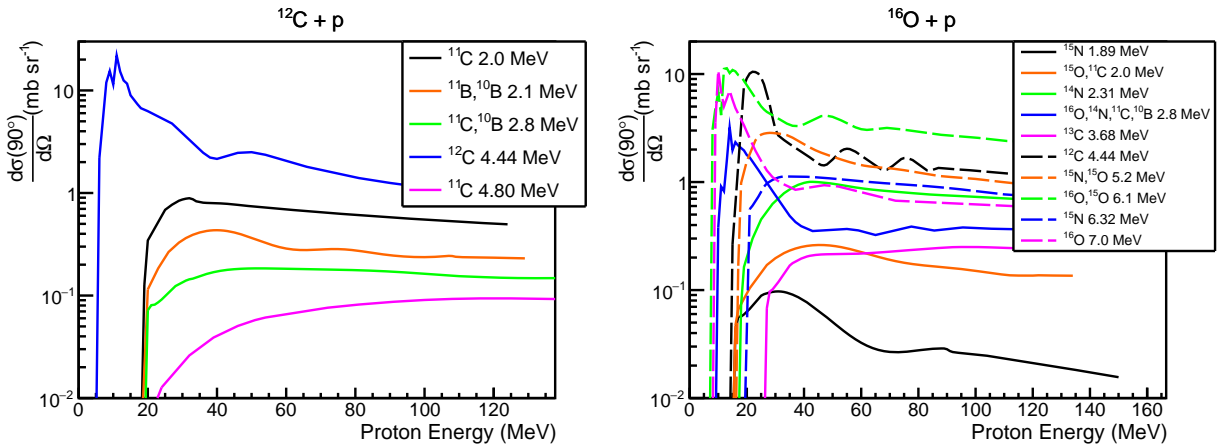


Figure 2.1.2.: Differential cross section data of prompt γ -ray production when irradiating ^{12}C and ^{16}O with protons taken from [50]. Several lines have been combined as they can not be resolved with the deployed scintillation detector.

point. Further strong γ -lines are: 4.44 MeV (from $^{12}\text{C}^*$), 7.0 MeV (from $^{16}\text{O}^*$), and 5.2 MeV (a combination of four different lines from $^{15}\text{O}^*$ and $^{15}\text{N}^*$). In conclusion, when irradiating soft tissue with protons and neglecting energies below 2 MeV as well as the high energetic continuum, mostly PGs between 4 and 7 MeV are emitted in the process.

Correlation to Proton Dose Deposition - the Spatial Emission Profile

One reason for the usage of PGs for range and dose verification purposes is the correlation between their spatial emission profile and the proton dose deposition [34]. This becomes clearly apparent from the combination of the cross section data for PG production with the proton stopping power and particle range. We can identify that protons have the highest stopping power for lower energies, which is, furthermore, the energy region with increased production cross sections of PGs. Simulation studies [68] and measurements [32, 34, 50] have been performed over the last years to investigate the spatial PG emission profile. Figure 2.1.3 presents the recent results published in [50] showing that the yield increases for most PG lines close to the Bragg peak. Hence, a variation of the particle range is also visible as shift in the spatial PG emission profile.

2.1.4. Background Events

Activation Products

Different atomic nuclei are produced in the nuclear reactions occurring in proton irradiations, whereas some are radioactive. Commonly, this so-called activation process results in a broad spectrum of unstable nuclei. Depending on their half-life $T_{1/2}$, the activation products decay via β^- , and β^+ -decay as well as electron capture (EC), which is a competing process to β^+ -decay, to a more stable nucleus. After the nuclear transition, the residual nucleus can further de-excite via

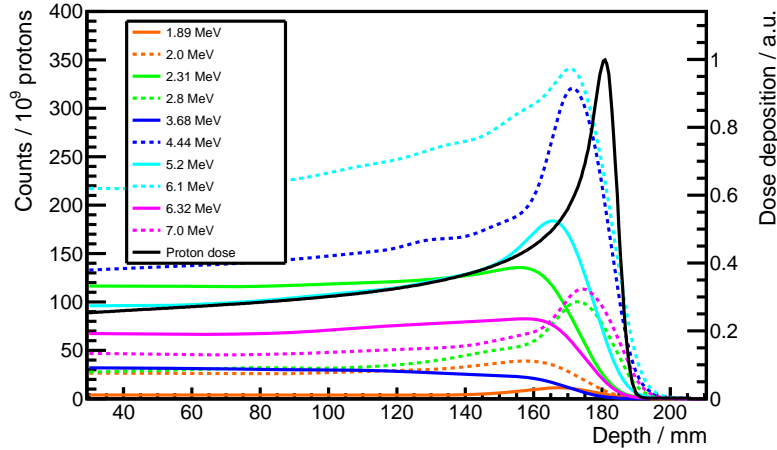


Figure 2.1.3.: Prompt γ -ray emission and proton dose deposition (black solid line) over the target depth for 165 MeV protons impinging on water. Reproduced with data from [50]. The proton depth dose curve was measured at UPTD. Courtesy by P. Wohlfahrt.

the emission of one or more γ -rays. Due to transitions within the atomic shell, X-rays and Auger electrons are emitted in the process. In case of β^+ -decaying nuclei, 511 keV photons emerge as a result of electron-positron annihilation. Summarizing, due to activation, photons (γ - and X-rays) from several keV to a few MeV as well as positrons and electrons are produced. For background considerations however, only the photons contribute in a real scenario as the charged particles (e^- , e^+) have usually not sufficient energy to leave the target material. Consequently, a high contribution of photons from background events is comprised in the energy spectrum (see figure 2.1.1), where especially the line at 511 keV from electron-positron annihilation is dominating.

High Energetic Nuclear Particles

Besides activated nuclei, high energetic nuclear fragments like single nucleons or light nuclei are also produced and emerge mainly in beam direction. They can reach energies up to the incident beam energy. However, the charged particles (protons, alphas, etc.) rapidly lose their energy due to Coulomb interactions with the atomic shell and are mostly stopped within the target. On the other hand, neutrons are electrical neutral and are therefore not slowed down by the Coulomb force. They mainly transfer part of their energy via elastic scattering with other nucleons which can produce further nucleon cascades. Hence, neutrons with a broad energy spectrum ranging from few meV (so-called thermal neutrons) to energies close to the incident proton energy of few hundred MeV are produced. The latter, the so-called fast neutrons, are sometimes directly interacting with the detector material causing background signals and, finally, radiation damage. The low energetic thermal neutrons however, are often an indirect source for γ -radiation due to neutron capture as this process has increased cross sections for lower energies. The emerging

photons are considered as uncorrelated background as the interactions occur in a time frame of micro to milliseconds due to the low neutron velocity. On average, several photons are produced per incident neutron. In our considerations, especially the thermal neutron capture in hydrogen is important as a γ -ray with 2.225 MeV is produced [60] when releasing the binding energy of the deuteron. The photon is therefore close to the energy region of PGs and, depending on the hydrogen content of the target material, a strong background source.

Scattered Primary Protons

When the primary proton beam is exiting the beam nozzle for the actual irradiation, it passes thin foils of different materials. A minor part of the primary protons is elastically scattered at the nuclei of the exit foils. The energy transfer to the target depends on the material composition as well as the scattering angle and can be, in case of heavier nuclei, nearly zero. Therefore, protons with more than 100 MeV are a potential background source for a detection system in proton therapy. The intensity of the protons decreases however rapidly with increasing scattering angle and is, therefore, strongly depending on the geometry of the measurement setup.

2.2. Principles for the Detection of High Energetic Photons

After discussing the different PG lines, their production yield, and the spatial emission, we have to take a closer look to the principles of detection and measurement of high energetic photons. Particle detection is based on interactions between a particle and a sensitive volume. As a result, energy from the particle is transferred to the detection volume. Hence, for our further considerations, we have to discuss both the interaction probability and the energy transfer. For photons with energies between 100 keV and 15 MeV, energy is primarily deposited by three processes: photoelectric absorption, incoherent scattering, and pair production [54]. The interaction probability is conventionally described by a mass attenuation coefficient and is a function of the incident photon energy as well as the material composition.

2.2.1. Interactions of Photons with Material

Photoelectric Absorption

The photoelectric absorption was first observed by Hertz in 1887. In the process, a photon interacts with an atomic electron completely transferring its energy. After the interaction, the photon has disappeared and the photoelectron can emerge from its bound state in the atomic shell. For photons with sufficient energy, the highest interaction probability exists with the tightly bound electrons from the K shell. The residual energy of the photoelectron E_e is the difference of the initial photon energy E_γ and the atomic binding energy E_b of the electron [54]

$$E_e = E_\gamma - E_b. \quad (2.2.1)$$

Consequently, when absorbing photons with several hundred keV or more, the electron obtains most of the initial energy. After the photoelectron leaves the atomic shell, the ionized atom is left with a vacancy in one of its lower states, which is quickly filled by an electron from a higher level. In the transition process, the difference in the binding energy is released as X-rays or Auger electrons. Although the photons are mostly reabsorbed by other electrons, they can also emerge from the atom and leave the material.

The photoelectric absorption is the dominant interaction mode for photons with low energy. Furthermore, it depends highly on the atomic number Z of the target material. A rough approximation of the interaction probability P depending on photon energy E_γ and Z can be found in [54]:

$$P \propto \frac{Z^n}{E_\gamma^{3.5}}, \quad (2.2.2)$$

where n is between 4 and 5. We see that especially high Z materials are ideal for photoabsorption of γ -rays, which is utilized in radiation protection by deploying lead shielding around photon sources.

Incoherent Scattering

Incoherent scattering (sometimes denoted as Compton scattering) takes also place with the bound electrons. In the interaction, the incident photon with energy E_γ is scattered by the angle θ at an electron (assumed to be initially in rest [54]). Furthermore, the photon transfers part of its energy to the electron, which is then called recoil electron. The energy transfer depends on the scattering angle, which can vary from 0 to 180° [54]. Thus, the energy of the electron can vary from nearly zero to a maximum fraction of the initial photon energy. The correlation between energy transfer and scattering angle is derived from the momentum and energy conservation and can be expressed by the following equation:

$$E'_\gamma = \frac{E_\gamma}{1 + \frac{E_\gamma}{m_e c^2} (1 - \cos\theta)}, \quad (2.2.3)$$

where E'_γ is the energy of the scattered photon and $m_e c^2$ the rest mass of the electron. The energy transfer reaches its maximum for $\theta = 180^\circ$.

The probability of incoherent scattering increases linearly with Z as more scattering partners are available. The energy dependence is rather complex, as the probability of an interaction raises until a certain energy and then decreases for further increased photon energies. In general, incoherent scattering is very dominant for photon energies between several hundred keV and a few MeV.

Pair Production

If the energy of a photon exceeds twice the rest mass of an electron (i.e. $2 \times 511 \text{ keV} = 1022 \text{ keV}$) [54], it is possible for the photon to create an electron-positron pair while disappearing in the process. This mechanism is called pair production and takes place in the Coulomb field of a nucleus. The excess energy above the 1.022 MeV threshold is shared between both emerging particles as their kinetic energy. In the following, the electron and the positron are subsequently slowed down in the material. In a next step, the positron annihilates with a nearby electron and, predominantly, two photons each with an energy of 511 keV are released. Due to momentum conservation, the photons are emitted back-to-back.

The probability of pair production is approximately proportional to the square of the atomic number of the absorbing material. Furthermore, the process has only a small probability for photon energies barely above the threshold but increases strongly for higher energies. Consequently, it is dominant compared to the other two processes for energies above several MeV.

2.2.2. Attenuation Coefficients

The interaction probability of a monoenergetic collimated photon beam passing through an absorber material can be described as exponential attenuation over the thickness of the material. Each of the previously discussed processes removes a photon from the beam due to scattering or absorbing, lowering the overall intensity. The interaction probability can be described as a fixed value per unit path length of absorbing material [54]. Consequently, the total interaction probability is the sum of all involved processes and is described by the linear attenuation coefficient μ :

$$\mu = \tau + \sigma + \kappa, \quad (2.2.4)$$

where τ , σ , and κ represent the attenuation coefficients due to the photoelectric effect, incoherent scattering, and pair production, respectively. The intensity of the photon beam I after passing the absorber can be described as an exponential function over the material thickness t :

$$I = I_0 e^{-\mu t}, \quad (2.2.5)$$

where I_0 is the initial intensity. Furthermore, one can define the mean free path λ , which is a figure for the average distance travelled by a photon before interacting with the material:

$$\lambda = \frac{\int_0^\infty x e^{-\mu x} dx}{\int_0^\infty e^{-\mu x} dx} = \frac{1}{\mu}. \quad (2.2.6)$$

The parameter λ is consequently the reciprocal of μ and takes in the energy region of PGs values from mm to cm.

As the linear attenuation coefficient varies with the density ρ even for the same element, the

mass attenuation coefficient μ/ρ is introduced. If the absorbing material is a compound of different elements, the total mass attenuation coefficient is the weighted sum of each individual contribution:

$$\left(\frac{\mu}{\rho}\right)_{\text{total}} = \sum_i w_i \left(\frac{\mu}{\rho}\right)_i, \quad (2.2.7)$$

where w_i represents the weight abundance of element i in the compound [54].

2.3. Scintillation Detectors

A radiation detector detects not the photon itself but its energy deposition to charged secondary particles like e^- and e^+ within a sensitive volume. In the next step, electrons and positrons ionize the material creating further electron-hole or electron-ion pairs. The number of those pairs is proportional to the deposited energy of the photon. Depending on the type of detector, the electron-hole or electron-ion pairs are used in different ways to create a measurable signal, like electric charge or photons of longer wavelength. In most applications for radiation detection of high energetic photons, one distinguishes between gas-filled ionization chambers (electron-ion pairs), semi-conducting devices (electron-hole pairs are collected to retrieve a measurable current) and scintillating materials (photons are produced as a result of the recombination of the electron-hole pair). With the detection of this signal, a radiation detector can measure several parameters of an incident photon, like its energy E or the time of the interaction t .

Scintillation detectors based on inorganic solid crystals are, currently, the only affordable option for the detection of high energetic photons in combination with fast timing capabilities, which is later required in case of PGT (see section 2.4.4). Thick semi-conductors, which would provide sufficient efficiency, and ionization chambers lack the required time resolution.

The scintillation principle is based on the conversion of the incident energy to a measurable signal of scintillation light, due to the excitation and de-excitation of the material. The scintillation photons are then collected by a light detector like a PMT or a photo diode both converting the signal into an electric pulse. In the next step, this pulse can be further processed to determine the required properties of the incident particle.

Consequently, the scintillation principle as well as the most important parameters of inorganic scintillators are discussed in the following. In the next step, the basics of different light detectors are presented. The combined scintillation detector is then mainly characterized by its energy and time resolution as both are important parameters in γ -ray measurements. Both attributes will be discussed in more detail.

2.3.1. Properties of Scintillation Materials

Scintillation Mechanism of Inorganic Scintillators

With the energy deposition of an incident photon in the inorganic crystal lattice, high energetic electrons and positrons ionize the material. As a result, prior bound electrons from the valence band are excited over the band gap to the conduction band leaving holes in their original position. The electrons can now go back to the valence band by emitting a photon with an energy equal to the band gap. However, in a pure crystal, the transition back to the valence band is an inefficient process [54], the emitted photons have too much energy to be in the visible spectrum, and self-absorption further reduces the number of detectable photons. Therefore, small amounts of impurities, so-called activators, are added to the inorganic crystal to increase the probability of the emission of visible photons. The activators create additional levels within the forbidden band close to the valence and the conducting band. When an electron-hole pair is generated, the electron and the hole can get trapped in the activator states. When their orbital functions overlap, electron and hole recombine and a scintillation photon is emitted. Due to the lower energy difference compared to the band gap of the pure crystal, the photon energy is shifted into the visible spectrum. The de-excitation sites are called luminescence centres and their level structure within the crystal determines the emission spectrum of a scintillator [54]. The time required to excite the luminescence centres, which is between 10^{-12} and 10^{-8} s, determines mainly the rise time of the scintillation pulse [69].

After the excitation of the activator site, the state returns to the ground state by non-radiative processes (quenching) or by emitting photons. According to Knoll [54], typical lifetimes are of the order of 30 to 500 ns. Because all excited activator sites are formed at much shorter times, they will decay with the half-life of each state determining the time characteristics of the material.

Scintillation Efficiency and Light Yield

The scintillation efficiency is defined as the fraction of produced scintillation light energy per incident energy unit. For example, thallium doped sodium iodide-NaI(Tl) has about 12 % scintillation efficiency which means that the absorption of 1 MeV yields in 0.12 MeV total light energy [54]. This efficiency value can be used to determine the Light Yield (LY) of a scintillation material, i.e. the number of emitted photons per incident energy. With an average energy per photon of 3 eV, NaI(Tl) has a LY of 40.000 photons per MeV (ph/MeV) [54].

The LY of inorganic crystals can vary from very small values (like for PbWO₄ with 200 ph/MeV [70]) to higher numbers (e.g. SrI₂(Eu) with up to $1.2 \cdot 10^5$ ph/MeV [71]).

Rise and Decay Time

The rise time is a measure of how fast the transition levels are occupied by the excited electrons and the activators are ionized by the holes in the valence band. In most cases, the rise time is very short with values of few nanoseconds which is sufficiently fast for most applications. Consequently,

the rise time is rarely mentioned as an important parameter but can become crucial in very demanding cases requiring a superb time resolution [72].

The decay time τ of a scintillator defines how fast the scintillation light is emitted after the excitation process. The value is determined by the life-time of the excited state and is a measure, in combination with the LY, of the timing capabilities of a scintillator. Depending on the number of occupied excitation states, there can be further components in the structure of the scintillation pulse. Hence, some materials have two or more components with different intensities and decay times.

The value τ can vary from few nanoseconds to several microseconds. There are very fast inorganic materials like Lutetium-Yttrium-Oxy-Orthosilicate ($\text{Lu}_{2(1-x)}\text{Y}_{2x}\text{SiO}_5$) (LYSO) and CeBr_3 with $\tau = 50 \text{ ns}$ and 17 ns , respectively, and very slow scintillators like $\text{CaF}_2(\text{Eu})$ with 940 ns . An example for a scintillator with several decay times is BGO which has a faster component with $\tau_{\text{fast}} = 60 \text{ ns}$ and a slower decaying one with $\tau_{\text{slow}} = 300 \text{ ns}$. Hereby, the fast pulse has a total intensity of 10 % while the slower component is stronger with 90 % [73].

Emission Spectrum

The emission spectrum $\Phi(\lambda)$ of a scintillation material depends on the states which are mainly occupied in the excitation process. Usually, the photon emission wavelengths vary from about 300 to 600 nm, with a maximum emission wavelength at around 400-500 nm.

Rather extreme cases are CeBr_3 (peak at 370 nm) and $\text{CsI}(\text{Tl})$ (550 nm), both demanding for special light sensors.

Material Composition

Inorganic scintillators can consist of very heavy atoms like bismuth and lutetium but also lighter materials like calcium and silicon. Usually, they are mixtures of different atoms resulting in a broad spectrum of materials with very different densities and values for Z_{eff} . BGO for example is one of the heaviest inorganic scintillators with a density of $\rho = 7.13 \frac{\text{g}}{\text{cm}^3}$ and $Z_{\text{eff}} = 75$, while $\text{CaF}_2(\text{Eu})$ on the other hand is less dense ($\rho = 3.18 \frac{\text{g}}{\text{cm}^3}$) and has lower $Z_{\text{eff}} = 16$. Consequently, the absorption capabilities of inorganic crystals differ vastly.

Several materials like CeBr_3 are furthermore hygroscopic and have to be encapsulated to prevent damage from air moisture. Other materials have radioactive components in their atomic composition, like ^{176}Lu in LYSO, which gives rise for a constant intrinsic background.

2.3.2. Light Readout

Photomultiplier Tube

Photomultiplier Tubes (PMTs) have been widely used in radiation detection based on scintillators. Their principle is based on converting the scintillation photons to electrons within a semitransparent photocathode. Hereby, the photon is absorbed and transfers energy to an electron of the

Table 2.3.1.: Selection of inorganic scintillation materials with their most important properties like density ρ , effective atomic number Z_{eff} , Light Yield (LY) in 10^3 ph/MeV, the peak wavelength of the emission spectrum λ_{peak} , the main decay time τ_1 , if available the second decay time τ_2 , the refractive index n , and several other features. The intensities of the decay branches are given in brackets if there is more than one decay time.

	NaI(Tl)	BGO	LYSO	GAGG	CeBr ₃	GSO	CsI(Tl)	CaF ₂ (Eu)
ρ (g/cm ³)	3.67	7.13	7.20	6.63	5.10	6.71	4.51	3.18
Z_{eff}	50	75	65	54	46	59	54	16
LY	43.0	8.2	33.8	57.0	60.0	9.0	65.0	30.0
λ_{peak} (nm)	415	480	420	520	370	440	550	435
τ_1 (ns)	230	300(0.9)	41	88(0.9)	17	41(0.7)	680(0.64)	940
τ_2 (ns)	-	60(0.1)	-	258(0.1)	-	297(0.3)	3340(0.36)	-
n	1.85	2.15	1.81	*	2.09	1.85	1.79	1.47
Radioactive	no	no	yes	no	no	no	no	no
Hygroscopic	yes	no	no	no	yes	no	slightly	no

Values are taken from [54, 73, 74, 75, 76, 77, 78, 79, 80, 81, 82, 83, 84].

*: no existing data on the refractive index of GAGG [85].

photocathode depending on the band gap of the material. The electron then migrates and escapes the surface of the photocathode. The spectral response, or Quantum Efficiency (QE), i.e. the fraction of emitted photoelectrons to incident photons, is a function of the wavelength of the photon. The QE depends mainly on the photocathode material and can reach values of up to 30 % [54].

In a next step, an electric field is generated by a set of dynodes and the anode using a high-voltage (HV). The electron is accelerated from the photocathode towards the first dynode and hits the dynode material releasing more than one secondary electron. This process is repeated at each dynode creating a measurable current due to electron multiplication. In the end, the electrical charge creates a measurable signal which can be further processed. Achievable gains vary up to factors of 10^7 [54].

Due to the long electron drift paths and the low electron velocities, PMTs usually do not work properly in high magnetic fields which is required in certain applications.

Light Sensors based on Semiconductors

Semiconductor based light sensors are an alternative to conventional PMTs due to their higher efficiency in converting the scintillation photos. Here, we speak of the Photon Detection Efficiency (PDE) which can reach values of up to 80 % [54]. Furthermore, they have a more compact size, are sensitive in a broader wavelength region, and can be used in magnetic fields.

Semiconducting light sensors are distinguished in three categories: conventional photodiodes (PDs), avalanche photodiodes (APDs) and Silicon Photomultipliers (SiPMs). All three are based

on the same principle to convert the incident scintillation photon to free moving electron-hole pairs within a semiconducting p-n junction of doped silicon. The photon transfers its energy to an electron, releasing it from the valence band of the material and creating thus an electron-hole-pair. The charge carriers are then collected at opposite sites of the PD due to an electric field.

In case of conventional PDs, the number of charge carriers is roughly the same as the incident number of scintillation photons absorbed in the p-n junction as there is no internal gain of the signal. Consequently, the output signal is very small and prone to electronic noise which makes PDs only applicable for very bright scintillators or at high photon energies.

The problem of electronic noise can be circumvented by increasing the number of charge carriers per incident scintillation photon. Here, the high voltage is increased until the PD is operated in the so-called avalanche mode [54]. Due to the high electric field, the charge carriers are accelerated sufficiently to create additional electron-hole-pairs in collisions. The gain factor of such APDs is of the order of hundred and depends heavily on the applied voltage and surrounding temperature demanding for a well regulated environment and HV supply.

If the applied voltage is sufficiently high to operate the APD in “Geiger”-mode, leading to a self-sustaining signal, the Single Photon Avalanche Diode (SPAD) can produce a large output pulse with just one incident photon. In order to reset the SPAD, the device has to be quenched for example with a resistor which leads in presence of an avalanche to a voltage drop. In scintillation detection, the usage of one SPAD is of little interest as the information about the energy deposition is virtually lost in the process. However, by using arrays of several hundreds to thousands of such SPADs, creating a SiPM, it is possible to measure the energy deposition of a photon.

2.3.3. Properties of Scintillation Detectors

Energy Resolution

The energy resolution ε is a measure of the response of a detector in case of monoenergetic energy deposition. The parameter ε describes the combined magnitude of the blurring effects with respect to the incident and deposited energy E as follows [54]

$$\varepsilon = \frac{\Delta E}{E}, \quad (2.3.1)$$

where ΔE is the total uncertainty determined as Full Width at Half Maximum (FWHM) of the peak with deposited energy E . The energy resolution depends on several factors coming from intrinsic properties of the scintillation crystal ΔE_{int} like a non-proportional response [86], its optical properties ΔE_{opt} (light collection etc.), the light sensor ΔE_{light} (gain stability etc.), and the electronics ΔE_{elec} (electronic noise). In general, ΔE can be written as following

$$\Delta E^2 = \Delta E_{\text{stat}}^2 + \Delta E_{\text{int}}^2 + \Delta E_{\text{opt}}^2 + \Delta E_{\text{light}}^2 + \Delta E_{\text{elec}}^2, \quad (2.3.2)$$

where ΔE_{stat} describes the statistical uncertainty, which is proportional to the number of photoelectrons $N_{\text{p.e.}}$ ($\Delta E_{\text{stat}} \propto \sqrt{N_{\text{p.e.}}}$). $N_{\text{p.e.}}$ on the other hand depends on several parameters: the LY of the material, the light collection efficiency η_{col} of the crystal, i.e. the proportion of light guided onto the area coupled to the light sensor, and the QE of the light sensor η_{QE} . It can be written as

$$N_{\text{p.e.}} \propto \eta_{\text{col}} \cdot \eta_{\text{QE}} \cdot LY. \quad (2.3.3)$$

Following the derivation from Knoll [54], the relative statistical energy uncertainty $\varepsilon_{\text{stat}}$ is proportional to $\frac{1}{\sqrt{N_{\text{p.e.}}}}$ and reduces with increasing η_{QE} and LY. Thus, the energy resolution improves with higher energies as more scintillation photons are produced [79]. Values for ε measured with a ^{137}Cs source with $E_\gamma = 662 \text{ keV}$ can vary from 3% for LaBr_3 and up to 13% for LYSO [79].

Time Resolution

The time resolution ΔT of a detector setup is a measure of how precise the interaction time of a particle can be determined. It can be described in a similar way as the energy resolution [87, 88]:

$$\Delta T^2 = \Delta T_{\text{stat}}^2 + \Delta T_{\text{int}}^2 + \Delta T_{\text{crystal}}^2 + \Delta T_{\text{TTS}}^2 + \Delta T_{\text{elec}}^2 + \Delta T_{\text{trig}}^2, \quad (2.3.4)$$

where each parameter is discussed in the following:

- ΔT_{stat} is the statistical contribution describing the average arrival time of the first charge carrier above the trigger threshold within the light sensor, which would be the first one [89] in case of a perfect detector. According to the Hyman theorem [90], ΔT_{stat} is proportional to $\frac{\tau}{\sqrt{N_{\text{p.e.}}}}$. Thus, a bright and fast scintillating material coupled to a light sensor with high QE provides the best time resolution when considering the statistical factors. Furthermore, the time resolution of a detector should increase with higher incident energy. In case of very fast scintillators, also the rise time τ_{rise} is of concern for the time resolution [91].
- The intrinsic time resolution ΔT_{int} is the theoretical limit of the timing capabilities of a material determined mainly by its rise and decay time [72], i.e. by the excitation and de-excitation of the luminescence centres, respectively. ΔT_{int} is usually unknown and subject of measurements.
- $\Delta T_{\text{crystal}}$ is a measure for the photon travel time uncertainty due to reflection and an unknown depth of interaction. It depends primarily on the size and the surface finishing. Small crystals with etched surfaces (except for the one coupled to the light readout) provide the best time properties [87].
- The transit time spread through the light detector ΔT_{TTS} describes the charge collection and the drifting of the charge carriers. Hence, small light sensors with high electric fields

often result in favourable timing properties.

- The contribution from electronic noise ΔT_{elec} is primarily of concern for the timestamp generation ΔT_{trig} . The standard in realistic timing measurements would be the detection of the 3rd to the 5th photon, depending on the time jitter of the photo detector [88]. However, this standard cannot be reached in reality due to electronic noise. As a consequence, different trigger methods are used like leading-edge or constant fraction timing [54].

Summarizing, to achieve the best time resolution, small, bright, and fast scintillators should be coupled to fast, noise-free, and highly efficient light sensors and electronics. In reality, measurements performed with small Lutetium-Oxy-Orthosilicate (LSO:Ce) crystals, co-doped with Ca, and coupled to SiPMs, have shown the current limit on time resolution with scintillation detectors by achieving values of $\Delta T = (60 \pm 3)$ ps (FWHM) at 511 keV [92].

2.4. Prompt Gamma-Ray Timing Method

The technology to determine the proton range using the timing information of the PG emission is currently been developed at OncoRay, Dresden (Germany) and has briefly been introduced in section 1.3.2. As the Prompt Gamma-ray Timing (PGT) method is the underlying theoretical frame of this work and required for understanding the following chapters, we will deepen the knowledge about the basic idea behind PGT as well as the practical approach of TOF measurements. Furthermore, the experimental path of PGT will be drawn: from the first occasionally obtained results to a dedicated study at a clinical accelerator showing the potential of detecting range variations of few millimetres at clinical doses. In a last step, existing drawbacks and limitations for a clinical application of PGT are presented and discussed, as they are the main motivation of this work.

2.4.1. Principle

The PGT approach utilizes a basic physical effect: protons need a finite time between entering a target material and stopping at the end of their range. This so-called proton transit time t_p varies between 1-2 ns for typical therapeutic proton ranges of 10-20 cm [51]. Along the track, PGs are emitted almost until the end of the particle range. A γ -ray detector can be deployed to measure the time difference between the target entrance of the proton and the detection of the PG by measuring the width of the time distribution of PGs (see figure 2.4.1). In the measurement, not only t_p is determined but also the TOF distribution of the photons (see below for details). Golnik et al. named the resulting time distribution PGT spectrum [51].

At a certain depth and therefore also time, the PG emission depends on the material composition and the energy of the protons. Consequently, this information is encoded in the PGT spectrum. In reality, the time measurement is smeared out by several effects which can have the same or even a larger magnitude as the proton transit time [12, 51]. Nevertheless, the range information

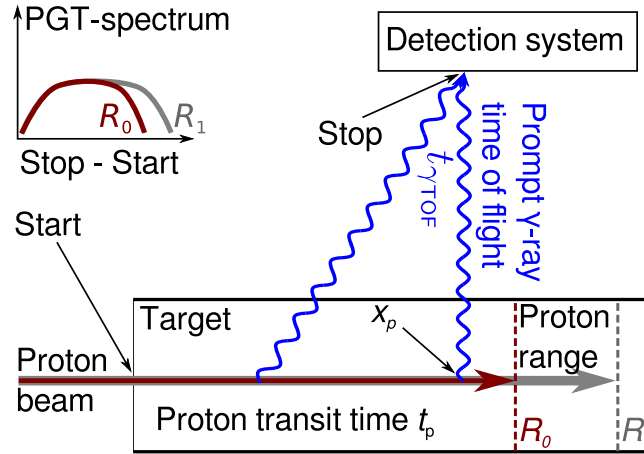


Figure 2.4.1.: Detection principle of the PGT method. The proton beam is impinging on the target and produces PGs. A detection system measures the entrance of the beam into the target as start signal and the detection of the emitted photon as stop signal. The information contains the proton transit time t_p and the TOF distribution of the PGs. With a higher range R_1 , the PGT spectrum broadens. Reproduced with permission from C. Golnik [11].

can still be retrieved by determining the first and second momenta (i.e. mean and variance) of the PGT spectrum. It is thus possible, with a sufficient number of events, to determine the proton range by measuring the PGT spectrum.

Proton Transit Time

When a proton with kinetic energy E_0 is entering a material, it continuously deposits energy along its track (see equation 1.1.1). The magnitude of the energy deposition is depending on the stopping power $S(E)$. In the process, the proton is slowed down until it stops at the particle range $x_p(E_p = 0) = R_0(E_0)$. The velocity of the proton $v_p(E_p)$ as function of its energy E_p can be calculated as following [51]:

$$v_p(E_p) = \frac{dx_p}{dt} = c \sqrt{1 - \left(\frac{m_0 c^2}{E_p + m_0 c^2} \right)^2}, \quad (2.4.1)$$

where m_0 is the proton rest mass. E_p on the other hand is the difference between incident kinetic energy E_0 and the already deposited one, therefore depending on the position x_p :

$$E_p(x_p) = E_0 - \int_{x_0}^{x_p} S(E_p(x)) dx. \quad (2.4.2)$$

The proton transit time can now be derived also as a function of x_p and E_p using (1.1.1) and

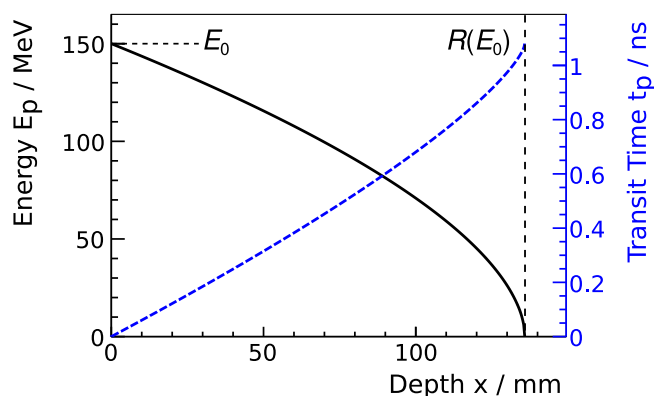


Figure 2.4.2.: Proton transit time (blue dashed line) and kinetic energy (black solid line) as a function of the target depth for 150 MeV protons impinging on PMMA. Reproduced with permission from C. Golnik [51].

(2.4.1) [51], which is exemplary shown in figure 2.4.2 for 150 MeV protons:

$$t_p(x_p) = \int_{x_0}^{x_p} \frac{1}{v_p(E_p(x))} dx = \int_{E_p(x_p)}^{E_0} \frac{1}{v_p(E)S(E)} dE. \quad (2.4.3)$$

We see from the correlation between proton range and transit time that protons require more time for travelling longer distances. In combination with the energy dependent PG production cross section (see section 2.1.3), we can identify that also the PG emission time is increased for longer particle ranges. Figure 2.4.3 shows the simulated PGT spectrum for 150 MeV protons impinging on a PMMA target with genuine and artificially lowered material density. When the protons exhibit a larger range, the emission time window of the PGs is consequently extended, which can potentially be used for determining the range [51].

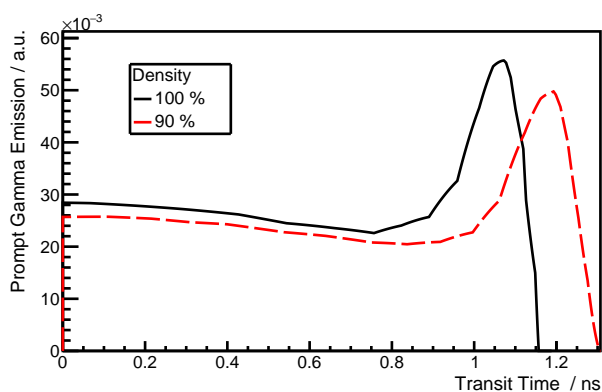


Figure 2.4.3.: Simulated PGT spectrum for 150 MeV protons impinging on PMMA with genuine density (black solid line) and artificially lowered density (red dashed line). Reproduced with permission from C. Golnik [51].

Time Reference Signal

The experimental realization of the measurement procedure is based on a TOF setup [52], where the photon detection is measured relative to a reference signal. Here, the arrival time of the protons in a reference plane perpendicular to the beam axis seems to be a natural choice. This could be realized by a thin charged particle detector in the beam path giving a start signal when a proton passes through. However, with about 100 protons per bunch in clinical treatment conditions [13], an individual assignment between proton and γ -ray is not feasible.

The RF of an accelerator can alternatively be used as a reference signal. If the protons are continuously accelerated and extracted with a constant frequency, the RF signal is a stable reference signal. However, the arrival time of the incident and interacting proton is not directly measured but a logical pulse resembling the proton bunch separation. Nevertheless, as the RF is constant (e.g. in case of isochronous cyclotrons) the bunch separation between the extracted protons is equidistant and can be regarded as an offset in the measurement. In addition to a constant frequency, utilizing the RF as time reference requires the signal to have low time jitter.

System Time Resolution

In contrast to the simulated PGT spectra (see figure 2.4.3), there are several sources for time uncertainties when measuring the PG emission released due to interactions with a proton beam. Those additional effects can be approached by a convolution of the PGT spectrum with a Gaussian function with a σ value resembling the time uncertainty.

The sum of all those uncertainties is defined as the system time resolution ΔT_{STR} [51]:

$$\Delta T_{\text{STR}}^2 = \Delta T_{\text{Det}}^2 + \Delta T_{\text{BTS}}^2 + \Delta T_{\text{RF}}^2 \quad (2.4.4)$$

where ΔT_{Det} is the time resolution of the detector which is in case of scintillators of the order of few hundred picoseconds (see section 2.3.3 for details). Thus, this effect smears out the structures of the PGT spectrum (target entrance, peak of increased yield etc.) but the overall shape is still conserved. A further uncertainty to determination of the PGT spectrum results from the bunch time structure which we will refer to as Bunch Time Spread (BTS) ΔT_{BTS} . The BTS describes the time width of the proton bunch and is highly depending on the type of accelerator and the beam transport system and can reach values up to several nanoseconds. Depending on the magnitude of the BTS, the PGT spectrum can be completely smeared out and the proton range measurement is only possible by determining the statistical momenta. A further effect on the time measurement can result from instabilities of the RF signal ΔT_{RF} like time jitter on the pulse structure due to electronic noise etc.

The uncertainty of the mean of the PGT spectrum $\Delta\mu$, which determines the sensitivity of the

PGT method, is depending on ΔT_{STR} and can be written as follows:

$$\Delta\mu \propto \sqrt{\frac{\Delta T_{\text{STR}}^2 + \Delta t_p^2}{N}}, \quad (2.4.5)$$

where N is the number of measured PGs and Δt_p is a measure of the broadening of the PGT spectrum due to the proton transit time. Consequently, for the detection of small range deviations, a low system time resolution and a high number of events is required.

2.4.2. Discovery

The idea of PGT was discovered in an experimental campaign studying the capabilities of a Compton camera prototype for PGI as well as the radiation environment produced by protons with clinically relevant energies interacting with PMMA and other phantoms. The experiment was performed at the AGOR cyclotron of KVI-Center for Advanced Radiation Technology, Groningen, the Netherlands (KVI-CART).

Experimental Setup

PGs were produced by a 150 MeV proton beam with a current of about 10 pA impinging on a PMMA target. The photon emission was monitored by a scintillation detector which consisted of a Gadolinium-Aluminum-Gallium-Garnet ($\text{Gd}_3\text{Al}_2\text{Ga}_3\text{O}_{12}$) (GAGG) crystal coupled to a PMT and readout by analog electronics (Versa Module Eurocard (VME) bus as well as Nuclear Instrumentation Module (NIM) standards). The detector was operated in a TOF setup with the RF of the cyclotron of 55 MHz as reference, resulting in a bunch separation of about 18.2 ns.

Results - First Hints towards PGT

Exemplary data of the single GAGG scintillation detector taken during the irradiation of a PMMA target is presented in figure 2.4.4-left showing the two dimensional energy versus relative time histogram. PGs are hereby represented by the structure between 1-4 ns which we will later refer to as PG peak. When analysing the width of the PG peak (figure 2.4.4-right), which should be a measure of the detector performance, Golnik et al. were wondering about the obtained value of more than 1.4 ns (FWHM) in contrast to the expected time resolution of 900 ps [51]. In fact, not the time resolution of the detector was measured but a combination of detector, BTS, and, more importantly, the proton transit time. Thus, the idea of PGT was developed. Furthermore, Golnik et al. named the projection of the 2D histogram onto the time scale as ‘‘PGT spectrum’’ comprising the basic measurement parameters [51].

Results - Stacked Target Experiment

Especially in the so-called ‘‘stacked target experiment’’, the basic idea behind the method is exemplarily shown. Here, the irradiated phantom consisted of PMMA slices of different thicknesses.

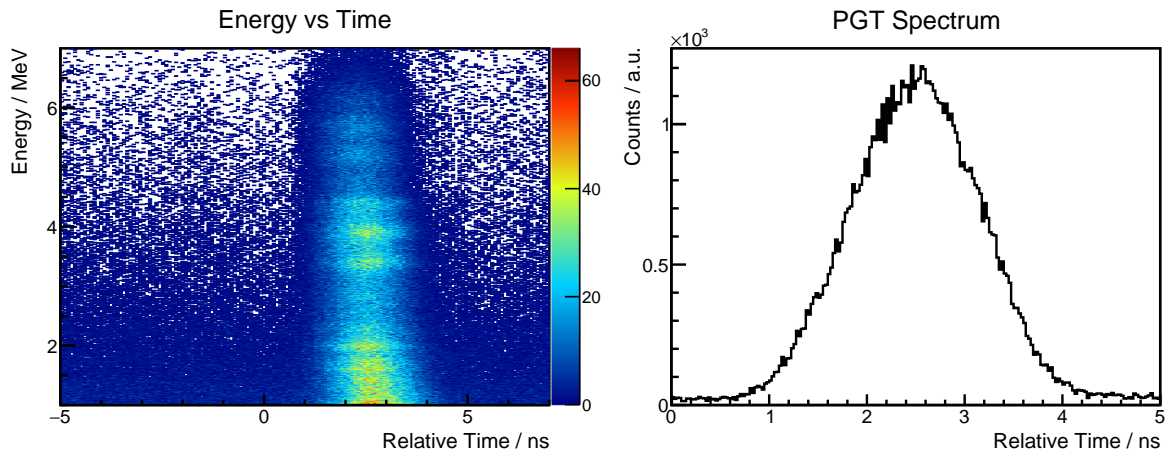


Figure 2.4.4.: Energy versus relative time distribution (left) and PGT spectrum (right) measured with the GAGG detector at KVI-CART. An energy window between 3.1-4.6 MeV is applied for the PGT spectrum. Reproduced with permission from C. Golnik [51].

Consecutively, from each measurement to the next the target thickness d was increased from 5 to 15 cm in a total of 7 steps (i.e. 5, 8, 11, 12, 13, 14, and 15 cm). The corresponding range of the 150 MeV protons is about 13.7 cm in PMMA [5]. Thus, for the measurements with $d < 14$ cm the beam was not stopped in the target. This can also be seen in the PGT spectra of each target configuration (figure 2.4.5-left). We can clearly identify that the PGT peak increases in height and width with increasing target thickness until the proton range is finally reached for $d = 14$ cm. Between the last two measurements where the protons are stopped (i.e. $d = 14, 15$ cm) there is no difference in the PGT spectrum.

The findings were also compared with simulations (figure 2.4.5-right), showing excellent agreement between measurement and theoretical prediction [51]. Consequently, the PGT effect is a quantifiable measure for the proton range.

Conclusion of the Groningen Experiment

In summary, the obtained results have verified the basic idea behind PGT: to observe an increase in proton range as a shift of the momenta of the PGT spectrum even though the system time resolution shadows the intrinsic shape of the PG emission time distribution. As the experiment was planned for a different purpose of testing a Compton camera, a further study should focus on faster detectors, the detection of actual range shifts, and also the usage of a medical accelerator to prove the feasibility of the PGT method in a clinical environment.

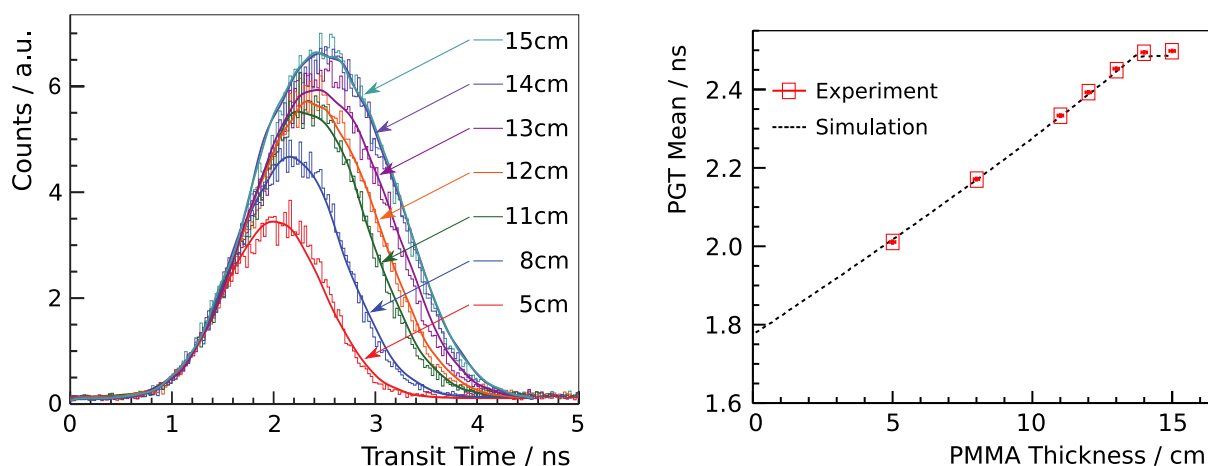


Figure 2.4.5.: Left: Experimental (histogram data) and simulated (solid lines) PGT spectra for the stacked target experiment conducted at KVI-CART. Right: Comparison between experimental (red markers) and simulated (dashed line) PGT mean values. Reproduced with permission from C. Golnik [51].

2.4.3. PGT at a Clinical Accelerator

After the first results obtained at KVI-CART, a dedicated experiment was conducted by Hueso-González et al. at the Westdeutsches Protonentherapiezentrum Essen, Germany (WPE) [12]. Here, the focus was set to test the feasibility of PGT at a clinical facility as well as the potential to detect range shifts.

Experimental Setup

The proton beam was provided by a Cyclone 230 (C230) cyclotron from IBA which is a fixed energy isochronous cyclotron operated in several clinical facilities worldwide [10]. Fast scintillation crystals coupled to PMTs were deployed for measuring the PG emission exhibiting better time resolutions compared to the GAGG detector used at KVI-CART. Among them were a BaF_2 and a LaBr_3 detector providing a time resolution of 210 and 250 ps at 2 MeV, respectively. Again, the detectors were used in TOF mode with the RF of the accelerator of 106 MHz as reference, and the electronics was based on VME and NIM modules.

In the experiment, protons with energies of 100, 160, and 230 MeV were impinging on a PMMA target made out of hollow half cylinders. The target was filled with compositions of small discs of different material (diameter of 5 cm and variable thickness) like PMMA (i.e. creating a homogeneous target), air (i.e. an empty position), and bone-equivalent material. Due to the limited throughput rate of the system, currents at the beam nozzle of about 10 to 100 pA were used, which is far below the clinical current of about 2 nA [13].

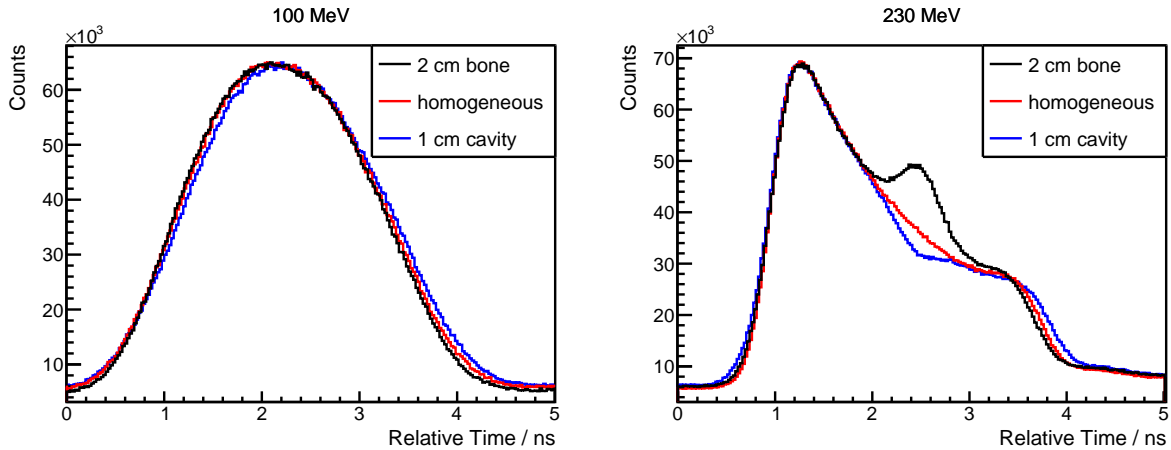


Figure 2.4.6.: PGT spectra measured at WPE. 100 (left) and 230 MeV (right) protons are impinging on a PMMA target with different inhomogeneities. The spectra are normalized on their corresponding maxima for comparison purposes. Reproduced with permission from F. Hueso-González [12].

Results - Consequences at a Clinical Accelerator

During the experimental study, several implications due to the usage of a clinical accelerator, the C230 have been observed. First of all, the BTS turned out to depend strongly on the selected beam energy. This issue is obvious when comparing the PGT spectra measured for different beam energies. While for an energy of 230 MeV the PGT spectrum had visible structures (see figure 2.4.6-right), like a small dip from an air cavity or an increased PG emission coming from the presence of a bone-insert, it is more or less a Gaussian distribution in case of lower energies (see figure 2.4.6-left). Thus, the BTS as function of beam energy was investigated by detecting the PG emission from a thin PMMA target. Hueso-González et al. found that the BTS changes from about 0.25 ns (at 230 MeV) to about 1.5 and 2.5 ns (for 160 and 100 MeV), respectively [12]. They furthermore investigated the possibility to confine the BTS by varying the Momentum Limiting Slit Opening (MLSO) of the Energy Selection System (ESS) of the facility. The MLSO acts as a kind of a proton filter. By lowering the opening from the default value of 25 mm to 5 mm, the BTS could be reduced in case of 100 MeV by more than a factor of 2 which would increase the sensitivity of the PGT method.

An additional effect was observed when comparing the PGT spectra of repeated measurements with same beam energy. Even though the geometry of the setup was not changed, the rising edge of the PGT spectrum shifted from measurement to measurement to higher relative times. Hueso-González et al. concluded that this behaviour results from phase drifts between the RF signal and the proton bunch [12]. The phase drift was attributed to slight variations in the magnetic field level of the main coils leading to small changes in the orbital frequency. To verify this assumption, the current of the main coils of the cyclotron was varied in very small steps and the peak position in the PGT spectrum was measured for a fixed setup. It was found that the PGT peak shifted

about 1 ns for mail coil current variations of 0.01 % [12].

Results - Detection of Range Shifts

When inserting air cavities or bone discs into the PMMA target, slight variations in the PGT spectra could be detected. In particular, after correcting for RF drifts, variations of the falling edge can be identified. In case of the air cavity we see a longer emission time and a shorter one for the bone insert compared to the homogeneous case (see figure 2.4.6). Furthermore, when normalizing the data on incident proton number, slightly increased or lowered PG yields become visible when the bone disc or an air cavity were inserted, respectively. However, the visibility of the incorporated inhomogeneity in the PGT spectrum depends highly on the beam energy due to the different BTS.

Nevertheless, it was shown that an air cavity of 5 mm or a bone insert of 20 mm are detectable when about 10^4 PGs are measured [12].

Conclusion - Lessons Learned from WPE

The experiment at WPE was a successful proof that PGT is, in principle, applicable in a clinical facility. Nevertheless, Hueso-González et al. state that the usage of a medical accelerator brings several problems with it, like phase drifts of the proton bunches relative to the RF signal as well as the energy dependent BTS [12]. They propose the usage of an additional proton detector for directly measuring the proton arrival time [12]. The detector could monitor protons which are scattered at the thin exit foils of the beam nozzle. As a result, an additional time reference would be available to correct for the phase drifts. Additionally, information on the BTS is also obtained in a more direct fashion.

Furthermore, Hueso-González et al. show that the sensitivity of PGT (i.e. the limit on possibly detectable range shifts) depends on the number of detected PGs and on the BTS [12]. Key to detect range shifts as low as 5 mm or less is hereby to increase the efficiency of the detector system as the incident proton dose is fixed. Thus, a combination of increasing the throughput of the detector system and using a higher number of detectors is one suggestion [12]. In conclusion, PGT seems feasible to detect range shifts for individual (and strong) spots in PBS mode.

2.4.4. Requirements for a Clinical PGT System

Continuing with the results and experience obtained at WPE, we will now further discuss the requirements to apply PGT at a clinical facility. Here, we will set a special focus on the requirements at UPTD which is also based on a C230. Furthermore, the focus is set on range verification during PBS mode as each single spot can be analysed individually in contrast to DS where the PGT spectrum is more complex due to the extended field size.

At first, following the discussions in [12, 51], the system time resolution should be as low as possible to have the best range sensitivity achievable. Consequently, a detector material with su-

perior timing properties and the sufficient detection efficiency at high photon energies is required. The time resolution should be at least of the order of the lowest available BTS of the C230 which is about 250 ps [12]. An even better time resolution has on the other hand no practical impact as the BTS dominates the system time resolution even in the best case for PGT. Furthermore, the material should be commercially available and exhibit a fast decay time to cope with event rates of about 2 Mcps in a clinical scenario [13] without running into pile-up.

Secondly, the RF bunch phase drift has to be corrected for the application of PGT at UPTD which comprises a C230 accelerator. Otherwise, an interfractional comparison of PGT data may not be feasible. Consequently, an alternative time signal has to be deployed and tested. In a further step, the BTS needs to be characterized as a function of the beam energy to obtain reliable parameters for simulation studies and to predict the PGT spectra for a given treatment. Additionally, ways to decrease the BTS should be evaluated and tested to potentially improve the sensitivity of the PGT method.

As a final step, a suitable readout electronics is required providing sufficient capabilities regarding time and energy resolution as well as a high throughput rate. Following the discussion presented by Pausch et al. [13], the throughput rate of the system determines the number of measured PGs as the number of protons for an individual spot is more or less fixed. A strong spot exhibits about 10^8 incident protons which are delivered in about 8 ms [13]. Consequently, to obtain at least 10^4 events, which are required to detect 5 mm range shift [12], the readout electronics should exhibit about 1.2 Mcps throughput rate. Alternatively, if this value is not achievable, more than one detector units could be deployed requiring the readout electronics to be scalable and compact.

3. Time Resolution of Scintillation Detectors

This chapter tries to answer the following question: Which scintillation material has the best time resolution in the energy region of PGs? The investigation was originally performed in the framework of finding a suitable scintillation detector for the absorber plane of a two-stage Compton camera (CC) prototype. Here, good time resolution is required to suppress uncorrelated background and to reduce the number of random coincidences. The study was motivated by the results from Hueso-González et al. [93] showing that, due to the high energies of PGs, scintillation materials can exhibit better time and energy resolution as expected from the literature. As the focus of the work shifted towards PGT, the obtained results are even more important and can be used to find a suitable material for a PGT detector.

First, time resolution data from the literature, obtained at lower energies, is discussed. The next step is to investigate the time resolution of the materials at energies relevant for PG measurements. In order to do so, a novel digital Silicon Photomultiplier (dSiPM) is being used as light sensor as it exhibits superior time resolution capabilities and has promising features due to its digital design. The expected performance of each material on the dSiPM according to the Hyman theorem is determined. Finally, an experimental campaign is designed and conducted at the ELBE accelerator using high energetic bremsstrahlung to test the performance of each material and to compare it with the expectations.

3.1. Investigated Scintillation Materials

As discussed in section 2.3.3, the time resolution of a scintillation detector depends on the deployed crystal and the light readout. Furthermore, the statistical component ΔT_{stat} affects the timestamp determination. It is a function of the LY of the scintillator, the efficiency of the light sensor, and also of the energy deposition. Due to the higher incident energies of PGs and therefore a reduction of the statistical uncertainty, other factors like e.g. the intrinsic material properties could be more relevant compared to lower energies. As there is no existing literature for this energy region¹, a selection of scintillation materials with different properties will be further investigated for a possible application in PGT.

Here, the focus is set on the inorganic materials already mentioned in table 2.3.1, except for NaI(Tl), as they have very different properties like LY, τ , and atomic composition. Consequently, different behaviour might be observed at higher photon energies.

¹Except for published data from Roemer et al. [79] where the measurements were performed simultaneously and in cooperation to the study shown in this work

BGO and LYSO are commonly used in medical applications, especially in PET. Both are very dense and have a very high Z_{eff} , however, LYSO has compared to BGO by far the higher LY ($33.8 \cdot 10^3$ vs $8.2 \cdot 10^3$ photons per MeV) and the faster main decay time (41 vs 300 ns). Nevertheless, the internal radioactivity of LYSO leads to intrinsic background and potentially to pile-up events. Experimental time resolution values of BGO vary from 1.33 ns (at 511 keV [94]) to about 1 ns (energies above 1 MeV from ^{60}Co [73]). For LYSO however, excellent results from PET measurements have been reported for small (about 110 ps [95]) and larger crystals (about 160 ps [96]).

The relatively new ceramics material GAGG provides high LY, moderate τ as well as moderate density and Z_{eff} . Its most prominent property is the emission spectrum which peaks at 520 nm and extends far in the yellow. Consequently, the crystal requires a different spectral response of the light sensor. The time resolution of GAGG was measured to be about 550 ps at 511 keV [97].

CeBr_3 is one of the fastest inorganic scintillators ($\tau = 17$ ns). Furthermore, it has very high LY and is known for very good energy resolution. However, it is hygroscopic requiring encapsulation and it is also less dense compared to BGO, LYSO, and GAGG. The material can be seen as an alternative to LaBr_3 which has limited availability on the market and a slower rise time resulting in a slightly worse timing performance [98]. Measured time resolutions of 164 ps (at 511 keV) and 119 ps (at ^{60}Co energies) have been reported [99].

Gadolinium-Oxy-Orthosilicate (Gd_2SiO_5) (GSO) is also a rather fast material with, however, relatively poor LY (about $9.0 \cdot 10^3$ photons per MeV). Experimental values of 700 ps have been reported [76]. The material has furthermore a high density and Z_{eff} providing sufficient photoabsorption efficiency at high photon energies.

The very slow materials $\text{CsI}(\text{Tl})$ and $\text{CaF}_2(\text{Eu})$ ($\tau = 680$ and $\tau = 940$ ns, respectively) are conventionally not used in timing applications. Thus, data on the time resolution is not available except from measurements performed by Roemer et al. [79] stating a value for $\text{CaF}_2(\text{Eu})$ of roughly $4 \mu\text{s}$ at 511 keV. However, both have high LY and could thus be an effective material at higher energies.

Even though BaF_2 is usually considered as one of the materials with the best timing capabilities due to its very fast scintillation component ($\tau_1 = 0.6$ ns [54]), the scintillator is not considered in our study as the scintillation photons of this fast component are emitted at very low wavelengths with a peak at around 220 nm, which requires special light sensors. Additionally, the results from Hueso-González et al. [12] have indicated a rather low energy resolution for BaF_2 . Therefore, an individual selection of PG lines is not feasible and the reduction of low energetic background is hardly possible.

3.2. Digital Silicon Photomultiplier

In addition to the scintillation crystal itself, the light sensor and the further signal processing (time pick-off method and electronics) are important factors when considering a detector with

good timing properties. Here, high PDE and very low time jitter from the electronics and the light sensor are desirable. Regarding the time pick-off method, the best option would be triggering on the 3rd to 5th photon arriving shortly after the first one [88]. Consequently, only few photons contribute to the timing signal and are used for timestamp generation. However, this procedure is hardly realizable in practice as the obtained signal includes electronic noise which shadows the very small pulse from the photons. Nevertheless, the dSiPM comes close to this approach as it applies a complex trigger and validation scheme for event selection directly on the chip.

3.2.1. Sensor Layout

The dSiPM from Philips Digital Photon Counting, Aachen, Germany (PDPC), also called Digital Photon Counter (DPC), is a semiconducting light detector which was introduced in 2009 [95] as a novel approach for a light sensor with integrated readout electronics. It provides excellent timing capabilities with an intrinsic resolution of 44 ps [100]. The design is based on micro cells operated as SPADs. In contrast to analog SiPMs, the digital design can be used to control the recharge cycle of the device. Additionally, in case of the dSiPM, the number of discharged cells, i.e. the number of SPADs with an avalanche breakdown, is directly counted after a variable time window.

Currently, the DPC is available as the so-called *tile* sensor (dimensions of $32.6 \times 32.6 \text{ mm}^2$, for details see [100, 101]) which comes in two versions: the DPC-3200 and the DPC-6400. The versions differ concerning their layout (i.e. the number of micro cells) but also with respect to their firmware architecture. Here, only the DPC-3200 is applicable for our later considerations with timing measurements using an external reference signal (see section 3.3.5).

A DPC-3200 tile consists of 16 individual *dies* arranged in a 4×4 matrix (dimensions of $7.15 \times 7.875 \text{ mm}^2$, figure 3.2.1) and is covered by a single glass plate (thickness of $100 \mu\text{m}$) for protection of the sensors. A die comprises a matrix of 2×2 *pixels* (dimensions $3.2 \times 3.8775 \text{ mm}^2$). Each pixel further consists of 3200 SPADs which are arranged in rows and columns and have a pitch size of about $59.4 \times 64 \mu\text{m}^2$ [101]. The pixel structure is further divided into *sub-pixels* (also as 2×2 matrix) which are important for the trigger and validation scheme. In summary, a tile is a matrix of 8×8 pixels with a total of about $2.0 \cdot 10^5$ SPADs.

3.2.2. Data Acquisition

The DPC features a trigger and validation scheme (figure 3.2.2) which is unique for a light detector. The acquisition of an event is started when the number of registered photons within a pixel is above an initially set threshold, the Trigger Level (TL). The TL can be set in 4 different options defining different combinations of required sub-pixels with at least one discharged cell [101]. For example, in case of TL 1, only one discharged SPAD is needed in any sub-pixel [101]. The average number of required photons increases for higher TL (see table 3.2.1 for details).

The trigger also defines the timestamp of the corresponding event. The timestamp generation is done on the die-level as each die comprises two Time to Digital Converters (TDCs). Within a selectable time period of 5-40 ns after the trigger point, the so-called Validation Length (VL), the

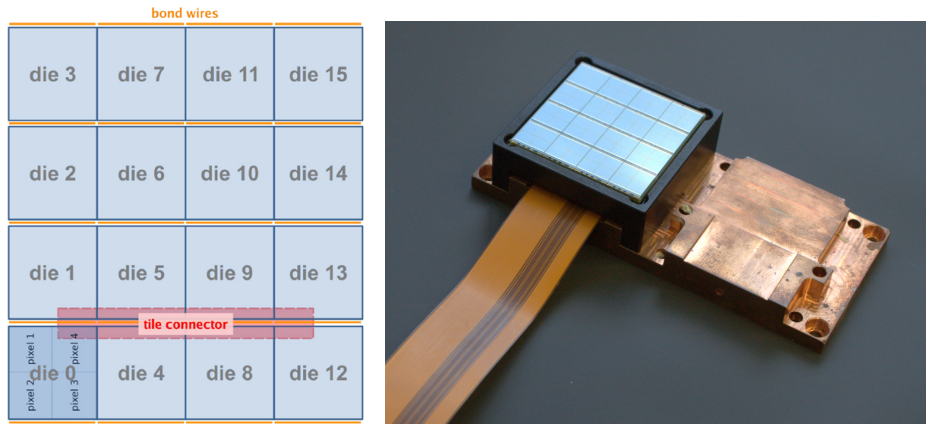


Figure 3.2.1.: Schematic drawing and a photography of the DPC-3200 tile (courtesy of G. Pausch). The proprietary flat band cable and the copper heat exchange plates are also visible (see section 3.3.3 for details). The drawing is taken from [101].

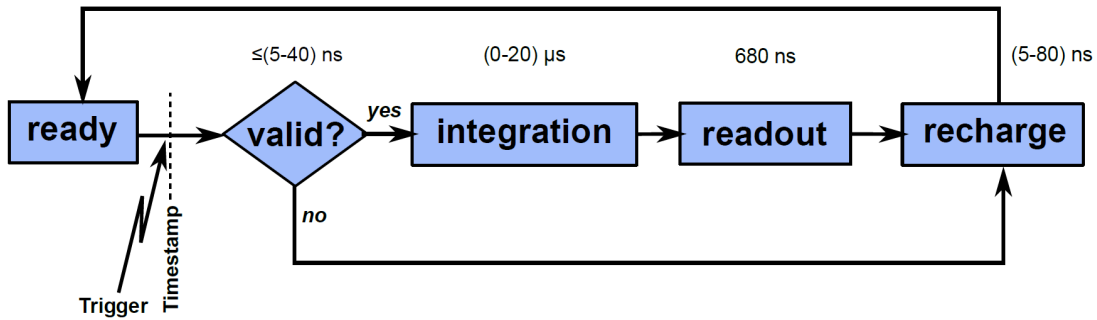


Figure 3.2.2.: Event acquisition sequence of the DPC for a single event. See text for explanation. Reproduced from [101].

event is validated using a second photon threshold. This so-called Validation Scheme (VS) again works as a threshold and can be set in 6 options (from 1, 2, 4, 8, 16, to 32). The VS defines a certain logical combination of micro cell rows of the same sub-pixel to have a fired SPAD. Like for the TL, a higher VS requires on average more incident photons, e.g. 1 photon for VS 1 and 53 for VS 8 [101, 102]. Further details are shown in table 3.2.1.

If the validation procedure is passed, a time window is started for collecting and counting all incident scintillation photons. The length of this integration gate is adjustable from 0-20 μs . Here, the number of discharged cells is summed up on a pixel level to evaluate the incident number of photons, which is a measure of the deposited energy. Consequently, the number of micro cells determines the maximum number of detectable photons per event for a tile. After the readout procedure, all cells of a die are recharged so that another measurement cycle can be started. In case the validation is not successful, the recharge procedure is started immediately. Thus, the usage of the trigger and validation scheme is an approach mainly for handling the problem of dark

counts or dark current, i.e. randomly triggered SPADs, without losing the ability to measure with low thresholds.

Further data post-processing is performed directly on the tile and on the control unit which is connected to the tiles using proprietary flat cables. The DPC is controlled using a command-line based software called “dpc-shell”, where all relevant parameters can be set and the measurements are conducted.

Table 3.2.1.: Different trigger level (TL) and validation scheme (VS) settings of the DPC. The minimum and the average number of fired cells, required for successful triggering or validation, are shown. The data is taken from [100, 102].

	Setting	Minimum # of cells	Average # of cells
TL	1	1	1.0
	2	2	2.3
	3	2	3.0
	4	4	8.3
VS	1	1	1
	2	2	5
	4	4	17
	8	11	53
	16	*	54
	32	*	132

*: no data available.

3.2.3. Dark Count Map

A further design feature of the DPC is the possibility to disable individual micro cells. This is primarily used to inhibit certain cells with the highest Dark Count Rate (DCR) as they might have been damaged due to radiation etc. To evaluate the DCR of each cell, the DPC contains the function to measure the so-called Dark Count Map (DCM), which is the DCR distribution for the whole sensor. The biggest contribution to the DCR is usually caused by a few percent of the active cells [101]. Thus, by deactivating the noisiest cells (e.g. 10% of the total number), the DCR can be significantly reduced by nearly 70% [101]. This is however paid by a lower active sensor area and is therefore a trade-off for each application. The matrix of disabled cells is called *inhibit map* and is stored in a flash memory on the chip.

The DCR varies heavily with the temperature and can e.g. be reduced by one order of magnitude when lowering the operating temperature from 20 °C to 0 °C [103]. Consequently, for a constantly low DCR, the sensor temperature should be stable and as low as possible.

3.2.4. Photon Detection Efficiency

The PDE of the DPC-3200, already including the geometrical pixel fill factor of 74 % [100], is shown in figure 3.2.3. It is obvious that the device exhibits higher PDE in contrast to the QE of conventional PMTs with a peak value of 38 % at around 450 nm suiting most materials. Furthermore, the spectral response extends even in the far red of the visible spectrum (about 10 % PDE are achieved at around 740 nm). Consequently, a high number of detected scintillation photons is expected resembling a major advantage in timing measurements (see section 3.3.1).

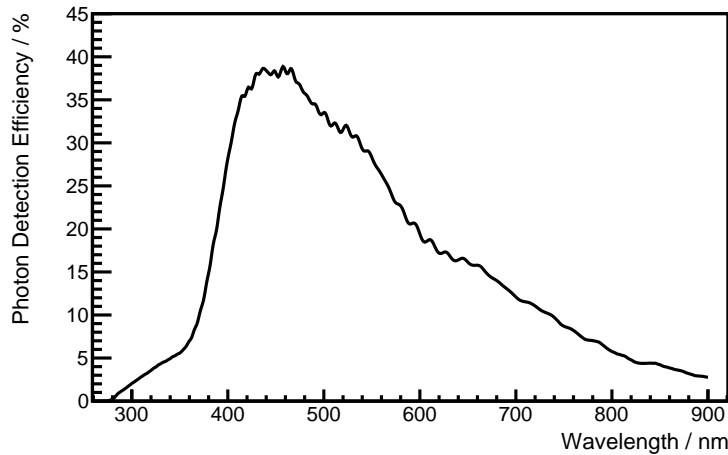


Figure 3.2.3.: Photon detection efficiency of the DPC-3200. Reproduced with data from [100].

3.2.5. Bias Voltage

The bias voltage of the DPC is a crucial parameter determining the functionality of the device. For example, if the bias voltage V_{bias} is too low, the PDE is decreased compared to the maximal value. However, increasing the voltage too far causes a higher DCR and could also damage the sensor. The optimum bias voltage is furthermore a function of the temperature and should be determined prior to each measurement cycle. The DPC has an internal calibration procedure measuring the breakdown voltage V_{break} of the tile by slowly ramping up the applied voltage and measuring the event rate until the breakdown point is reached. This step is repeated several times with decreasing step size and increased starting voltage. V_{bias} is given by

$$V_{\text{bias}} = V_{\text{break}} + V_{\text{excess}}, \quad (3.2.1)$$

where V_{excess} , the excess voltage, is used to operate the DPC in “Geiger”-mode and is set per default to 3 V. This parameter can be adjusted according to the application.

3.2.6. Data Handling and Timestamp Generation

Validated events are sent from the die to the Field Programmable Gate Array (FPGA) of the tile for further data processing which is done in frame intervals of $327.68 \mu\text{s}$. After processing, the data is streamed in list mode via USB to a PC. Each event has the following structure: event ID, tile number, die number, photon count of pixel 0-3, timestamp (see below for details), temperature, and frame number.

The DPC can be operated in “normal” and raw mode. In normal mode, several corrections and calibrations are performed like a TDC correction and time skew calibration. The TDC correction is necessary as the TDC has no linear response which furthermore varies with temperature and clock frequency (which is important for later considerations). Thus, the DPC has a function creating a look-up-table (LUT) for each die while measuring the DCM. Additionally, due to small signal runtime differences between dies (e.g. due to cable lengths), each TDC has a small time shift in the clock cycle. This effect has to be determined and the results can be uploaded to the tile. Finally, the two timestamps per die (due to two TDCs) are combined in one *corrected* timestamp (including all calibrations).

In raw mode however, no corrections are applied and both TDCs are read out per event. Each TDC value is divided into two counter values: the Coarse Counter (CC) and the Fine Counter (FC). The CC is hereby increased by one for every second clock cycle of the tile which is by default every 10 ns (as the clock runs at 200 MHz). The TDCs are however covering the full cycle due to a phase shift of one clock cycle. The 9 bit FC on the other hand is incremented from 0 to 511 within each CC cycle. The bin width of the FC is independent of the clock frequency and fixed with $10 \text{ ns}/512 \approx 19.5 \text{ ps}$ [101]. In raw mode, the real timestamp per event has to be manually calculated in an offline analysis (including all corrections and calibrations).

3.2.7. Practical Considerations

Photon Saturation As the DPC consists of a limited number of SPADs, high photon count values bear the risk of multiple hits on a single micro cell. Consequently, as each cell can only count one photon per acquisition, all further photons are not counted and information is lost. This effect is called saturation and can be corrected for by using the following relation [101, 103]:

$$p = -N \cdot \ln\left(1 - \frac{k}{N}\right), \quad (3.2.2)$$

where N is the number of active cells on a pixel, k the number of discharged cells, and p the actual photon count value. The saturation effect becomes stronger the closer k approaches N and is for example around 30 % when half of the cells of a pixel have triggered. Thus, this 30 % of photons are lost resulting in non-linearity effects. Nevertheless, the photon saturation correction can be applied on an offline analysis procedure restoring the initial information. Note that the correction is only valid for relatively homogeneous illumination of the tile sensor which is, however, ensured in the following measurements.

Thermal Stabilization The architecture of the DPC with the readout electronics directly on the chip has a major disadvantage: Heating due to the thermal power of the electronics (readout and recharge process) is distributed towards the SPADs. The proper functionality of the micro cell depends on the bias voltage which is on the other hand a function of the temperature. In case of small temperature variations, the bias voltage is adjusted automatically. If the variations become too high, this adjustment process is not reliable anymore. Consequently, the DPC requires a thermal stabilization system which could further be used for cooling of the device to reduce the DCR [101]. Indeed, in most applications the DPC is cooled down to values around 0°C or even lower temperatures round −15°C [104].

Limited Event Rate The events gathered from the DPC are stored on the control unit. Here, the data is filtered for erroneous entries and coincidences can be created. After the post-processing, the data is sent via USB 2.0 port to the readout computer. This connection however forms the main bottleneck of the system due to the low bandwidth for data transmission. Consequently, the maximum obtainable event rate is limited to 120kcps in contrast to the 1.3Mcps which could be possible [104]. However, even with this artificial limitation events might be discarded due to the low transmission rate.

3.3. Experimental Study on the Time Resolution at High Photon Energies

In this section, we will present an experimental study investigating the time resolution of the different scintillation materials coupled to the DPC-3200 at high photon energies relevant for PG measurements. Consequently, several practical considerations are discussed prior to the experiment like the expected performance as well as the optimum crystal size. In a next step, the experiment will be fully discussed ranging from the experimental setup, several corrections which have to be applied as well as the energy calibration and data selection. The data analysis is discussed using the results from CeBr₃. For each material, the achieved time resolution is presented as a function of the energy.

3.3.1. Expected Timing Performance

If only considering the statistical component ΔT_{stat} , the theoretical timing performance of a scintillation material can be described by a figure of merit (FoM) using the Hyman theorem [90, 105] as follows:

$$\Delta T_{\text{stat}} \propto \text{FoM} = \frac{\tau}{\sqrt{\text{LY}_{\text{eff}}}}, \quad (3.3.1)$$

where LY_{eff} is the effective LY (i.e. $\text{LY}_{\text{eff}} = \text{LY} \times \text{PDE}_{\text{avg.}}$) describing the number of detected scintillation photons. The value is proportional to the number of created electron-hole pairs for

Table 3.3.1.: Integral photon detection efficiency, effective light yield and theoretical timing performance according to the Hyman theorem for different materials investigated in this chapter. LY and LY_{eff.} are given in units of 10³ ph/MeV. The FoM is determined separately for both decay components if applicable, where the first value shows the results for the main decay component. The LY, τ_1 , and τ_2 are taken from table 2.3.1. The corresponding intensities are mentioned in brackets if there is more than one decay time. In case of multiple references of the emission spectrum, PDE_{avg.} is given as a mean value. Deviations of LY_{eff.} are caused by rounding errors.

	BGO	LYSO	GAGG	CeBr ₃	GSO	CsI(Tl)	CaF ₂ (Eu)
PDE _{avg.}	0.32*	0.34	0.27*	0.15	0.36*	0.26	0.37
LY	8.2	33.8	57.0	60.0	9.0	65.0	30.0
LY _{eff.}	2.0	8.6	11.2	6.5	1.9 ⁺	12.6	8.3
τ_1 (ns)	300(0.9)	41	88(0.9)	17	41(0.7)	680(0.64)	940
τ_2 (ns)	60(0.1)	-	258(0.1)	-	297(0.3)	3340 (0.36)	-
FoM	7.22/4.25	0.44	0.87/8.11	0.21	1.12/12.40	7.58/49.65	10.32

*: mean values using input from more than one reference for the emission spectrum.

Emission spectra taken from [80, 97, 107, 108, 109, 110, 111, 112, 113, 114, 115, 116, 117].

The PDE curve is taken from [100].

⁺: LY_{eff.} of GSO already includes the shape of the crystal. See text for details.

a given device and can be estimated by determining the average PDE (PDE_{avg.}) for a given scintillation material. Here, the emission spectrum of the scintillator $\Phi(\lambda)$ and the PDE(λ) of the DPC (see figure 3.2.3), both as function of the wavelength, are required as input parameters [106]. PDE_{avg.} can be calculated using the following relation

$$\text{PDE}_{\text{avg.}} = \frac{\int_{\lambda_{\text{min}}}^{\lambda_{\text{max}}} \Phi(\lambda) \cdot \text{PDE}(\lambda) d\lambda}{\int_{\lambda_{\text{min}}}^{\lambda_{\text{max}}} \Phi(\lambda) d\lambda}, \quad (3.3.2)$$

where we integrate over the spectral region and normalize on the emission spectrum data. Values on $\Phi(\lambda)$ are taken from the literature and data sheets from the manufacturer. The obtained results of PDE_{avg.} as well as LY_{eff.} of the investigated materials coupled to the DPC-3200 are presented in table 3.3.1 including an additional effective fill factor of 0.74 resembling the tile structure² [100]. The highest LY_{eff.} is reached by CsI(Tl) with about $1.3 \cdot 10^4$ ph/MeV. The second highest value is obtained by GAGG ($1.1 \cdot 10^4$ ph/MeV), followed by LYSO and CaF₂(Eu) (between $(8.3-8.6) \cdot 10^3$ ph/MeV). The very bright CeBr₃ has only moderate effective LY ($6.5 \cdot 10^3$ ph/MeV) due to its relatively poor PDE_{avg.} of only 15%. GSO and BGO obtain the lowest values which is a result of their overall low LY.

The obtained values of LY_{eff.} can now be used in combination with τ to calculate the FoM

²The pixel fill factor of 0.74 is already included in the PDE, nevertheless, [100] states a total tile fill factor of 0.55 which also includes the pixel factor. Consequently, an effective tile fill factor of around 0.74 can be determined.

of each material according to the Hyman theorem [90]. The calculation is done for each decay component separately. The results are also shown in table 3.3.1, where a lower FoM means a better expected performance with respect to the statistical component. Due to its very fast decay time, CeBr₃ is expected to have the best timing capabilities followed by LYSO, GAGG, and GSO. BGO with its low effective LY and moderate τ should perform worse. The two slow materials CsI(Tl) and CaF₂(Eu) are expected to have the worst performance. However, the FoM describes only the statistical component without taking intrinsic properties into account.

3.3.2. The Need for Monolithic Crystals

The usage of the DPC at high photon energies needs further consideration regarding the limited number of SPADs per sensor. This figure is of concern as it resembles the maximum number of photons which can be detected. Hence, for bright scintillators and high photon energies, this number might be exceeded and saturation effects might not be correctable.

Here, we can use the results of LY_{eff} obtained in the previous section. For example in the case of CsI(Tl) which has the highest LY_{eff} , around $1.3 \cdot 10^4$ photons are detected per deposited MeV. Considering the energy range of PGs (1-8 MeV), up to $1.0 \cdot 10^5$ photons have to be detected by the DPC. As one die only consists of around $1.3 \cdot 10^4$ SPADs, only a 1-to-1 coupling of one monolithic crystal with a whole tile comprising $\approx 2.0 \cdot 10^5$ micro cells seems reasonable to measure the energy information. Consequently, monolithic crystals matching the surface of the sensor area are used in our experiment. BGO, CaF₂(Eu), CsI(Tl), and LYSO have hereby a surface area of $32 \times 32 \text{ mm}^2$, while GAGG and CeBr₃ were slightly bigger with $33 \times 33 \text{ mm}^2$. The thicknesses of the crystals varied from 10 mm (for LYSO), over 15 mm (CeBr₃) to 20 mm (all other except for GSO). Additionally, a cylindrical GSO crystal with a diameter of 40 mm and a thickness of 25 mm was used. Even though the GSO crystal is not matching the tile dimensions (slightly bigger, not quadratic), it can be used for our timing measurements as about 80 % of the sensor area are covered. To achieve complete light collection, all crystals except for CeBr₃ were wrapped in several layers of white Teflon tape with an additional layer of black tape to prevent light from outside. The hygroscopic CeBr₃ crystal was encapsulated by the manufacturer.

3.3.3. Experimental Setup

The DPC tile is thermally stabilized and actively cooled using Peltier elements. The heat exchange is guaranteed by using CNC machined copper plates fitting the exact dimensions of the tile. Additional thermally conductive paste is used providing direct contact between tile and copper plate. The heat of the Peltier elements is dissipated by a hollow steel plate which is flushed by temperature regulated water. Overall, the temperature, measured with the internal sensor of the DPC, was kept stable at around $(2.0 \pm 0.8)^\circ\text{C}$. To prevent water condensation and therefore damaging of the DPC, the device is constantly flushed by nitrogen gas. The whole setup is housed in a light tight box which is shown in figure 3.3.1.

The crystals were optically coupled to the sensor using silicon grease, type EJ 550 from Eljen

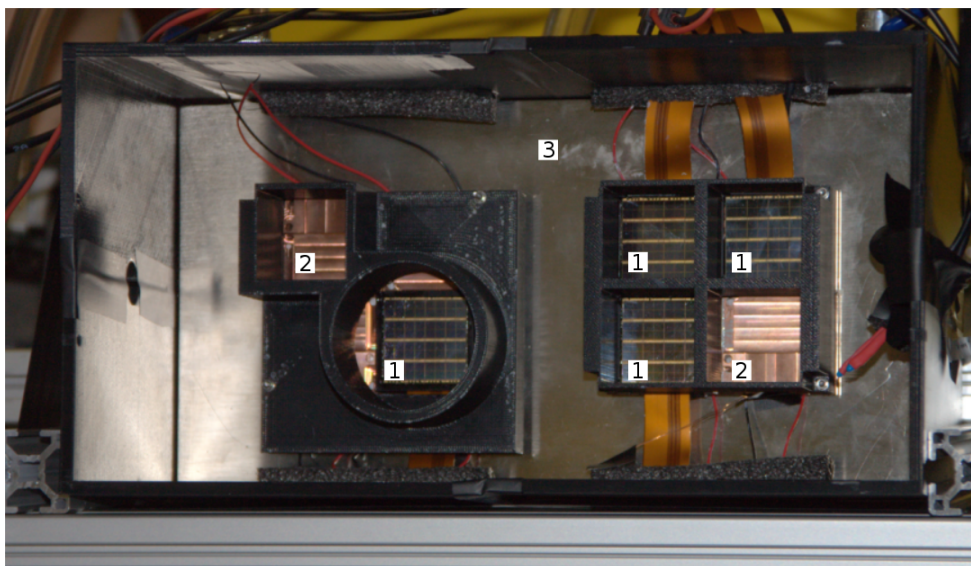


Figure 3.3.1.: Experimental setup of the DPCs used at the bremsstrahlung facility of ELBE. The surrounding box, 4 DPCs (1), the copper plates (2) as well as the water cooling plate (3) are visible. The crystals can be mounted to the DPC and are kept in place by a specially designed holder. After mounting the crystals, the box is closed and covered by a black cloth to prevent light from outside.

Technology. As the LY of a scintillator varies with the temperature, thermal equilibrium between cooling, tile, and crystal was obtained after about 30 minutes.

3.3.4. ELBE Accelerator: Excellent Timing Capabilities

Time resolution measurements at PG energies require a suitable signal providing photon energies far beyond the standard laboratory sources. The Electron Linear accelerator of high Brilliance and low Emittance (ELBE) facility at Helmholtz-Zentrum Dresden-Rossendorf, Germany (HZDR) is an ideal source as it provides bremsstrahlung beams with energies of up to 20 MeV and low time jitter. It has also successfully been used in similar studies [79, 118]. The layout of the facility is shown in figure 3.3.2.

In our experiment, the ELBE accelerator provides an electron beam with an energy of 13 MeV and a repetition rate of $f_{\text{ELBE}} = 13 \text{ MHz}$. The primary electron beam is guided onto a thin niobium foil (the radiator) producing bremsstrahlung with an end-point energy of about 12.5 MeV. In the purging magnet, the combined beam (electrons and photons) is separated as the electrons are deflected into a beam dump. The bremsstrahlung beam is then sent through a 10 cm thick hardener made of high-purity aluminium reducing the ratio of low to high energetic photons. The beam passes an aluminium collimator with an exit opening of 24 mm which is surrounded by lead and concrete. This further reduces the contamination from electrons and neutrons and confines the beam spot to a few cm^2 . Consequently, a clean bremsstrahlung beam is produced with a continuous energy spectrum between 100 keV and 12.5 MeV.

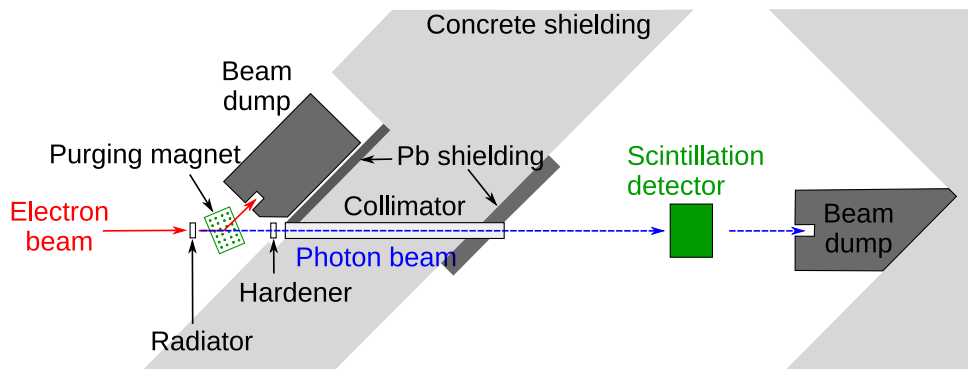


Figure 3.3.2.: Layout of the bremsstrahlung facility of ELBE at HZDR. The drawing was adapted by A. Rinscheid from [119].

Concerning the time capabilities, the electron pulses have a duration of about 5 ps [120], and measurements on the overall time jitter (including the RF signal etc.) have shown results of 50 ps. Consequently, as we expect results above 100 ps, the ELBE accelerator is a suitable source for timing measurements with high energetic photons.

Further details on the setup of the bremsstrahlung facility can be found in [119, 120].

3.3.5. TOF Setup - RF as Clock Signal

The RF of the ELBE accelerator can be used as a reference for the incident bremsstrahlung beam. In case of the DPC, the RF pulse can be used to clock the sensor. Thus, the digital counters of the device (like the TDC) are consequently incremented and reset in phase with the acceleration process which is on the other hand in phase with the impinging bremsstrahlung photons.

Usually, the DPC and the controlling unit are run with an internal clock of 200 MHz. The possibility of external clocking was not implemented in the firmware yet. Nevertheless, PDPC provided on request a special firmware version for the sensors to allow for external clocking. The user, however, has to ensure that the device is finally clocked with a frequency between about 150 to 210 MHz³. The controlling unit offers the possibility to use a Phase-Locked-Loop (PLL), which can vary a frequency to lower or higher ones by dividing or multiplying with integer values. A maximum multiplication factor of 8 is possible with the PLL which only allows a frequency of 104 MHz when using the 13 MHz input from ELBE.

Consequently, an additional external PLL system, developed by the *Zentralabteilung für Forschungstechnik* at HZDR, was installed in the controlling room of the bremsstrahlung facility close to the switching plate for the cable routing into the bunker. Here, the logical 13 MHz pulse is connected to a controller and further guided into the PLL. This device, with a time jitter less than 5 ps, has a fixed multiplication factor of 14, providing an output frequency of 182 MHz. The signal was then routed to the bremsstrahlung bunker. Due to the cable length of around 50 m,

³Private communication with the PDPC team

the peak level and the shape of the signal were degenerated to only 40 mV amplitude (which is not a sufficient input level). Consequently, the pulse was fed in a fast timing discriminator, type TD 2000 from FAST ComTec, recovering the logical pulse form and amplifying the peak level to around 2 V. The shaped output of the discriminator was then delivered to the controlling unit and the DPC could be clocked with 182 MHz.

Using a clock frequency different from 200 MHz has several implications for the usage of the DPC. First of all, validation and integration lengths are changing as they are set in multiples of clock ticks. Thus, as the frequency changes, the translation from ticks to real time varies and the lengths differ from the original values. For example, when setting a validation length of 20 ns (with reference to 200 MHz input), the actual length at 182 MHz becomes $20 \text{ ns} \times \frac{200 \text{ MHz}}{182 \text{ MHz}} \approx 22 \text{ ns}$. Thus, in our settings all lengths are increased by roughly 10 %. Furthermore, the TDCs have to be re-calibrated for a linear response which is done by measuring the DCM [101].

3.3.6. DPC Settings

Different combinations of TL, VS, and VL were investigated in the experimental campaign at ELBE. All four values of the TL as well as each possibility of the VL (5.5, 11, 22, and 44 ns) were combined with most of the VS settings. In total, 48 different settings were used for each scintillation material (see table A.1.1 in the appendix for details). The integration time was however fixed for each crystal and chosen to be at least three times the decay time of the scintillation material. The following effective integrations lengths were set: CeBr₃: 50 ns, GAGG: 360 ns, BGO: 1400 ns, LYSO and GSO: 180 ns, and CaF₂(Eu) and CsI(Tl): 5600 ns.

The data was taken in raw mode using coincidence settings with a window of 35 ns and a minimum die number of 2 (for details, see [101]). This approach is reasonable as monolithic crystals were used and the events could be pre-filtered on the controlling unit to lower the amount of data to be transferred due to the bandwidth limitation. For each measurement, $1 \cdot 10^5$ frames were taken representing a real time duration of around 32.8 s. The dead time varied depending on the count rate. In all measurements, the inhibit map was set to 10 %.

3.3.7. Data Analysis Procedure

The offline data analysis was performed using the “libPDPC” library⁴ which is based on C++ and ROOT [121]. The data is read event-wise and photon saturation as well as TDC non-linearity were corrected for.

Complete Light Collection

The photon count value of an event is represented by the sum of all saturation corrected pixel-values of all dies triggered and validated within the coincidence window. When using monolithic

⁴libPDPC was written by F. Hueso-González, with minor updates and changes made by K. Roemer and the author.

crystals, the number of validated dies N_{dies} in an event can vary from 2 to all 16. Low die values are a result of insufficient illumination of the sensor or dies being in recharge due to a non-validated event. On the other hand, only events with complete light collection should be considered in our analysis. This is mainly of concern for an energy calibration as the “photon count to incident energy”-relation is not constant and restorable. The photon count versus N_{dies} distributions of two exemplary measurements performed with CeBr_3 at the bremsstrahlung beam using different DPC settings are shown in figure 3.3.3. We can identify that the number of detected photons changes with the number of validated dies until it saturates for a certain N_{dies} . This value however depends strongly on the selected DPC settings and has to be evaluated for each set of data. The number of dies required for complete light collection is then used as a filter for the further data analysis. In all cases, the minimum number of required dies per an event is 13 or higher (all values can be found in the appendix in table A.1.1).

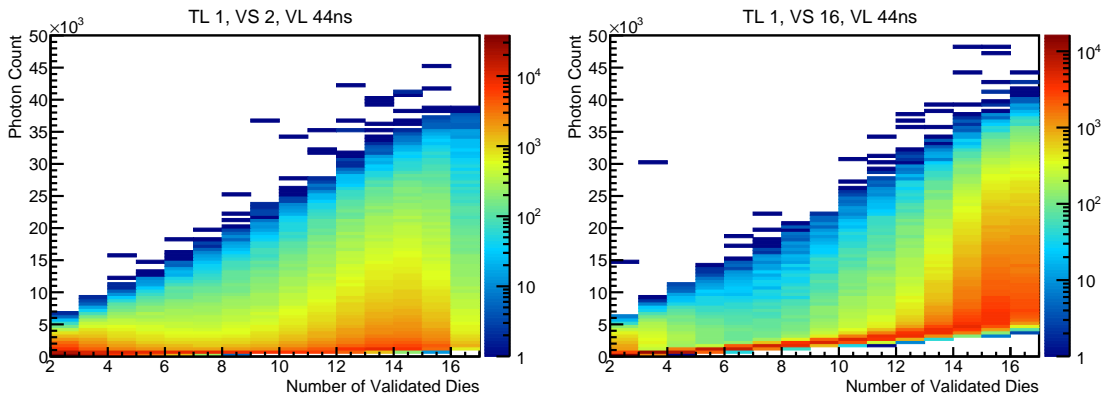


Figure 3.3.3.: Photon count versus number of validated dies measured with CeBr_3 under different DPC settings at the ELBE bremsstrahlung beam. Photon saturation correction is applied.

Energy Calibration

Source Measurements As we are mainly interested in energies of several MeV, standard γ -ray sources like ^{22}Na and ^{60}Co are used. ^{22}Na provides two lines at 511 and 1275 keV as well as the sum peak at 1786 keV (figure 3.3.4-left). In case of ^{60}Co , two γ -ray lines with energies of 1173 and 1332 keV, and the sum peak with 2505 keV can be used.

When measuring with GSO and BGO, insufficient scintillation light is produced to illuminate the whole sensor and validate enough dies. Consequently, no data points are available for both materials. Similar constraints apply for other crystals, e.g. the 511 keV is not visible or that the detection efficiency was too low to detect the sum peak of ^{22}Na (like for CaF_2).

Tandetron Photon energies above 3 MeV are not available from conventional γ -ray sources, and other ways have to be followed to increase the range of the energy calibration. One possibility

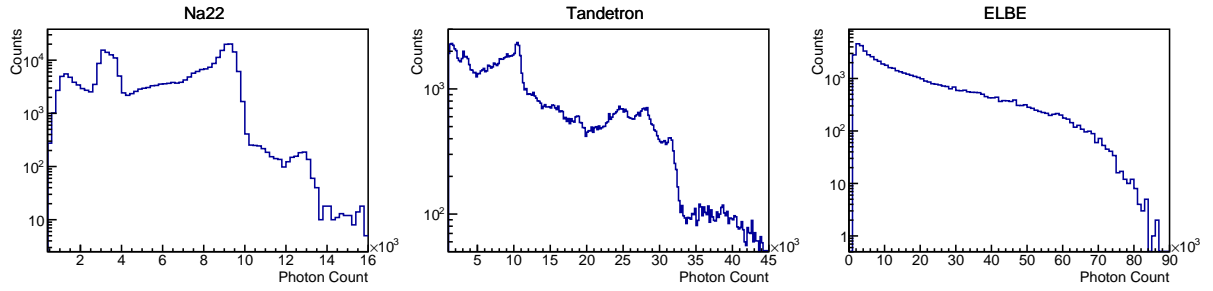


Figure 3.3.4.: Photon counts measured with GAGG for different photon sources like ^{22}Na (left), the 4.44 MeV field at Tandetron (middle) as well as the bremsstrahlung beam at ELBE (right). Following settings were used for ^{22}Na and Tandetron: TL 2, VS 8, VL 40 ns. In case of ELBE, TL 1, VS 4, VL 44 ns was used. The minimum required number of dies was set to 15.

arises by utilizing proton resonance capture reactions which are followed by a photon de-excitation. The Tandetron (a tandem accelerator) at the Ion Beam Center of HZDR provides the possibility to create 4.44 MeV γ -rays by sending a proton beam with about 900 keV onto a TiN foil. The resulting proton resonance reaction $^{15}\text{N}(p, \alpha\gamma)^{12}\text{C}$ occurs releasing a photon with an energy of 4.44 MeV. Further details can be found in [37, 79, 122].

Due to the low proton energy, no additional secondary particles are produced giving rise to a clean field of 4.44 MeV photons. Even though beam currents of about $10\ \mu\text{A}$ are used, the number of events is very low and long acquisition times of several hours are required in order to obtain sufficient counting statistics. However, due to the temperature stabilization, the temperature variation was below $0.7\ ^\circ\text{C}$ and no gain drifts were visible.

Figure 3.3.4-middle shows a measurement performed at Tandetron using the GAGG crystal. The peak positions of the photopeak, the single, and double escape peak (all three visible between photon counts of 20,000 to 35,000) have been fitted using a Gaussian function. Furthermore, due to the long measurement time, the 1460 keV line from ^{40}K is visible at around 10,000 photon counts and can be used for the calibration.

End Point Energy of the Bremsstrahlung Beam The end point energy of the bremsstrahlung spectrum with 12.5 MeV is further used for the energy calibration (figure 3.3.4-right).

Linear Energy Calibration Functions A linear energy calibration function was determined for each crystal (figure 3.3.5-left). GSO and BGO, both with the lowest effective LY, have, as expected, the steepest calibration curve. CsI(Tl) and GAGG on the other hand have the lowest slope which is also expected as both have the highest LY_{eff} . The intersection with the x -axis differs for all materials and is mainly resulting from the uncertainties of the determined peak positions. Thus, the offsets in the linear interpolation vary from a few hundred keV for most materials to 900 keV in case of CaF_2 . Nevertheless, this has only minor implications at higher

energies which are more relevant in our case.

The calibration data can also be used to determine the relative LY, i.e. the fraction between the measured LY and the expected values. Here, the reciprocal of the slope of the linear energy calibration function resembles the number of detected photons per MeV. Using this procedure, we obtain for the relative LY of all crystals (figure 3.3.5-right) a nearly constant fraction between measurement and theoretical value of 0.53 ± 0.05 . Thus, roughly 50% of the expected light is detected when measuring with the DPC indicating a systematic deviation from the expectations. This might be a result of light loss and reflections at the crystal surfaces. Nevertheless, as all materials behave similarly, a comparison of the energy dependent time resolution can still be performed.

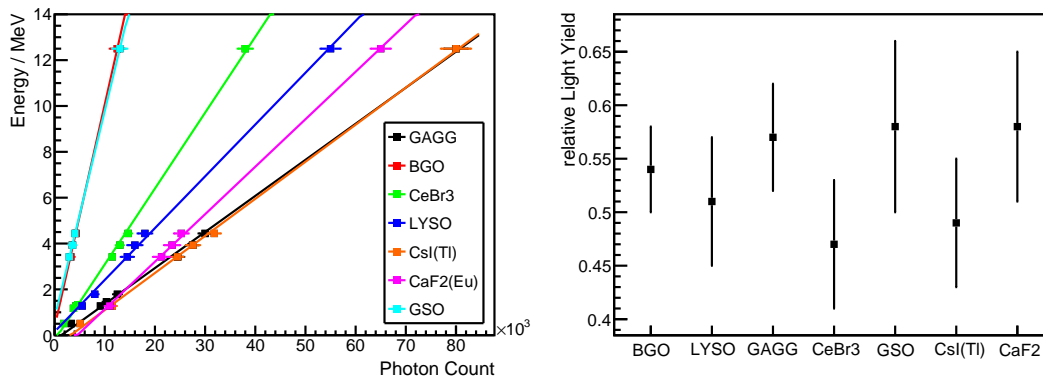


Figure 3.3.5.: Linear energy calibration functions (left) and the relative light yield (right), i.e. the fraction of measured to expected LY, of all crystals when used with the DPC. The calibration points are also shown.

Timestamp Determination

As 13 or more dies are validated per event, the same number of TDC values (each further divided into two FC values) are available for determining the timestamp of an event. Consequently, several methods could be applied for timestamp generation. In this work, the first triggered die is used as it provides the best results compared to other procedures like e.g. using the brightest die.

As we obtain two FC values per die in raw-mode, an average value is calculated as averaged timestamp. The same approach is internally performed when measuring with the DPC in normal mode [101].

Time Skew Correction

For each tile, a time skew correction has to be applied due to different cable lengths between the dies. Hence, the energy versus relative time distribution for each individual die is created and the rising edge of the bremsstrahlung peak is determined. Both resulting FC values per die

are then averaged, normalized on the first die (which is set to zero skew), and written in a skew correction file, which is further used in the offline analysis. As the correction is different for each tile, selected data sets with sufficient number of events were used. An exemplary energy versus relative time distribution of a LYSO measurement without and with skew correction is shown in figure 3.3.6. Without skew correction, several peaks resembling the bremsstrahlung can be identified. However, when applying the skew correction procedure, the peaks are shifted on top of each other improving the obtainable time resolution.

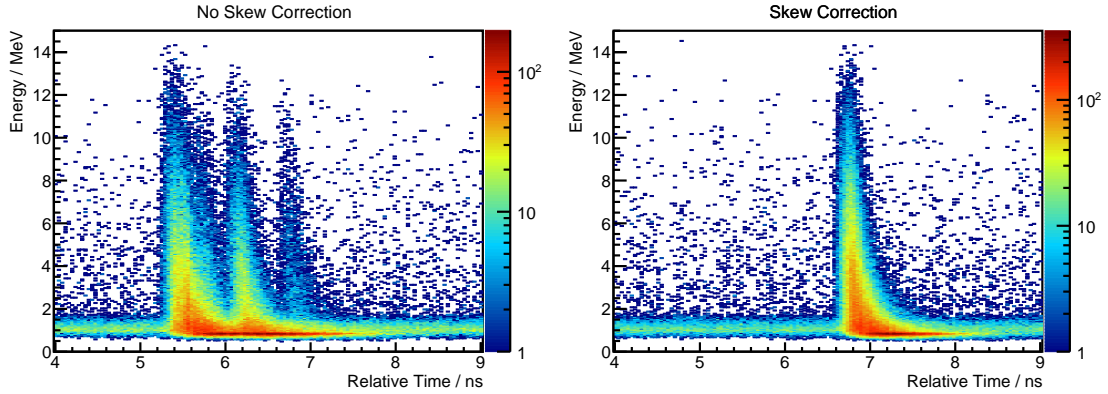


Figure 3.3.6.: Energy versus relative time measured with LYSO without and with skew correction.

3.3.8. Results

The results on the time resolution depend not only on the used scintillation crystal but also on the DPC settings. Consequently, the influence of TL, VS and VL on the time performance will be evaluated by using the measurements obtained with CeBr_3 as it resembles the material with the best theoretical properties (high LY and short τ). In the next step, the results of each material will be discussed including their characteristic features. Quantitative results are presented in a separate paragraph.

CeBr_3 as Standard Probe

Validation Length The VL has no influence on the time resolution but on the light collection process for the validation procedure. In case of a small VL, an energy threshold is visible (figure 3.3.7-left) as more scintillation light is required to validate sufficient dies in the short validation period. On the other hand, the energy threshold is not visible for 44 ns VL. Consequently, the full VL will be used in most of the data shown in the following sections.

Trigger Level and Validation Scheme Figure 3.3.8 shows the energy versus relative time distribution for variable TL and VS with fixed VL of 44 ns. We see qualitatively from TL 1 (figure 3.3.8

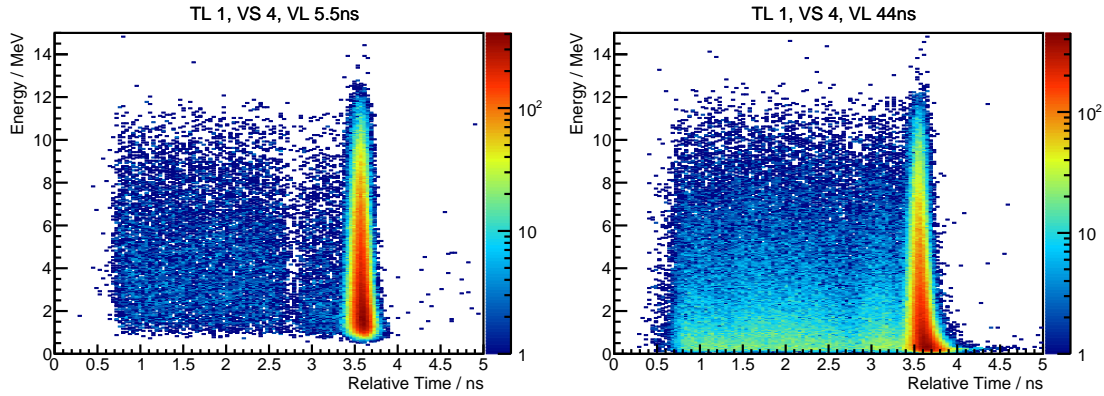


Figure 3.3.7.: Energy versus relative time measured with CeBr_3 for different VLs.

top left) over TL 2 (figure 3.3.8 bottom left) to the highest value TL 4 (figure 3.3.8 bottom right) that the peak resembling the bremsstrahlung beam becomes slightly broader. This shows the statistical uncertainty for detecting sufficient photons for the timestamp generation as more light is required for triggering. When varying the VS however, the width of the peak is not changing but a lower energy threshold is introduced which resembles the energy required to validate and illuminate the tile sensor [101]. For example, when increasing the VS from 2 (figure 3.3.8 top left) to 16 (figure 3.3.8 top right), the energy threshold is raised from 0 to about 1 MeV.

The time resolution as a function of the energy can be determined from the 2D histograms by projecting energy slices onto the energy axis and fitting the resulting time peak with a Gaussian function. The results as a function of energy are shown in figure 3.3.9 for different TL and VS settings. As expected, the measurements with TL 1 (black and red line) show the best results of about 150 ps at 4.44 MeV. Increasing the TL to 2 and 4 worsens the performance to 180 ps and 300 ps, respectively. The maximum achievable time resolution of CeBr_3 is somehow at 140 ps.

LYSO

The energy versus relative time distribution of LYSO is shown in figure 3.3.10 using TL 1 and selected VS settings. Like for CeBr_3 , a narrow bremsstrahlung peak can be seen. However, due to the intrinsic background from ^{176}Lu , uncorrelated events are visible at lower energies.

The background to signal ratio is worse for low VS (e.g. for VS 2, see figure 3.3.10-left) compared to higher settings like VS 4 (figure 3.3.10-right). When increasing the VS, less background events are validated by the DPC and the bremsstrahlung peak is more dominant.

GAGG

The results of GAGG are shown in figure 3.3.11 using the theoretically preferable DPC settings obtained with CeBr_3 (TL 1, VS 2). Due to an artefact of the time measurement with FC 1 (figure 3.3.11-left), where the bremsstrahlung peak was closely located at the TDC switching

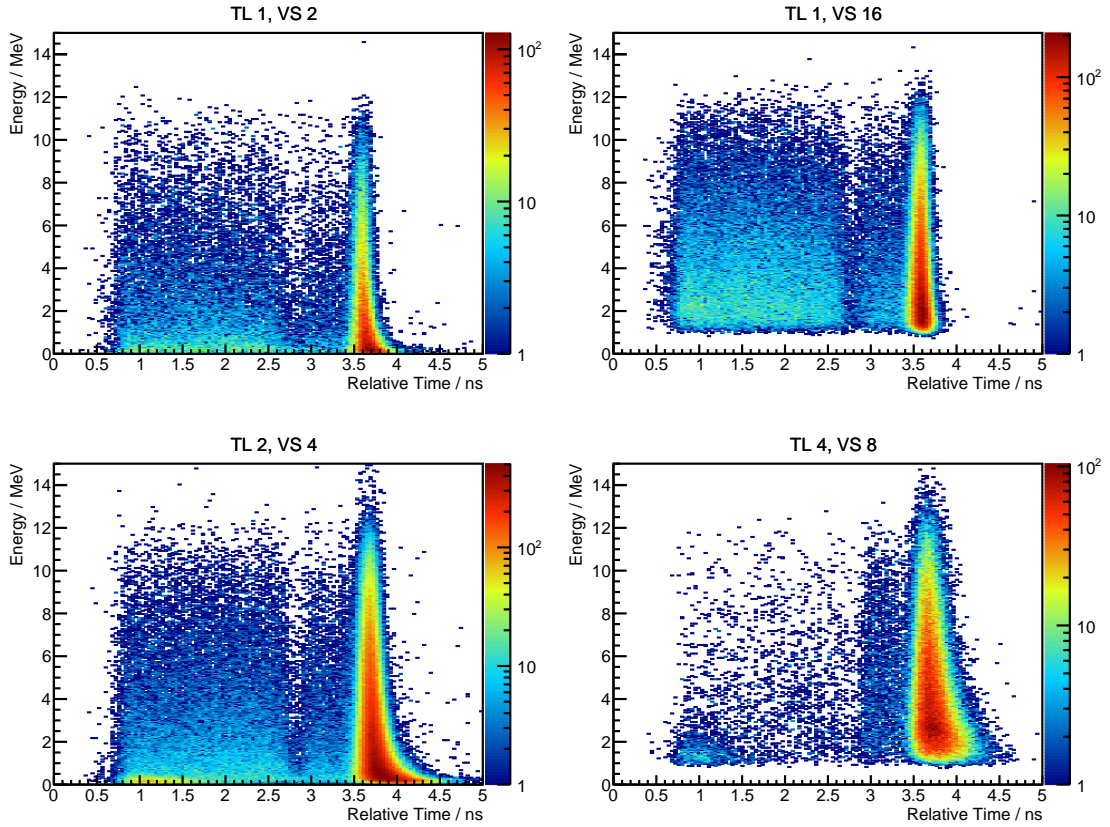


Figure 3.3.8.: Energy versus relative time measured with CeBr_3 for different TL and VS settings. VL is fixed at 44 ns.

point, not the averaged time distribution is used in our analysis but the information from FC 2 (figure 3.3.11-right). The bremsstrahlung peak is relatively broad at low energies and becomes, as expected, more narrow for higher energies.

GSO and BGO

GSO and BGO have the lowest effective LY when combined with the DPC compared to the other crystals and differ only by their main decay times (41 versus 300 ns). As a result, TL 1, VS 2, and the longest VL of 44 ns had to be applied to obtain sufficient light collection over the whole tile.

Again, like in case of GAGG, the time measurement with FC 1 is at the TDC switching point producing artefacts and, thus, FC 2 has to be used for the time information. As expected due to the low LY, a high energy deposition of about 2 and 3 MeV is required for GSO and BGO, respectively, to fully validate the tile sensor (see figure A.1.1 in the appendix). Nevertheless, the contribution coming from the bremsstrahlung beam is still visible for both materials, where BGO seems to perform better than GSO with respect to the time resolution.

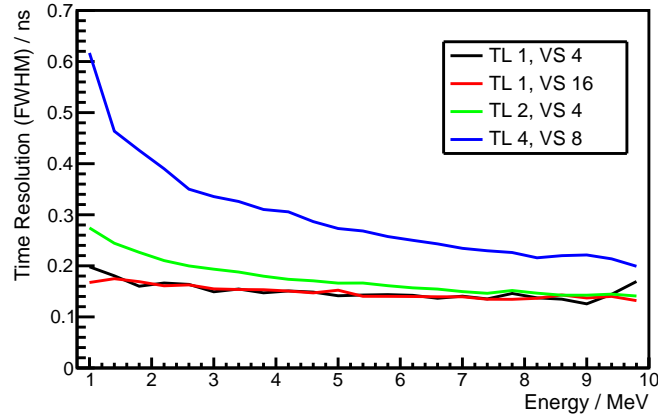


Figure 3.3.9.: Time resolution versus energy measured with CeBr_3 for different TL and VS settings. VL is fixed at 44 ns.

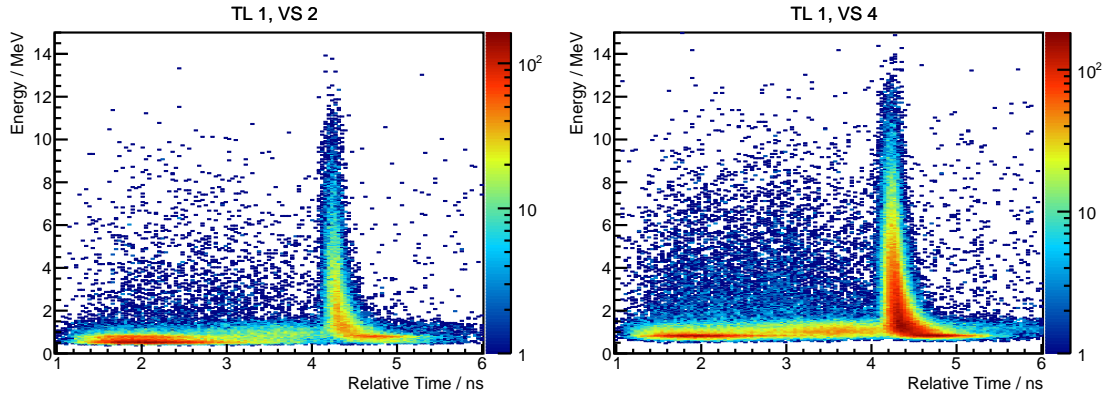


Figure 3.3.10.: Energy versus relative time measured with LYSO for TL 1 and selected VS settings. VL is fixed at 44 ns.

$\text{CaF}_2(\text{Eu})$ and $\text{CsI}(\text{Tl})$

When selecting appropriate and, in contrast to the previous materials, very different DPC settings, the bremsstrahlung beam is visible in each energy versus relative time distribution (see figure A.1.2 in the appendix). For both crystals, higher TL and VS had to be applied in order to obtain sufficient light collection during the validation phase. In case of $\text{CaF}_2(\text{Eu})$, TL 3, VS 4, and a VL of 22 ns were set (as the measurement with the full validation time gave no result due to artefacts), while for $\text{CsI}(\text{Tl})$, TL 2 was used in combination with VS 4 and the highest VL. Furthermore, only the FC 2 information could be used, as, for FC 1, the bremsstrahlung peak was again close to the TDC switching point. The peaks are relatively broad, but still visible. Both materials have an energy threshold of around 1 MeV.

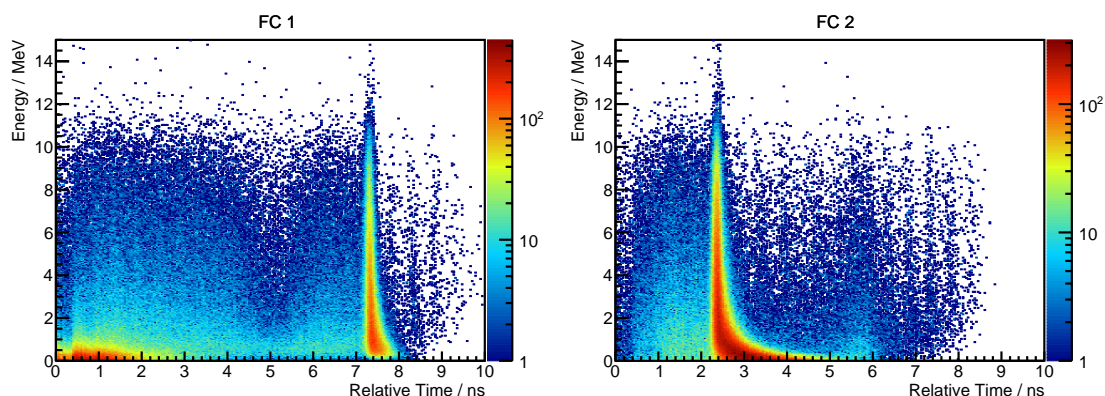


Figure 3.3.11.: Energy versus relative time measured with GAGG using FC 1 (left) and FC 2 data (right). DPC settings are: TL 1, VS 2, and VL = 44 ns.

Selected Results of All Crystals

The energy versus relative time distribution of each material obtained under optimal DPC settings were analysed as described for CeBr₃, to obtain the energy dependent time resolution (figure 3.3.12). As expected, an improvement of the time resolution of all materials is visible for higher photon energies. Furthermore, we can distinguish the materials in two different groups with time resolutions of different magnitude. Firstly, values above 500 ps ($E > 2$ MeV) achieved by CsI(Tl), CaF₂(Eu), and GSO. The second group consists of CeBr₃, LYSO, GAGG, and BGO which all achieve a time resolution below 500 ps ($E > 2$ MeV) and even values below 200 ps at energies above 5 MeV.

3.4. Discussion

In this chapter, the time resolution performance of several scintillation materials at high photon energies has been investigated. Different materials have been tested at the ELBE bremsstrahlung beam with photon energies of up to 12.5 MeV using the novel DPC light sensor as readout. Additionally, the theoretical performance according to the Hyman theorem has been presented.

The best performance is obtained with CeBr₃ achieving a time resolution of 150 ps (FWHM) at 4 MeV. This was already expected from the theoretical discussion as the material exhibits the highest LY per time and therefore the lowest Figure of Merit (FoM, see section 3.3.1 for details) according to the Hyman theorem [90]. Similar results were also observed in a parallel study using conventional PMTs [79].

As expected from the literature [96] and the low FoM, LYSO performs very reasonable with a time resolution of 170 ps at energies above 2 MeV. However, due to the intrinsic background, the value degrades for lower energies ($E < 1.5$ MeV) to several nanoseconds. This is usually not a problem in timing measurements as LYSO is mainly used in PET where coincidence conditions

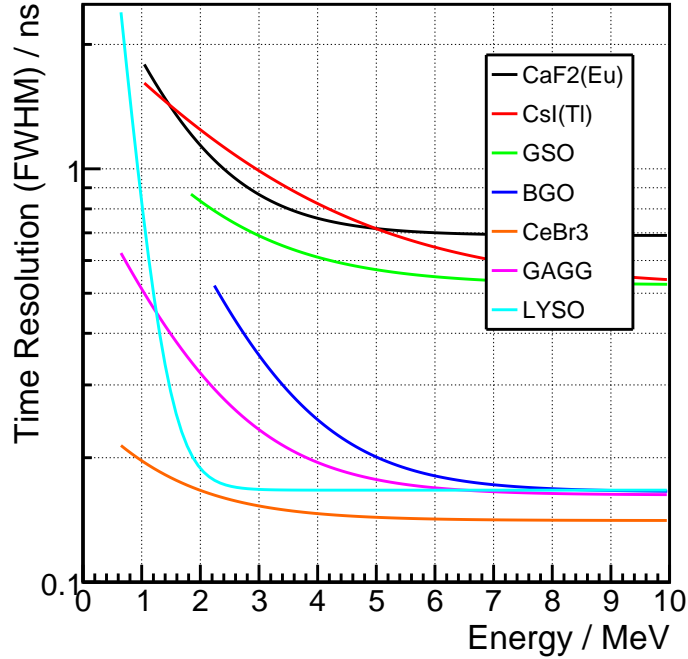


Figure 3.3.12.: Time resolution versus energy of all investigated materials using the optimal DPC settings for each crystal. The lower energy thresholds are a result of the requirement of a complete illumination of the sensor.

are applied. However, no background suppression could be applied in our experiment. On the other hand, only the higher energy range is relevant for PGT.

The time resolution of GAGG is also strongly depending on the deposited energy. While the relatively poor results at lower energies are in agreement with data from the literature [97], GAGG achieves a time resolution similar to LYSO at energies above 4 MeV, which is a factor of 3 better than the results from a measurement using PMTs [79].

Another material performing below the 200 ps mark is BGO. This is, in contrast to the other materials, very unexpected as BGO exhibits a relatively high FoM compared to the other well performing materials, and results from the literature (measured at energies around 1 MeV) indicate few nanoseconds time resolution. Nevertheless, with increasing energy, the time resolution enhances to around 170 ps. Information about the performance at energies below 2 MeV could not be obtained due the energy threshold. The unexpected performance might be a result of Cherenkov radiation. Due to energy depositions in the MeV region, high energetic Compton electrons are produced within the crystal. Because BGO has a very high refractive index of 2.15, Cherenkov radiation is produced for electrons with energies above 580 keV. The prompt photons could then have triggered the DPC, while the event is validated due to the incident scintillation light. However, Römer et al. made no similar observations in their study indicating that the performance of BGO is a result of the broad spectral response as well as the trigger and validation

scheme of the DPC [79].

The results of GSO are comparable with data from the literature, around 600 ps can be achieved at 4 MeV. This is also better than the value from Roemer et al. with around $1\ \mu\text{s}$ [79]. On the other hand, the time resolution is worse than expected from the Hyman theorem where GSO should have a similar performance as GAGG.

$\text{CaF}_2(\text{Eu})$ and $\text{CsI}(\text{Tl})$ are usually not considered for timing applications due to their very long decay times, which is also reflected in their high FoM values. Nevertheless, for both materials it is possible to obtain a time resolved measurement of the bremsstrahlung beam with time resolutions of about 800 ps at 4 MeV. This result is more or less in agreement with the study from Roemer et al., where $\text{CaF}_2(\text{Eu})$ achieves 900 ps and $\text{CsI}(\text{Tl})$ 1.2 ns [79].

In conclusion, several materials, namely CeBr_3 , LYSO, and GAGG, seem to be suitable for a potential application in PGT due to their good timing properties. In case of the other scintillators, either the time resolution is not sufficient or, like BGO, the detector based on the DPC exhibits a high energy threshold. Furthermore, the effectiveness from a registered photon to a fully validated DPC sensor differs heavily with the materials. While CeBr_3 and LYSO have a high fraction of “true” events, most of the events in case of the slow scintillators had to be discarded due to insufficient light collection.

3.5. Applicability of the DPC in Clinical Practice

By deploying the novel light sensor DPC, exceptional results on the time resolution can be obtained for a wide range of materials. However, not only the best possible time resolution is in our focus but also a fast translation of the PGT method into the clinical practice. In this context, the DPC seems not to be a reasonable choice.

First of all, even though the tile sensor is a very compact device with integrated electronics, it still requires a temperature stabilization and preferably a cooling system. Consequently, the complexity and footprint of the system is increased depending on the kind of cooling system.

Furthermore, the sensors are still in an experimental stage which is especially visible when considering the data connection using USB 2.0. Even though the sensors could handle event rates of around 1 Mcps, the data transfer limits the device to only 122 kcps, which is one order of magnitude lower than the requirements for PGT [13]. The problem might be solved by the development of new readout boards [123], however, since the presentation in 2013, no prototype has been made available for external users.

Lastly, the problems when measuring with monolithic crystals, which are required for PGs, became evident in our study at ELBE. In order to obtain usable data, all scintillation photons should be collected which requires a minimum number of dies. However, because of dies in recharge mode or with insufficient number of scintillation photons during the validation phase, most events have to be discarded, which reduces the efficiency of the detector. This could be encountered by using the neighbour logic of the DPC, where all dies are readout when one initial die is validated

[101]. However, this increases the load of dark counts reducing the already limited throughput of “real” events.

Summarizing, the DPC is currently no suitable light sensor for an application in PGT. The alternative for a fast translation into the clinical practice would be the usage of conventional PMTs with a special focus on time resolution. Nevertheless, choosing PMTs reduces the potential candidates of scintillation crystals as the triggering and timestamp generation is not as promising as for the DPC. This is also reflected in the study by Römer et al. [79], where only CeBr_3 and LYSO seem reasonable choices with respect to the time resolution. Compared to the results of our study, GAGG and BGO seem not usable in PGT due to an insufficient timing performance. LYSO on the other hand struggles with the high internal background which would reduce the ratio between detected PGs to the number of total events and therefore the sensitivity of PGT. Consequently, CeBr_3 is the optimal scintillator in combination with a PMT due to the achievable time resolution and the absence of internal background while still providing sufficient absorption capabilities for high energetic photons. Furthermore, the material exhibits very good energy resolution which is required for selecting energy windows for background reduction.

4. Implications for PGT at a Clinical Facility

In this chapter, the applicability of the PGT method at a clinical proton therapy facility is discussed. As introduced in section 2.4.3, the energy dependent Bunch Time Spread (BTS) and RF-bunch phase drifts have been identified in the experiment at WPE. Both effects have been investigated using the PGT setup resulting in measurements with high background rates. As a result, a dedicated experimental setup comprising two detectors in coincidence is introduced which measures a clearly correlated proton signal from the primary beam to reduce the background contribution as far as possible. The obtained data is used to determine the proton arrival time to correct for RF-bunch phase drifts. In addition, corrected PGT data from the irradiation of a PMMA phantom with inhomogeneities is used for the first 2D-imaging of heterogeneities using PGs. In the next step, the BTS as well as further beam parameters, like the energy spread and the proton transmission rate are determined as a function of beam energy and Energy Selection System (ESS) settings.

Part of the presented results have been published in a scientific paper [124].

4.1. Motivation

In the translation of PGT from the research accelerator at KVI-CART [51] towards the therapeutically used clinical cyclotron C230 [12], several implications have been identified which could potentially destroy the detection of range shifts based on PGT.

First of all, by detecting the PG emission from a thin PMMA target, Hueso-González et al. [12] found that the BTS is increasing for lower beam energies and that it could be reduced by lowering the Momentum Limiting Slit Opening (MLSO) which is part of the ESS. Nevertheless, the indirect method struggled with high background coming from scattered primary protons and neutron induced events overlaying the actual signal. Furthermore, the variation of the proton transmission rate, i.e. the number of protons at the nozzle exit relative of the ones extracted at the cyclotron, was not determined at WPE. However, this number might be reduced when lowering the MLSO which is crucial for the operation of a clinical facility and could influence the patient treatment time. A systematic study should therefore comprise a detection system suppressing the background and being able to measure beam current and time structure of the proton bunches with reasonable precision.

Secondly, Hueso-González et al. observed variations of the leading edge positions of PGT spectra in consecutive measurements without changing the settings [12]. They concluded that this effect stems from phase drifts between RF signal and proton bunch extraction and that

drifts of 100 ps per hour can occur [12]. The RF-bunch phase drifts can overlay potential range variations which would be visible as shift in PGT peak centroids and thus have to be corrected for. Consequently, another reference time signal is required that allows for the correction of these shifts.

Combining the observations made at WPE, the correction of RF-bunch phase drifts as well as the systematic evaluation and possible reduction of the BTS are required to bring PGT closer to the clinical application.

As a consequence, the so-called Proton Bunch Monitor (PBM) setup was developed in the framework of this thesis to answer the following questions:

- Is it possible to utilize the mean arrival time of the proton bunches as time reference to correct the PGT spectra for RF-bunch phase drifts?
- What is the magnitude of the BTS and how does it depend on beam energy and MLSO?
- How does the proton transmission rate change when varying the MLSO?

The questions are investigated in two different experimental campaigns with slightly different setups. *Campaign 1* deals hereby with the phase drift correction and *Campaign 2* with the measurement of the BTS and the proton transmission rate.

Furthermore in campaign 1, the PBM setup is used to correct PGT data obtained while scanning a heterogeneous phantom with a proton pencil beam. Using further capabilities of the PBM setup, this allowed for the first time the 2D imaging of an inhomogeneities target based on PGs.

4.2. Experimental Setup

4.2.1. The IBA Proteus 235 System at UPTD

Like WPE, the UPTD is based on the Proteus 235 Proton Therapy System by IBA. The system (figure 4.2.1) comprises the proton accelerator, the beam delivery system with sub-units like the Energy Selection System (ESS), the experimental room with a fixed beamline, and the gantry treatment room (GTR2) with a universal nozzle for patient treatment.

The accelerator is a fixed-energy isochronous cyclotron (type C230), which is used in several treatment facilities worldwide [10]. The C230 is operated with a RF of 106.3 MHz accelerating the protons to 230 MeV and extracting them with a microbunch separation of 9.4 ns. The resulting proton beam has a range of about 32 cm in water [5] which is more than usually required for patient treatment. The particles are slowed down to the desired energy in a sub-unit of the ESS, the *degrader*, using material of appropriate thickness. After deceleration, the protons are further guided through sub-units of the ESS like collimating slits in x and y direction. This is to ensure the proper spot size as well as the requested energy according to the treatment specifications.

After the beam preparation, the protons are transported through several dipole and quadrupole magnets and are then finally sent through the rotating beamline of the gantry to the GTR2 or

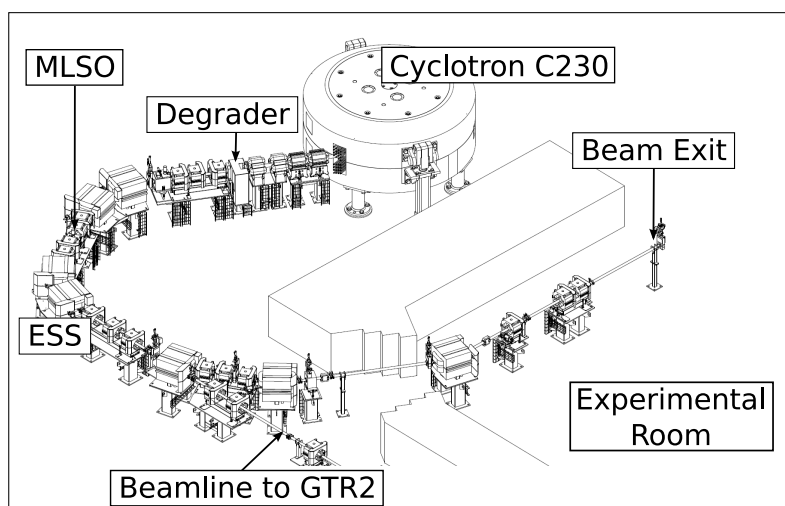


Figure 4.2.1.: Schematic drawing of the proton therapy system of the UPTD facility. The system consists of the accelerator C230, the energy selection system (ESS) which comprises the degrader and the momentum limiting slit opening (MLSO), as well as the gantry treatment room (GTR2), and the experimental room. The drawing was provided by IBA.

through the fixed beamline in the experimental room. Both rooms can be used in parallel with a switching time of few seconds due to an in-house developed hardware setup and controlling software [125].

When decelerating in the degrader, an energy straggling is introduced into the proton bunches due to the statistical distribution of the energy transmission between particle and absorbing material [126]. The energy distribution translates to a momentum spread within the proton bunch. As a result, the beam disperses time-wise through its path along the beamline. The size of this dispersion depends on the distance between degrader and the point of observation (e.g. detector), the mean velocity of the protons, as well as the magnitude of the energy straggling. In combination with an intrinsic time width (due to the acceleration process and from an additional energy straggling from thin foils within the beamline), the effect of the beam dispersion is called the Bunch Time Spread (BTS). Hueso-González et al. [12] observed that the BTS is higher for lower proton energies and that it can be controlled in the ESS. By lowering the Momentum Limiting Slit Opening (MLSO), the momentum spread is confined and with that the BTS. However, in this process more protons are filtered out of the primary beam reducing the overall proton transmission rate, i.e. the ratio between particles irradiating the patient and the number of protons extracted at the cyclotron. As a consequence, higher activation occurs in the ESS, the lower transmission has to be countered by increasing the beam current or the treatment time, and the ion source of the cyclotron has to sustain a higher strain. In total, the proton transmission rate is an important parameter in the operation of a treatment facility.

Another effect relevant for PGT occurs in the acceleration process. In principle, the proton extraction has a fixed phase correlation to the RF of the cyclotron. However, the orbital fre-

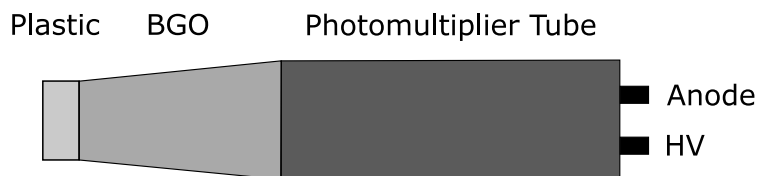


Figure 4.2.2.: Schematic drawing of the proton bunch monitor showing the phoswich setup comprising the plastic scintillator and the BGO crystal. Details are explained in the text.

quency of the protons can slightly change due to tiny variations of the main magnetic field of the accelerator. After a large number of cycles, those small changes add up to an observable shift between RF phase and proton extraction time. Hueso-González et al. [12] have evoked this effect artificially by varying the operational current in the main coil of the cyclotron by 0.01 %, resulting in a phase drift of about 1 ns. Consequently, as those tiny variations are hardly controllable, RF-bunch phase drifts may occur during the irradiation.

4.2.2. Proton Bunch Monitor

For detecting high energetic protons and characterizing the time structure of the proton bunches, the PBM setup has to fulfil several requirements like particle identification, absorption capabilities for protons of more than 100 MeV, as well as excellent time resolution of few hundred picoseconds (for details on the time resolution see sections 4.4.3 and 4.4.4). The required timing capabilities are necessary to correct PGT data for RF-bunch phase drifts of few picoseconds as a range shift of 1 cm means a PGT centroid shift of only 50 ps [51].

Consequently, the phoswich concept [127, 128] was utilized in our experiment exploiting the combination of two scintillation materials with different decay times. The phoswich detector (i.e. the PBM) consists of a fast plastic scintillator¹ (dimensions $2.00 \times 2.00 \times 0.94 \text{ cm}^3$) and a slower BGO crystal with tapered shape (front surface from $2.00 \times 2.00 \text{ cm}^2$ to rear surface with $2.45 \times 2.45 \text{ cm}^2$, thickness of 5 cm). The plastic scintillator is stacked on top of the BGO crystal, which is then coupled using silicon grease, type EJ 550 from Eljen Technology, to a PMT (Photonis XP 2972). A schematic drawing is shown in figure 4.2.2.

Particles can be identified by using the dE/dx information from the plastic material (as each type of particle has different energy loss) and the full energy deposition in the BGO crystal. Furthermore, using a plastic scintillator with its very fast light pulse provides the PBM with excellent timing capabilities.

Throughout both campaigns, two identically built PBMs are used which will be referred to as

¹The plastic material is not exactly known as it was an old “shelf finding” without labels. However, the pulse shape is similar to the one from BC-408 (also known as EJ-200).

PBM0 and PBM1.

4.2.3. PGT Detector

PGT spectra are measured in our experiment either to have data for the phase drift correction or for the comparison between direct and indirect BTS measurement using γ -rays or protons, respectively.

In campaign 1, using the results obtained in chapter 3, a CeBr_3 detector, which is referred to as C1, was deployed to measure PGs. The scintillation crystal from Scionix Holland BV with dimensions of $33 \times 33 \times 10 \text{ mm}^3$ is optically coupled with silicon grease EJ 550 to a PMT, type R2059 from Hamamatsu, which is then connected to an in-house made stabilized Voltage Divider (VD). The detector was already used in [79] and its time resolution was determined to be 235 ps FWHM for photon energies above 2 MeV.

A commercial CeBr_3 detector from Scionix Holland BV with dimensions of $\varnothing 2'' \times 2''$, later referred to as C2, was deployed in campaign 2. The detector is characterized in section 5.2.1, showing a time resolution of 240 ps FWHM for $E > 2 \text{ MeV}$.

4.2.4. Readout Electronics

The experimental setup is based on Nuclear Instrumentation Module (NIM) and Versa Module Eurocard (VME) readout electronics. The data acquisition uses a custom software environment based on the C++ framework ROOT [121]. Further details are discussed in [118].

4.2.5. Signal Processing

The anode output of each PBM is split on a fast amplifier (CAEN N797). Here, one signal is fed to a Constant Fraction Discriminator (CFD) (Canberra 454), while the second signal is passively split and each output given on a Charge to Digital Converter (QDC) (CAEN V975). One QDC operates with a short gate of 75 ns to integrate the fast pulse from the plastic scintillator, and the other QDC is used with a longer gate of about 560 ns to integrate the sum of both pulses (plastic and BGO). A Time to Digital Converter (TDC) (CAEN V1290N), with a resolution of about 24.4 ps per channel, is used to determine the relative time between detected events and RF signal of the accelerator. In this context, the CFD output signal is connected to the TDC for creating the detector timestamp. In case of the reference time, the RF pulse is given on another CFD (Phillips Scientific 6915), whose logical output is then connected to the TDC. In case of an event, both timestamps are recorded and the difference between both timestamps is determined. Furthermore, a logic module (CAEN V1495) is deployed to determine the gross and net count rates of the detectors, i.e. the free running trigger rate and triggers not inhibited by the busy signal of the data acquisition. The information can be further used to evaluate the dynamic dead time of the setup. Additionally, the logic module can be used to define the coincidence regime, the so-called *majority*. Here, a pre-selected value is defined in the data acquisition routine defining the

number of required detector signals for a valid event. For example, majority two means that at least two triggered detectors with overlapping gate signals are needed to trigger the data analysis. The majority setting can be used to reduce the number of processed events as the throughput of the electronics is limited to about 10 kcps in our setup.

After completing campaign 1, the electronics setup was completely rebuilt for campaign 2 using the same hardware modules but different CFD settings like delay length and walk correction. Here, special focus was set on the best obtainable time resolution of the PBMs.

The C1 detector, used in campaign 1, has a stabilized VD with two output signals: Anode and last dynode. The dynode signal is shaped by a spectroscopic shaping amplifier (Ortec 855 with $0.5 \mu\text{s}$ shaping time) whose output is then given on a peak sensing Analog to Digital Converter (ADC) (CAEN V785N) for determining the energy deposition. The trigger and timestamp generation is based on the anode signal. The usage of CFD, TDC, and logical module is similar as described for the PBMs.

In case of the C2 detector, nearly the same setup as for C1 was used. However, anode and last dynode signal were swapped, i.e. the last dynode was inverted and connected to the CFD for trigger and timestamp generation, while the anode signal was plugged into the shaping amplifier for the energy information. This was done in order to use the signal with less noise (here the dynode) for the timing information, while the anode provided the better signal in case of C1.

An overview of the signal processing is given as block scheme in figure 4.2.3, while a summary of the detector types is given in table 4.2.1.

Table 4.2.1.: Summary of the detector types used in both campaigns. Purpose, high voltage, readout for the energy information and experimental time resolution values of the PGT detectors are given. Results on the time resolution of the PBMs are presented in the corresponding sections 4.4.3 and 4.4.4.

Name	Detector type	Purpose	HV (V)	Readout	Time resolution FWHM (ps)
PBM0	phoswich	protons	-950	QDC	-
PBM1	phoswich	protons	-1000	QDC	-
C1	CeBr ₃	gammas	-1400	ADC	235 (at 2 MeV)
C2	CeBr ₃	gammas	-1200	ADC	240 (at 2 MeV)

Note: The PBMs were used in both campaigns, while C1 and C2 were used only in campaign 1 or 2, respectively.

4.2.6. Experimental Setup

Both campaigns are realized in the experimental room of UPTD (see figure 4.2.1 for details), which comprises a horizontally fixed beamline. Beam parameters like energy and extracted current at the cyclotron are set using the in-house made controlling system [125]. Additionally, in case of campaign 2 a calibrated Ionization Chamber (IC) was monitoring the extracted beam current at

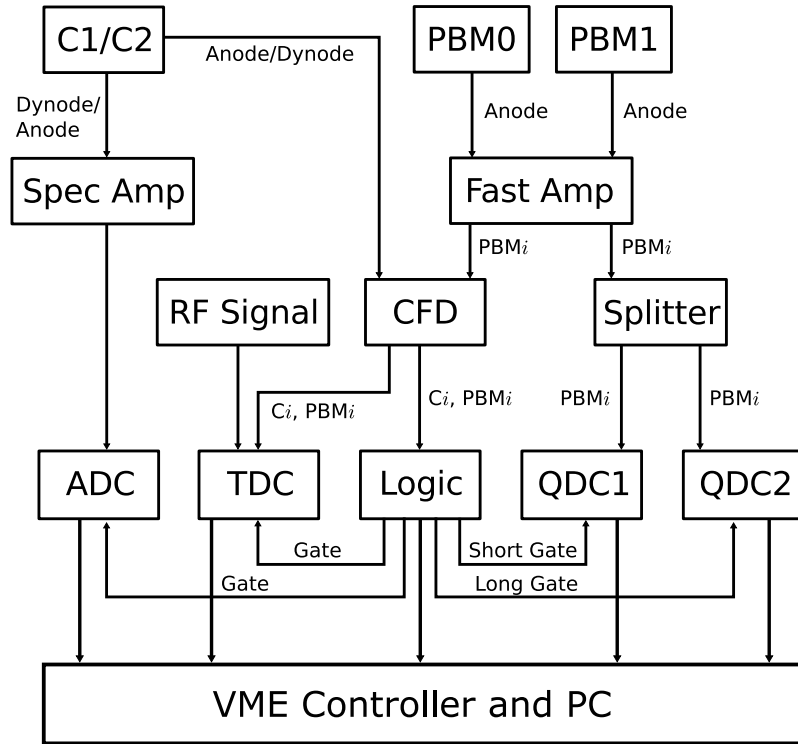


Figure 4.2.3.: Block diagram of the experimental setup used to measure the proton bunches with the PBMs and PGT data with a CeBr_3 detector. Details are explained in the text.

the exit window of the beamline in the experimental room.

After extraction, the proton pencil beam is impinging on a thin scattering target made out of polypropylene (for campaign 1) or PMMA (for campaign 2), each with a thickness of about 1 mm. Due to the hydrogen content of the foils, elastic pp -scattering occurs and is utilized to create two coincident protons emerging from the target. The energy of the incident proton is partially transferred to the resting hydrogen nucleus. The resulting kinetic energy of both protons depends on the scattering angle and is equally shared if both particles are scattered by the same angle of about 45° relative to the beam axis. By setting up two PBMs in this configuration (figure 4.2.4-top and figure 4.2.4-bottom right), both protons, each with half the beam energy, can be detected in coincidence. Note that due to relativistic effects, the scattering angle for equally shared energy is slightly smaller than 45° , e.g. it is about 43.4° at the highest available beam energy of 225 MeV. Nevertheless, the solid angle of the detectors is sufficient for all used settings. The distance s between scattering target and detectors is varied between both campaigns from 30 cm (campaign 1) to 20 cm (campaign 2).

By deploying the coincidence setup, single events can be suppressed in our measurement routine in order to reduce the background contribution. Additionally, with suitable energy windows, the background can be reduced even further (see section 4.3.1 for details). Furthermore, the setup of two PBMs in coincidence can be utilized to individually determine the time resolution of each

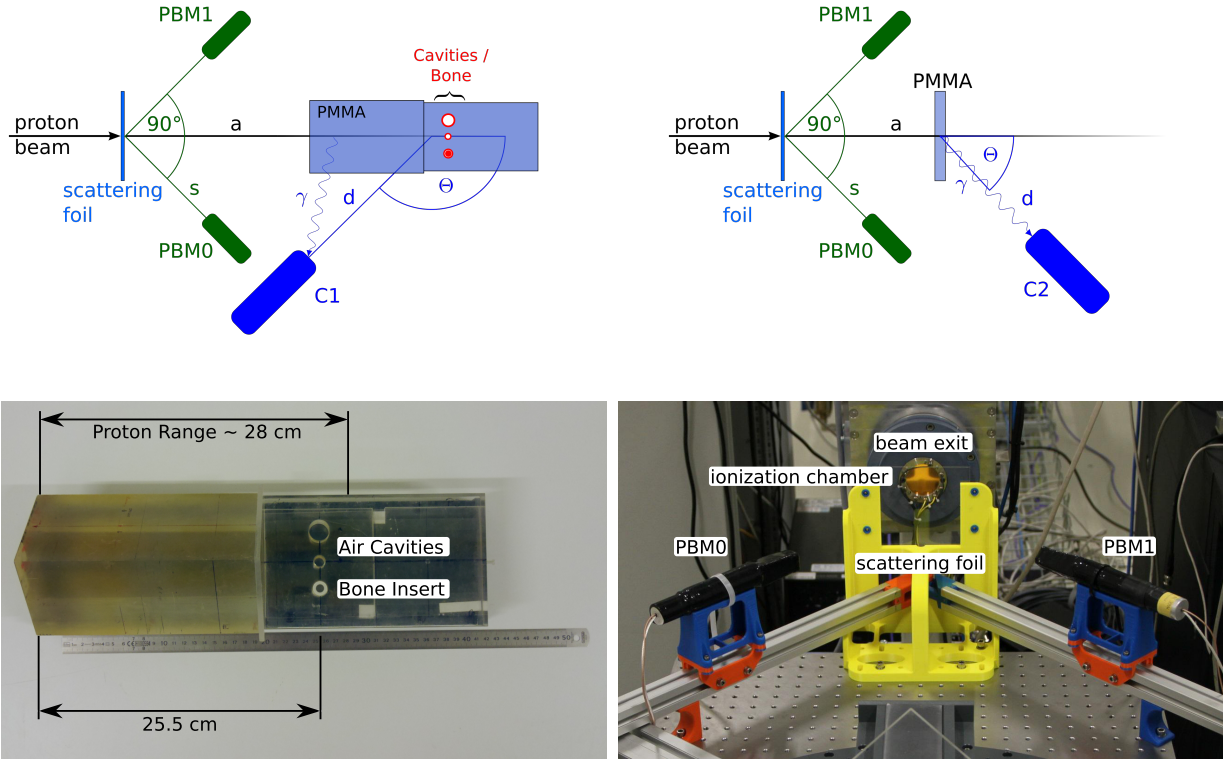


Figure 4.2.4.: Schematic drawing of the setup of campaign 1 (top, left) and campaign 2 (top, right). The proton beam is impinging on a thin scattering foil made out of PMMA or polypropylene. Due to elastic pp -scattering, two coincident protons emerge from the target and can be detected by the PBMs. A CeBr_3 detector (C1 or C2) monitors the PG emission from a PMMA target (thick and inhomogeneous in case of campaign 1, thin for campaign 2). The distances d and s as well as the angle Θ are varied between the campaigns (see table 4.2.2 for details). Bottom-left: Photography of the inhomogeneous target (used in campaign 1) with two air cavities and a bone insert (at 25.5 cm target depth). Bottom-right: Photography of the PBM setup used in campaign 2.

detector and to extract the BTS from the measured data (see section 4.3.1 for details).

The majority of protons undergoes only electromagnetic interactions in the thin scattering target and is just slightly slowed down. Hence, the beam can be used to irradiate another PMMA target which serves as PG emitter. The photon emission is monitored by a CeBr_3 scintillation detector, namely C1 or C2, respectively (figure 4.2.4-top).

In campaign 1, the distance a between the PMMA phantom (thickness of 40 cm) and the scattering target was 30 cm. The target was made of two PMMA blocks, where the rear one had three holes (diameters: 9, 13, and 18 mm). The medium sized hole was filled with a hollow cylinder of bone-equivalent material (wall thickness 3 mm, type SB3 cortical bone, model 450 from Gammex-RMI, further details can be found in [129]) and the residual cavity of 7 mm diameter was filled with PMMA. The other two holes served as air cavities. A photography of the phantom

is shown in figure 4.2.4-bottom left.

The PG emission from the thick target was monitored by the C1 detector. The detector was placed upstream ($\Theta = 135^\circ$ with respect to the beam axis, see figure 4.2.4-top left) and was aligned to a target depth of about 23 cm at a distance of 41 cm. 24 individual measurements were performed to observe potential RF-bunch phase drifts using the maximum available beam energy of 225 MeV. Relatively low beam currents of 100 pA were used to cope with the limited throughput capabilities of the VME data acquisition. The trigger rate alone for C1 was about 15-20 kcps. Each measurement had a duration of about 10-15 minutes and the campaign lasted about 8 hours. After most measurements, the inhomogeneous target was shifted on a linear stage perpendicular to the beam axis in steps of 4 mm. As a result, the phantom was scanned by the pencil beam. All three detectors (2 PBMs and C1) were operated in parallel with majority setting 1.

In case of campaign 2, the thick target was replaced by a thin slice of PMMA (thickness 5 mm) which again serves as PG source. The data measured by the PBM setup and the PGT detector C2 can then be compared for potential differences in the time-wise shape of the bunches. The γ -ray detector was positioned downstream ($\Theta = 45^\circ$ with respect to the beam axis, see figure 4.2.4-top right) to minimize the TOF contribution [51]. The distance d was about 60 cm to reduce the detector load. The PBM setup was used with majority setting 2 (coincident mode) and C2 was operated separately. Therefore, for the PBM measurement, both the background contribution as well as the measurement time was reduced. 8 different beam energies between 69 and 225 MeV were used. Additionally for selected energies, the MLSO was reduced from the default setting of 30 mm to smaller values (20, 10, and 5 mm). Each measurement lasted around 2-5 minutes with beam currents at the nozzle exit between 0.4-0.8 nA.

An overview of the experimental settings of each measurement campaign is given in table 4.2.2.

4.3. Methods

4.3.1. Data Analysis

Time Slewing Correction The time walk of all detectors is corrected by applying the procedure described in [118]. The energy versus relative time distribution is fitted in several energy slices over the full range to determine the position of the beam induced peak. The resulting data (position versus energy) is fitted using a polynomial of second order. The function is then used to correct the relative timestamp.

Event Filter PBMs Only coincident events in the PBMs were selected for the further analysis (software-sided filtering in campaign 1, hardware-sided in campaign 2). As slight gain variations may occur in the PMT, for each measurement and detector, energy windows on the short gate (mainly resembling the energy deposition in plastic) and the long gate (approximately the full energy information) are set to comprise the full peak region corresponding to the energy deposition

Table 4.2.2.: Summary of the experimental settings used in both campaigns. The abbreviations are explained in the text and in figure 4.2.4-top.

	Campaign 1	Campaign 2
Purpose	exploration and correction of RF-bunch phase drifts	quantification of BTS and proton transmission rate
Detectors	2 PBMs, C1	2 PBMs, C2
Measurement mode	parallel in Maj1	PBMs Maj2, C2 Maj1
Scattering target	1 mm polypropylene	1 mm PMMA
PG production target	PMMA, thickness 40 cm	PMMA, thickness 5 mm
Distance s PBMs (cm)	30	20
Distance d C1/C2 (cm)	41	60
Distance a (cm)	30	40
(Scatter to PG target)		
Angle Θ C1/C2 ($^\circ$)	135	45
Beam energy (MeV)	225	69, 90, 110, 130, 160, 180, 200, 225
Slit opening (mm)	30	5, 10, 20, 30
Beam current (nA)	≈ 0.1	0.4-0.8
Duration (min)	10-15	2-5

of the elastically scattered protons (figure 4.3.1).

Event Filter PG Detectors The CeBr_3 detectors are deployed to measure PGs and to analyse their time distribution. A lower and higher energy threshold are used in the offline analysis to reduce uncorrelated background (from neutrons, charged particles, and scattered photons). The dominant energy region for PGs produced in PMMA is between 3.0 and 6.5 MeV (see section 2.1.3 and table 2.1.1). Subsequently, the same thresholds are applied as energy window for C1. In case of C2, the energy cut is limited to 3.0-5.0 MeV to account for the worse signal to background ratio due to the thinner PMMA target.

Determination of the Bunch Time Spread In the measured time distributions, the BTS T_{BTS} is folded with the finite time resolution $\Delta T_{\text{detector},i}$ of detector i and the time uncertainty of the emission point of the protons inside the scattering target ΔT_{target} . This parameter depends on the transit time uncertainty due to the target thickness as well as the spot size of the beam. An extended proton field allows a variation of scattering angle-combinations to be detected by the PBMs which has implications on the proton scattering kinematics and therefore on the travel times to the detector.

In case of Gaussian distributions, the FWHM of the time distribution $\Delta T_{\text{meas},i}$ measured with

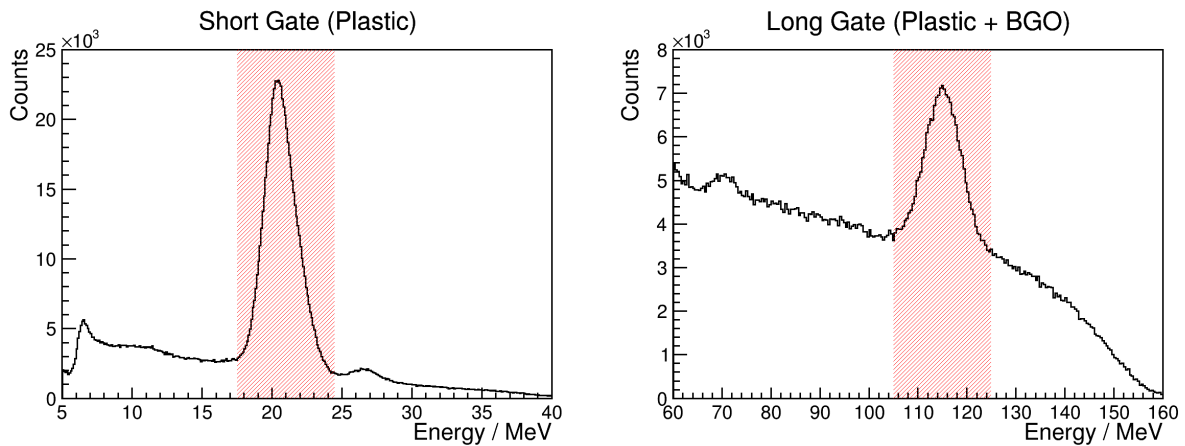


Figure 4.3.1.: Energy deposition in plastic (left) and both scintillators (right) of PBM0. The highlighted areas show the applied energy windows to filter out background contributions. The measurement was performed at a beam energy of 225 MeV.

detector i can be written as follows:

$$\Delta T_{\text{meas},i}^2 = T_{\text{BTS}}^2 + \Delta T_{\text{detector},i}^2 + \Delta T_{\text{target}}^2. \quad (4.3.1)$$

Concerning ΔT_{target} , the transit time through the 1 mm target is below 10 ps and therefore negligible. The spot size in the experimental room was determined as function of the beam energy using a Lynx detector from IBA Dosimetry (Schwarzenbruck, Germany). The beam has approximately a circular shape with a diameter between 23 mm FWHM for the lowest energy of 69 MeV and about 15 mm for 225 MeV. In the extreme case of interaction points at the edge of the circle, one determines a maximum time uncertainty due to the spot size between 65 ps (for 225 MeV) and 190 ps (for 69 MeV). However, those values are the worst case and furthermore negligible as the value for the highest energy is well below the expected detector time resolution of 150 ps, and for lower beam energies, the BTS will be significantly higher (see section 4.4.4). As a consequence, (4.3.1) shortens to

$$\Delta T_{\text{meas},i}^2 = T_{\text{BTS}}^2 + \Delta T_{\text{PBM}i}^2. \quad (4.3.2)$$

In addition to the measured time spread, it is possible to obtain the Coincidence Resolving Time (CRT) ΔT_{CRT} between both PBMs. This parameter is independent of the beam structure, because the elastic pp -scattering is triggered by an individual proton. Thus, the CRT is defined by both detector time resolutions:

$$\Delta T_{\text{CRT}}^2 = \Delta T_{\text{PBM0}}^2 + \Delta T_{\text{PBM1}}^2. \quad (4.3.3)$$

Combining 4.3.2 and 4.3.3, $\Delta T_{\text{PBM},i}$ for each PBM and T_{BTS} can be calculated as follows:

$$\Delta T_{\text{PBM},i}^2 = \frac{1}{2} \cdot (\Delta T_{\text{meas},i}^2 + \Delta T_{\text{CRT}}^2 - \Delta T_{\text{meas},j}^2), \quad (4.3.4)$$

$$T_{\text{BTS}}^2 = \Delta T_{\text{meas},i}^2 - \Delta T_{\text{PBM},i}^2, \quad (4.3.5)$$

$$= \frac{1}{2} \cdot (\Delta T_{\text{meas},i}^2 + \Delta T_{\text{meas},j}^2 - \Delta T_{\text{CRT}}^2), \quad (4.3.6)$$

with $i \neq j$ and $i, j = 0, 1$.

The approach (4.3.1) is not applicable for non Gaussian-shaped distributions. In this case, the BTS can be extracted numerically using the ROOT function *TSpectrum::Deconvolution* by unfolding the detector time resolution from the measured data [121]. The function is based on the Gold deconvolution algorithm, which is conventionally applied in γ -spectrometry to decompose individual γ -lines [130]. The detector time resolution is approached as a Gaussian using the experimentally determined time resolution as input (see section 4.4.4 for details).

4.4. Results

4.4.1. Particle Identification

Figure 4.4.1 shows an exemplary 2D distribution of the short gate integral (energy deposition in plastic) versus the long gate integral (energy deposition in plastic and BGO) for events collected in campaign 1 (PBM0, majority 1, beam energy 225 MeV). The energy deposition corresponding to the short gate integral is approximated using the minimum energy required by protons and deuterons to penetrate the plastic material. The energy deposition in the long gate is calibrated with the expected peak positions of the protons from elastic pp -scattering, i.e. half of the beam energy, using data from several beam energies.

A peak between 105-125 MeV full energy deposition (i.e. the long gate) shows the distribution of elastically scattered protons (see also figure 4.3.1-right). A banana-shaped branch around the peak represents protons with a maximum energy deposition of 160 MeV from scattering at heavier nuclei like ^{12}C and ^{16}O . Protons with energies above 160 MeV pass through the detector due to the finite thickness of the BGO crystal. In such a case, the energy deposition is reduced in both materials, which is visible as falling distribution to lower energies.

Furthermore, in our experiment deuterons and tritons are also produced which can be identified as separate banana-shaped branches with higher energy depositions in the short gate integral. Similar observations were made in [131, 132].

4.4.2. Event Filtering

The time versus time distribution of both PBMs without and with energy filter is shown in figure 4.4.2 (measured in campaign 2, beam energy 225 MeV, MLSO 30 mm)

While the non-filtered distribution has some background contributions (vertical and horizontal

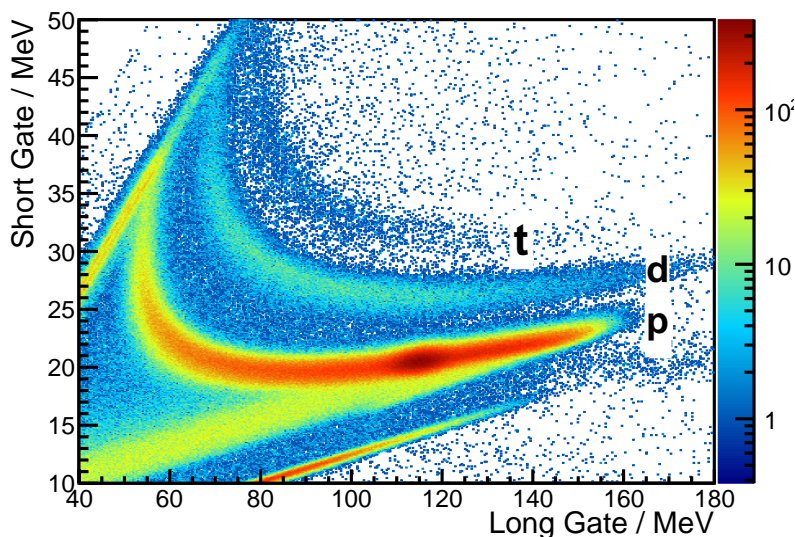


Figure 4.4.1.: Exemplary 2D distribution of the short gate integral (energy deposition in plastic) versus the long gate integral (energy deposition in plastic and BGO) measured with PBM0 (majority 1, beam energy 225 MeV). A distinct peak at about half the beam energy (105-125 MeV) is visible and reveals protons (p) from elastic pp -scattering. Additionally, deuterons (d) and tritons (t) are visible in separated branches.

structures), most background events could be suppressed in the filtered data and just the central spot, resembling the proton beam, is visible. Thus, the background level can significantly be reduced by using appropriate energy windows and by filtering for coincident events.

It should be noted that this procedure does not require the phoswich principle and that two fast scintillation detectors in coincidence would also be sufficient. The phoswich detectors were used at first to evaluate the overall possibilities to measure the bunch structure. Furthermore, the coincidence regime might not be applicable in the clinical scenario as no extra scattering target could be placed behind the beam nozzle and only thin scattering foils like thin aluminium coated Mylar foils at the beam exit window etc. are available. As a result, the number of scattered protons might be very low prohibiting the coincidence measurement and other filters like particle identification have to be applied, which then requires the phoswich construction.

4.4.3. Correction of RF-Bunch Phase Drifts and 2D PGT Imaging

Time Spread and Time Resolution of the PBMs

The time width measured for each of the 24 irradiations is shown in figure 4.4.3-top left as function of the measurement start time. The time resolution of the detectors (figure 4.4.3-top right) and the BTS (figure 4.4.3-bottom left) are calculated using the measured data and the CRT between both PBMs (figure 4.4.3-top right).

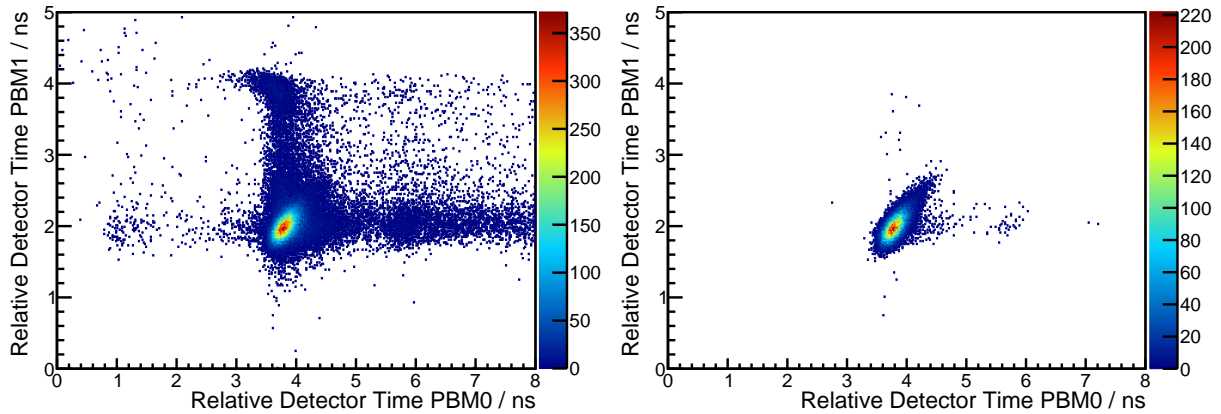


Figure 4.4.2.: Coincident time versus time of both PBMs without (left) and with (right) energy filters (campaign 2, beam energy 225 MeV, MLSO 30 mm). The detector time is measured relative to the RF. In case of the non-filtered distribution, several background contributions can be identified, while in case of the filtered data, most of the background is suppressed.

It can clearly be identified that the measured time width of the proton bunches varies within the first 340 min measurement time. After this period, the beam delivery was interrupted and the main magnetic field of the cyclotron had to be re-tuned by the operator team. After continuing the beam delivery, the time width was reduced by about 100 ps. The performance of the PBMs, however, was stable over the whole measurement period. PBM0 performs slightly better with a mean time resolution of (266 ± 9) ps, while PBM1 achieves (350 ± 10) ps. Hence, the BTS, which varied between 210-360 ps, and the detector time resolution are of the same order.

Stabilization of PGT Spectra

The centroid of the measured proton bunch time distribution with respect to the RF signal was determined for each PBM and in case of all 24 measurements using a Gaussian fit (see section 4.4.4 for detailed explanation). The centroids were offset-corrected to the first measurement so that $T_{\text{meas},1} = 0$. The time centroids versus the measurement time are shown in figure 4.4.3-bottom right.

Phase drifts, i.e. a non-stability of the centroids, can clearly be identified within the first 340 min measurement time. A maximum phase drift of about 4.5 ps per minute occurs between 0-100 min. After the previously mentioned beam re-tuning, a sudden shift of the time centroids of about 1 ns was observed. Furthermore, after the retuning, the time centroid remained stable within the measurement uncertainties.

The phase drift is also visible in the PGT data (figure 4.4.4-left) which is expected as it is also measured in reference to the RF signal. Thus, the effect has to be corrected for in the PGT measurements.

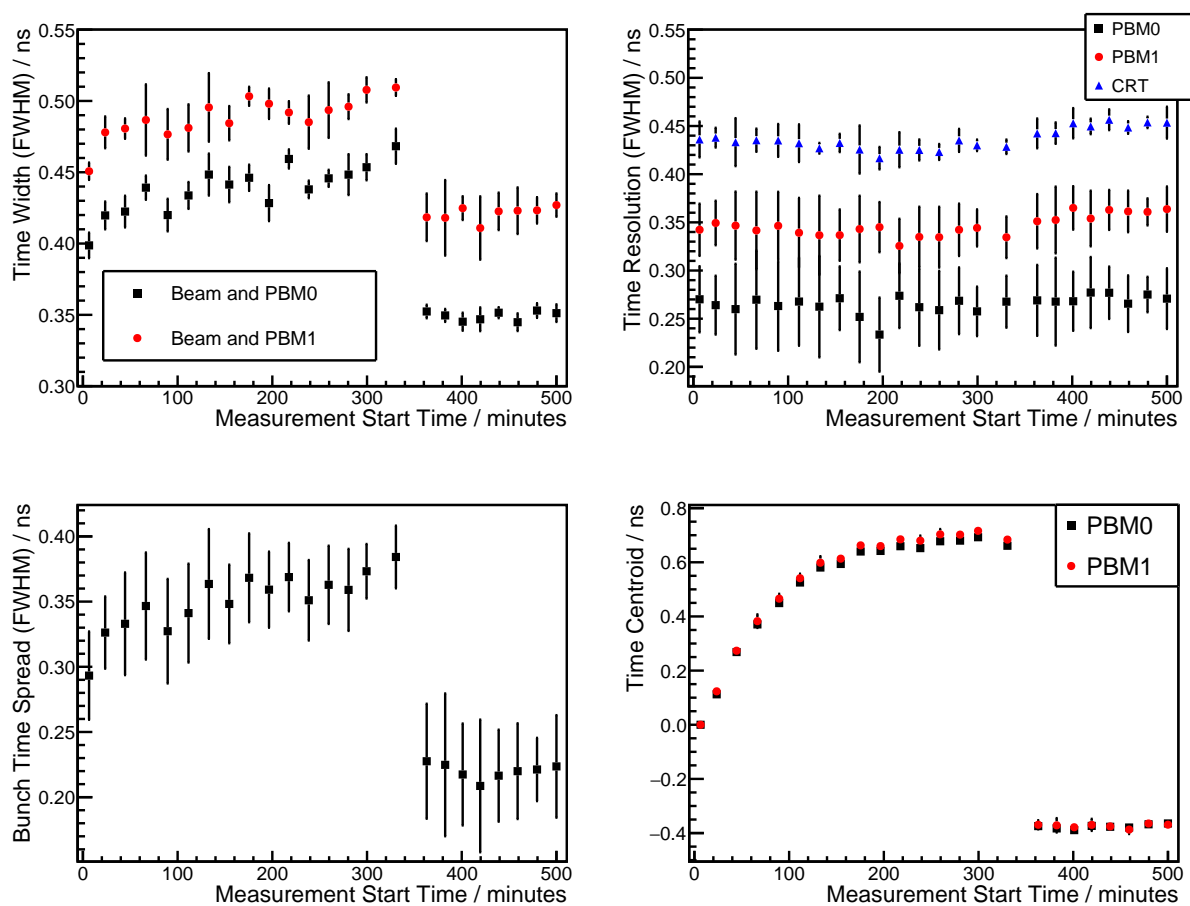


Figure 4.4.3.: Experimental data obtained with the PBM setup in campaign 1. Top left: Measured time width including the detector time resolution (black squares for PBM0 and red circles for PBM1). Top right: The time resolution of PBM0 (black squares) and PBM1 (red circles), as well as the CRT (blue triangles). Bottom left: Calculated BTS. Bottom right: Time centroid of the proton bunches measured with both PBMs relative to the RF over the measurement time. The beam delivery was interrupted at 340 min measurement time and the main magnetic field of the cyclotron was re-tuned. The beam energy was fixed at 225 MeV.

The correction is based on monitoring the phase drift Δt_{drift} using the PBM setup. As the phase drift is continuous and relatively slow, the correction procedure can be used event-wise for the PGT data.

By using the centroids of the time distributions $T_{\text{cent. PBM0}}$ and $T_{\text{cent. PBM1}}$, obtained by the PBMs, an average time centroid $T_{\text{avg. PBM}}$ can be determined as follows:

$$T_{\text{avg. PBM}} = \frac{1}{2}(T_{\text{cent. PBM0}} + T_{\text{cent. PBM1}}). \quad (4.4.1)$$

$T_{\text{cent. PBM}i}$ ($i = 0, 1$) is determined from the time distribution of PBM i , which is based on the timestamps $t_{\text{PBM}i}$ of each event relative to the RF:

$$t_{\text{PBM}i} = t_{\text{abs. PBM}i} - t_{\text{RF}}, \quad (4.4.2)$$

with $t_{\text{abs. PBM}i}$ as the absolute timestamp of an event in PBM i and t_{RF} being the timestamp of the corresponding RF signal. With a sufficient number of events, the timestamp of a single event $t_{\text{PBM}i}$ can be approached with the time centroid $T_{\text{cent. PBM}i}$. By combining (4.4.1) and (4.4.2), the average centroid in dependency of the RF can be obtained:

$$T_{\text{avg. PBM}} = \frac{1}{2}(t_{\text{abs. PBM0}} + t_{\text{abs. PBM1}}) - t_{\text{RF}}. \quad (4.4.3)$$

The timestamp of a single PGT event t_{PGT} is similarly determined as shown for the PBMs in (4.4.2) by using the RF as reference:

$$t_{\text{PGT}} = t_{\text{abs. PGT}} - t_{\text{RF}}. \quad (4.4.4)$$

By subtracting the average time centroid $T_{\text{avg. PBM}}$ from the PGT data, the corrected PGT timestamp $t_{\text{cor. PGT}}$ is given as follows:

$$t_{\text{cor. PGT}} = t_{\text{PGT}} - T_{\text{avg. PBM}} \quad (4.4.5)$$

$$= t_{\text{abs. PGT}} - \frac{1}{2}(t_{\text{abs. PBM0}} + t_{\text{abs. PBM1}}). \quad (4.4.6)$$

Hence, $t_{\text{cor. PGT}}$ is now independent of the RF as time reference and the PGT spectra can be corrected for RF-bunch phase drifts (figure 4.4.4-right)

One may wonder about the slightly different shapes of the PGT spectra presented in figure 4.4.4-right, especially in the region between 2 – 3 ns. As this time region corresponds to a target depth of homogeneous composition, no difference in the spectra should be observable. Nevertheless, the target is shifted towards the C1 detector due to the scanning procedure. Therefore, the amount of PMMA between the point of the γ -ray emission and the CeBr₃ detector increases for each irradiation, which raises the photon attenuation inside the material. However, the spectra shown in figure 4.4.4 are not corrected for attenuation which explains the shown behaviour.

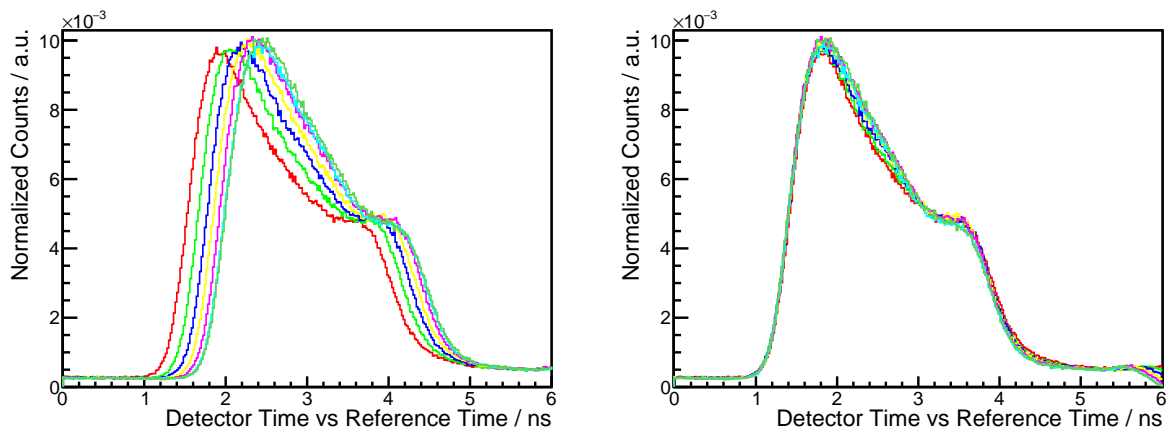


Figure 4.4.4.: PGT spectra of the first seven measurements of campaign 1 measured with the C1 detector without (left) and with (right) phase drift correction. For illustration purposes, the PGT spectra are normalized to matching levels between 0-1 ns.

Imaging of an Inhomogeneous Phantom

The structure of the inhomogeneous phantom (figure 4.4.5-top) can be imaged by using the corrected PGT spectra (figure 4.4.4-right). The target was scanned in 20 single measurements with a step size of 4 mm. For the two-dimensional PGT imaging of the phantom, each PGT spectrum is compared to a reference data set measured without inhomogeneities (i.e. a *full PMMA spectrum*). Here, the knowledge of the target is exploited to create a reference spectrum PGT_{ref} by averaging over several full PMMA spectra. Subsequently, the difference $\text{PGT}_{\text{diff},i}$ is calculated for each measurement PGT_i as follows:

$$\text{PGT}_{\text{diff},i} = \text{PGT}_i - \text{PGT}_{\text{ref}}. \quad (4.4.7)$$

The spectra are normalized to the incident number of protons determined by the PBMs. Furthermore, as a result of the setup, a solid angle-, a TOF- and an exponential photon attenuation correction are required for each measurement. The solid angle and the TOF correction are identical for all measurements as it only considers the distances or travel times of the PGs between each point of emission and the detector [12], respectively. However, when correcting for the photon attenuation inside the phantom, the amount of PMMA between the detector and each emission point has to be determined individually for each measurement. Additionally, the energy dependent attenuation coefficient $\mu(E)$ is required for calculating the correction factor. For simplification purposes, a mean photon attenuation coefficient μ/ρ in PMMA for an energy range between 3.0 – 6.5 MeV is determined using the XCOM database [133]. The value μ/ρ is $0.03 \text{ cm}^2/\text{g}$, and a density $\rho_{\text{PMMA}} = (1.18 \pm 0.01) \text{ g/cm}^3$ is used for PMMA [12].

An exemplary PGT difference spectrum between the measurement with $y = 88 \text{ mm}$ and a

reference set is shown in figure 4.4.5-bottom left. Subsequently, all PGT difference spectra can be combined in a 2D-distribution (figure 4.4.5-bottom right). Here, the z -axis resembles the difference in expected γ -rays at a certain point in time. A bluish colouring means less PGs than expected, while a yellowish and reddish colouring reflects an overproduction of PGs. The y -axis and the x -axis represent the target dimensions (see figure 4.4.5-top for details), where the x -axis is still in units of relative time. This, however, can be translated in spatial length units (see the upper x -axis) by using the conversion between transit time and proton range [51] (see also section 2.4 for details) and by defining the target front face to be at $x = 0$. The range of 225 MeV protons in PMMA is marked at a depth of about $x = 28$ cm [5]. The three red crosses in figure 4.4.5-bottom right mark the inhomogeneities in the phantom at a depth of 25.5 cm. In case of the bone insert, an overproduction of PGs close to the position is visible, while less photons than expected can be observed at the positions of the air cavities. Additionally, in case of the air cavities, the over-range of the protons is visible as a reddish area behind the actual proton range. The intensities of over- and underproductions scale furthermore with the size of the cavities.

4.4.4. Systematic Measurements of Beam Parameters

Shape of the Time Distributions of the Bunches

Figure 4.4.6 shows exemplary relative time distributions measured with C2 and PBM0 at beam energies of 69 and 225 MeV. In each measurement, a distinct peak is visible, which can be assigned to interactions of the primary proton bunches. The direct proton measurements with PBM0 (including the coincidence and energy filtering criteria of PBM1) show almost no background, while the PG based measurements include significant background contributions. Furthermore, the peak assigned to the proton bunches is broader in case of the PG measurement. It is apparent from the energy versus relative time distribution that the broadening is caused by an additional time-correlated signal from protons which are scattered at the PMMA target. In case of the PG measurement at 225 MeV (black curve in figure 4.4.6-right), a smaller peak at around 8 ns results from protons which have been scattered at the beam nozzle (exit foil or IC) or the 1 mm PMMA target. Similar observations were made by Hueso-González et al. at WPE [12].

Figure 4.4.7 shows the shapes of the relative time distributions measured with PBM0 for different proton energies and settings of the MLSO. The peak resembling the proton bunches becomes narrower and more Gaussian like for higher beam energies and for smaller MLSOs. At MLSOs of 10 or 5 mm and for 225 MeV, the peak can be approached by a Gaussian function.

However, in the further analysis, the FWHM of each peak is determined numerically and not by a Gaussian fitting routine to account for the varying shapes and for a better comparison of different beam settings (i.e. energy and MLSO).

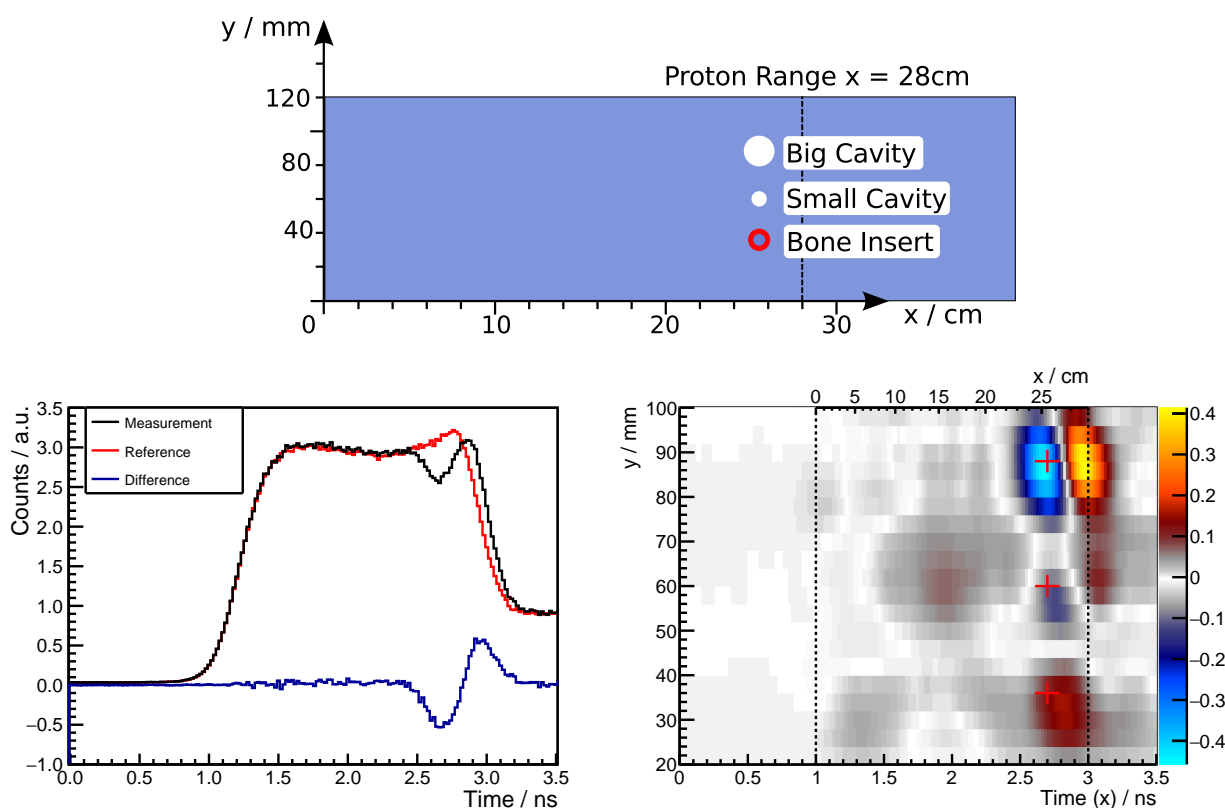


Figure 4.4.5.: Top: Schematic drawing of the inhomogeneous target. Bottom left: Corrected PGT spectrum (measurement at $y = 88$ mm, black curve), a reference set of a homogeneous target (red curve) and the difference between the two (blue curve). Bottom right: 2D distribution of the difference in produced PGs compared to a homogeneous PMMA phantom. The target front face is shown at $x = 0$ (left dashed line) and the proton range in PMMA is marked at about 28 cm (right dashed line). Three red crosses mark the inhomogeneities at a target depth of 25.5 cm, one bone insert (at $y = 36$ mm) and two air cavities (small one at $y = 60$ mm, big one at $y = 88$ mm).

Time Resolution of the PBMs

Due to the rebuild of the setup between campaign 1 and campaign 2, the time resolution of the PBMs was again determined according to (4.3.4) for campaign 2. The PBMs should have the best timing for lower beam energies as the energy deposition is increased in the plastic scintillator compared to higher energies. This gives rise to more scintillation light and better timing capabilities. Nevertheless, the analytical calculation of the time resolution of each detector was done using the measurements with 225 MeV beam energy due to the nearly Gaussian shape of the time distribution. With the additional adjustment of the PBM setup compared to campaign 1, an improvement of the mean time resolution to (178 ± 7) ps (PBM0) and to (190 ± 13) ps (PBM1) could be achieved.

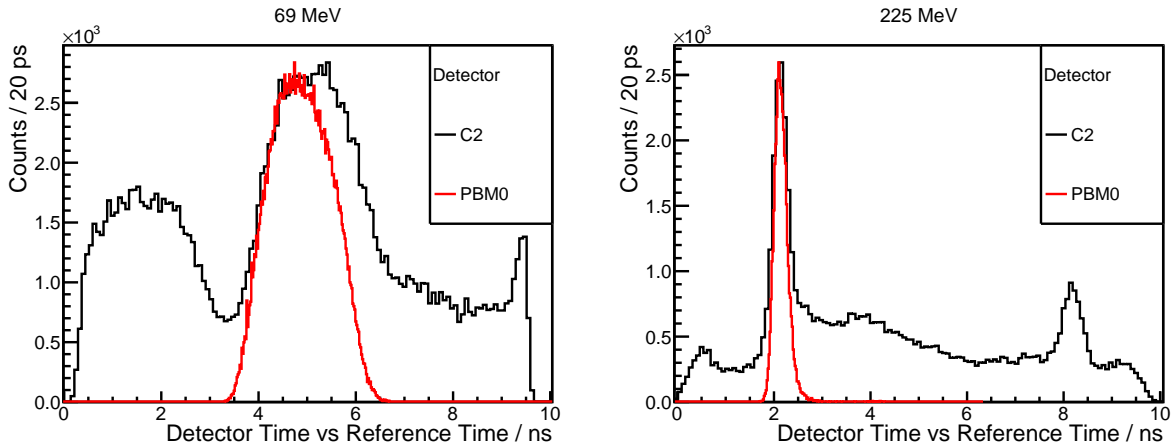


Figure 4.4.6.: Comparison between the shapes of the relative time distributions measured with C2 (black curves) and PBM0 (red curves) for different beam energies (left 69 MeV, right 225 MeV). The MLSO is fixed at 30 mm. For comparison purposes, the data obtained with C2 is normalized to match the maxima of the PBM0 measurements, respectively. Energy filters are applied.

Bunch Time Spread

In case of the Gaussian shaped peaks (i.e. for 225 MeV beam energy or MLSOs of 5 and 10 mm), the BTS is determined according to (4.3.6). For the other data sets, the BTS is extracted using the *TSpectrum::Deconvolution* function from ROOT (see section 4.3.1). The results are presented in figure 4.4.8 as function of the beam energy and for different MLSOs.

The BTS decreases for higher beam energies from about 1.8 ns at 69 MeV to 230 ps at 225 MeV. Additionally, the BTS can be partially controlled by the MLSOs. When lowering the MLSO from 30 to 10 mm for energies below 225 MeV, the BTS is reduced by a factor of two, e.g. at 110 MeV from 1.4 ns to a value below 600 ps. However, no significant reduction can be observed when further lowering the MLSO to 5 mm, which points towards a maximum achievable momentum spread confinement. The BTS at 225 MeV is more or less independent from the settings of the MLSO which indicates an intrinsic time spread. This lower limit on the BTS is potentially coming from the acceleration process and from an intrinsic energy spread due to presence of thin foils within the beamline system (see next paragraph for details).

Extension to other Treatment Rooms and Facilities

For extrapolating the results on the BTS to other treatment rooms and facilities, the origin of the BTS has to be further discussed.

The BTS T_{BTS} , which is observed with our detectors, is a combination of the time-wise dispersion of the bunch $\Delta T_{\Delta E}$ caused by the energy spread introduced in the degrader and the intrinsic time spread T_{int} (resulting from the acceleration process and thin foils in the beam delivery sys-

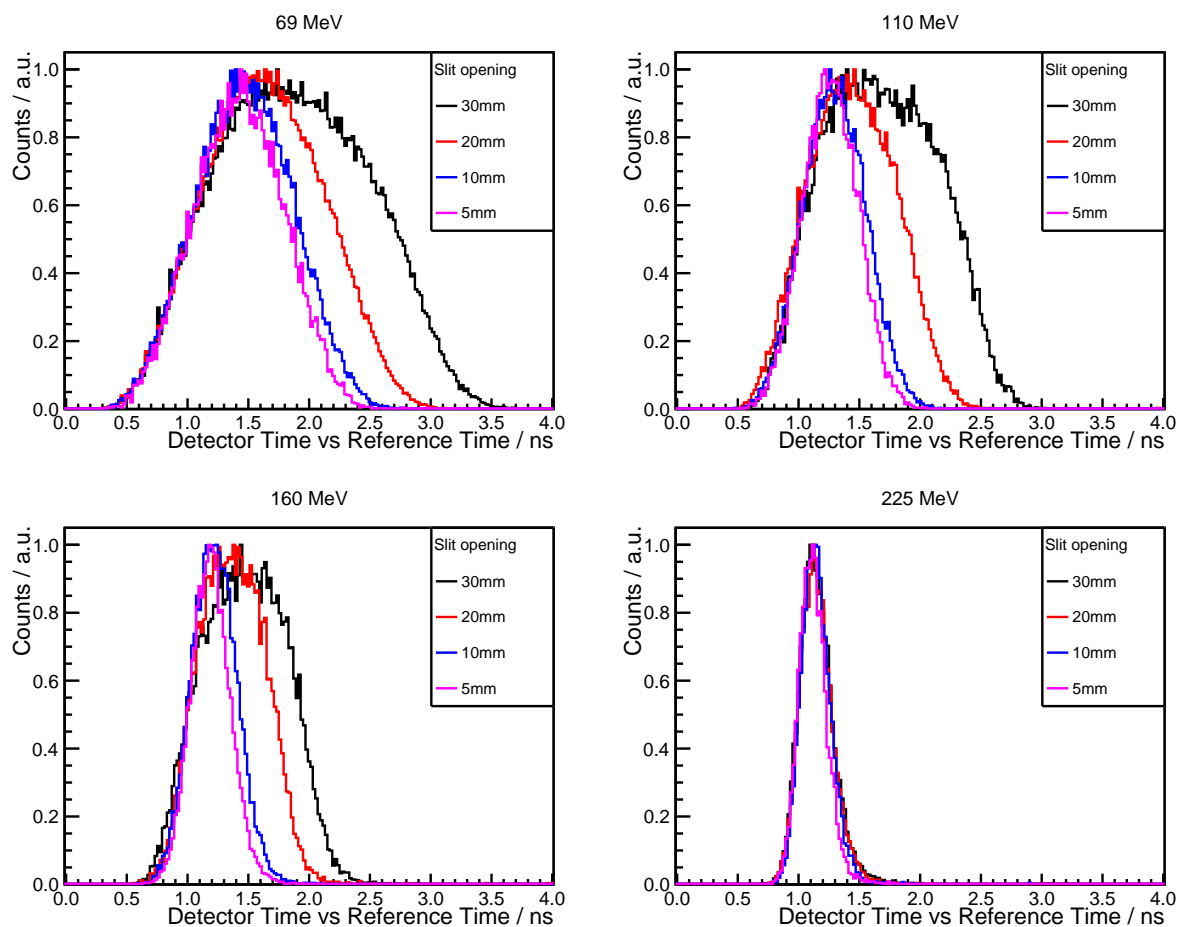


Figure 4.4.7.: Relative time distributions measured with PBM0 for different beam energies and MLSOs. For comparison purposes, the maxima of each distribution is normalized to 1. Energy filters are applied.

tem). Thus, T_{BTS} can be described as follows:

$$T_{\text{BTS}}^2 = T_{\text{int}}^2 + \Delta T_{\Delta E}^2. \quad (4.4.8)$$

T_{int} can be estimated from the measurements at 225 MeV for an assumed MLSO of 0 mm, which seems justified as the BTS is nearly independent from the MLSO at this beam energy (see figure 4.4.8). To obtain this virtual parameter, a linear fit is applied to the BTS at 225 MeV as function of the MLSO (figure 4.4.9). Subsequently, the intrinsic time spread is determined to be $T_{\text{int}} = (170 \pm 20)$ ps.

How can the time dispersion of the proton bunches $\Delta T_{\Delta E}$ due to the energy straggling be described in more detail? Using the relativistic energy relation, the connection between the

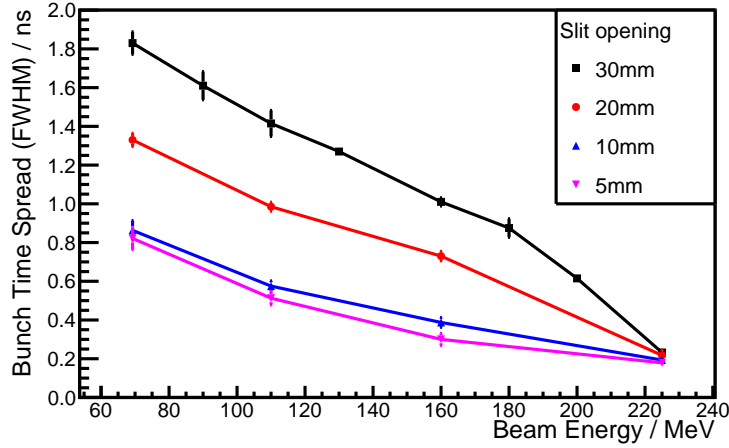


Figure 4.4.8.: Bunch time spread as a function of the beam energy for different MLSOs. The BTS is reduced when increasing the beam energy and can be controlled by lowering the MLSO. The connecting lines help to guide the eye.

energy E of a proton and the distance s , which is covered in a certain time t , is given by:

$$E = \frac{m_p c^2}{\sqrt{1 - \left(\frac{v}{c}\right)^2}} = \frac{m_p c^2}{\sqrt{1 - \left(\frac{s}{c \cdot t}\right)^2}}, \quad (4.4.9)$$

where m_p is the proton mass and c the speed of light in vacuum. The energy spread can be obtained by analysing the uncertainty of the energy for a varying transit time

$$\Delta E = \left(\frac{\partial E}{\partial t}\right) \Delta t = \left(\frac{m_p s^2}{t^3 \left[1 - \left(\frac{s}{c \cdot t}\right)^2\right]^{\frac{3}{2}}}\right) \Delta t, \quad (4.4.10)$$

where the proton travel time t can be expressed according to (4.4.9) as follows:

$$t = \frac{s}{c \sqrt{1 - \left(\frac{m_p c^2}{E}\right)^2}}. \quad (4.4.11)$$

It is therefore apparent that t is proportional to s for a fixed energy. By substituting (4.4.11) into (4.4.10), and by cancelling out the result, one obtains

$$\Delta E \propto \frac{\Delta t}{s} \quad \text{or} \quad \Delta T_{\Delta E} = \Delta t \propto \Delta E \cdot s. \quad (4.4.12)$$

Hence, when assuming a constant energy $\Delta T_{\Delta E}$ is proportional to the product of distance s and energy spread ΔE .

Thus, the BTS can be calculated according to (4.4.8) for a known energy spread and for a fixed

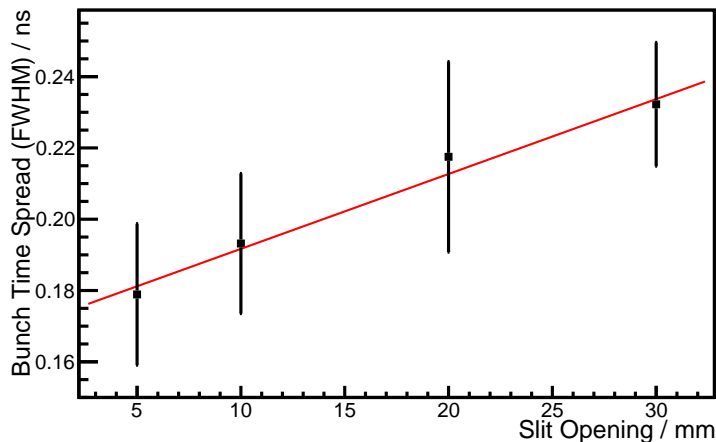


Figure 4.4.9.: Bunch time spread at 225 MeV beam energy as a function of MLSO in the experimental room. The intrinsic time spread T_{int} is determined by approaching a linear fit (red line) to the data points to deduce a virtual BTS at 0 mm MLSO.

beam energy as a function of the distance s (or the beamline length l). On the other hand, ΔE can be extracted (at least for UPTD) from the experimental values $T_{\text{BTS,exp}}$. For this purpose, (4.4.10), (4.4.8), T_{int} , and the distance between degrader and experimental room l_{exp} are required. Using the construction plans of the beam delivery system provided by IBA, l_{exp} was determined to be (27 ± 1) m. Summarizing, the BTS at UPTD $T_{\text{BTS,UPTD}}$ is calculated for a fixed beam energy as a function of the beamline length l as follows:

$$T_{\text{BTS,UPTD}}^2(l) = \left(\frac{l}{l_{\text{exp}}}\right)^2 (T_{\text{BTS,exp}}^2 - T_{\text{int}}^2) + T_{\text{int}}^2. \quad (4.4.13)$$

If $\Delta T_{\Delta E}$ is large compared to the intrinsic time spread T_{int} (which is the case in all clinically relevant settings), the following simplification can be used: $\Delta T_{\Delta E}^2 + T_{\text{int}}^2 \approx \Delta T_{\Delta E}^2$, which shortens (4.4.13) to

$$T_{\text{BTS,UPTD}}(l) = \frac{l}{l_{\text{exp}}} T_{\text{BTS,exp}}. \quad (4.4.14)$$

Hence, for all clinically relevant setups, the BTS increases linearly with the beamline length.

Figure 4.4.10 shows the generalised BTS as function of the beamline length l for selected beam energies (110 and 160 MeV, covering most of the used energies for patient treatment) and MLSOs (30 and 10 mm). The distances between degrader and the experimental room (27 m), the gantry treatment room (GTR2) of UPTD (49 m), and GTR4 of WPE (71 m, used in [12]) are marked as vertical dashed lines. The linear dependence of the BTS with the beamline length is visible, as well as the potential reduction of the BTS when lowering the MLSO.

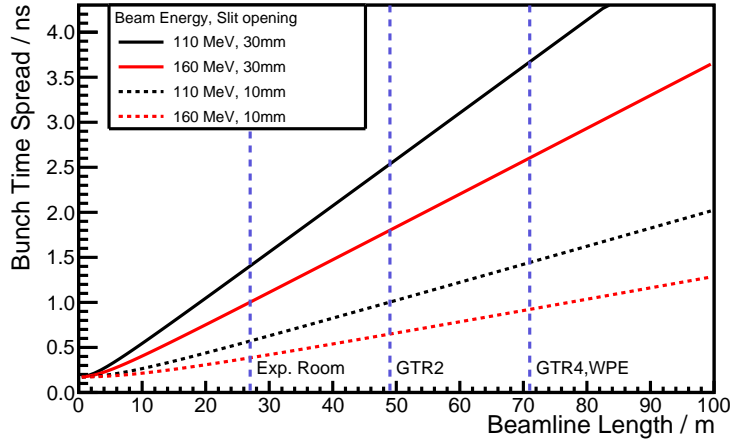


Figure 4.4.10.: Calculated BTS for 110 MeV (black curves) and 160 MeV (red curves) for the default MLSO of 30 mm (solid lines) and 10 mm MLSO (dashed lines) as a function of the beamline length l . The distances between degrader and the experimental room (27 m), the gantry treatment room GTR2 of UPTD (49 m) and GTR4 of WPE (71 m) are marked as dashed vertical lines. Both facilities comprise C230 cyclotrons.

Proton Transmission Rate

Reducing the BTS by lowering the MLSO is advantageous for the PGT method. However, in order to confine the momentum spread, more protons are absorbed inside the ESS which ultimately lowers the proton transmission rate.

In our case, the proton transmission rate is defined as the beam current at the beam exit I_{exit} in the experimental room relative to the beam current extracted from the cyclotron I_{cyclo} . The delivered beam current I_{exit} is determined by the calibrated IC mounted at the beam exit, while I_{cyclo} is requested in the controlling software. By using both parameters, the proton transmission rate can be determined. However, for non-default MLSOs (i.e. values different from 30 mm), the beam delivery had to be controlled in the main control room by the local operators and the IC could not be read out in the controlling software.

Nevertheless, the proton transmission rate can still be retrieved using the absolute value measured at 30 mm MLSO and the gross count rates of the PBMs for all MLSO settings. For a fixed beam energy, the gross count rates are proportional to the beam current due to the low count rates occurring in the experiment (less than 10 kcps per PBM) and the corresponding low dead time $< 15\%$ (in most cases even below 7%). With the absolute proton transmission rate value, I_{exit} can be calculated for the other MLSOs.

The results are shown in figure 4.4.11 as a function of the beam energy and for different MLSOs. The transmission rate is decreased for lower MLSO and when reducing the proton energy. The proton transmission is maximum at 225 MeV and 30 mm with about 30% . The value is reduced by two orders of magnitude to 0.3% when changing the beam energy to 69 MeV. Changing the

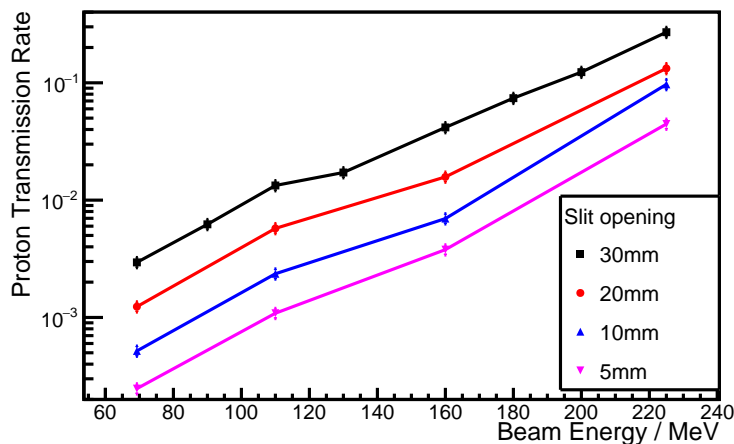


Figure 4.4.11.: Proton transmission rate versus as a function of the beam energy and for different MLSOs. A decrease of the transmission rate can be observed for smaller MLSOs and lower beam energies. The connecting lines help to guide the eye.

MLSO from the default value of 30 to 10 mm further reduces the transmission rate by a factor of ten. An even further decrease by about three is visible when the MLSO is changed to 5 mm, however, without significantly changing the momentum spread.

Energy Spread

As a by-product of our measurements performed in campaign 2, the energy spread ΔE , which is an important input parameter for simulation studies e.g. on the dose deposition, can be determined. By combining (4.4.10) with (4.4.11), and using the experimental values $T_{\text{BTS,exp}}$, T_{int} as well as l_{exp} , ΔE can be determined as follows:

$$\Delta E = \left(\frac{E^2}{m_p c \cdot l_{\text{exp}} \cdot \left[1 - \left(\frac{m_p c^2}{E} \right)^2 \right]^{\frac{3}{2}}} \right) \cdot \sqrt{T_{\text{BTS,exp}}^2 - T_{\text{int}}^2}. \quad (4.4.15)$$

It should be noted that the square root term is only valid for Gaussian distributions of the time spread, which is not the case for beam energies below 225 MeV or for MLSOs of 20 and 30 mm. However, in those cases, the BTS is large compared to the intrinsic one, which then can be neglected. For all other setups, (4.4.15) can be used to determine the energy spread.

Figure 4.4.12 shows the absolute and relative energy spread (both as FWHM) as a function of beam energy and for different MLSOs. In case of the absolute energy spread, the maximum occurs at 160 and 180 MeV and a MLSO of 30 mm with about 2.3-2.4 MeV, corresponding to 1.4 % relative uncertainty. The relative energy spread follows a relatively similar trend as the BTS (see

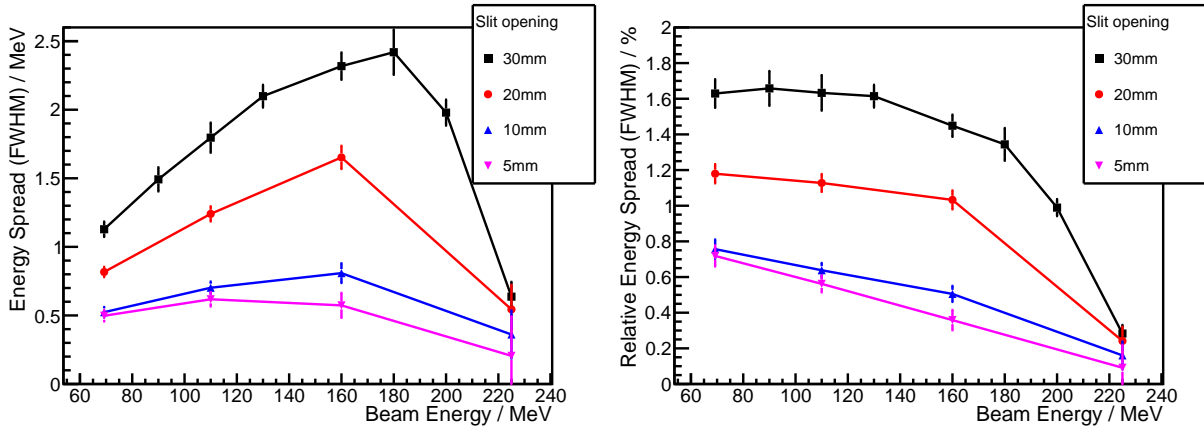


Figure 4.4.12.: Absolute and relative energy spread as a function of the beam energy for different MLSOs. The connecting lines help to guide the eye.

figure 4.4.8) as it reduces with the beam energy. However, it is relatively constant between 69-130 MeV with a maximum relative uncertainty of about 1.6 % (MLSO 30 mm). As expected, the energy spread can be reduced by a factor of more than two when lowering the MLSO from 30 to 10 mm. A further reduction to 5 mm has only small impact with a nearly constant value of about 0.5 MeV, hinting towards a maximum reachable confinement. For the highest beam energy, ΔE is minimal which agrees well with the expectation as the degrader is not used for this energy.

4.5. Discussion

The first measurement of the microbunch time structure of the commonly used clinical proton accelerator C230 [10] was conducted in this study. The data obtained is required to understand the limitations of the PGT method and to design a system usable in patient treatments.

The PBM setup, consisting of two phoswich detectors, measured coincident protons emerging from a thin hydrogen-containing foil due to elastic pp -scattering. The approach enables a significant reduction of background events. In the experiment, phase drifts between proton bunches and the RF of the accelerator could be observed in data obtained with a γ -ray detector and the PBM setup. Using the time information from the PBM data, the phase drifts could be corrected in the PGT spectra.

Using the corrected data, the first 2D imaging of an inhomogeneous phantom based on PGs was possible. The positions of two incorporated air cavities and a bone-insert could be identified. Even though the data was obtained at the highest beam energy and with a very high number of incident protons (over 7.5×10^{11} per measurement), which is unrealistic compared to the clinical scenario [12, 13], the imaging of the inhomogeneous phantom still shows the potential of the PGT method when using a PBM setup.

In an additional study deploying the PBM setup, the time structure of the microbunches (i.e.

the shape and the BTS) was characterized as function of the beam energy and for different MLSOs in the experimental room of UPTD. The shape of the bunches and the BTS are both required as input parameters for simulation studies to predict the PGT spectrum of an actual treatment. The simulated PGT spectrum can then be compared to the measurement as a verification of the range. The BTS, on the other hand, is also of major importance as it partially determines the sensitivity of the PGT method (see section 2.4.1 for details), i.e. which range shift is still detectable for a certain pencil beam spot or number of detected PGs. A corresponding evaluation of the sensitivity will be performed in section 5.3.4 using data measured under clinical conditions.

Since the BTS was determined for a rather ideal environment (experimental room with a relatively short beamline length), the analysis is extended for varying beamline lengths to include for example the gantry treatment room of UPTD. A linear correlation between BTS and beamline length can be seen for all clinically relevant cases. A generalization of the findings to further treatment rooms, at least of the same treatment facility, seems also possible. For example, the BTS should increase by a factor of about 1.8 when measuring in GTR2 of UPTD, which has indeed been observed in measurements (see section 5.3.2 for details). However, in case of other facilities, the results are not comparable as different default beamline settings are used. For example, the values measured by Hueso-González et al. at WPE for a similar cyclotron are smaller compared to our predictions which might be a result of the lower default MLSO of 25 mm used in the facility [12]. Therefore, the BTS has to be characterized for each individual facility.

The energy spread of the proton pencil beam causing the BTS is derived from the experimental data as it also influences the dose deposition. Consequently, the parameter is required as input for simulation studies and treatment planning routines. Relative energy uncertainties are below 2% which is in agreement with information provided by the manufacturer.

Ideally, the BTS would be reduced by lowering the MLSO to increase the sensitivity of the PGT method or to lower the number of required PGs with the consequence to enable a range verification also for weaker spots in PBS mode (see section 2.4.1 for details). A maximum reduction of the BTS of a factor of two could be observed when lowering the MLSO from the default setting to 10 or 5 mm. However, this improvement comes with the price of a reduced proton transmission through the beamline. Therefore, the proton transmission was also determined as a function of beam energy and for the different MLSOs. A strong correlation could already be seen for the default MLSO, as the transmission rate is drastically reduced with the proton energy. When lowering the MLSO to the, for PGT, interesting case of 10 mm, the proton transmission is reduced by about one order of magnitude which could partially be counteracted by increasing the requested beam current at the cyclotron. However, this is only possible to a maximum value which is about 300 nA for the C230. This might not be sufficient for lower beam energies as the clinical current may not be delivered due to the low transmission which potentially increases the treatment time. However, this additional time does not equal the beam current reduction, but is a fraction of it, as most of the treatment time in PBS mode is actually used for scanning magnets sweeping between the spots and beam energy switching between the layers (see section 5.3.2 for details).

A variation of the MLSO also has consequences for the beam generation as a ripple effect might be introduced on the SOBP or the beam spot size might change, requiring a re-commissioning of the beam structure, which seems not feasible in a running facility. In summary, changing the MLSO would be ideal for the PGT method but at the expense of several critical parameters, which can only be assessed in cooperation with the manufacturer of the therapy system.

As the thin PMMA scattering target is not realizable in clinical routine, other sources of scattered protons have to be identified and used without affecting the beam generation inside the nozzle. Following ideas are currently being discussed:

- a) Scattering chamber within the beamline, positioned close to the beam nozzle. The proton beam is monitored by the PBM setup through thin windows. Further modifications of the beam like the additional bunch dispersion within the remaining beamlength to the beam nozzle could be calculated according to our findings.
- b) Monitoring of protons scattered at the exit foils of the ICs using a PBM inside the nozzle. As the foils are usually very thin² (about $10\ \mu\text{m}$), the coincidence method may not be applied due to the low number of scattered protons. Hence, particle identification via the phoswich principle of the PBM could be exploited to obtain a clear signal of the arrival time of the proton bunches. However, this idea further struggles with the scanning process in PBS mode, as the beam position to the detector varies for each spot.
- c) Detection of backscattered protons coming from the patient. The signature has been observed all along in our experiments and could potentially even be used for a position verification of the patient. Experiments to explore this option are currently being conducted.

A further problem of the PBM setup is the limited throughput rate of the VME electronics of few kcps which is not sufficient for measurements in PBS mode as the spot duration is only few milliseconds [13]. However, dedicated readout electronics has been developed and recently tested [13] and will be further discussed in chapter 5.

²Private communication with G. Krier from IBA.

5. Prototype PGT Detector System under Therapeutic Conditions

In this chapter, the requirements for a prototype system for the application of PGT in clinical practice are summarized based on the obtained results. The specifications for the PGT prototype are furthermore presented. As a result, customized scintillation detectors have been ordered and a novel digital spectrometer, serving as readout electronics, was designed and developed by an industrial partner according to the specifications. Both parts of the prototype system have together been optimized to work as a combined detector unit. The delivered prototypes are further characterized and the results are compared with the initial requirements. Furthermore, the system is used for phantom studies under clinical conditions with 3D PBS treatment plans. The experimental setup is described as well as data analysis procedures. Selected results will be presented in order to show the potential of the PGT prototype system. First of all, the number of detected photons per spot is evaluated along with the TOF distribution. Finally, the detection of inhomogeneities based on PGT and photon yield information is shown.

5.1. Introduction

The PGT prototype is primarily designed for the usage in PBS mode at UPTD. The requirements of such a detector system have been shown in the previous considerations and also in [13]. Summarizing, a suitable PGT system should exhibit the following properties:

- At least 10^4 PG events are necessary for a successful range verification on a 5 mm level [12, 13]. As a strong spot (with about 10^8 incident protons) is delivered in about 10 ms, a detection system needs therefore at least 1.2 Mcps throughput rate [13]. Alternatively, if the required throughput is not achievable, more than one detection unit has to be deployed to collect the required number of events.
- The system needs to achieve a time resolution which is close to the minimum BTS as the detector has the highest contribution to the PGT measurement in this case. For a higher BTS, the detector contribution is more or less negligible. Referring to section 4.4.4, the minimal BTS is around 230 ps at the highest beam energy. This value defines the requirement for our detection system which should have a time resolution of 200-250 ps FWHM.

- A decent energy resolution of the system is important to resolve individual γ -ray lines for setting energy thresholds in order to reduce the background. Furthermore, the better the energy resolution, the higher is the precision on the thresholds and the better is the reproducibility of PGT spectra.
- CeBr_3 should be deployed as scintillation material as it has a fast decay time to cope with the high expected detector load without risking pile-up events. Furthermore, the material exhibits sufficient time and energy resolution. As light readout, a dedicated timing PMT should be used.
- The readout electronics should be compatible with a CeBr_3 detector, thus, having a high sampling rate. It should also be compact, robust, and handy as the device might be used by non-experts in a clinical environment with limited space. Furthermore, the RF of the accelerator must be included into the data collection to obtain the reference time.

5.2. Solution - CeBr_3 and the Digital Spectrometer U100

5.2.1. CeBr_3 Detector Setup

The idea of using a scintillation detector based on a CeBr_3 crystal connected to a PMT results from the measurements at ELBE in combination with the discussion about a suitable light sensor (see section 3). Therefore, CeBr_3 detectors were specified and purchased from Scionix Holland BV with two crystal sizes ($\varnothing 2'' \times 1''$ and $\varnothing 2'' \times 2''$). The encapsulated crystals are mounted to dedicated timing PMTs from Hamamatsu, type R13089 and R13089-100 equipped with a conventional 14-pin connector. A customized pin layout of the 14-pin socket was required to fit with the later used U100 plug-on spectrometer. A photography of the detector is shown in figure 5.2.1.

5.2.2. U100 - Design

Concerning the readout electronics, no suitable hardware was commercially available. Therefore, we triggered the development of the novel digital spectrometer “U100” by Target Systemelektronik (Wuppertal, Germany) based on the above mentioned requirements and specifications. The U100 was designed and optimized in combination with the CeBr_3 detectors (see above).

The U100 is a compact device (dimensions $\varnothing 2.5'' \times 6.1''$) which can be directly connected to the 14-pin base of commercial 2'' detectors [134]. The device comprises all necessary readout electronics as well as the HV supply for the PMT with a maximum voltage of 1500 V (see figure 5.2.2 for details). It is supplied with Power-over-Ethernet (PoE), requiring only a conventional Ethernet cable and a suitable network switch for powering the device. The communication procedure (data streaming and controlling the device) is managed via the Ethernet interface.

If a signal exceeds an initially set trigger threshold, the data acquisition procedure is started. Two ADCs with up to 310 MHz sampling rate digitize the anode signal as well as one of the dynodes

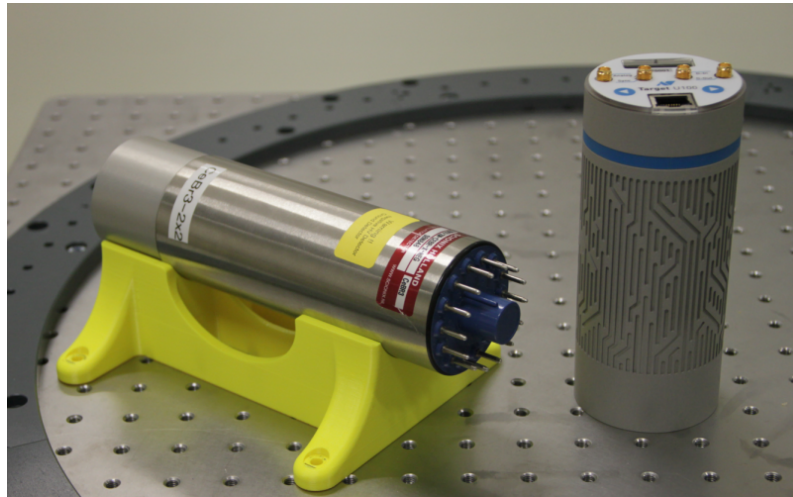


Figure 5.2.1.: Photography of the $CeBr_3$ scintillation detector and the U100 digital spectrometer. Reproduced with permission from G. Pausch [13].

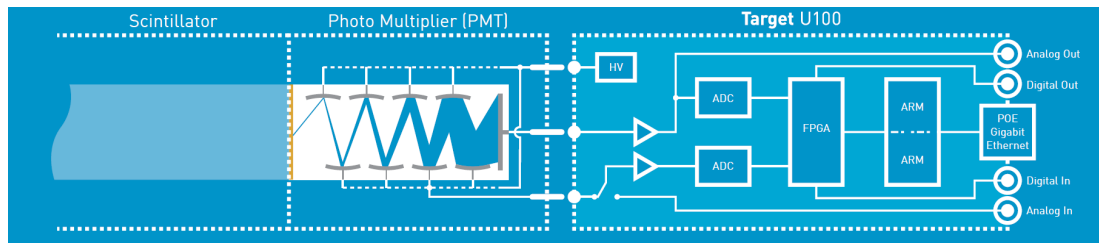


Figure 5.2.2.: Schematic drawing of the U100 digital spectrometer as readout of a scintillation detector. Reproduced with permission from [135].

or an external signal with 14-bit precision [134]. The pulse is shaped, filtered, and sampled with a frequency corresponding to the clock frequency. Filter functions etc. are depending on the firmware settings and are currently designed for the usage the existing hardware ($CeBr_3$ and PMT combination). At least 5 sampling points are used to determine the rising edge of the pulse shape¹. The timestamp is defined at 50% pulse height and is obtained by using a linear interpolation with 10 bit accuracy between the sampling points to achieve a timing precision on a ps level. The digitized signals are further processed in the FPGA which has a fixed dead time of $1\ \mu s$ to avoid overload of the internal serial interface to the processing unit. Thus, in principle, processed event rates of 1 Mcps are possible with the U100. The data is streamed to a dual core Advanced RISC² Machines (ARM) processor, where a Multi Channel Analyser (MCA) software is implemented to create list mode data [134]. An internal web server is included for displaying data like the energy spectrum and the energy versus relative time distribution as well as for controlling the instrument settings. Hence, any web browser can be used to control the U100 device and

¹Private communication with the developers.

²RISC stands for Reduced Instruction Set Computer.

perform measurements. Additionally, the U100 comprises an Application Programming Interface (API) for operating the device with software developed by the user. As a result, list mode data can be directly streamed to a PC for further offline data analysis.

Besides the internal clock, an external signal can be connected to the “digital-in” and be used to clock the U100 with the help of an internal PLL. Consequently, the RF of an accelerator can be used as reference for relative time measurements. The ADC sampling points are in phase with the clock and therefore the RF signal. As a result, an incident event is measured in reference to the accelerator signal.

For each event, the data structure comprises a 64-bit “energy” value (later referred to as signal charge), obtained by baseline-corrected pulse integration, for the deposited energy, and the timestamp consisting of the coarse counter of clock cycles and the interpolated fraction corresponding to the 50% level of the leading edge of the signal. The timestamp can be translated in real time values using the clock frequency, which varies if an external clock signal is used.

Summarizing, the U100 spectrometer offers the possibility to read out a γ -ray detector with a throughput rate up to 1 Mcps.

5.2.3. Experimental Characterization based on Classical Analogue Electronics

Before taking the step of using the digital spectrometer as readout, the scintillation detectors were tested at the ELBE bremsstrahlung facility (see section 3.3.4 for details) regarding their timing capabilities using classical analogue electronics. The readout is based on NIM and VME electronics using a similar setup as described in [79]. The detectors were equipped with customized voltage dividers fitting to the pin layout of the socket.

Energy calibration was performed using a ^{60}Co source (1173 and 1333 keV) and the endpoint energy of the bremsstrahlung beam of 12.5 MeV.

The time resolution as a function of the energy is shown in figure 5.2.3 for both crystal sizes. The smaller detector achieves around 200 ps at 2 MeV while the larger one is slightly worse with 240 ps. The difference of 40-50 ps can be seen over the whole energy region and results from the difference in size due to the longer photon transit time and increased uncertainty of the depth-of-interaction. By determining the difference in photon travel times Δt in air (with $n = 1$) and in the scintillation crystal with refractive index n_{scint} , the magnitude of those effects can be roughly estimated as follows:

$$\Delta t = \frac{d}{c/n_{\text{scint}}} - \frac{d}{c} = \frac{d}{c} \cdot (n_{\text{scint}} - 1), \quad (5.2.1)$$

where d is the thickness of the scintillator. In case of $d = 1.0''$ and for the refractive index of CeBr_3 of 2.09 (see table 2.3.1), Δt is about 92 ps, which is, assuming quadratic error propagation for all parameters determining the time resolution, in agreement with the additional offset of 40-50 ps in case of the bigger crystal. Nevertheless, the PMT based detectors perform well within the, for PGT, required limits ($\Delta T < 250$ ps).

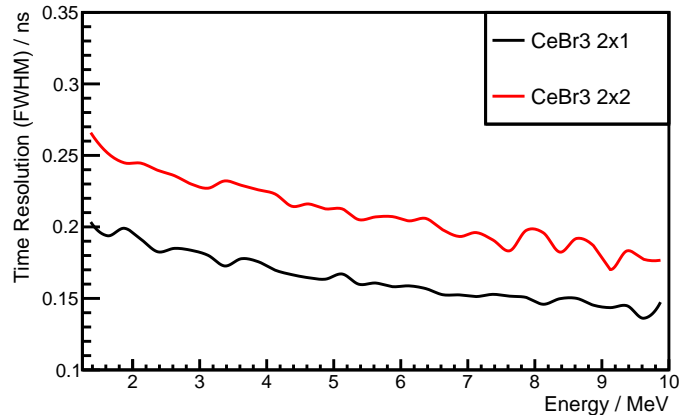


Figure 5.2.3.: Time resolution as a function of energy measured with CeBr_3 and PMT readout. Both crystal sizes have been tested at the ELBE bremsstrahlung beam.

5.2.4. Experimental Characterization based on the U100 Spectrometer

For investigating the capabilities of the U100 concerning time and energy resolution as well as throughput rate, a further experimental campaign was conducted in the bremsstrahlung facility at the ELBE accelerator at HZDR (see section 3.3.4 for details). The experiment was performed within the framework of the master thesis of A. Rinscheid [136] to characterize the U100 spectrometer.

Setup

Several U100 devices were coupled to CeBr_3 detectors of both crystal sizes. The detection units were positioned in the bremsstrahlung beam and an additional ^{60}Co γ -ray source was attached to the crystal for determining the energy resolution. The 13 MHz RF signal of ELBE was connected to the U100 and was scaled by the internal PLL of the U100 to 208 MHz which then served as clock frequency. A high voltage of 800 V was set for each PMT throughout the entire experiment.

Two different trigger settings were investigated, trigger 50 and 1000, in order to identify differences regarding the performance of the detector system. With the used HV, the lower threshold corresponds to about 50-100 keV, while trigger 1000 corresponds to 1.2 MeV. The dependency of energy and time resolution on the throughput rate was determined by increasing the electron beam current and with that the photon flux of the bremsstrahlung beam. The throughput rate as a directly measure parameter can be translated to a detector load which is corrected for dead time (i.e. the gross count rate) and considers also photons below the trigger threshold (which are not included in the dead time determination). In case of trigger 50, the detector load is approximately the dead time corrected throughput rate. For the higher trigger threshold, the results obtained with trigger 50 are used for calibrating a correction function connecting the throughput rate and the dead time with the detector load [136].

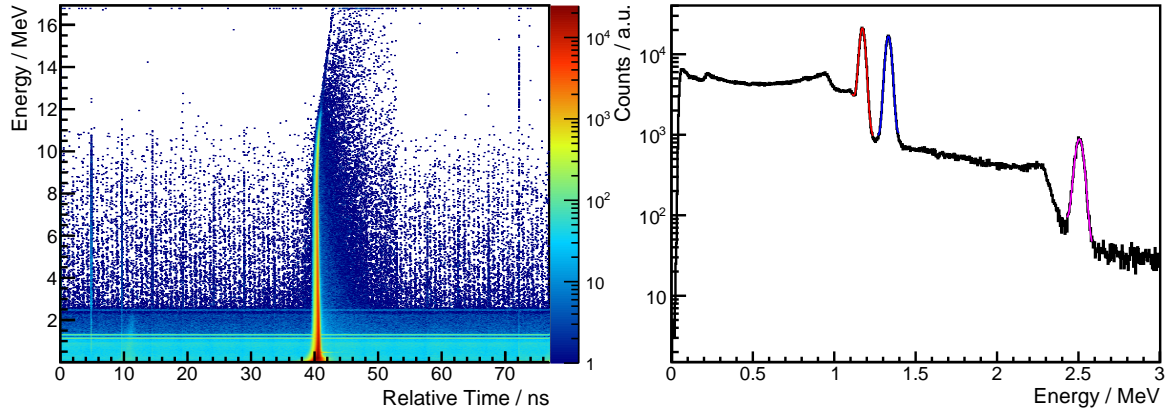


Figure 5.2.4.: Left: energy versus relative time distribution measured at ELBE. The bremsstrahlung beam is visible between 39-41 ns. The horizontal lines stem from the ^{60}Co source and represent the two γ -lines (1.173 and 1.333 MeV) as well as the sum peak (2.506 MeV). Right: energy spectrum measured using a ^{60}Co source without the bremsstrahlung beam distribution (selection on all relative times except 39-41 ns). The detector load was 55.6 kcps and the trigger was set to 50. Reproduced with permission from A. Rinscheid [136].

Again, like for the DPC measurements (see section 3.3.4), energy versus relative time distributions show the bremsstrahlung beam (figure 5.2.4) [136]. The data is further used to evaluate energy and time resolution as function of the throughput rate. In case of the energy resolution, the time window without a bremsstrahlung contribution (i.e. selection on all relative times except 39-41 ns) is projected on the energy axis and the FWHM of each visible peak is determined (figure 5.2.4-right). For the time resolution, the 2D histogram is divided into energy slices of 100-200 keV which are projected on the time scale for determining the FWHM of the timing peak.

Results

Throughput Rate For the small CeBr_3 crystal, stable measurements (visible peaks from ^{60}Co in the energy spectrum) could still be performed with a detector load of 1.4 Mcps (figure 5.2.5-left). This value corresponds to about 600 kcps throughput rate in case of trigger 50. For the measurement with the higher detector load of 2.36 Mcps (corresponding to about 710 kcps throughput rate), the energy spectrum was distorted and a reasonable measurement seems not possible. Consequently, a detector load of 1.4 Mcps seems feasible for the detector setup.

With increasing detector load, gain drifts have been observed in the measurements (figure 5.2.5). Up to a certain detector load, the gain decreases. However, for even higher detector loads like 2.36 Mcps, the gain increases again. The cause has not yet been understood and should be aim of further investigations. However, the gain drifts might be a result of instabilities of the HV supply which might cause slight variations of the electrical field between the dynodes resulting in a different electron multiplication. Alternatively, space charge effects could potentially change

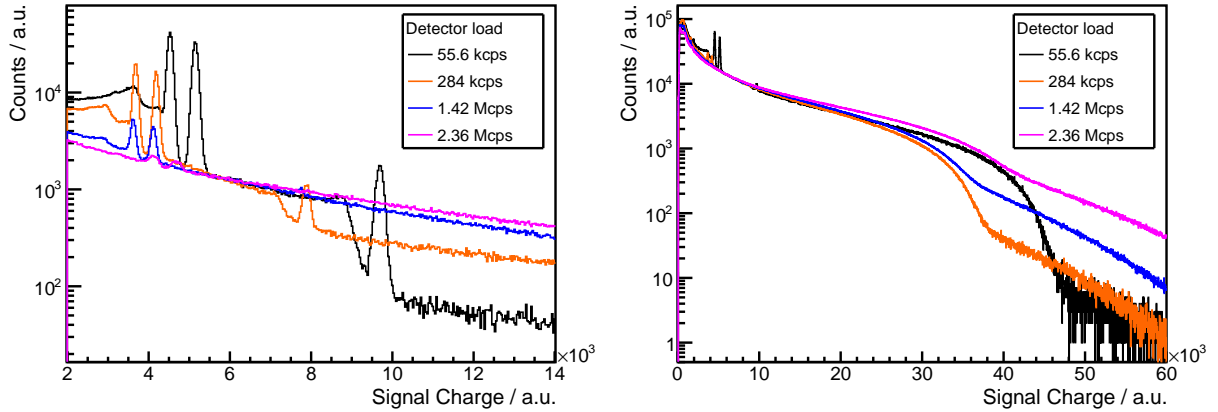


Figure 5.2.5.: Measured signal charge of the small CeBr₃ detector as a function of detector load. Left: data without the bremsstrahlung peak. Except for the highest detector load (pink solid line), two peaks corresponding to 1.173 and 1.333 MeV from ⁶⁰Co are visible. For the two lower detector loads (black and orange solid lines), also the sum peak (2.506 MeV) is visible. Right: the bremsstrahlung spectrum as a function of the detector load. The trigger was set to 50. Reproduced with permission from A. Rinscheid [136].

the electrical field within the PMT and therefore also the gain.

Energy Resolution The energy resolution as function of detector load, trigger setting, and crystal size is shown in figure 5.2.6. In case of varying trigger (and for a fixed detector load of 509 kcps), a nearly constant energy resolution of about 3.5 % (for 1.173 and 1.333 MeV) and 2.5 % (for 2.506 MeV) is visible. Only few outlying values can be identified which are mainly caused by artefacts in the energy spectrum [136]. When increasing the detector load, the energy resolution at around 1 MeV slightly worsens from initially 3.2 % (at 55 kcps) to 3.5 % (at 509 kcps) until it drops to over 6 % at detector loads of 2.3 Mcps. Furthermore, no difference can be seen between small and larger crystal.

Time Resolution The time resolution was determined as function of energy, detector load, trigger setting, and crystal size (figure 5.2.7). The expected trend of an improving performance for increased photon energies can be seen. Values of 290 ps (FWHM) are obtained for $E = 2$ MeV in case of the smaller crystal. The time resolution improves to about 240 ps at 4 MeV. When increasing the trigger, only small deviations are visible. Using a larger crystal decreases the timing capabilities by a constant offset of about 60 ps. In case of higher detector loads, the performance slightly degrades by few picoseconds.

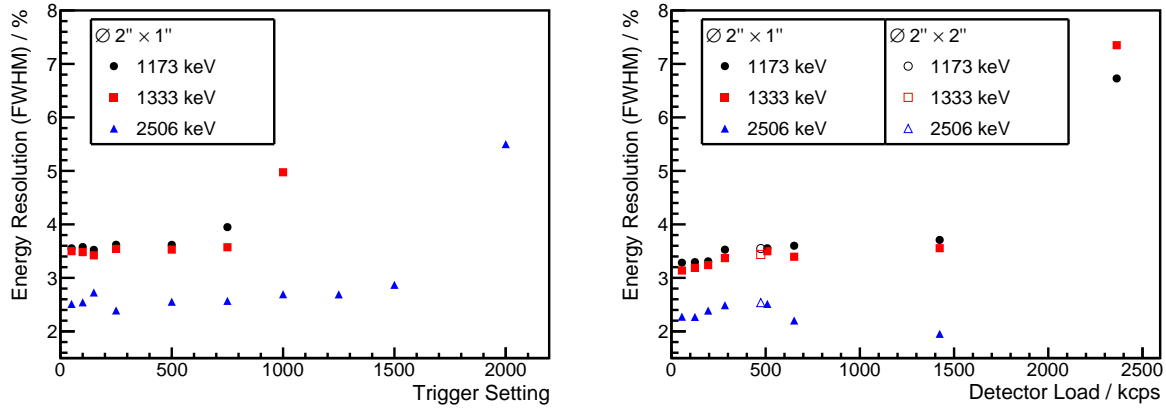


Figure 5.2.6.: Energy resolution as a function of trigger threshold (left) and detector load (right) for the two photon energies from ^{60}Co and the sum peak. Results for the smaller (filled markers) and the larger crystal (empty markers) are shown. Reproduced with permission from A. Rinscheid [136].

Discussion

The PGT prototypes based on CeBr_3 detectors with U100 readout have been successfully characterized at ELBE concerning detector load and throughput capabilities as well as energy and time resolution. Stable measurements could be performed with detector loads of around 1.4 Mcps which corresponds in this experiment to 600 kcps throughput at low trigger settings. Consequently, the desired throughput rate of 1.2 Mcps is not achieved by one detector but by at least two devices.

Furthermore, the influence of trigger settings and crystal size on energy and time resolution has been investigated. For most settings, both energy and time resolution are within the requirements for PGT. Varying the trigger has no implication on the energy resolution and the timing capabilities decrease only by few picoseconds. In case of the larger crystal, the time resolution is slightly worse by about 60 ps, which is about the same difference observed when measuring with analog electronics (see section 5.2.1).

In summary, the CeBr_3 -U100 combination fits with the requirements and specifications.

5.3. PGT under Clinical Conditions

After the successful characterization at ELBE, the PGT prototype is further tested under clinical conditions at UPTD. Here, a 3D PBS plan is delivered to PMMA phantoms (with the possibility to incorporate inhomogeneities) using the clinical mode of the proton therapy system. The beam current is controlled automatically and will reach values of up to 2 nA [13]. As the beam current is fixed, the degrees of freedom to control the detector load are the distance between target and detector, the angle with respect to the beam axis, as well as the detector size. In the following experiments, the $\varnothing 2'' \times 1''$ CeBr_3 detectors will be used as the time resolution is slightly better.

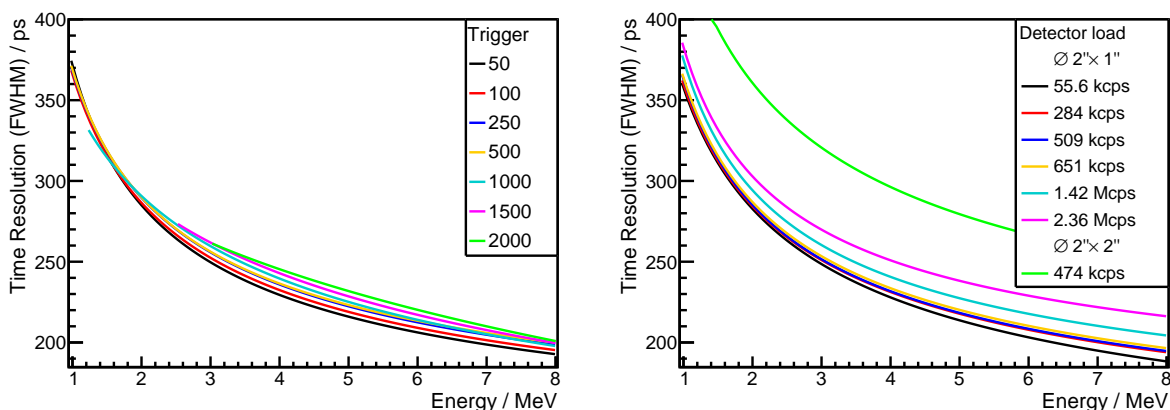


Figure 5.2.7.: Time resolution as a function of energy for different trigger settings with fixed detector load of 509 kcps (left) and for different detector loads with fixed trigger threshold of 50 (right) for both crystal sizes. Reproduced with permission from A. Rinscheid [136].

This leaves both the angle and distance as further variable parameters.

The PGT measurements under clinical conditions have been used to answer the following questions:

- Are measurements of reasonable quality and stability possible under realistic treatment conditions with the PGT prototype?
- What is a suitable detector position providing a trade-off between detector load and sufficient number of events?
- Can the layer and spot structure of the PBS plan be identified?
- Can the PGT data be spot-wise assigned and analysed in order to realize a range verification on a spot-by-spot base?
- Which limitations of the CeBr₃-U100 combination can be identified?
- How many PGs are detected per spot?
- Can we identify range variations on a spot level?

5.3.1. Materials and Methods

The PBS irradiation was performed in GTR2 of UPTD. The target and detector holding system used by Hueso-González et al. [12] were used as well as the same naming conventions in order to describe the setup. Target and detector setup are positioned using the laser system of the in-room patient positioning system.

Target A hollow PMMA cylinder (dimensions $\varnothing 15 \times 10 \text{ cm}^2$ with inner diameter of 5 cm) made out of two halves was used as target (figure 5.3.1-top). The inner cylinder was filled with small discs of different materials like PMMA, air, and SB3 cortical bone equivalent material with variable thicknesses (further details can be found in [12]). The target is mounted on a holder so that the middle axis of the phantom is aligned with the central beam axis. The target holder is further placed in a ring which is used for positioning the detectors. The center of the ring (i.e. the point of view of the detectors) is $(15.3 \pm 0.2) \text{ cm}$ downstream the isocenter of GTR2 and at the half of the range of the distal layer (see below for details).

PBS Plan A 3D PBS plan, the so-called “dose cube” (figure 5.3.1-bottom) was delivered to the phantom. The dose cube has a planning volume of $8 \times 8 \times 8 \text{ cm}^3$ WET with a distal layer at 18 cm WET [5] (in z -direction with respect to the positioning in GTR2). This corresponds to a beam energy of 162 MeV which is a realistic value for patient treatment. In case of PMMA, the distal range is reduced to 15.8 cm and the modulation to 7.0 cm [5]. The plan consists of 22 layers which comprise a total number of 5298 spots. The layer and spot information is encoded in the so-called “PLD”-file, which further contain the x and y coordinates of each spot as well as the incident dose in Monitor Units (MUs). Even though a uniform volume is irradiated, the incident dose per spot varies over several orders of magnitude. The horizontal and vertical distance between the spots is constant with 6 mm and the distance between succeeding layers is about 4 mm WET.

The dose cube is planned as a realistic 1 Gy field and as one with 5 Gy for increased statistics. The plan was delivered to the PMMA target with the possibility to incorporate inhomogeneities with thickness t at the target depth a . In some cases, consecutive irradiations of the same 1 Gy plan were performed to obtain increased statistics. The list of the irradiated target setups is shown in the appendix in table A.2.2 and details on the dose cube plan are shown in table A.2.1.

Detectors Two CeBr_3 detectors (dimensions $\varnothing 2'' \times 1''$) with U100 readout were used to monitor the PG emission from the target (figure 5.3.1-top). The U100s have the identification numbers “p0006” and “p0007” and both detectors will be labeled according to those numbers in the following. The HV was set for each detector to around 800 V. As time reference, the 106.3 MHz RF signal of the accelerator was shaped using a fast timing discriminator, type TD 2000 from FAST ComTec, and each of the two output signals was connected to the digital-in of a U100. With the internal PLL, this frequency is scaled to the double value of about 212.6 MHz resulting in a sampling point distance of 4.7 ns.

Finding the Optimum Detector Distance In preparation of the PBS measurements, the optimal detector positions for both devices were determined as a trade-off between sufficient number of detected PGs and still manageable detector load. In a first approach using the experience from Hueso-González et al. [12], device p0007 was placed upstream under $\Theta = 130^\circ$ and p0006 downstream with $\Theta = 50^\circ$ relative to the beam axis. Both detectors had a distance d of 50.0 cm

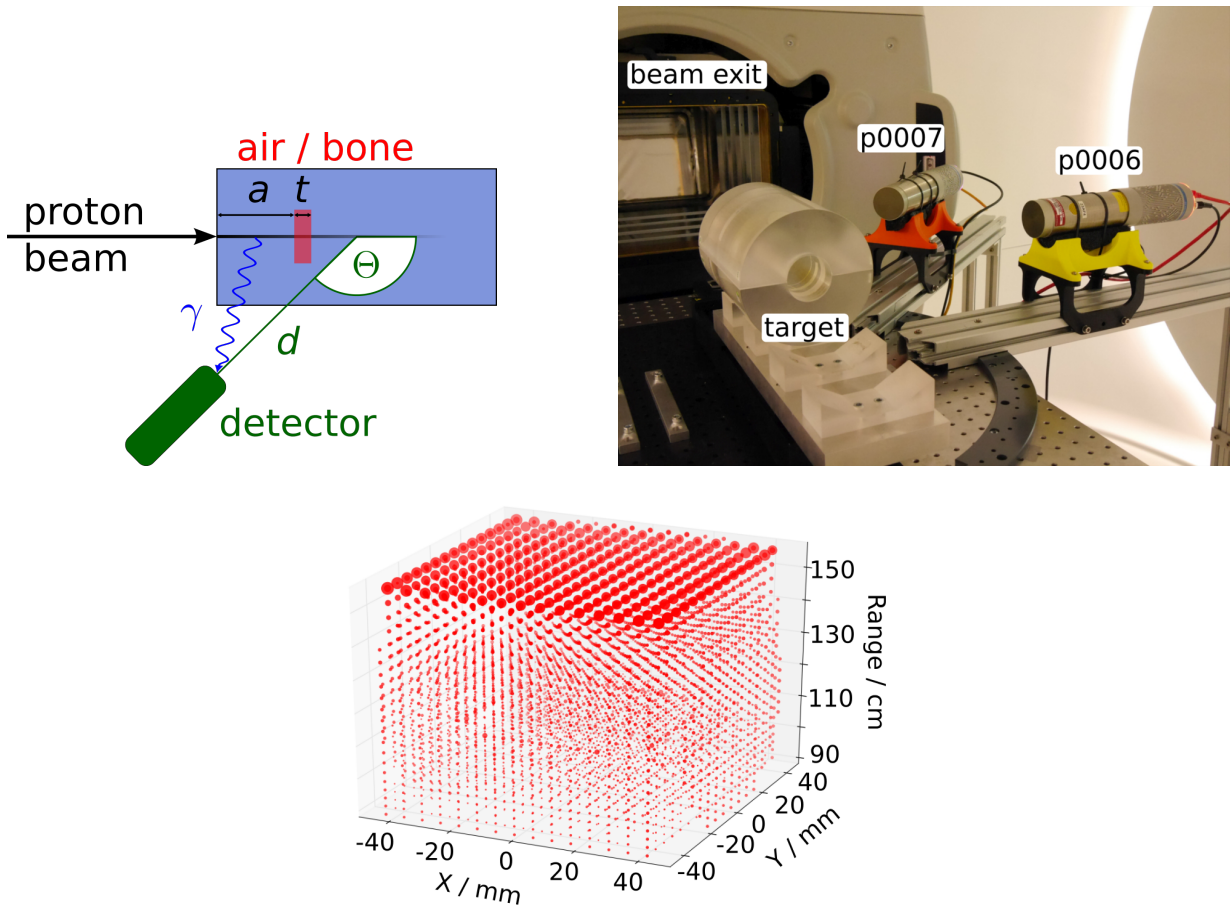


Figure 5.3.1.: Schematic drawing (top left) and photography (top right) of the experimental setup for PGT measurements under clinical conditions at UPTD. A PBS plan is delivered to a PMMA phantom made out of two hollow half cylinders. The inner cylinder can be filled with different materials like PMMA, bone-equivalent inserts or air. Two detectors are measuring the PG emission. Naming conventions are adapted from [12] and are also explained in the text. Bottom: dose cube plan obtained from the PLD file. The range is calculated for PMMA. Reproduced with permission from J. Berthold [137].

to the ring centre. A central proton pencil beam with the highest beam energy of the dose cube plan (i.e. 162 MeV) was used for testing the setup.

Both detectors measured consecutively the PG emission with a trigger threshold of about 1.2 MeV. In the analysis, attention was paid to the throughput rate as well as the form of the energy spectrum. For both devices, the energy spectra were acceptable as the 4.44 MeV peak as well as single and double escape were visible and separated. Furthermore, no additional pile-up contribution was visible. The throughput rate was 350 and 270 kcps for p0006 and p0007, respectively. Consequently, the distances were lowered to $d = 40.0$ (p0006) and $d = 35.0$ cm (p0007) in order to increase the number of detected photons. Again, the spectra were acceptable and the throughput rates increased to 500 (p0006) and 450 kcps (p0007), which are reasonable values.

In case of p0006, it became later evident in the PBS measurements that the detector load strongly increased for certain spots in contrast to the central spot measurement and that throughput rates up to 900 kcps were obtained. It turned out that the energy spectrum was distorted and an increased contribution of high energetic events was visible. The signal stems from scattered protons escaping the target when the scanning beam was approaching the outer target surface. Consequently, p0006 was positioned under $\Theta = 90^\circ$ with the same distance d of 40.0 cm. A schematic drawing and a picture of the final setup are shown in figure 5.3.1

Data Analysis The data analysis is performed offline using the C++ framework ROOT [121]. Energy calibration is applied based on the PG peaks at 4.44 and 6.1 MeV, including single and double escape peaks. The timestamps are translated in real time values based on the conversion factor of 4.6 ps per fine counter bin. No further corrections have been applied.

5.3.2. First Results

Count Rates

The count rate (i.e. detector throughput) versus measurement time for the dose cube irradiation obtained by p0006 is presented in figure 5.3.2 showing the whole plan, the distal layer, and individual spots from the distal layer. The dose cube plan is delivered within 55 s and its structure, comprising 22 layers, is visible. Over the full plan, the measured event rate varies from 100 to 500 kcps. As expected, the maximum rate occurs in the distal layer. Between the layers, a time interval of 2 s is required for changing the energy and delivering a tuning pulse (small peaks between two layers). The intensity is decreasing from layer to layer which is in accordance with the PLD file (see table A.2.1 in the appendix). Furthermore, in each layer, a constant rise in the count rate is visible, which is a result of the changing solid angle to the detector due to the scanning process. When zooming to the distal layer (figure 5.3.2-top right), this can also be seen as an additional oscillation.

The distal layer has the longest irradiation time with around 3 s, even though it does not have the highest number of spots. This is a result of the therapy system which adapts for patient safety

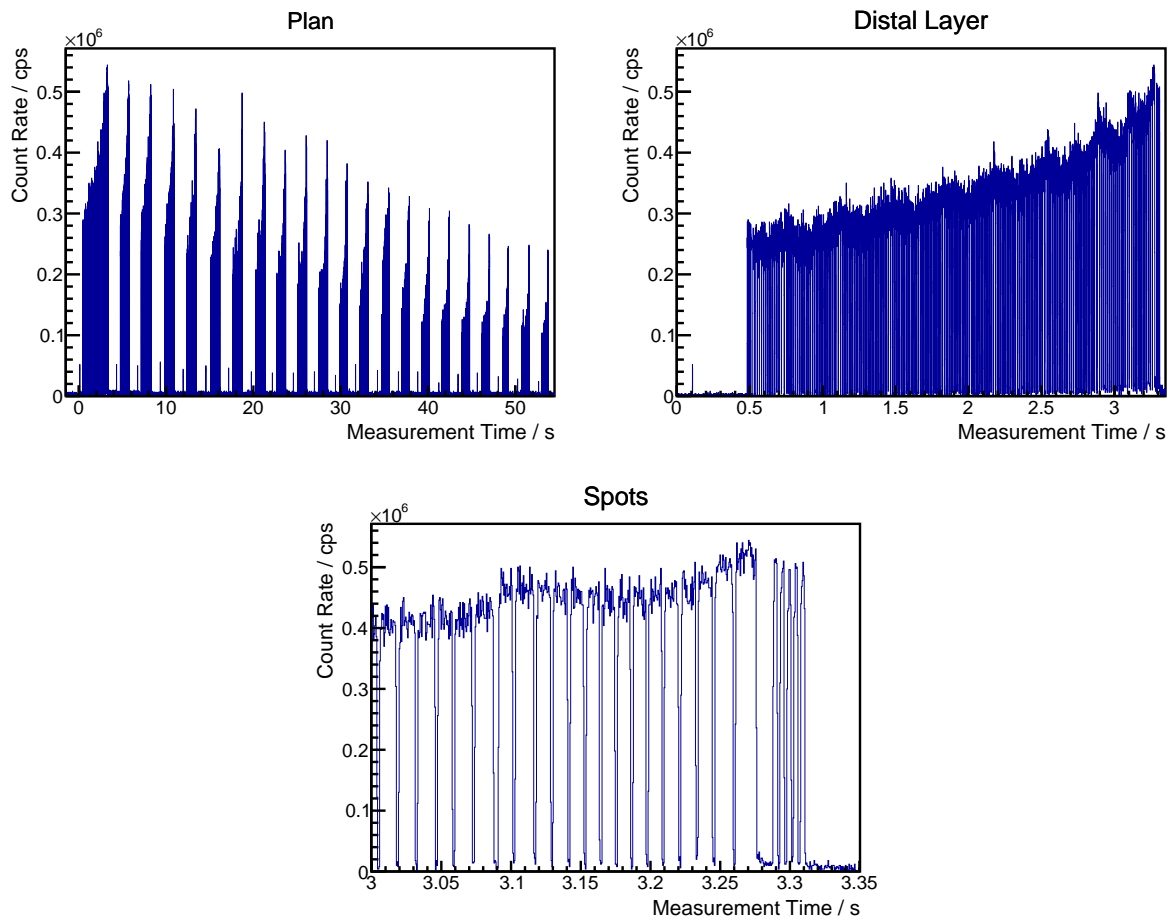


Figure 5.3.2.: Count rate versus measurement time of the PBS dose cube irradiation measured with p0006. The full dose cube plan (top left), the distal layer (top right), and selected spots of the distal layer (bottom) are shown.

reasons the beam current to the incident proton number until a maximum current is reached. Then, the total number of particles per spot can only be controlled by increasing the irradiation time. In this particular plan, the irradiation time for a spot varies from around 2-3 to nearly 20 ms (figure 5.3.2-bottom). Between the spots, beam pauses between 1-10 ms are visible which are attributed to changing the magnetic field of the dipole magnets for the scanning process.

Gain Stability

A stable PMT gain is mandatory for the PGT prototype to ensure a proper energy calibration. In case of the dose cube irradiation, the situation is depicted in figure 5.3.3 showing the signal charge integrated by the FPGA versus the measurement time for the distal layer measured with p0006. Each vertical projection of the so-called “waterfall plot” is hereby an uncalibrated energy spectrum where the intensities are encoded in the colour scale. The energy deposition corresponding to the 4.44 MeV region is mainly visible between 13,000 and 20,000 (barely visible as two lines).

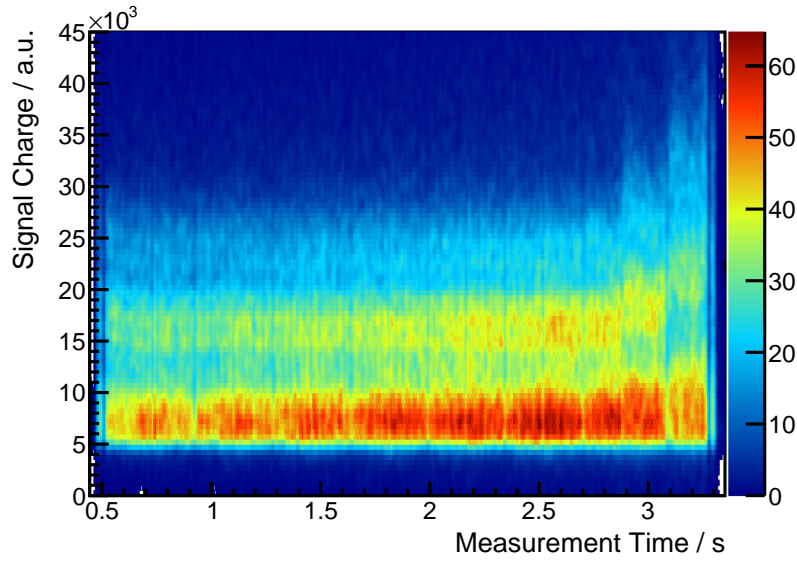


Figure 5.3.3.: Signal charge versus measurement time in PBS mode measured with p0006. The distribution shows the distal layer of the dose cube plan.

However, in the beginning of the layer, the distribution is slightly curved indicating a decrease of the PMT gain. Additionally, at around 3 s measurement time, the gain is again increased. It turns out that the PMT gain is not stable during the irradiation of the layer and drifts towards an equilibrium state where it remains constant. The same observation has also been made in the characterization measurements at ELBE, where an increased detector load caused a gain decrease. The PMT gain increased again for an even higher detector load. In case of the distal layer, this is also consistent with the measured count rate (see figure 5.3.2), which increases at the end of the layer. A similar behaviour was also observed for p0007.

A variable gain can have severe effects on the measurement and on further data analysis. The energy thresholds are not valid anymore and data is hardly comparable. As a consequence, the gain has to be corrected for drifts and the source of the instability has to be investigated.

In the dose cube irradiation however, a numerical gain correction could not be applied due to the insufficient number of events in the PG lines. Nevertheless, in later experiments using lower trigger settings, the 511 keV line was used for determining a gain correction function over the measurement time [136].

Energy Spectra

The calibrated energy spectra integrated over the whole dose cube plan and the distal layer are shown in figure 5.3.4. In case of the full plan, the PG regions at 4.44 MeV and 6.1 MeV are visible with a clear peak separation indicating relatively stable performance (except for the gain instability discussed above). Furthermore, the 2.225 MeV line from neutron capture at hydrogen is visible and can be separated for further analysis from the PG region.

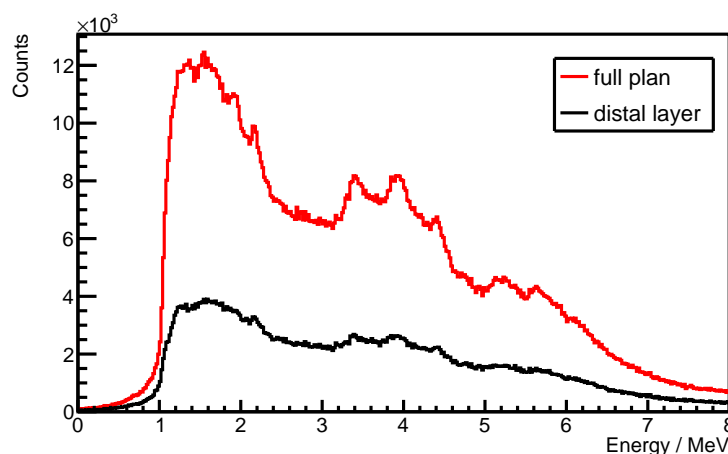


Figure 5.3.4.: Energy spectra measured in PBS mode with p0006 for the full dose cube plan (red) and the distal layer (black). Gain correction could not be applied.

For the distal layer, the number of events in the spectrum is about a factor 3 lower compared to the whole plan (see corresponding maxima in figure 5.3.4). This is in accordance with the treatment plan (i.e. the PLD file) as the distal layer has a relative dose of $\approx 33\%$ (see table A.2.1). Nevertheless, the PGs can also be identified for the single layer and background suppression is possible by removing low energetic events.

PGT Data

The energy versus relative time distribution for the distal layer as well as the corresponding PGT spectra of the distal layer and of a selected spot are shown in figure 5.3.5. The PG peak can be identified between 2 and 4.5 ns and the dominant 4.44 MeV region is visible. Furthermore, uncorrelated background with energies below 2.5 MeV is represented by the horizontal stripe. Two artefacts can be further seen in the histogram. First of all the vertical line at 4.7 ns, which is caused by a firmware setting writing events with false timestamp into the zero bin of the interpolation. As the U100 is clocked with twice the RF, there is also such a zero bin at half of the clock cycle, i.e. at 4.7 ns. The second artefact are the curved stripes between 1 and 3 MeV. The stripes are a result of the event processing within the U100³ and have also been observed in the characterization measurements at ELBE. According to the manufacturer, the artefacts might be caused by the high trigger threshold as the device is not designed for such settings.

The PGT spectra are created from the 2D histograms as a projection on the time scale using an energy window of $2.5 < E < 7$ MeV. The vertical line artefact was corrected by a linear interpolation between the surrounding bins. The PGT profile of the layer (black curve, normalized with a factor of 0.01) shows a smooth peak with a FWHM of about 2.5 ns which sits on top of a non-linear background distribution. In case of the selected spot, the PGT spectrum is more noisy

³Private communication with the manufacturer.

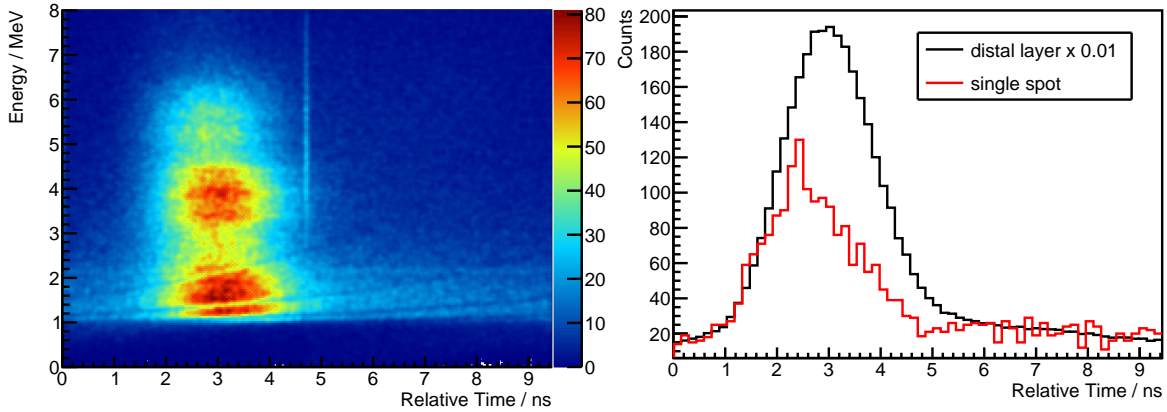


Figure 5.3.5.: Left: energy versus relative time distribution of the distal layer measured with p0006 in PBS mode. Right: PGT spectra of the distal layer (black) and a selected spot (red). For illustration purposes, the PGT spectrum of the layer was multiplied by 0.01. An energy window of 2.5-7 MeV is applied.

and the peak is less broad with around 2 ns FWHM (which is in agreement with the predictions made in section 4.4.4). Both observations are expected as the full layer comprises 235 individual spots. Therefore, the PGT spectrum of the layer is the sum of all PGT spectra from the spots with their individual TOF distributions (due to the different positions between detector and spots).

5.3.3. Spot-by-Spot Data Analysis

PBS Spot Sorting

The PGT data from each individual spot should ideally be used for a spot-by-spot range verification. However, as the spot order changes between the planning phase (written in the PLD file) to the actual beam delivery, the relevant parameters (x and y position as well as dose) cannot be directly assigned to the measured data. The changing spot order is a result of an optimization process from the therapy system to reduce the delivery time of the treatment. Nevertheless, the machine logs of the irradiation can be utilized as they contain the actual irradiation order. They are created for each layer and comprise further parameters like current settings for the scanning magnets, beam current, irradiation time, and ionization chamber readout.

The electrical current of the scanning magnets was chosen as the measure of choice for the spot sorting. The current of the x or y magnet increases with the requested spot coordinate⁴ and is thus an equivalent parameter. The sorting algorithm starts with the x values and ends with the y position. In this procedure, a spot ID array is created which connects the positions from the PLD file with the ID from the machine log. In the next step, this matrix is sorted for the spot ID for obtaining the irradiation sequence. As a result, x and y position as well as incident dose

⁴Note that the x and y dimensions are swapped between PLD file and machine log.

can be assigned to each individual spot within the measured data. The results of the spot sorting were also compared with the algorithm used by IBA and complete agreement was found.

Layer and Spot Identification

For the spot-wise assignment of the measured data, an automated spot and layer identification is required as a full PBS irradiation comprises several thousand spots. Therefore, an algorithm has been developed in the bachelor thesis of J. Berthold [137]. In this framework, the software environment “PGT_analysis” has been written in Python.

The software requires data input from three sources: the measured list mode data, the PLD file, and the machine logs. After reading the list mode data, the count rate histogram is created with an adjustable binning. A time window can be set for variable analysis of one or more layers or even the full plan. In a first step, the layer structure is identified by determining the content of each bin and comparing it with a fixed threshold. The first irradiated layer (i.e. the distal one) is reached if the bin content is above the threshold for the first time. Within the layer, the program searches for the next bin below the threshold which is followed by a beam pause of more than 1 s. This point marks the end of the layer. Until the end of the time window is reached, the procedure is repeated and all start and end points of the layers are determined.

For identifying the spots within a layer, the mean bin content (i.e. count rate) of the corresponding layer is determined. An adjustable fraction of this value is then used as a fixed threshold for the spot identification. The beginning of a spot is marked when the bin content is above the threshold for two consecutive bins. When the content drops below the threshold, the end of the spot is reached. In this manner, the timestamp of spot begin and end are written in an array which can then be assigned to the list mode data.

The threshold parameters are not fixed but have to be adapted for each irradiated plan and detector setting. For example, when measuring with low trigger settings, high count rates could be present due to material activation even during beam pauses which would require a higher spot detection threshold. On the other hand, spots with very low dose might be hard to detect in such a case.

Furthermore, the obtained number of spots and layers is compared to the planned values from the PLD file. If the numbers are not matching, “PGT_analysis” tries another identification procedure with lower and higher threshold settings. In case of the dose cube with high trigger however, the identification procedure was successful and all 22 layers and 5298 spots were detected.

Prompt Gamma Rays per Spot

The number of detected PGs is of highest concern regarding the sensitivity of the PGT method [12, 13, 51] (see also section 2.4 for details). Consequently, the number of measured photons was determined for each spot of the distal layer for an irradiation of a full PMMA target. Figure 5.3.6-left shows the total number of detected photons per spot and the, on 10^8 incident protons, normalized number per spot measured with both detectors. The incident proton number is hereby

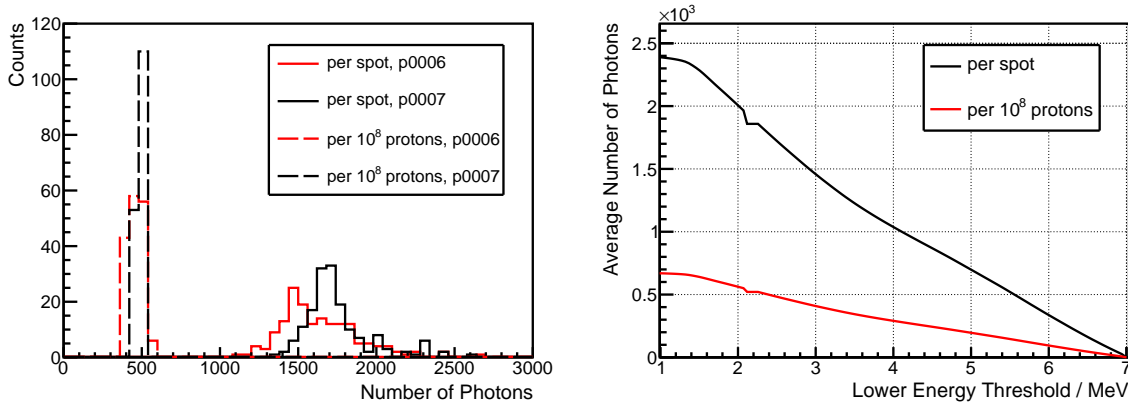


Figure 5.3.6.: Left: Number of detected photons per spot of the distal layer and per incident number of protons measured with both detectors. An energy window of 2.5–7 MeV is applied. Right: Average number of detected photons as a function of the lower energy threshold per spot and normalized on 10^8 protons per spot measured with p0007. An upper energy threshold of 7 MeV is applied. The graphs show the averaged results from 5 successive irradiations. Furthermore, only the spots within the region of stable gain were used for a better comparison of the data.

calculated from the MUs using calibrated data of the nozzle⁵. For reducing the uncertainties, the analysis was performed on 5 consecutive irradiations and the results show the averaged values. An energy window of 2.5 – 7 MeV was applied to reduce the contribution from background events. Therefore, only the spots within the region of stable gain were chosen for the analysis.

The number of detected photons per spot (solid lines) shows for both detectors a relatively broad distribution around a mean value of 1640 and 1750 photons for p0006 and p0007, respectively. When normalizing the data on the incident proton number per spot (dashed lines), the distribution becomes more narrow with a mean of 460 (p0006) and 490 (p0007) photons per 10^8 protons. Consequently, the broader distribution of the photons per spot is a result of the variation of incident protons per spot. The slightly higher numbers in case of p0007 are expected as the detector was placed closer to the target (35 vs. 40 cm) and the angular dependence of the PG emission favours p0007 [56]. However, from the geometrical point of view, the difference should be higher with $\approx 20\%$ compared to the measured 6%. This difference might be a result of the increased absorption within the target, as the path length through the PMMA is increased for p0007.

The energy window was chosen to reduce the background mainly coming from the 2.225 MeV line. However, the question arises if a larger energy window might improve the PGT sensitivity despite the additional background contribution. Therefore, the number of detected photons per spot and 10^8 protons has been investigated as a function of the energy window. The upper

⁵The calibration data was provided by F. Vander Stappen from IBA.

threshold of 7 MeV was fixed, as nearly no PGs are measured at higher energies. The lower threshold was varied from 1.2 MeV to the upper threshold and the photon number was determined for each individual energy window using the procedure described above. The region around the 2.225 MeV line was not considered in the analysis as it resembles a purely constant background contribution. The results for p0007 are presented in figure 5.3.6-right showing the number of photons per spot and normalized on 10^8 protons as a function of the lower energy threshold. About 2380 (per spot) and 660 (normalized per spot) photons are detected with the biggest energy window, which is an increase of about 30% compared to the conventional energy window (2.5-7 MeV).

Photon Time-of-Flight

A further spot-wise analysis was performed aiming at the determination of the TOF distribution of the distal layer as each spot has a different distance to the detectors. For the full PMMA target, data of 5 Gy incident dose was summed up for increasing the number of events. The centroid of the PGT spectrum of each spot was determined and combined with the position information of the PLD file. No energy window was applied as all spots are investigated (including those with different PMT gain). The distribution map of the PGT mean values for each spot is shown figure 5.3.7.

For both detectors, a relatively smooth distribution is visible over the distal layer representing the different TOF contributions of each spot. Lower x values tend to have a longer TOF contribution which is in agreement with the detector position on the positive x -axis. In case of p0007, a diagonal trend is visible which is counter intuitive to the expectations of a vertical behaviour of the TOF effect. This might be a result of an additional time shift due to the gain instability as the electron transit time through the PMT might vary with HV supply instabilities. A similar behaviour is also visible for p0006. For the detector, the PGT centroids of the spots with $y > 30$ mm are also in contrast to the otherwise relatively smooth TOF distribution. Using the order of spot delivery, we can see that those spots fall into the region of increased gain (see figure 5.3.3) due to the higher detector load. Hence, gain instability and time variation might be connected. Alternatively, the time shift could also be caused by RF-bunch drifts. Nevertheless, the small TOF variations between the spots are visible as shifts in the PGT spectra despite the system time resolution of about 2 ns.

Detection of Inhomogeneities

The obtained data can be used to determine differences between the measurements with an inhomogeneity (e.g. air cavity or bone insert) with respect to a reference with a homogeneous PMMA target. Using a spot-by-spot analysis procedure, the PGT information as well as the number of photons can be compared. In all further presented results, data obtained with a total dose of 5 Gy is used for increased statistics.

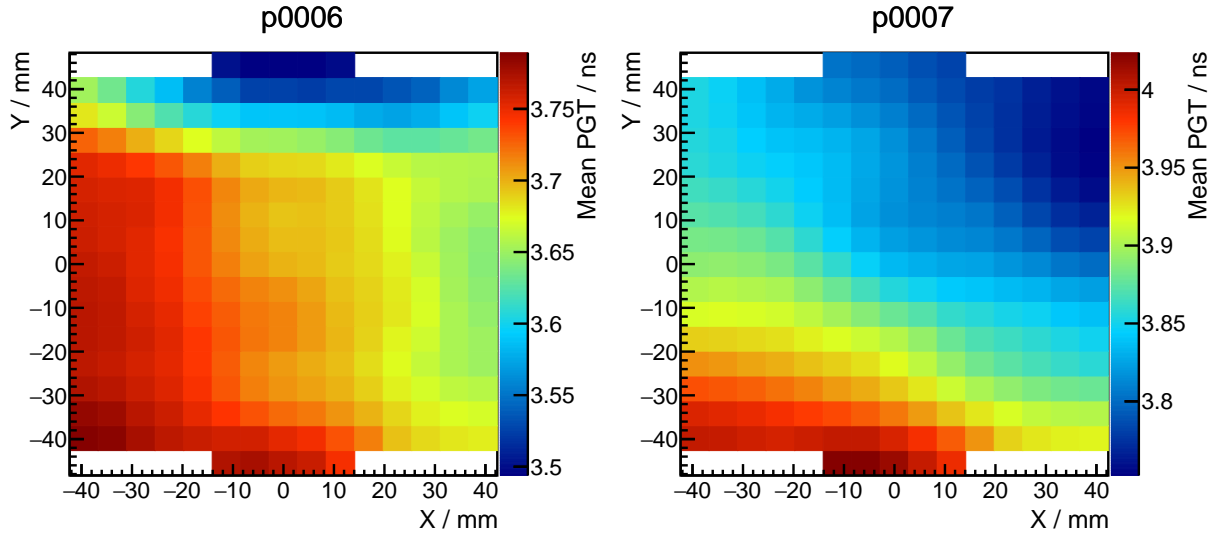


Figure 5.3.7.: PGT mean values of each spot of the distal layer measured with both detectors. For better visibility, the data was smoothed using an averaging algorithm over neighbouring spots. The detectors are located towards positive x values. The figures were produced using the primary data analysed in [137].

Detection of Range Variations using PGT Data Using the data of 5 cumulative 1 Gy measurements, the number of photons per spot is with roughly 8,500 close to the crucial number of 10,000 which is required to detect a range shift of 5 mm [12, 13]. Like in section 4.4.3, the measurement with inhomogeneous target composition (5 mm air cavity at a depth of 11 cm) will be compared with a reference measurement (homogeneous PMMA phantom). For both target settings, the PGT centroid of each spot is determined. An energy window of 2.5-7 MeV (without gain correction) is applied to reduce the background contribution. For each spot i , the difference of the centroids $\text{PGT}_{\text{diff},i}$ is calculated as follows:

$$\text{PGT}_{\text{diff},i} = \text{PGT}_{\text{PMMA},i} - \text{PGT}_{\text{air},i}. \quad (5.3.1)$$

Figure 5.3.8 shows the result in form of a map of the distal layer. In both cases, a variation of the PGT mean values can be observed close or even within the air cavity (black circle). The maximum difference is about 18 ps, which is in rough agreement with the 25 ps shift claimed in [51]. The measurement with p0006 is more noisy which might be a result of the slightly lower number of detected photons. Nevertheless, the air cavity can be identified with both detectors.

The same procedure was performed to identify a bone insert (thickness 2 cm, at 11 cm depth). However, in this particular case and for both detectors, no clear evidence for a shift in the PGT spectra could be observed. Hueso-González et al. [12] made similar observations when varying the position of the bone insert towards the end of the particle range.

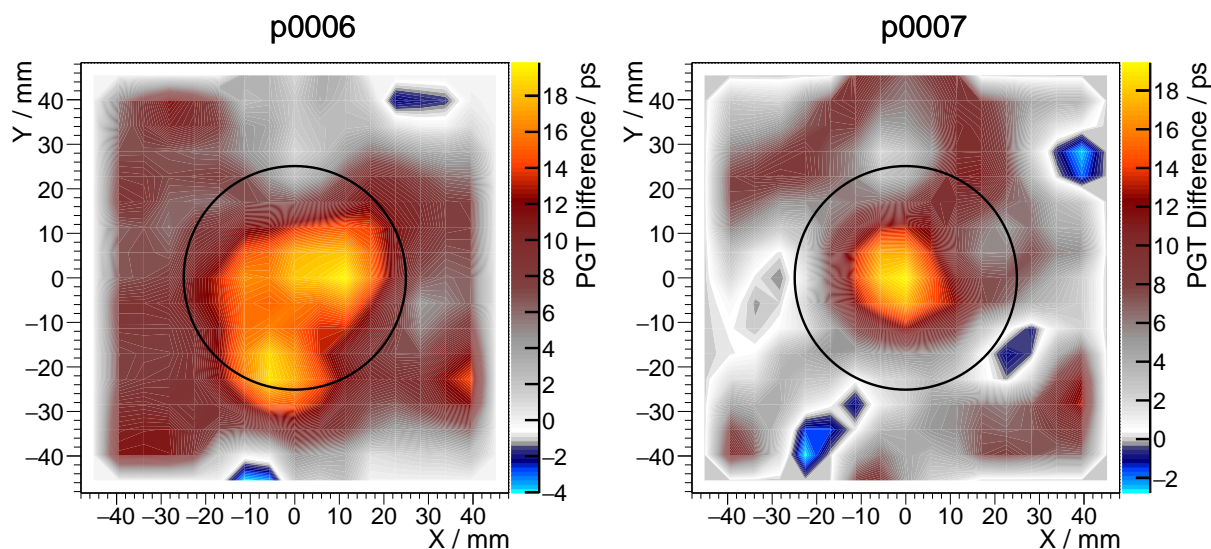


Figure 5.3.8.: PGT shift due to a 5 mm air cavity in reference to a full PMMA measurement for each spot of the distal layer measured with both detectors. For better visibility, the data was smoothed using an averaging algorithm over neighbouring spots. The location of the air cavity is represented by a black circle.

Detection of a Bone Insert using Photon Yield Variations The increased photon yield due to a bone insert might limit the detectability of a range variation based on PGT data. However, this drawback in case of PGT could also be utilized for the identification of the inhomogeneity based on the detected number of photons per spot. Therefore, a similar procedure as for the PGT analysis is applied. For the irradiation with and without bone insert, the distal layers of 5 consecutive measurements are added spot-wise. The measured value is hereby not the PGT centroid but the number of photons per spot. No energy windows were applied to account for the non stable gain. The relative photon yield is calculated as the difference between the measurement with bone-equivalent insert in reference to the homogeneous case. The value is then further normalized to the number of photons determined for the reference.

The results for both detectors are shown in figure 5.3.9. A photon excess can be detected where the bone insert (black circle) is located. A maximum value of 5% is reached in the center of the bone insert and the magnitude decreases towards the edges of the disc. This might be a result of the finite spot size of the beam. The measurement with p0006 is again more noisy towards the edges of the layer, nevertheless, the bone insert is also visible in this case.

5.3.4. Discussion

In this section, the prototype system designed for range verification based on PGT has been introduced. The detector system was characterized concerning energy and time resolution as well as throughput rate in the bremsstrahlung facility at the ELBE accelerator at HZDR. Here,

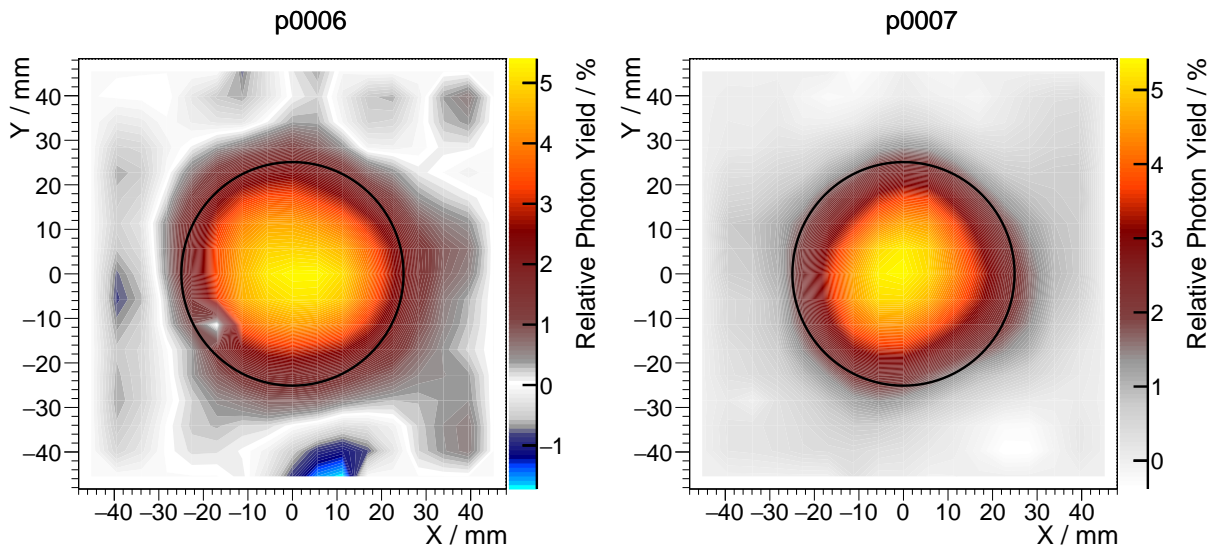


Figure 5.3.9.: Relative photon yield of the distal layer of a target with a bone equivalent insert in reference to a full PMMA measurement. The insert (thickness of 2 cm) is clearly visible as an overproduction of photons. For better visibility, the data was smoothed using an averaging algorithm over neighbouring spots. The location of the bone insert is represented by a black circle. The figures were produced using the primary data analysed in [137].

the properties were tested using a ^{60}Co source and the high energetic bremsstrahlung beam with energies of up to 12.5 MeV. The energy resolution was found to be stable with 2.5% (for $E \approx 2.5$ MeV). A time resolution of 250-300 ps (depending on the crystal size) was achieved for energies above 3 MeV which is within the requirements for a clinical PGT system. Acceptable detector loads of 1.4 Mcps could be tolerated which were, in this particular experiment using high trigger thresholds, corresponding to throughput rates of 500 kcps.

As a last step, two prototypes with the smaller CeBr_3 crystals were used to perform, for the first time, PGT measurements under clinical conditions. A dose cube plan was delivered on a PMMA target in PBS mode in the treatment room of UPTD. The experiment was designed as a first test to gather experience regarding a suitable detector position (distance and angle to the beam axis). The correct setup is crucial as it mostly determines the detector load and therefore the number of acquired events. The positioning was performed with a rather simple mounting system and will be improved in further experiments with e.g. by mounting the detectors at the beam nozzle.

In the data of the irradiation, the layer and spot structure of the PBS plan could be identified and used for a spot-by-spot data analysis. The PGT detector operated relatively stable, however, variations in the gain of the PMT were visible. With start of the irradiation, the gain decreased toward a point of equilibrium until the gain raised due to higher count rates. The gain variation has to be corrected to guarantee stable energy thresholds for further data analysis. The correction

is not depending on the incident energy as the U100 determines a baseline corrected signal charge. Consequently, the 511 keV line could be used as it has the highest yield. Nevertheless, this would require a lower trigger threshold of the U100 which would possibly decrease the measured number of high energetic PG signals. A potential solution would be a 2-step threshold - a lower threshold, slightly below the 511 keV line, and a higher one. Events between the thresholds would not be always processed but e.g. in 10% of the cases. Events above the higher threshold will be processed nevertheless. In this manner, the lower energies are less favoured in the signal processing but the 511 keV line would still be measurable. A corresponding firmware update is currently being developed. The bigger problem of the gain variation concerns the transit time of the electrons through the PMT. If the gain instability is an effect of a HV breakdown in the PMT, the transit time changes and the PGT spectrum shifts. Indeed, such time shifts are visible in the TOF distribution of the distal layer and in dedicated measurements with about 10 ps shift per 1 V. A correction of this effect is therefore mandatory.

Nevertheless, reasonable energy spectra could be obtained as well as the timing information in reference to the cyclotron RF.

In order to evaluate the data spot-by-spot, a reliable automated layer and spot scanning procedure was developed. Additionally, the measured data was connected to the treatment planning from the PLD file. Both processes have been developed and implemented in a software environment.

Using the spot-by-spot analysis, the first question concerned the number of detectable photons as this parameter determines the sensitivity of the PGT method [12, 13, 51]. For both detectors, the distal layer was analysed to obtain the number of photons per spot and a, on 10^8 protons, normalized value per spot. In case of the particular dose cube plan, around 1,700 γ -rays per spot and 475 per 10^8 protons have been obtained. Comparing this figure to the calculations from Pausch et al. [13], a factor of 20 is missing to the expected 10,000 PGs per 10^8 protons. However, this estimated number lacks several effects compared to the realistic case:

- 1) The throughput rate was about a factor of 3 smaller than anticipated (400 kcps vs 1.2 Mcps).
- 2) No energy window was given, i.e. the results for the lowest energy threshold (in our experiment) of around 660 photons per 10^8 protons should be considered.
- 3) The distance between detector and target was slightly higher with 35-40 cm compared to the 30 cm from the estimate, resulting in a variation of 26-43%.
- 4) No photon absorption within the target was anticipated, however, the intensity of a 4.44 MeV photon beam is reduced by 24% after passing 7.5 cm of PMMA [133].
- 5) The original estimate is based on a $\varnothing 2'' \times 2''$ LaBr₃ detector. Even though CeBr₃ can be considered as relatively similar concerning the detection efficiency, the used detectors had only half the thickness. Consequently, the detection efficiency would increase for a 4.44 MeV photon by 60% when using a crystal with a thickness of 2''.

Combining all those correction factors, around 5000 photons per 10^8 protons should be detectable using the conditions from Pausch et al. [13]. This is still a factor of 2 away from the estimate, nevertheless, the considerations like target absorption and energy window are rather conservative and the actual number of photons is potentially higher.

The number of measured photons can also be utilized for determining the sensitivity of a given PGT setup. The detectable mean shift between two PGT spectra is according to (2.4.5) a function of the width of the PGT peak and the detected number of events N . The PGT peak on the other hand depends on the system time resolution and the proton transit time. This measure can be assessed using the obtained data of the BTS (see section 4.4.4) and the time resolution of the detector (see section 5.2.4) as input parameters for a simple modelling. N can be evaluated as the number of PGs per proton and detector (see section 5.3.3) multiplied with the incident number of protons and the number of deployed detectors.

Two different scenarios are considered: a realistic one and the best case. The first scenario is based on the parameters obtained in our measurements like an incident proton number of $3 \cdot 10^8$ per spot, 475 PGs per 10^8 protons (2.5-7 MeV energy window), and the BTS in GTR2 of UPTD with default Momentum Limiting Slit Opening (MLSO) of 30 mm. Furthermore, 8 detectors are used for the calculation as this number is currently considered for experimental studies and the detectors are already in stock. The best case scenario uses for PGT more favourable settings like 16 detectors, $5 \cdot 10^8$ protons per spot, 660 PGs per 10^8 protons (1.2-7 MeV), and a reduced BTS when lowering the MLSO to 10 mm. Hence, N is set by the input parameters. For determining the width of the time peak, PGT spectra are modelled using the simulation tool from F. Hueso-González [138]. Using the time width and N as input for the calculation of the detectable mean shift (see equation 2.4.5) as well as a PGT conversion factor of 50 ps per cm [51], the detectable range shift in mm for a treatment in GTR2 of UPTD can be evaluated as a function of the proton range (figure 5.3.10). The safety margin applied at UPTD is also shown as a function of the range.

For the realistic case, range shifts below 8 mm are detectable and the safety margin could be reduced for ranges above 12 cm. Even though the best case seems currently unrealistic, it still shows the potential of PGT. Range shifts of about 2 mm can be measured which would reduce the safety margins in all cases.

The PGT data of each individual spot was analysed concerning different aims. For increasing the statistics towards the crucial number of 10,000 PGs per spot, 5 consecutive measurements of the same target setup were added up for further analysis. First of all, the TOF distribution of the distal layer was obtained for both detectors by determining the mean value of the PGT spectrum of each spot. When combining the results with the spot positions, a smooth trend of the TOF distribution was visible which is also in agreement with the detector location. However, the trend had a different behaviour than expected which might be a result of time drifts due to HV variations of the PMT or coming from additional effects which are not yet fully understood.

The TOF information could further be used in a setup comprising two detectors, positioned on

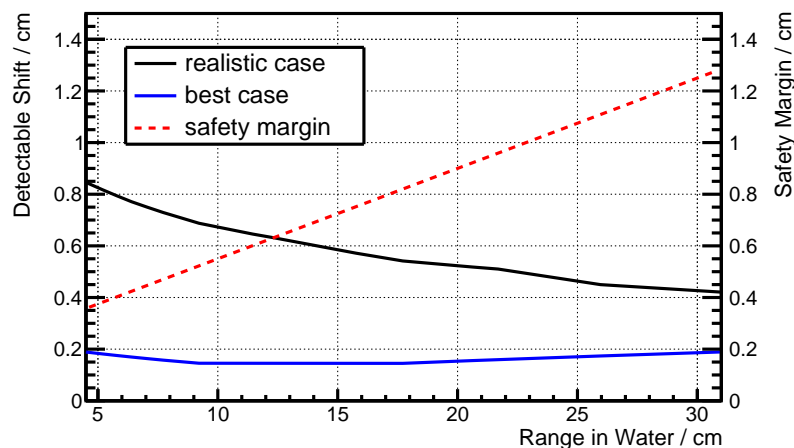


Figure 5.3.10.: Sensitivity of the PGT method under different scenarios as a function of the range in water for GTR2 of UPTD. The safety margin applied at UPTD is shown to identify the treatment cases where a range verification based on PGT would be beneficial.

opposite sites of the target, for determining the beam position within the patient.

In a next step, an air cavity with a thickness of 5 mm could be identified by setting the corresponding PGT data of the distal layer in reference to the results obtained with a homogeneous target. Hence, this resembles the first identification of inhomogeneities based on PGs under clinical beam conditions with an uncollimated detector system. Currently, the number of detected events was artificially increased by the cumulation of several irradiations, however, this problem can be solved by adding the data from several detector units. Corresponding measurements using up to 6 detectors are underway.

In addition to the air cavity, a bone-equivalent insert (thickness 2 cm) could also be imaged. However, an analysis based on PGT information did not lead to a positive result. Alternatively, photon yield data was compared between the measurement with the bone insert and the homogeneous case. Here, an increased number of detected photons was indeed visible at the location of the inserted disc. The results might encourage the combination of PGT data with photon yield determination, as the information is already included in the data. Further test and procedures could be tested already on existing data but have not been performed in the framework of this thesis.

A still unsolved and not verified problem within the PBS measurements are the phase drifts of the proton bunches relative to the RF. The obtained data of a 1 Gy field lacks the sufficient number of events to identify such drifts. Deploying a proton detector is therefore mandatory, however, using classical readout analog electronics seems not reasonable. Nevertheless, the U100 spectrometer could also be deployed to process the signals from a phoswich detector. Even though the required firmware has not been delivered yet, first proton measurements with an U100 system have been conducted using a phoswich detector based on CeBr_3 and BGO. The signals of the

events were read out using the scope mode of the spectrometer. The data analysis was performed offline using variable short and long integration gates to account for both scintillation signals. The results are promising as the individual proton line can be identified and the system could be operated as a PBM in PBS irradiations.

The obtained results of the prototype detector setup encourage the translation of the PGT method toward a clinical application. Future efforts should aim at the correction of different hardware induced artefacts and on the combination of data from multiple detectors for increased sensitivity.

6. Summary

The aim of this work was to bring range verification based on the Prompt Gamma-ray Timing (PGT) method closer to clinical application. In this context, three different topics have been investigated and ultimately been combined:

- 1) To find a suitable scintillation material for a PGT detector with sufficient timing capabilities and detection efficiency.
- 2) The detection and characterization of different beam parameters at the proton therapy system of UPTD.
- 3) The characterization of a PGT prototype detection unit, with special focus on the newly developed readout electronics, as well as the usage under clinical conditions.

Motivated by previous results [93], a dedicated study was conducted to investigate the time resolution of seven scintillation materials. Crystals with different properties have been used like GAGG, BGO, CeBr₃, LYSO, CsI(Tl), GSO, and CaF₂(Eu). While some of them are conventionally used in timing measurements, others, like BGO, CaF₂(Eu), and CsI(Tl), are not considered to have suitable timing properties. However, most experiments are conducted in the context of PET at photon energies of 511 keV. PGs on the other hand are in the region of few MeV resulting in a smaller statistical contribution of the time resolution. To experimentally evaluate the timing capabilities, the novel Digital Photon Counter (DPC) was deployed as it exhibits an excellent intrinsic time resolution and a unique trigger and validation scheme. The scintillator coupled to the DPC were tested at the ELBE accelerator which provides photon energies of up to 12.5 MeV. The results of the study were on one hand in accordance with the theoretical considerations and on the other hand very surprising. First of all, the fast materials CeBr₃, LYSO, and GAGG performed more or less as expected as well as the very slow ones CsI(Tl) and CaF₂(Eu). GSO was seen as an alternative to the conventional materials for timing measurements due to its fast main decay time but exceeded only moderate results. The biggest surprise however was BGO which performed well above the expectations which might be a result of the detection of Cherenkov radiation. In summary, several materials could be used for the PGT method in combination with the DPC as their time resolution is better than the required 250 ps. However, the DPC as light sensor is not yet suitable for a clinical application due to the required cooling and the bandwidth limitation of the setup. Consequently, a PGT prototype system will be based on PMTs as light readout which reduces the number of applicable scintillators. CeBr₃ is hereby the material of choice as it exhibits the best timing properties and has no intrinsic background.

The second topic of this thesis is motivated by the PGT measurements at WPE [12], where several implications like RF-bunch phase drifts and the energy dependency of the Bunch Time Spread (BTS) have been identified. The findings needed further investigation as they interfere with the applicability and the sensitivity of the PGT method. Thus, a Proton Bunch Monitor (PBM) setup comprising two phoswich detectors has been developed to measure and characterize the proton bunches. The obtained data was used to correct PGT spectra for phase drifts and to perform the first 2D imaging of a heterogeneous phantom based on the detection of PGs. In a further experimental study, the BTS and the proton transmission rate were determined as a function of the beam energy and the Momentum Limiting Slit Opening (MLSO). It was shown that the BTS varies over nearly one order of magnitude from the lowest to the highest available beam energy and that it can be partially controlled by reducing the MLSO. However, this has severe consequences for the proton transmission rate as it is reduced by one order of magnitude for the interesting MLSO settings compared to the default value. Hence, the usage of a lower MLSO is desirable as it increases the sensitivity of the PGT method but on the cost of several implications for the beam generation and delivery process. Nevertheless, the obtained results are valuable as input for the simulation of PGT data which can be compared to measurements.

Using the findings from the first two parts of the thesis and by the results and suggested requirements from Hueso-González et al. [12] and Pausch et al. [13], a PGT prototype system based on a CeBr₃ scintillation crystal, a dedicated timing PMT, and the novel digital spectrometer U100 was developed. The device was characterized at the ELBE accelerator concerning throughput rate as well as energy and time resolution. The prototyped performed within the specifications reaching about 230 ps time resolution ($E = 4$ MeV) and 3.5 % energy resolution ($E = 2.506$ MeV). The detector unit is subject to gain variations in dependency of the detector load which might be caused by load depending variations in the HV supply. Two prototypes have been further used in the first uncollimated PG measurement under clinical conditions. In this context, a Pencil Beam Scanning (PBS) plan was delivered on a PMMA target at UPTD. The layer and spot structure of the PBS plan could be identified and PGT data could be obtained. The detectors performed relatively stable, however, again gain variations were visible as a function of the detector load which changes in PBS mode from few kcps to more than 1 Mcps. The PGT data could be further sorted to individual spots and a spot-by-spot analysis was possible like for example the TOF distribution map of the distal layer. As a further result, the number of detected photons was determined and compared to the estimate from Pausch et al. [13], where, considering different effects, a reasonable agreement could be found. The results were also used to predict the sensitivity of a given PGT setup, showing that the detection of range shifts of 5 mm and below is feasible in most cases. In a last step, the detection of actual range variations was tested and indeed a 5 mm air cavity and a 2 cm bone insert could be identified using the measured data, demonstrating the first detection range variations under clinical conditions using an uncollimated detector system.

In conclusion, the presented work helped to develop a PGT prototype system and to potentially adapt the method as range verification in clinical practice.

A. Appendix

A.1. Time Resolution Measurements based on the DPC

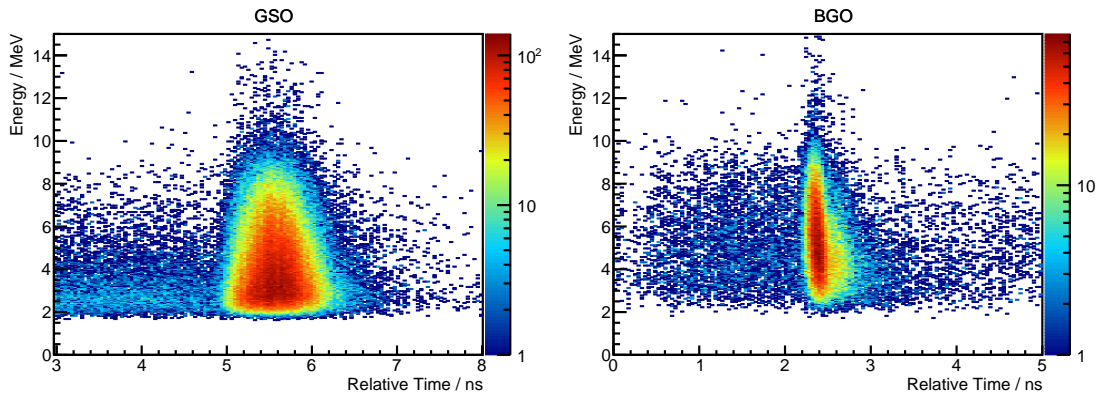


Figure A.1.1.: Energy versus relative time measured with GSO (left) and BGO (right) using FC 2 data. DPC settings are in both cases: TL 1, VS 2, and VL = 44 ns.

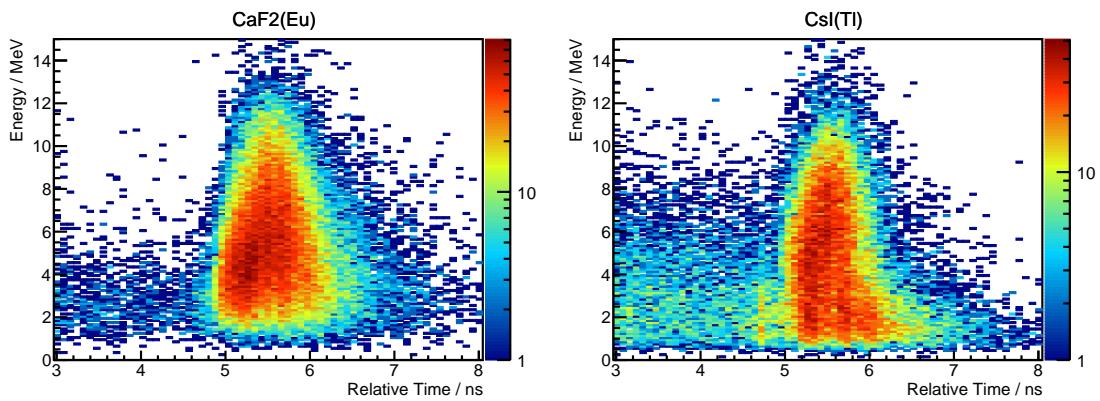


Figure A.1.2.: Energy versus relative time measured with CaF₂(Eu) and CsI(Tl) using FC 2 data measured with different TL and VS settings. Left: CaF₂(Eu) with TL 3, VS 4 and 22 ns VL. Right: CsI(Tl) with TL 2, VS 4 and 44 ns VL.

Table A.1.1.: Part one of the different settings used for the DPC at ELBE like Trigger Level (TL), Validation Scheme (VS), Validation Length (VL), and required number of dies for complete light collection.

TL	VS	VL (ns)	# of required dies
BGO			
1	2	5.5, 11, 22, 44	*, 15, 14, 14
	4	5.5, 11, 22, 44	*, *, *, *
2	8	5.5, 11, 22, 44	*, *, *, *
	16	5.5, 11, 22, 44	*, *, *, *
	4	5.5, 11, 22, 44	*, *, *, 14
	8	5.5, 11, 22, 44	*, *, *, *
3	16	5.5, 11, 22, 44	*, *, *, *
	4	5.5, 11, 22, 44	*, *, *, 14
	8	5.5, 11, 22, 44	*, *, *, *
4	16	5.5, 11, 22, 44	*, *, *, *
	8	5.5, 11, 22, 44	*, *, *, *
	16	5.5, 11, 22, 44	*, *, *, *
LYSO			
1	2	5.5, 11, 22, 44	15, 15, 14, 14
	4	5.5, 11, 22, 44	15, 15, 15, 14
	8	5.5, 11, 22, 44	16, 16, 15, 15
	16	5.5, 11, 22, 44	*, *, 16, 15
2	4	5.5, 11, 22, 44	16, 15, 15, 15
	8	5.5, 11, 22, 44	*, *, 16, 15
	16	5.5, 11, 22, 44	*, *, *, 16
3	4	5.5, 11, 22, 44	16, 16, 16, 15
	8	5.5, 11, 22, 44	*, 16, 16, 16
	16	5.5, 11, 22, 44	*, 16, 16, 16
4	8	5.5, 11, 22, 44	*, *, 16, 16
	16	5.5, 11, 22, 44	*, *, *, 16
GAGG			
1	2	5.5, 11, 22, 44	15, 15, 14, 14
	4	5.5, 11, 22, 44	*, 15, 15, 15
	8	5.5, 11, 22, 44	*, *, 15, 15
	16	5.5, 11, 22, 44	*, *, 16, 15
2	4	5.5, 11, 22, 44	15, 15, 15, 14
	8	5.5, 11, 22, 44	*, *, 16, 15
	16	5.5, 11, 22, 44	*, *, *, 16
3	4	5.5, 11, 22, 44	16,16,15,14
	8	5.5, 11, 22, 44	*, *, 16, 16
	16	5.5, 11, 22, 44	*, *, 16, 16
4	8	5.5, 11, 22, 44	*, *, 16, 16
	16	5.5, 11, 22, 44	*, *, 16, 16

*: no reasonable measurement possible.

Table A.1.2.: Part two of the different settings used for the DPC at ELBE like Trigger Level (TL), Validation Scheme (VS), Validation Length (VL), and required number of dies for complete light collection.

TL	VS	VL (ns)	# of required dies
CeBr₃			
1	2	5.5, 11, 22, 44	15,15,14,14
	4	5.5, 11, 22, 44	15,15,15,14
	8	5.5, 11, 22, 44	15,15,15,14
	16	5.5, 11, 22, 44	*,16,16,14
2	4	5.5, 11, 22, 44	15,15,15,15
	8	5.5, 11, 22, 44	15,15,15,15
	16	5.5, 11, 22, 44	*, 16,16,15
3	4	5.5, 11, 22, 44	16,16,16,15
	8	5.5, 11, 22, 44	16,16,16,16
	16	5.5, 11, 22, 44	16,16,16,16
4	8	5.5, 11, 22, 44	16,16,16,15
	16	5.5, 11, 22, 44	16,16,16,16
GSO			
1	2	5.5, 11, 22, 44	14, 14, 13, 13
	4	5.5, 11, 22, 44	*, *, 15, 14
	8	5.5, 11, 22, 44	*, *, *, *
	16	5.5, 11, 22, 44	*, *, *, *
2	4	5.5, 11, 22, 44	*, *, 16, 15
	8	5.5, 11, 22, 44	*, *, *, *
	16	5.5, 11, 22, 44	*, *, *, *
3	4	5.5, 11, 22, 44	*, *, 16, 16
	8	5.5, 11, 22, 44	*, *, *, *
	16	5.5, 11, 22, 44	*, *, *, *
4	8	5.5, 11, 22, 44	*, *, *, 16
	16	5.5, 11, 22, 44	*, *, *, *
CsI(Tl)			
1	2	5.5, 11, 22, 44	*, *, *, *
	4	5.5, 11, 22, 44	*, *, *, *
	8	5.5, 11, 22, 44	*, *, *, *
	16	5.5, 11, 22, 44	*, *, *, *
2	4	5.5, 11, 22, 44	*, *, 16, 15
	8	5.5, 11, 22, 44	*, *, *, *
	16	5.5, 11, 22, 44	*, *, *, *
3	4	5.5, 11, 22, 44	*, *, 16, 15
	8	5.5, 11, 22, 44	*, *, *, *
	16	5.5, 11, 22, 44	*, *, *, *
4	8	5.5, 11, 22, 44	*, 16, 16, 16
	16	5.5, 11, 22, 44	*, *, *, *

*: no reasonable measurement possible.

Table A.1.3.: Part three of the different settings used for the DPC at ELBE like Trigger Level (TL), Validation Scheme (VS), Validation Length (VL), and required number of dies for complete light collection.

TL	VS	VL (ns)	# of required dies
CaF₂(Eu)			
1	2	5.5, 11, 22, 44	*, *, *, *
	4	5.5, 11, 22, 44	*, *, *, *
	8	5.5, 11, 22, 44	*, *, *, *
	16	5.5, 11, 22, 44	*, *, *, *
2	4	5.5, 11, 22, 44	*, *, 16, 16
	8	5.5, 11, 22, 44	*, *, *, *
	16	5.5, 11, 22, 44	*, *, *, *
3	4	5.5, 11, 22, 44	*, *, 16, 16
	8	5.5, 11, 22, 44	*, *, *, *
	16	5.5, 11, 22, 44	*, *, *, *
4	8	5.5, 11, 22, 44	*, *, *, *
	16	5.5, 11, 22, 44	*, *, *, *

*: no reasonable measurement possible.

A.2. PGT under Clinical Conditions

Table A.2.1.: Layer structure of the dose cube plan including beam energy, range in PMMA, number of pencil beam spots, and relative dose with respect to the full field.

Layer ID	Energy (MeV)	Range in PMMA (cm)	# of Spots	Rel. Dose (%)
1	162.32	15.8	235	32.9
2	159.70	15.3	221	6.3
3	157.11	14.9	253	8.7
4	154.63	14.5	265	5.8
5	152.24	14.1	269	4.8
6	149.86	13.7	273	4.5
7	147.52	13.3	277	4.0
8	145.25	13.0	277	3.5
9	143.02	12.6	277	3.2
10	140.75	12.3	279	3.0
11	138.52	11.9	278	3.1
12	136.32	11.6	219	2.1
13	134.09	11.3	249	2.8
14	131.89	11.0	206	2.2
15	129.72	10.6	228	2.1
16	127.58	10.3	240	1.9
17	125.61	10.1	253	1.8
18	123.73	9.8	259	1.8
19	121.90	9.5	260	1.8
20	120.04	9.3	119	0.9
21	118.16	9.0	195	1.7
22	116.26	8.8	166	1.1

Table A.2.2.: List of delivered PBS plans and the corresponding target settings for both detectors.

Detector	Insert	Thickness t (cm)	Depth a (cm)	Dose (Gy)	# of Irradiations
p0006	air cavity	1	11	1	1
	air cavity	1	14	1	2
	SB3 bone	2	11	1	5
	air cavity	0.5	11	1	4
	PMMA	-	-	1	5
	air cavity	1	11	5	1*
	air cavity	1	14	5	1
	PMMA	-	-	5	1
p0007	air cavity	1	11	1	2
	air cavity	1	14	1	1
	SB3 bone	2	11	1	4
	air cavity	0.5	11	1	5
	PMMA	-	-	1	5
	air cavity	1	11	5	2
	air cavity	1	14	5	1
	PMMA	-	-	5	1

*: not completely irradiated due to interlocks.

Bibliography

- [1] H. Bethe. Bremsformel für Elektronen relativistischer Geschwindigkeit. *Zeitschrift für Physik*, 76(5):293, 1932. URL: <http://dx.doi.org/10.1007/BF01342532>.
- [2] F. Bloch. Zur Bremsung rasch bewegter Teilchen beim Durchgang durch Materie. *Annalen der Physik*, 408(3):285, 1933. URL: <http://dx.doi.org/10.1002/andp.19334080303>.
- [3] W. H. Barkas, J. N. Dyer, and H. H. Heckman. Resolution of the Σ^- -mass anomaly. *Phys. Rev. Lett.*, 11:26, 1963. URL: <http://link.aps.org/doi/10.1103/PhysRevLett.11.26>.
- [4] J. M. Verburg. *Reducing Range Uncertainty in Proton Therapy*. PhD thesis, Harvard Medical School, 2015. URL: https://pure.tue.nl/ws/files/9353099/20151120_Verburg.pdf.
- [5] M. J. Berger, J. S. Coursey, M. A. Zucker, and J. Chang. ESTAR, PSTAR, and ASTAR: Stopping-Power and Range Tables for Electrons, Protons, and Helium Ions. *NIST*, 2015. URL: <http://www.nist.gov/pml/data/star/index.cfm>.
- [6] R. R. Wilson. Radiological use of fast protons. *Radiology*, 47(5):487, 1946. URL: <http://dx.doi.org/10.1148/47.5.487>, arXiv:<http://dx.doi.org/10.1148/47.5.487>.
- [7] J. H. Lawrence. Proton irradiation of the pituitary. *Cancer*, 10(4):795, 1957. URL: [http://dx.doi.org/10.1002/1097-0142\(195707/08\)10:4<795::AID-CNCR2820100426>3.0.CO;2-B](http://dx.doi.org/10.1002/1097-0142(195707/08)10:4<795::AID-CNCR2820100426>3.0.CO;2-B).
- [8] PTCOG. Patient statistics. *Particle Therapy Co-Operative Group*, 2014. available at http://www.ptcog.ch/archive/patient_statistics/Patientstatistics-updateMar2014.pdf, accessed May 2016.
- [9] T. Kanai, K. Kawachi, Y. Kumamoto, H. Ogawa, T. Yamada, H. Matsuzawa, and T. Inada. Spot scanning system for proton radiotherapy. *Med Phys*, 7(4):365, 1980. URL: <http://scitation.aip.org/content/aapm/journal/medphys/7/4/10.1118/1.594693>.
- [10] PTCOG. Facilities in operation. *Particle Therapy Co-Operative Group*, 2016. available at <http://www.ptcog.ch/index.php/facilities-in-operation>, accessed May 2016.
- [11] C. Golnik. *Treatment verification in proton therapy based on the detection of prompt gamma-rays*. PhD thesis, Technische Universität Dresden, 2016.

- [12] F. Hueso-González, W. Enghardt, F. Fiedler, C. Golnik, G. Janssens, J. Petzoldt, D. Prieels, M. Priegnitz, K. E. Römer, J. Smeets, F. Vander Stappen, A. Wagner, and G. Pausch. First test of the prompt gamma ray timing method with heterogeneous targets at a clinical proton therapy facility. *Phys Med Biol*, 60(16):6247, 2015. URL: <http://stacks.iop.org/0031-9155/60/i=16/a=6247>.
- [13] G. Pausch, J. Petzoldt, M. Berthel, W. Enghardt, F. Fiedler, C. Golnik, F. Hueso-González, R. Lentering, K. Römer, K. Ruhnu, J. Stein, A. Wolf, and T. Kormoll. Scintillator-based high-throughput fast timing spectroscopy for real-time range verification in particle therapy. *Trans Nucl Sci*, 63(2):664, 2016. URL: <http://dx.doi.org/10.1109/TNS.2016.2527822>.
- [14] H. Paganetti. Range uncertainties in proton therapy and the role of monte carlo simulations. *Phys Med Biol*, 57(11):R99, 2012. URL: <http://stacks.iop.org/0031-9155/57/i=11/a=R99>.
- [15] N. Matsufuji, H. Tomura, Y. Futami, H. Yamashita, A. Higashi, S. Minohara, M. Endo, and T. Kanai. Relationship between CT number and electron density, scatter angle and nuclear reaction for hadron-therapy treatment planning. *Phys Med Biol*, 43(11):3261, 1998. URL: <http://stacks.iop.org/0031-9155/43/i=11/a=007>.
- [16] B. Schaffner and E. Pedroni. The precision of proton range calculations in proton radiotherapy treatment planning: experimental verification of the relation between CT-HU and proton stopping power. *Phys Med Biol*, 43(6):1579, 1998. URL: <http://stacks.iop.org/0031-9155/43/i=6/a=016>.
- [17] A. V. Chvetsov and S. L. Paige. The influence of CT image noise on proton range calculation in radiotherapy planning. *Phys Med Biol*, 55(6):N141, 2010. URL: <http://stacks.iop.org/0031-9155/55/i=6/a=N01>.
- [18] S. Espana and H. Paganetti. Uncertainties in planned dose due to the limited voxel size of the planning CT when treating lung tumors with proton therapy. *Phys Med Biol*, 56(13):3843, 2011. URL: <http://stacks.iop.org/0031-9155/56/i=13/a=007>.
- [19] R. A. Rutherford, B. R. Pullan, and I. Isherwood. Measurement of effective atomic number and electron density using an EMI scanner. *Neuroradiology*, 11(1):15, 1976. URL: <http://dx.doi.org/10.1007/BF00327253>.
- [20] N. Hünemohr, B. Krauss, C. Tremmel, B. Ackermann, O. Jäkel, and S. Greilich. Experimental verification of ion stopping power prediction from dual energy CT data in tissue surrogates. *Phys Med Biol*, 59(1):83, 2014. URL: <http://stacks.iop.org/0031-9155/59/i=1/a=83>.

- [21] M. Bucciantonio and F. Sauli. Proton computed tomography. *Mod Phys Lett A*, 30(17):1540024, 2015. URL: <http://www.worldscientific.com/doi/abs/10.1142/S0217732315400246>.
- [22] W. Enghardt, P. Crespo, F. Fiedler, R. Hinz, K. Parodi, J. Pawelke, and F. Pönisch. Charged hadron tumour therapy monitoring by means of PET. *Nucl Instr Meth Phys Res A*, 525(1-2):284, 2004. URL: <http://www.sciencedirect.com/science/article/pii/S0168900204004218>.
- [23] S. Helmbrecht, W. Enghardt, K. Parodi, B. Didingler, J. Debus, D. Kunath, M. Priegnitz, and F. Fiedler. Analysis of metabolic washout of positron emitters produced during carbon ion head and neck radiotherapy. *Med Phys*, 40(9):091918, 2013. URL: <http://scitation.aip.org/content/aapm/journal/medphys/40/9/10.1118/1.4818424>.
- [24] W. Enghardt, K. Parodi, P. Crespo, F. Fiedler, J. Pawelke, and F. Pönisch. Dose quantification from in-beam positron emission tomography. *Radiother Oncol*, 73, Supplement 2:S96, 2004. URL: <http://www.sciencedirect.com/science/article/pii/S0167814004800240>.
- [25] F. Fiedler, G. Shakirin, J. Skowron, H. Braess, P. Crespo, D. Kunath, J. Pawelke, F. Pönisch, and W. Enghardt. On the effectiveness of ion range determination from in-beam PET data. *Phys Med Biol*, 55(7):1989, 2010. URL: <http://stacks.iop.org/0031-9155/55/i=7/a=013>.
- [26] T. Kormoll, W. Enghardt, F. Fiedler, M. Iltzsche, G. Pausch, C. Tintori, and S. Helmbrecht. M04b-1: In-beam PET with pulse shape discrimination at a clinical cyclotron facility. In *Presentation at the IEEE Medical Imaging Conference 2016 in Strasbourg*, 2016.
- [27] S. Helmbrecht, W. Enghardt, F. Fiedler, M. Iltzsche, G. Pausch, C. Tintori, and T. Kormoll. In-beam PET at clinical proton beams with pile-up rejection. *Z Med Phys*, 2016. In Press. URL: <http://www.sciencedirect.com/science/article/pii/S0939388916300587>.
- [28] S. E. Combs, O. Jäkel, T. Haberer, and J. Debus. Particle therapy at the Heidelberg Ion Therapy Center (HIT) - Integrated research-driven university-hospital-based radiation oncology service in Heidelberg, Germany. *Radiother Oncol*, 95(1):41, 2010. URL: <http://www.sciencedirect.com/science/article/pii/S016781401000109X>.
- [29] T. Nishio, A. Miyatake, T. Ogino, K. Nakagawa, N. Saijo, and H. Esumi. The development and clinical use of a beam on-line PET system mounted on a rotating gantry port in proton therapy. *Int J Radiat Oncol Biol Phys*, 76(1):277, 2010. URL: <http://www.sciencedirect.com/science/article/pii/S0360301609009213>.
- [30] K. Parodi, H. Paganetti, H. A. Shih, S. Michaud, J. S. Loeffler, T. F. DeLaney, N. J. Liebsch, J. E. Munzenrider, A. J. Fischman, A. Knopf, and T. Bortfeld. Patient study of in vivo

- verification of beam delivery and range, using positron emission tomography and computed tomography imaging after proton therapy. *Int J Radiat Oncol Biol Phys*, 68(3):920, 2007. URL: <http://www.sciencedirect.com/science/article/pii/S036030160700377X>.
- [31] C. H. Min, X. Zhu, B. A. Winey, . Grogg, M. Testa, G. El Fakhri, T. Bortfeld, H. Paganetti, and H. A. Shih. Clinical application of in-room positron emission tomography for in vivo treatment monitoring in proton radiation therapy. *Int J Radiat Oncol Biol Phys*, 86(1):183, 2013. URL: <http://www.sciencedirect.com/science/article/pii/S0360301612039065>.
- [32] A. Schumann, J. Petzoldt, P. Dendooven, W. Enghardt, C. Golnik, F. Hueso-González, T. Kormoll, G. Pausch, K. Roemer, and F. Fiedler. Simulation and experimental verification of prompt gamma-ray emissions during proton irradiation. *Phys Med Biol*, 60(10):4197, 2015. URL: <http://stacks.iop.org/0031-9155/60/i=10/a=4197>.
- [33] C. H. Min, C. H. Kim, M. Y. Youn, and J. W. Kim. Prompt gamma measurements for locating the dose falloff region in the proton therapy. *Appl Phys Lett*, 89(18):3517, 2006. URL: <http://scitation.aip.org/content/aip/journal/apl/89/18/10.1063/1.2378561>.
- [34] J. M. Verburg, K. Riley, T. Bortfeld, and J. Seco. Energy- and time-resolved detection of prompt gamma-rays for proton range verification. *Phys Med Biol*, 58(20):L37, 2013. URL: <http://stacks.iop.org/0031-9155/58/i=20/a=L37>.
- [35] F. Stichelbaut and Y. Jongen. Verification of the proton beam position in the patient by the detection of prompt gamma-rays emission. In *Presentation at the 39th Particle Therapy Co-Operative Group (PTCOG) in San Francisco*, 2003.
- [36] T. Kormoll, F. Fiedler, S. Schöne, J. Wüstemann, K. Zuber, and W. Enghardt. A Compton imager for in-vivo dosimetry of proton beams - a design study. *Nucl Instr Meth Phys Res A*, 626-627(0):114, 2011. URL: <http://www.sciencedirect.com/science/article/pii/S0168900210022709>.
- [37] C. Golnik, D. Bemmerer, W. Enghardt, F. Fiedler, F. Hueso-González, G. Pausch, K. Römer, H. Rohling, S. Schöne, L. Wagner, and T. Kormoll. Tests of a Compton imaging prototype in a monoenergetic 4.44 MeV photon field - benchmark setup for prompt gamma-ray imaging devices. *J Instrum*, 11(06):P06009, 2016. URL: <http://stacks.iop.org/1748-0221/11/i=06/a=P06009>.
- [38] H. Seo, J. H. Park, A. Ushakov, C. H. Kim, J. K. Kim, J. H. Lee, C. S. Lee, and J. S. Lee. Experimental performance of double-scattering Compton camera with anthropomorphic phantom. *J Instrum*, 6(01):C01024, 2011. URL: <http://dx.doi.org/10.1088/1748-0221/6/01/C01024>.

- [39] S. Kurosawa, H. Kubo, K. Ueno, S. Kabuki, S. Iwaki, M. Takahashi, K. Taniue, N. Higashi, K. Miuchi, T. Tanimori, D. Kim, and J. Kim. Prompt gamma detection for range verification in proton therapy. *Curr Appl Phys*, 12(2):364, 2012. URL: <http://dx.doi.org/10.1016/j.cap.2011.07.027>.
- [40] G. Llosá, J. Cabello, S. Callier, J.E. Gillam, C. Lacasta, M. Rafecas, L. Raux, C. Solaz, V. Stankova, C. de La Taille, M. Trovato, and J. Barrio. First Compton telescope prototype based on continuous LaBr₃-SiPM detectors. *Nucl Instr Meth Phys Res A*, 718(0):130, 2013. URL: <http://dx.doi.org/10.1016/j.nima.2012.08.074>.
- [41] J. Krimmer, J. L. Ley, C. Abellan, J. P. Cachemiche, L. Caponetto, X. Chen, M. Dahoumane, D. Dauvergne, N. Freud, B. Joly, D. Lambert, L. Lestand, J. M. Létang, M. Magne, H. Mathez, V. Maxim, G. Montarou, C. Morel, M. Pinto, C. Ray, V. Reithinger, E. Testa, and Y. Zoccarato. Development of a Compton camera for medical applications based on silicon strip and scintillation detectors. *Nucl Instr Meth Phys Res A*, 787:98, 2014. URL: <http://dx.doi.org/10.1016/j.nima.2014.11.042>.
- [42] P.G. Thirolf, C. Lang, S. Aldawood, H.G. v.d. Kolff, L. Maier, D.R. Schaart, and K. Parodi. Development of a Compton camera for online range monitoring of laser-accelerated proton beams via prompt-gamma detection. *EPJ Web of Conferences*, (66):11036, 2014. URL: <http://dx.doi.org/10.1051/epjconf/20146611036>.
- [43] J. C. Polf, S. Avery, D. S. Mackin, and S. Beddar. Imaging of prompt gamma rays emitted during delivery of clinical proton beams with a Compton camera: feasibility studies for range verification. *Phys Med Biol*, 60(18):7085, 2015. URL: <http://stacks.iop.org/0031-9155/60/i=18/a=7085>.
- [44] F. Hueso-González, G. Pausch, J. Petzoldt, K. E. Roemer, and W. Enghardt. Prompt gamma rays detected with a BGO block Compton camera reveal range deviations of therapeutic proton beams. *Trans Rad Plas Med Sci*, 2016. accepted.
- [45] D. Kim, H. Yim, and J. Kim. Pinhole camera measurements of prompt γ -rays for detection of beam range variation in proton therapy. *J Korean Phys Soc*, 55(4):1673, 2009. URL: http://old.kps.or.kr/jkps/abstract_view.asp?articleid=12876DD7-938D-4F89-A349-D67C49C363FB.
- [46] J. Smeets, F. Roellinghoff, D. Prieels, F. Stichelbaut, A. Benilov, P. Busca, C. Fiorini, R. Peloso, M. Basilavecchia, T. Frizzi, J. C. Dehaes, and A. Dubus. Prompt gamma imaging with a slit camera for real-time range control in proton therapy. *Phys Med Biol*, 57(11):3371, 2012. URL: <http://stacks.iop.org/0031-9155/57/i=11/a=3371>.
- [47] J. Ready, R. Pak, L. Mihailescu, and K. Vetter. Development of a multi-knife-edge slit collimator for prompt gamma imaging during proton beam therapy. In *Presentation at the IEEE Medical Imaging Conference 2015 San Diego*, 2015.

- [48] C. Richter, G. Pausch, S. Barczyk, M. Priegnitz, I. Keitz, J. Thiele, J. Smeets, F. Vander Stappen, L. Bombelli, C. Fiorini, L. Hotoiu, I. Perali, D. Prieels, W. Enghardt, and M. Baumann. First clinical application of a prompt gamma based in vivo proton range verification system. *Radiother Oncol*, 2016. available online. URL: <http://www.sciencedirect.com/science/article/pii/S0167814016000074>.
- [49] M. Priegnitz, S. Helmbrecht, G. Janssens, I. Perali, J. Smeets, F. Vander Stappen, E. Sterpin, and F. Fiedler. Measurement of prompt gamma profiles in inhomogeneous targets with a knife-edge slit camera during proton irradiation. *Phys Med Biol*, 60(12):4849, 2015. URL: <http://stacks.iop.org/0031-9155/60/i=12/a=4849>.
- [50] J. M. Verburg and J. Seco. Proton range verification through prompt gamma-ray spectroscopy. *Phys Med Biol*, 59(23):7089, 2014. URL: <http://stacks.iop.org/0031-9155/59/i=23/a=7089>.
- [51] C. Golnik, F. Hueso-González, A. Müller, P. Dendooven, W. Enghardt, F. Fiedler, T. Kormoll, K. Roemer, J. Petzoldt, A. Wagner, and G. Pausch. Range assessment in particle therapy based on prompt γ -ray timing measurements. *Phys Med Biol*, 59(18):5399, 2014. URL: <http://stacks.iop.org/0031-9155/59/i=18/a=5399>.
- [52] E. Testa, M. Bajard, M. Chevallier, D. Dauvergne, F. Le Foulher, N. Freud, J.M. Létang, J.C. Poizat, C. Ray, and M. Testa. Dose profile monitoring with carbon ions by means of prompt-gamma measurements. *Nucl Instr Meth Phys Res B*, 267(6):993, 2009. URL: <http://www.sciencedirect.com/science/article/pii/S0168583X09002468>.
- [53] J. M. Verburg. O09: A clinical prompt gamma-ray spectroscopy system for proton range verification. In *Presentation at the 55th Particle Therapy Co-Operative Group (PTCOG) in Prague*, 2016.
- [54] G. F. Knoll. *Radiation Detection and Measurement*. Wiley, 4th edition, 2010.
- [55] P. Dendooven, H.J.T. Buitenhuis, F. Diblen, A.K. Biegun, F. Fiedler, M.-J. van Goethem, E.R. van der Graaf, and S. Brandenburg. Short-lived positron emitters in beam-on PET imaging during proton therapy. *Radiother Oncol*, 118(Supplement 1):S17, 2016. URL: [http://dx.doi.org/10.1016/S0167-8140\(16\)30034-2](http://dx.doi.org/10.1016/S0167-8140(16)30034-2).
- [56] E. Sheldon and D. M. Van Patter. Compound inelastic nucleon and gamma-ray angular distributions for even- and odd-mass nuclei. *Rev Mod Phys*, 38:143, 1966. URL: <http://link.aps.org/doi/10.1103/RevModPhys.38.143>.
- [57] B. Kozlovsky, R. J. Murphy, and R. Ramaty. Nuclear deexcitation gamma-ray lines from accelerated particle interactions. *Astrophys J Suppl Ser*, 141(2):523, 2002. URL: <http://stacks.iop.org/0067-0049/141/i=2/a=523>.

- [58] R.R. Kinsey, C.L. Dunford, J.K. Tuli, and T.W. Burrows. *The NUDAT/PCNUDAT program for nuclear data*. 1996. URL: <http://www.osti.gov/scitech/servlets/purl/380330>.
- [59] J. C. Polf, S. Peterson, M. McCleskey, B. T. Roeder, A. Spiridon, S. Beddar, and L. Trache. Measurement and calculation of characteristic prompt gamma ray spectra emitted during proton irradiation. *Phys Med Biol*, 54(22):N519, 2009. URL: <http://stacks.iop.org/0031-9155/54/i=22/a=N02>.
- [60] A. H. Kazi, N. C. Rasmussen, and H. Mark. Measurement of the deuteron binding energy using a Bent-Crystal spectrograph. *Phys Rev*, 123:1310, 1961. URL: <http://link.aps.org/doi/10.1103/PhysRev.123.1310>.
- [61] A. B. Clegg, K. J. Foley, G. L. Salmon, and R. E. Segel. Gamma radiation from the medium energy proton bombardment of lithium, beryllium, boron, carbon and nitrogen. *Proceedings of the Physical Society*, 78(5):681, 1961. URL: <http://stacks.iop.org/0370-1328/78/i=5/a=305>.
- [62] K.J. Foley, G.L. Salmon, and A.B. Clegg. Gamma radiation from the bombardment of ^{16}O and ^{19}F nuclei with 150 MeV protons. *Nucl Phys*, 31:43, 1962. URL: <http://www.sciencedirect.com/science/article/pii/0029558262907277>.
- [63] P. Dyer, D. Bodansky, A. G. Seamster, E. B. Norman, and D. R. Maxson. Cross sections relevant to gamma-ray astronomy: Proton induced reactions. *Phys Rev C*, 23:1865, 1981. URL: <http://link.aps.org/doi/10.1103/PhysRevC.23.1865>.
- [64] J. Narayanaswamy, P. Dyer, S. R. Faber, and Sam M. Austin. Production of 6.13 MeV gamma rays from the $^{16}\text{O}(p,p'\gamma)^{16}\text{O}$ reaction at 23.7 and 44.6 MeV. *Phys Rev C*, 24:2727, 1981. URL: <http://link.aps.org/doi/10.1103/PhysRevC.24.2727>.
- [65] F. L. Lang, C. W. Werntz, C. J. Crannell, J. I. Trombka, and C. C. Chang. Cross sections for production of the 15.10 MeV and other astrophysically significant gamma-ray lines through excitation and spallation of ^{12}C and ^{16}O with protons. *Phys Rev C*, 35:1214, 1987. URL: <http://link.aps.org/doi/10.1103/PhysRevC.35.1214>.
- [66] J. Kiener, M. Berheide, N. L. Achouri, A. Boughrara, A. Coc, A. Lefebvre, F. de Oliveira Santos, and Ch. Vieu. γ -ray production by inelastic proton scattering on ^{16}O and ^{12}C . *Phys Rev C*, 58:2174, 1998. URL: <http://link.aps.org/doi/10.1103/PhysRevC.58.2174>.
- [67] A. Belhout, J. Kiener, A. Coc, J. Duprat, C. Engrand, C. Fitoussi, M. Gounelle, A. Lefebvre-Schuhl, N. de Séréville, V. Tatischeff, J. P. Thibaud, M. Chabot, F. Hammache, and H. Benhabiles-Mezhoud. γ -ray production by proton and α -particle induced reactions on ^{12}C , ^{16}O , ^{24}Mg , and Fe. *Phys Rev C*, 76:034607, 2007. URL: <http://link.aps.org/doi/10.1103/PhysRevC.76.034607>.

- [68] J. M. Verburg, H. A. Shih, and J. Seco. Simulation of prompt gamma-ray emission during proton radiotherapy. *Phys Med Biol*, 57(17):5459, 2012. URL: <http://stacks.iop.org/0031-9155/57/i=17/a=5459>.
- [69] S.E. Derenzo, M.J. Weber, E. Bourret-Courchesne, and M.K. Klintonberg. The quest for the ideal inorganic scintillator. *Nucl Instr Meth Phys Res A*, 505(1 - 2):111, 2003. URL: <http://www.sciencedirect.com/science/article/pii/S0168900203010313>.
- [70] A. A. Annenkov, M. V. Korzhik, and P. Lecoq. Lead tungstate scintillation material. *Nucl Instr Meth Phys Res A*, 490(1-2):30, 2002. URL: <http://www.sciencedirect.com/science/article/pii/S0168900202009166>.
- [71] E. V. van Loef, C. M. Wilson, N. J. Cherepy, G. Hull, S. A. Payne, W. S. Choong, W. W. Moses, and K. S. Shah. Crystal growth and scintillation properties of strontium iodide scintillators. *IEEE Trans Nucl Sci*, 56(3):869, 2009. URL: <http://dx.doi.org/10.1109/TNS.2009.2013947>.
- [72] Y. Shao. A new timing model for calculating the intrinsic timing resolution of a scintillator detector. *Phys Med Biol*, 52(4):1103, 2007. URL: <http://stacks.iop.org/0031-9155/52/i=4/a=016>.
- [73] M. Moszynski, C. Gresset, J. Vacher, and R. Odru. Timing properties of BGO scintillator. *Nucl Instr Meth Phys Res*, 188(2):403, 1981. URL: <http://www.sciencedirect.com/science/article/pii/0029554X81905218>.
- [74] I. Holl, E. Lorenz, and G. Mageras. A measurement of the light yield of common inorganic scintillators. *IEEE Trans Nucl Sci*, 35(1):105, 1988. URL: <http://dx.doi.org/10.1109/23.12684>.
- [75] F. Daghighian, P. Shenderov, K. S. Pentlow, M. C. Graham, B. Eshaghian, C. L. Melcher, and J. S. Schweitzer. Evaluation of cerium doped lutetium oxyorthosilicate (LSO) scintillation crystals for PET. *IEEE Trans Nucl Sci*, 40(4):1045, 1993. URL: <http://dx.doi.org/10.1109/NSSMIC.1992.301022>.
- [76] M. Moszynski, T. Ludziejewski, D. Wolski, W. Klamra, and V.V. Avdeychikov. Timing properties of GSO, LSO and other Ce doped scintillators. *Nucl Instr Meth Phys Res A*, 372(1-2):51, 1996. URL: <http://www.sciencedirect.com/science/article/pii/S0168900295012443>.
- [77] L. Pidol, A. Kahn-Harari, B. Viana, E. Virey, B. Ferrand, P. Dorenbos, J. T. M. de Haas, and C. W. E. van Eijk. High efficiency of lutetium silicate scintillators, Ce-doped LPS, and LYSO crystals. *IEEE Trans Nucl Sci*, 51(3):1084, 2004. URL: <http://dx.doi.org/10.1109/TNS.2004.829542>.

- [78] M. Balcerzyk, M. Moszynski, and M. Kapusta. Comparison of $\text{LaCl}_3\text{:Ce}$ and NaI(Tl) scintillators in gamma-ray spectrometry. *Nucl Instr Meth Phys Res A*, 537(1):50, 2005. URL: <http://www.sciencedirect.com/science/article/pii/S0168900204017814>.
- [79] K. Roemer, G. Pausch, D. Bemmerer, M. Berthel, A. Dreyer, C. Golnik, F. Hueso-González, T. Kormoll, J. Petzoldt, H. Rohling, P. Thirof, A. Wagner, L. Wagner, D. Weinberger, and F. Fiedler. Characterization of scintillator crystals for usage as prompt gamma monitors in particle therapy. *J Instrum*, 10:P10033, 2015. URL: <http://iopscience.iop.org/article/10.1088/1748-0221/10/10/P10033>.
- [80] K. Kamada, T. Yanagida, T. Endo, K. Tsutumi, Y. Usuki, M. Nikl, Y. Fujimoto, and A. Yoshikawa. 2-inch size single crystal growth and scintillation properties of new scintillator; $\text{Ce:Gd}_3\text{Al}_2\text{Ga}_3\text{O}_{12}$. In *IEEE Nuclear Science Symposium and Medical Imaging Conference (NSS/MIC) 2011 in Valencia*, page 1927, 2011. URL: <http://dx.doi.org/10.1109/NSSMIC.2011.6154387>.
- [81] F. R. Schneider, K. Shimazoe, I. Somlai-Schweiger, and S. IZiegler. A PET detector prototype based on digital SiPMs and GAGG scintillators. *Phys Med Biol*, 60(4):1667, 2015. URL: <http://stacks.iop.org/0031-9155/60/i=4/a=1667>.
- [82] P. Schotanus. Development and application of novel scintillators on an industrial scale. In *Presentation at the Workshop on the Applications of Novel Scintillators for Research and Industry*, 2015. available at ssmr.ucd.ie/ansri2015/talks/Monday/Schotanus.pdf, accessed August 2016.
- [83] Furukawa. *Datasheet on GAGG*. available at www.furukawa-denshi.co.jp/cgi-bin/pdfdata/20140428162950.pdf, accessed August 2016.
- [84] Hellma Materials. *Datasheet on CeBr_3* . available at http://www.hellma-materials.com/html/seiten/output_adb_file.php?id=63, accessed August 2016.
- [85] S. Gundacker, F. Acerbi, E. Auffray, A. Ferri, A. Gola, M.V. Nemallapudi, G. Paternoster, C. Piemonte, and P. Lecoq. State of the art timing in TOF-PET detectors with LuAG, GAGG and L(Y)SO scintillators of various sizes coupled to FBK-SiPMs. *J Instrum*, 11(08):P08008, 2016. URL: <http://stacks.iop.org/1748-0221/11/i=08/a=P08008>.
- [86] M. Moszynski. Inorganic scintillation detectors in gamma-ray spectrometry. *Nucl Instr Meth Phys Res A*, 505(1-2):101, 2003. URL: <http://www.sciencedirect.com/science/article/pii/S0168900203010301>.
- [87] W.-S. Choong. The timing resolution of scintillation-detector systems: Monte Carlo analysis. *Phys Med Biol*, 54(21):6495, 2009. URL: <http://stacks.iop.org/0031-9155/54/i=21/a=004>.

- [88] S E. Derenzo, W.-S. Choong, and W. W. Moses. Fundamental limits of scintillation detector timing precision. *Phys Med Biol*, 59(13):3261, 2014. URL: <http://stacks.iop.org/0031-9155/59/i=13/a=3261>.
- [89] R. F. Post and L. I. Schiff. Statistical limitations on the resolving time of a scintillation counter. *Phys Rev*, 80:1113, 1950. URL: <http://link.aps.org/doi/10.1103/PhysRev.80.1113>.
- [90] L. G. Hyman. Time resolution of photomultiplier systems. *Rev Sci Instrum*, 36(2):193, 1965. URL: <http://scitation.aip.org/content/aip/journal/rsi/36/2/10.1063/1.1719516>.
- [91] S. Seifert, H. T. van Dam, and D. R. Schaart. The lower bound on the timing resolution of scintillation detectors. *Phys Med Biol*, 57(7):1797, 2012. URL: <http://stacks.iop.org/0031-9155/57/i=7/a=1797>.
- [92] M. V. Nemallapudi, S. Gundacker, P. Lecoq, E. Auffray, A. Ferri, A. Gola, and C. Piemonte. Sub-100 ps coincidence time resolution for positron emission tomography with LSO:Ce codoped with Ca. *Phys Med Biol*, 60(12):4635, 2015. URL: <http://stacks.iop.org/0031-9155/60/i=12/a=4635>.
- [93] F. Hueso-González, A.K. Biegun, P. Dendooven, W. Enghardt, F. Fiedler, C. Golnik, K. Heidel, T. Kormoll, J. Petzoldt, K.E. Römer, R. Schwengner, A. Wagner, and G. Pausch. Comparison of LSO and BGO block detectors for prompt gamma imaging in ion beam therapy. *J Instrum*, 10(09):P09015, 2015. URL: <http://stacks.iop.org/1748-0221/10/i=09/a=P09015>.
- [94] T. Szczesniak, M. Grodzicka, M. Moszynski, M. Szawlowski, D. Wolski, and J. Baszak. Characteristics of scintillation detectors based on inorganic scintillators and SiPM light readout. *Nucl Instr Meth Phys Res A*, 702:91, 2013. URL: <http://www.sciencedirect.com/science/article/pii/S0168900212010261>.
- [95] C. Degenhardt, G. Prescher, T. Frach, A. Thon, R. de Gruyter, A. Schmitz, and R. Ballizany. The digital silicon photomultiplier - a novel sensor for the detection of scintillation light. In *IEEE Nuclear Science Symposium Conference Record (NSS/MIC) 2009 in Orlando*, page 2383, 2009. URL: <http://dx.doi.org/10.1109/NSSMIC.2009.5402190>.
- [96] G. Borghi, V. Tabacchini, and D. R. Schaart. Experimental characterization of an emulated clinical TOF-PET ring using two monolithic scintillator detector modules based on 32 mm × 32 mm × 22 mm LYSO:Ce crystals and DPC arrays. In *Presentation at the IEEE Nuclear Science Symposium Conference Record (NSS/MIC) 2015 in San Diego*, 2015.
- [97] J. Iwanowska, L. Swiderski, T. Szczesniak, P. Sibczynski, M. Moszynski, M. G., K., K. Tsutsumi, Y. Usuki, T. Yanagida, and A. Yoshikawa. Performance of cerium-doped

- Gd₃Al₂Ga₃O₁₂ (GAGG:Ce) scintillator in gamma-ray spectrometry. *Nucl Instr Meth Phys Res A*, 712:34, 2013. URL: <http://www.sciencedirect.com/science/article/pii/S0168900213001848>.
- [98] J. Glodo, W. W. Moses, W. M. Higgins, E. V. D. van Loef, P. Wong, S. E. Derenzo, M. J. Weber, and K. S. Shah. Effects of Ce concentration on scintillation properties of LaBr₃:Ce. *IEEE Trans Nucl Sci*, 52(5):1805, 2005. URL: <http://dx.doi.org/10.1109/TNS.2005.856906>.
- [99] L.M. Fraile, H. Mach, V. Vedia, B. Olaizola, V. Pazy, E. Picado, and J.M. Udias. Fast timing study of a CeBr₃ crystal: Time resolution below 120 ps at ⁶⁰Co energies. *Nucl Instr Meth Phys Res A*, 701:235, 2013. URL: <http://www.sciencedirect.com/science/article/pii/S0168900212013010>.
- [100] Philips Digital Photon Counting. *Data Sheet on the Digital Photon Counter*, 2015. available at www.digitalphotoncounting.com/wp-content/uploads/PDPC_leaflet_A4_2015_10.pdf, accessed May 2016.
- [101] Philips Digital Photon Counting. *Tile-TEK User Manual version 1.02*, 2016. available at http://www.digitalphotoncounting.com/wp-content/uploads/Tile-TEK-User-Manual-v1_02.pdf, accessed in June 2016.
- [102] V. Tabacchini, V. Westerwoudt, G. Borghi, S. Seifert, and D. R. Schaart. Probabilities of triggering and validation in a digital silicon photomultiplier. *J Instrum*, 9(06):P06016, 2014. URL: <http://stacks.iop.org/1748-0221/9/i=06/a=P06016>.
- [103] T. Frach, G. Prescher, C. Degenhardt, R. de Gruyter, A. Schmitz, and R. Ballizany. The digital silicon photomultiplier - principle of operation and intrinsic detector performance. In *2009 IEEE Nuclear Science Symposium Conference Record (NSS/MIC)*, page 1959, 2009. URL: <http://dx.doi.org/10.1109/NSSMIC.2009.5402143>.
- [104] P. C. Lopes, E. Clementel, P. Crespo, S. Henrotin, J. Huizenga, G. Janssens, K. Parodi, D. Prieels, F. Roellinghoff, J. Smeets, F. Stichelbaut, and D. R. Schaart. Time-resolved imaging of prompt-gamma rays for proton range verification using a knife-edge slit camera based on digital photon counters. *Phys Med Biol*, 60:6063, 2015. URL: <http://stacks.iop.org/0031-9155/60/i=15/a=6063>.
- [105] L. G. Hyman, R. M. Schwarcz, and R. A. Schluter. Study of high speed photomultiplier systems. *Rev Sci Instrum*, 35(3):393, 1964. URL: <http://scitation.aip.org/content/aip/journal/rsi/35/3/10.1063/1.1718829>.
- [106] M. Moszynski, M. Kapusta, M. Mayhugh, D. Wolski, and S. O. Flyckt. Absolute light output of scintillators. *IEEE Trans Nucl Sci*, 44(3):1052, 1997. URL: <http://dx.doi.org/10.1109/23.603803>.

- [107] G. Blonar, H. Dietl, J. Dobbins, G. Eigen, E. Lorenz, F. Pauss, W. Pimpl, H. Vogel, and P. Weissbach. Photodiode readout for scintillating crystals of BGO and NaI(Tl). *Nucl Instr Meth Phys Res*, 203(1):213, 1982. URL: <http://www.sciencedirect.com/science/article/pii/0167508782906299>.
- [108] H. Ishibashi, K. Shimizu, K. Susa, and S. Kubota. Cerium doped GSO scintillators and its application to position sensitive detectors. *IEEE Trans Nucl Sci*, 36(1):170, 1989. URL: <http://dx.doi.org/10.1109/23.34427>.
- [109] K. Kurashige, Y. Kurata, H. Ishibashi, and K. Susa. Monte Carlo simulation of scintillator efficiency for GSO single crystal. In *IEEE Nuclear Science Symposium and Medical Imaging Conference Record*, volume 3, page 1534, 1995. URL: <http://dx.doi.org/10.1109/NSSMIC.1995.500318>.
- [110] C. W.E van Eijk. Inorganic scintillators in medical imaging detectors. *Nucl Instr Meth Phys Res A*, 509(1-3):17, 2003. URL: <http://www.sciencedirect.com/science/article/pii/S0168900203015420>.
- [111] C. Furetta. *Handbook of Thermoluminescence*. World Scientific Publishing Co. Pte. Ltd., 2003.
- [112] S. Ra, S. Kim, H. J. Kim, H. Park, S. Lee, H. Kang, and S. H. Doh. Luminescence and scintillation properties of a CeBr₃ single crystal. *IEEE Trans Nucl Sci*, 55(3):1221, 2008. URL: <http://dx.doi.org/10.1109/TNS.2008.920253>.
- [113] A. Suzuki, S. Kurosawa, J. Pejchal, V. Babin, Y. Fujimoto, A. Yamaji, M. Seki, Y. Futami, Y. Yokota, K. Yubuta, T. Shishido, M. Kikuchi, M. Nikl, and A. Yoshikawa. The effect of different oxidative growth conditions on the scintillation properties of Ce:Gd₃Al₃Ga₂O₁₂ crystal. *Physica status solidi (c)*, 9(12):2251, 2012. URL: <http://dx.doi.org/10.1002/pssc.201200327>.
- [114] Saint Gobain. *Datasheet on CaF₂(Eu)*. available at [http://www.crystals.saint-gobain.com/uploadedFiles/SG-Crystals/Documents/CaF₂\(Eu\)%20data%20sheet.pdf](http://www.crystals.saint-gobain.com/uploadedFiles/SG-Crystals/Documents/CaF2(Eu)%20data%20sheet.pdf), accessed May 2016.
- [115] Saint Gobain. *Datasheet on PreLude 420 (LYSO)*. available at www.crystals.saint-gobain.com/uploadedFiles/SG-Crystals/Documents/PreLude%20420%20data%20sheet.pdf, accessed May 2016.
- [116] Saint Gobain. *Datasheet on BGO*. available at www.crystals.saint-gobain.com/uploadedFiles/SG-Crystals/Documents/BGO%20data%20sheet.pdf, accessed May 2016.
- [117] Saint Gobain. *Datasheet on CsI*. available at www.crystals.saint-gobain.com/uploadedFiles/SG-Crystals/Documents/CsI%28Tl%29%20and%20%28Na%29%20data%20sheet.pdf, accessed May 2016.

- [118] F. Hueso-González, C. Golnik, M. Berthel, A. Dreyer, W. Enghardt, F. Fiedler, K. Heidel, T. Kormoll, H. Rohling, S. Schöne, R. Schwengner, A. Wagner, and G. Pausch. Test of Compton camera components for prompt gamma imaging at the ELBE bremsstrahlung beam. *J Instrum*, 9(05):P05002, 2014. URL: <http://stacks.iop.org/1748-0221/9/i=05/a=P05002>.
- [119] A. Wagner, R. Beyer, M. Erhard, F. Dönaue, E. Grosse, A. Hartmann, A. R. Junghans, L. Käubler, K. Kosev, S. Mallion, C. Nair, N. Nankov, G. Rusev, K. D. Schilling, W. Schulze, and R. Schwengner. The new bremsstrahlung facility at the superconducting electron accelerator ELBE. *J Phys G Nucl Part Phys*, 31(10):S1969, 2005. URL: <http://stacks.iop.org/0954-3899/31/i=10/a=112>.
- [120] R. Schwengner, R. Beyer, F. Dönaue, E. Grosse, A. Hartmann, A.R. Junghans, S. Mallion, G. Rusev, K.D. Schilling, W. Schulze, and A. Wagner. The photon-scattering facility at the superconducting electron accelerator ELBE. *Nucl Instr Meth Phys Res A*, 555:211, 2005. URL: <http://www.sciencedirect.com/science/article/pii/S0168900205018164>.
- [121] R. Brun and F. Rademakers. ROOT - an object oriented data analysis framework. *Nucl Instr Meth Phys Res A*, 389:81, 1997. URL: <http://www.sciencedirect.com/science/article/pii/S016890029700048X>.
- [122] M. Marta, E. Trompler, D. Bemmerer, R. Beyer, C. Brogini, A. Caciolli, M. Erhard, Z. Fülöp, E. Grosse, G. Gyürky, R. Hannaske, A. R. Junghans, R. Menegazzo, C. Nair, R. Schwengner, T. Szücs, S. Vezzú, A. Wagner, and D. Yakorev. Resonance strengths in the $^{14}\text{N}(p,\gamma)^{15}\text{O}$ and $^{15}\text{N}(p,\alpha\gamma)^{12}\text{C}$ reactions. *Phys Rev C*, 81:055807, 2010. URL: <http://link.aps.org/doi/10.1103/PhysRevC.81.055807>.
- [123] Holger Nöldgen. Recent developments in Jülich with Philips Digital Photon Counting. In *Presentation at the PDPC Users Meeting in Seoul*, 2013.
- [124] J. Petzoldt, K. E. Roemer, W. Enghardt, F. Fiedler, C. Golnik, F. Hueso-González, S. Helmbrecht, T. Kormoll, H. Rohling, J. Smeets, T. Werner, and G. Pausch. Characterization of the microbunch time structure of proton pencil beams at a clinical treatment facility. *Phys Med Biol*, 61(6):2432, 2016. URL: <http://stacks.iop.org/0031-9155/61/i=6/a=2432>.
- [125] T. Kormoll, A. Duplity, W. Enghardt, S. Helmbrecht, and F. Hueso González. A beam control system for an experimental beam line operated parallel to a therapeutic beam line. *Radiother Oncol*, 110:S52, 2014. URL: <http://www.sciencedirect.com/science/article/pii/S016781401534127X>.
- [126] M. G. Payne. Energy straggling of heavy charged particles in thick absorbers. *Phys Rev*, 185:611, 1969. URL: <http://link.aps.org/doi/10.1103/PhysRev.185.611>.

- [127] D. H. Wilkinson. The phoswich - a multiple phosphor. *Rev Sci Instrum*, 23:414, 1952. URL: <http://scitation.aip.org/content/aip/journal/rsi/23/8/10.1063/1.1746324>.
- [128] C. Pastor, F. Benrachi, B. Chambon, D. Drain, A. Dauchy, A. Giorni, and C. Morand. Detection of charged particles with a phoswich counter. *Nucl Instr Meth Phys Res*, 212:209, 1983. URL: <http://www.sciencedirect.com/science/article/pii/0167508783906932>.
- [129] S. Helmbrecht, P. Kuess, W. Birkfellner, W. Enghardt, K. Stützer, D. Georg, and F. Fiedler. Systematic analysis on the achievable accuracy of PT-PET through automated evaluation techniques. *Z Med Phys*, 25(2):146, 2015. URL: <http://www.sciencedirect.com/science/article/pii/S0939388914000993>.
- [130] M. Morháč, J. Kliman, V. Matoušek, M. Veselský, and I. Turzo. Efficient one- and two-dimensional gold deconvolution and its application to γ -ray spectra decomposition. *Nucl Instr Meth Phys Res A*, 401:385, 1997. URL: <http://www.sciencedirect.com/science/article/pii/S0168900297010589>.
- [131] K. Gunzert-Marx, H. Iwase, D. Schardt, and R. S. Simon. Secondary beam fragments produced by 200 MeV/u ^{12}C ions in water and their dose contributions in carbon ion radiotherapy. *New J Phys*, 10(7):075003, 2008. URL: <http://stacks.iop.org/1367-2630/10/i=7/a=075003>.
- [132] P. Krizan. Advances in particle-identification concepts. *J Instrum*, 4(11):P11017, 2009. URL: <http://stacks.iop.org/1748-0221/4/i=11/a=P11017>.
- [133] M.J. Berger, J.H. Hubbell, S.M. Seltzer, J. Chang, J.S. Coursey, R. Sukumar, D.S. Zucker, and K. Olsen. XCOM: Photon Cross Sections Database. NIST Standard Reference Database 8 (XGAM). *NIST*, 2015. URL: <http://www.nist.gov/pml/data/xcom/index.cfm>.
- [134] Target Systemelektronik. *Technical Data Target U100*, 2016. available at http://target-sg.com/fileadmin/target/documents/Target_Technical-Data-U100.pdf, accessed July 2016.
- [135] Target Systemelektronik. *Brochure Target U100*, 2016. available at <http://target-sg.com/fileadmin/target/documents/U100-brochure.pdf>, accessed July 2016.
- [136] A. Rinscheid. *Characterization of a fast timing and energy spectroscopy system for real-time range verification in particle therapy*. Zwischenbericht zur Masterarbeit, Martin-Luther-Universität Halle-Wittenberg, 2016.
- [137] J. Berthold. *Analyse von Pencil Beam Bestrahlungen für die Reichweitenkontrolle in der Protonentherapie mittels Prompt Gamma Timing*. Bachelor thesis, Technische Universität Dresden, 2015.

- [138] F. Hueso-González. *Nuclear methods for real-time range verification in proton therapy based on prompt gamma-ray imaging*. PhD thesis, Technische Universität Dresden, 2015. URL: http://www.qucosa.de/fileadmin/data/qucosa/documents/20498/PhD_Thesis_FHG_public.pdf.

Publications

The work presented in this thesis is based on research carried out at the National Center for Radiation Research in Oncology, OncoRay, Dresden.

The following publication appeared in the process:

- 1) J. Petzoldt, K. E. Roemer, W. Enghardt, F. Fiedler, C. Golnik, F. Hueso-González, S. Helmbrecht, T. Kormoll, H. Rohling, J. Smeets, T. Werner, and G. Pausch. "Characterization of the microbunch time structure of proton pencil beams at a clinical treatment facility". In: *Phys Med Biol*, 61(6):2432, 2016. URL: <http://stacks.iop.org/0031-9155/61/i=6/a=2432>.

Danksagungen

Diese Arbeit wäre nicht ohne die zahlreiche Hilfe von vielen Kollegen, Freunden und meiner Familie entstanden. Zuallererst möchte ich mich bei Guntram Pausch für die exzellente Betreuung während meiner Doktorandenzeit bedanken und dass ich in einem so angenehmen und familiären Umfeld arbeiten durfte.

Ich danke Kai Zuber und Wolfgang Enghardt dafür, dass ich meinen wissenschaftlichen Interessen frei von Zwängen folgen und meine Arbeit auf internationalen Konferenzen vorstellen konnte.

Ein besonderer Dank geht an Katja, Fernando, Christian und Thomas, die mir nicht nur viel über Analogelektronik, Programmieren und ROOT beigebracht haben, sondern mir auch bei Experimenten und vielen Nachtschichten immer zur Seite standen. Theresa danke ich für die vielen von Kaffee begleiteten Diskussionen rund um Protonen und Politik. Ein großer Dank geht an Anne und Manfred, die mir erst mit ihren vielen mechanischen Konstruktionen die experimentelle Arbeit ermöglicht haben. Danke auch an David, der sogar noch am Abend vor der Strahlzeit mein Equipment repariert hat.

Ich möchte mich bei den Kollegen aus dem Doktorandenraum (Patrick, Sonja, Andreas, Stefan, Malte, Lena und Nagwa) für die entspannte, freundliche und lustige Atmosphäre bedanken. Vielen Dank auch an Jonathan und Andreas für die tolle Zusammenarbeit, ich hoffe ihr habt mindestens so viel gelernt wie ich. Den Mitarbeitern des OncoRay und des HZDR möchte ich für die viele Hilfe und die Unterstützung danken.

Ein großer Dank geht an meine Eltern und meine Schwester, ohne eure Unterstützung würde ich nicht dort stehen, wo ich jetzt bin. Richard und Jördis, euch möchte ich für die vielen aufmunternden Gespräche danken, vor allem in Zeiten nachlassender Motivation.

Meiner liebsten Johanna danke ich für ihre Geduld und ihr Verständnis, ohne dich wäre das alles nicht möglich gewesen.

Erklärung

Hiermit versichere ich, dass ich die vorliegende Arbeit ohne unzulässige Hilfe Dritter und ohne Benutzung anderer als der angegebenen Hilfsmittel angefertigt habe. Die aus fremden Quellen direkt oder indirekt übernommenen Gedanken sind als solche kenntlich gemacht. Die Arbeit wurde bisher weder im Inland noch im Ausland in gleicher oder ähnlicher Form einer anderen Prüfungsbehörde vorgelegt.

Die Arbeit wurde unter der wissenschaftlichen Betreuung von Prof. Dr. Wolfgang Enhardt und Dr. Guntram Pausch am National Center for Radiation Research in Oncology, OncoRay, Dresden, angefertigt.

Es haben keine früheren erfolglosen Promotionsverfahren stattgefunden.

Ich erkenne die Promotionsordnung der Fakultät Mathematik und Naturwissenschaften an der Technischen Universität Dresden vom 23.02.2011 in der Fassung vom 18.06.2014 an.

Johannes Petzoldt

Dresden, den 11. November 2016